PASSIVE MODE-LOCKING OF TE CO_2 LASERS

PASSIVE MODE-LOCKING OF TE CO_2 LASERS

by

RODERICK STEWART TAYLOR, B.Sc., M.Sc.

A Thesis
Submitted to the School of Graduate Studies
in Partial Fulfilment of the Requirements
for the Degree
Doctor of Philosophy

McMaster University
1977

DOCTOR OF PHILOSOPHY (1977)
(Physics)

McMASTER UNIVERSITY
Hamilton, Ontario

TITLE: Passive Mode-Locking of TE CO_2 Lasers

AUTHOR: Roderick Stewart Taylor, B.Sc. (Carleton University)
M.Sc. (McMaster University)

SUPERVISORS: Professor B.K. Garside, Professor E.A. Ballik

NUMBER OF PAGES: xiv, 245

SCOPE AND CONTENTS

It was the purpose of the work described in this thesis to develop a basic understanding of the passive mode-locking behaviour of TE CO_2 lasers employing the saturable absorbers SF_6 and germanium (Ge). An understanding of the dynamical processes, which occur in the gain and loss media on sub-ns to μs time scales, is necessary in order to predict the output characteristics of mode-locked pulse trains. In the case of SF_6 the complex dynamical behaviour was not known previous to our work. Therefore, a large portion of this thesis is devoted to investigating such processes. Transmission measurements, using ∿200 ns TE CO_2 laser pulses, are used to obtain the first complete measurements of the saturation characteristics of SF_6. The experiments are performed for a range of CO_2 wavelengths which characterize the entire SF_6 absorption at the 10.4 μm band (P(12) - P(28)) and for a range of SF_6 gas pressures which are most frequently used in SF_6-CO_2 mode-locking systems. These experiments demonstrate that, for low J-value CO_2 lines (less than P(24)), the rise in transmission at increased pulse intensities is due to intensity saturation effects. The pressure dependence of the saturation curves indicates that the level relaxation rates scale with SF_6 pressure. However, for CO_2 lines greater than P(22) (longer wavelength), the transmission curves and the transmitted pulse shaping cannot be accounted for solely by intensity saturation effects. It is shown that a multi-vibrational and rotational level treatment for the absorption of CO_2 radiation by SF_6

can fully account for the discrepancies between theory and experiment observed at longer CO_2 wavelengths. The model treats all the SF_6 vibrational and rotational levels as belonging to a bath of levels characterized by a single vibrational and a single rotational temperature. Energy absorbed from a laser pulse is rapidly distributed to the bath of levels, establishing new vibrational and rotational populations characteristic of a higher bath temperature. This type of absorption process depends on the energy rather than the intensity, of the laser pulse. Such a model, although expected to apply only at high SF_6 pressures (where fast equilibration times exist), can in fact be used to predict double-resonance signals observed at low SF_6 pressures (1-10 Torr). Infrared double-resonance experiments with mode-locked pump pulse trains and with ∿200 ns duration pump pulses demonstrate that the success of the model at these low pressures is due to very fast vibration-to-vibration and rotational energy transfer rates. The observed rates are much faster than those reported in the literature. It is shown that this heating model, combined with the previously mentioned intensity saturation processes, fully describes the transmission data for the wide range of CO_2 rotational lines and SF_6 pressures employed. This thesis also demonstrates that the mode-locking of a TE CO_2 laser using an SF_6 saturable absorber, can, for the first time, be understood from a knowledge of the above intensity saturation and vibrational bath heating effects. The mode-locking with SF_6 is reported over the widest range of CO_2 rotational lines and with the shortest pulse durations obtained to date. Pulse narrowing across the mode-locked pulse train (usually necessary to obtain

very short pulses) is absent in the SF_6-CO_2 mode-locking system. It is indicated that processes such as multi-level saturation, vibrational bath heating and multiple-photon absorptions may prevent such narrowing from occuring.

The mode-locking behaviour of p-type Ge is also investigated in this thesis. Computer simulations of the evolution of mode-locked pulses from noise are presented using a 2-vibrational level model, which includes rotational coupling, to describe the CO_2 amplifier. A steady-state inhomogeneously broadened saturation response is shown to be appropriate for the Ge absorber. A set of density equations is used to describe the growth of the pulse intensities in the amplifier. For the first time a theory is presented which quantitatively predicts the experimentally observed pulse narrowing across the mode-locked pulse trains, the pulse intensities and shape of the mode-locked train envelope. It is also shown that there is a progression from deterministic mode-locking at laser pressures of ∿300 Torr to statistical mode-locking at pressures substantially in excess of this pressure. Furthermore it is demonstrated that there is an optimum value in how close to lasing threshold one can operate to achieve repeatable, clean, short-duration, high intensity mode-locked laser pulses. In addition, it is shown that too large a linear loss cavity and/or too low a ratio of the non-linear to linear loss is detrimental to the production of short-duration pulses. It is also indicated that a laser cavity which diverges the laser beam at the absorber must be used to obtain optimum mode-locking for high pressure lasers (e.g., 5 atm). The choice of the correct cavity is the single most important consideration neces-

sary to achieve stable short-duration (< 100 ps) mode-locked pulses at these pressures. A comparison is given between the mode-locking performances of SF_6 and Ge. The ability of Ge to produce multi-line, multi-band mode-locked pulses with sub-ns duration makes it a more viable saturable absorber than SF_6 for use in low intensity mode-locked oscillators.

ACKNOWLEDGEMENTS

I would sincerely like to thank my supervisors, Dr. E.A. Ballik and Dr. B.K. Garside for the considerable guidance that they have given me in the course of this work. I would also like to thank my colleague T.A. Znotins for his important contribution in the construction of the vibrational bath heating model. Finally, my thanks go to my wife, Margie who gave me a great deal of support throughout this thesis.

TABLE OF CONTENTS

Page

CHAPTER 1 INTRODUCTION

1.1 Mode-Locking Concepts 1

1.2 CO_2 Lasers and Mode-Locking 5

1.3 Saturable Absorbers for CO_2 Mode-Locking 10

1.4 Outline of the Contents of the Thesis 10

CHAPTER 2 EXPERIMENTAL APPARATUS

2.1 Introduction 14

2.2 TE CO_2 Lasers 14

2.3 3-Mirror Laser Cavity 30

2.4 Adjustable Thickness Gas Cell 32

2.5 Detection Apparatus 33

2.6 Summary 34

CHAPTER 3 SMALL-SIGNAL AND LARGE-SIGNAL ABSORPTION IN SF_6

3.1 Introduction 36

3.2 Small-Signal Absorption Measurements 37

3.3 Large-Signal Absorption Measurements 43

CHAPTER 4 A VIBRATIONAL BATH MODEL FOR THE DYNAMICS OF SF_6 ABSORPTION NEAR 10.4 μm AS A FUNCTION OF WAVELENGTH AND ABSORBED ENERGY

4.1 Introduction 64

4.2 Vibrational Bath Model 66

4.3 Experimental 73

4.4 Results and Observations 78

4.5 Summary 90

Page

CHAPTER 5 HIGH PRESSURE SF_6 PULSE TRANSMISSION NEAR 10.4 μm

5.1 Introduction 93

5.2 Experimental 95

5.3 Results and Discussion 96

5.4 Summary 108

CHAPTER 6 MODE-LOCKING PROPERTIES OF GASEOUS SF_6

6.1 Introduction 110

6.2 Experimental Conditions for Stable Mode-Locking 111

6.3 Mode-Locking Observations and Discussions 116

6.4 Sub-ns Pulse Generation 123

6.5 Summary 129

CHAPTER 7 INVESTIGATION OF PASSIVE MODE-LOCKING USING A GERMANIUM SATURABLE ABSORBER - PART I

7.1 Introduction 132

7.2 Theoretical Model of Passive Mode-Locking 134

7.3 Noise Fluctuation Model 146

7.4 Summary 152

CHAPTER 8 INVESTIGATION OF PASSIVE MODE-LOCKING USING A GERMANIUM SATURABLE ABSORBER - PART II

8.1 Introduction 154

8.2 Brewster Angle Experiments 155

8.3 2-Mirror Cavity Experiments 162

8.4 Initial Conditions for the Comparison of Theory and Experiment 164

8.5 Influence of the Beam Area Parameter (m_0^2) on Mode-Locking 169

Page

8.6 Influence of Rotational Coupling on Mode-Locking 177

8.7 Influence of Gain on Mode-Locking 182

8.8 Influence of Linear Loss on Mode-Locking 189

8.9 Influence of Non-Linear Loss on Mode-Locking 194

8.10 Mode-Locking as a Function of Laser Gas Pressure 197

8.11 Pressure Scalability of the Mode-Locked Output Characteristics 203

8.12 Influence of Cavity Length on Mode-Locking 203

8.13 Comparison of SF_6 and Ge as Passive Mode-Lockers 204

8.14 Summary 207

CHAPTER 9 CONCLUSIONS 210

APPENDIX A CALCULATION OF 3-MIRROR CAVITY PARAMETERS 216

APPENDIX B FINITE DIFFERENCE METHOD 219

APPENDIX C BAND CONTOUR MODEL 224

APPENDIX D CONVERSION OF ELECTRIC FIELD AMPLITUDE TO INTENSITY 228

APPENDIX E CALCULATION OF THE INTENSITY OF SPONTANEOUS EMISSION 230

APPENDIX F CALCULATION OF NOISE PULSE BROADENING IN THE LINEAR AMPLIFICATION REGION 232

REFERENCES 238

LIST OF FIGURES

		Page
Fig. 1-1	Typical non-mode-locked and partially mode-locked pulse outputs from a 1 atm TE CO_2 laser	3
Fig. 1-2	Detailed transition diagram of laser oscillations in the 10.4 µm and 9.4 µm bands of CO_2	7
Fig. 1-3	Oscilloscope display of a typical TE CO_2 laser pulse	8
Fig. 1-4	Multiple exposure photograph of 10 consecutive mode-locked laser pulse trains	9
Fig. 2-1	Schematic diagram of the discharge circuit used for the double-discharge laser	18
Fig. 2-2	Photograph of a resistor pin-to-pin helical laser	20
Fig. 2-3	Photograph of two double-discharge modules	22
Fig. 2-4	Displays of the preionization and main current pulses	25
Fig. 2-5	Photograph of a typical laser discharge	27
Fig. 2-6	Plot of the small-signal gain as a function of the input electrical energy to the discharge	29
Fig. 2-7	Schematic diagram of the 3-mirror laser resonator	31
Fig. 3-1	Small-signal absorption as a function of SF_6 pressure	40
Fig. 3-2	Small-signal absorption as a function of SF_6 pressure	41
Fig. 3-3	SF_6 small-signal absorption as a function of wavenumber	44
Fig. 3-4	Four energy-level scheme for absorption in SF_6	49
Fig. 3-5	Transmission as a function of input intensity for the P(16), P(20), P(22), P(24) and P(26) CO_2 lines at an SF_6 pressure of 50 Torr	52

Page

Fig. 3-6 Transmission as a function of input intensity for the P(14) CO_2 line for various SF_6 pressures 54

Fig. 3-7 Transmission as a function of input intensity for the P(20) CO_2 line for various SF_6 pressures 57

Fig. 3-8 Transmission as a function of input intensity for the P(26) CO_2 line at various SF_6 pressures 59

Fig. 3-9 Multiple exposure photograph of four transmitted pulse shapes for the P(26) CO_2 line at an SF_6 pressure of 50 Torr 61

Fig. 4-1 Energy level diagram for SF_6 67

Fig. 4-2 Absorption coefficient as a function of vibrational temperature for selected CO_2 rotational lines 70

Fig. 4-3 Vibrational energy (above the ground state) for P, Q and R cross-section maxima as a function of CO_2 wavenumber 71

Fig. 4-4 Schematic diagram of the experimental double-resonance apparatus 74

Fig. 4-5 Typical double-resonance signals 76

Fig. 4-6 Absorption as a function of CO_2 wavenumber for double-resonance experiments using a P(26) pump pulse and 50 Torr of SF_6 80

Fig. 4-7 A comparison of experimental P(26) pump double-resonance curves at various CO_2 probe rotational lines with those predicted by the heating model 82

Fig. 4-8 Double-resonance signals to obtain information on energy transfer rates 86

Fig. 4-9 Mode-locked double-resonance signals to obtain information on energy transfer rates 89

Fig. 5-1 Transmission of SF_6 as a function of input intensity at the P(26) CO_2 line, showing theoretical calculations employing the vibrational bath heating model 94

Fig. 5-2 Comparison of theoretical (heating model) and experimental P(26) transmitted pulse shapes 99

Page

Fig. 5-3 Transmittance data at the P(14) CO_2 line for high SF_6 pressures together with the vibrational bath model predictions 102

Fig. 5-4 Transmittance data at the P(20) CO_2 line for high SF_6 pressures together with the vibrational bath model predictions 103

Fig. 5-5 Transmission of SF_6 as a function of input intensity at the P(28) CO_2 line, showing theoretical calculations employing the vibrational bath heating model 104

Fig. 5-6 Transmitted pulse shaping of a P(26) mode-locked pulse train 105

Fig. 5-7 Transmitted pulse shaping of a P(20) mode-locked pulse train 107

Fig. 6-1 Simultaneous mode-locked and Q-switched output at the P(26) CO_2 wavelength using an SF_6 saturable absorber 119

Fig. 6-2 Plot of SF_6 gas cell pressure as a function of the ratio of the laser beam area at the amplifier to that at the absorber necessary to obtain Q-switched outputs 121

Fig. 6-3 Photograph of two pulses from a mode-locked TEA CO_2 laser operating at the P(20) wavelength and with an SF_6 saturable absorber 125

Fig. 7-1 Schematic diagram of the laser cavity 135

Fig. 7-2 Temporal gain profile for a 1 atm CO_2 laser 137

Fig. 8-1 Plot of $\ell n(I_{IN}/I_{OUT})$ as a function of, $I_{IN} - I_{OUT}$, for Ge 159

Fig. 8-2 Variation of the theoretical output peak intensity as a function of the number of round trips for different m_0^2 values 171

Fig. 8-3 Comparison of theoretical and experimental pulse narrowing (FWHM) as a function of the number of round trips for different m_0^2 values 174

Fig. 8-4 An experimentally observed mode-locked pulse obtained from the pulse train tail for $m_0^2 = 4.5$ 176

Page

Fig. 8-5 Plot of the normalized vibrational inversion, D_2-D_1, as a function of time for various values of m_o^2 178

Fig. 8-6 Plot of the normalized vibrational inversion, D_2-D_1, and the normalized rotational population inversion $\delta^{J_o}/\kappa(J_o)$ as a function of time 180

Fig. 8-7 Theoretical prediction for the output pulse at the peak of the mode-locked train for $m_o^2 = 18.0$ 181

Fig. 8-8 Plot of mode-locked pulse energy as a function of the number of round trips for a 250 Torr CO_2 amplifier for various values of τ_R 183

Fig. 8-9 Theoretical predictions for the output peak intensity with the number of round trips for various values of $g_{max}L_a$ 185

Fig. 8-10 Plot of the theoretical prediction of pulse discrimination (D) as a function of $g_{max}L_a$ 187

Fig. 8-11 Theoretical and experimental pulse narrowing (FWHM) as a function of the number of round trips for various values of $g_{max}L_a$ 188

Fig. 8-12 Theoretical predictions for the output peak intensity with round trip number as a function of the linear loss (R^A) 190

Fig. 8-13 Comparison of an experimentally observed and theoretically predicted mode-locked pulse train 192

Fig. 8-14 Theoretical and experimental pulse narrowing (FWHM) as a function of the number of round trips for various values of R^A 193

Fig. 8-15 Variation of the theoretical output peak intensity as a function of the number of round trips for different values of $\alpha_o L^B$ 195

Fig. 8-16 Theoretical and experimental pulse narrowing (FWHM) as a function of the number of round trips for a range of non-linear loss values $\alpha_o L^B$ 196

Fig. 8-17 Experimentally observed mode-locked train output from a 250 Torr amplifier 199

Fig. 8-18 Theoretical predictions for the output intensity of a 5 atm CO_2 laser for m_o^2 values of 1.8(a) and 0.36(b) 202

LIST OF TABLES

		Page
Table 2-1	A summary of the double-discharge laser parameters	24
Table 3-1	SF_6 small-signal absorption coefficients for the P(20) CO_2 line	45
Table 3-2	Four-level model parameters appropriate to 50 Torr of SF_6	55
Table 8-1	Ge mode-locking parameters	172
Table 8-2	Comparison of Ge and SF_6 mode-lockers	206

CHAPTER 1

INTRODUCTION

1.1 Mode-Locking Concepts

For a laser resonator consisting of two mirrors, at a fixed separation L, one can identify a set of longitudinal (axial) modes ($\sim 10^5$ - 10^6 for a typical laser resonator) which have different electromagnetic field distributions. Each of these modes is an integer number of half wavelengths along the laser axis. The axial modes are separated in frequency by $\sim c/2L$, where c is the speed of light. However lasing action only occurs for a limited number of modes; these lie in the frequency region where the gain exceeds the cavity losses. For each of the longitudinal modes there exists a set of solutions for the light energy inside the resonator each of which gives a different energy distribution normal to the resonator axis. These solutions are called the transverse modes of the resonator. The lowest order mode has a Gaussian intensity distribution and is refered to as the fundamental mode (TEM_{00}). Since the higher transverse modes spread out from the resonator axis (inside the resonator), it is possible to isolate the fundamental mode by inserting a circular aperture inside the resonator. This introduces significant diffraction losses to all modes but the fundamental one. The output characteristics of the laser depends on the relative phases, amplitudes and frequencies of all the oscillating modes. If there are no processes to provide a fixed relationship between these parameters, then the output will vary in an unpredictable manner. The laser output for pulsed laser operation (which will be dealt with in this thesis) is characterized by a series of variable intensity spikes with a 2L/c periodicity similar to those shown in the top three photographs of Fig. 1-1.* On the other hand, if the oscillating modes are forced to have fixed relationships with each other, then the laser is said to be mode-locked or phase-locked [1]. A laser operating on a single longitudinal mode can exhibit mode-locking of the transverse modes (transverse mode-locking) [2]. However, for all the mode-locking experiments in this thesis, we always selected the TEM_{00} transverse mode. Consequently, we deal only with the locking of the longitudinal modes.

Under certain conditions, non-linear effects associated with the interaction of the gain medium and the laser radiation may result in fixed phase relations between oscillating modes. When this action occurs in the absence of any other mode-locking element the laser is said to be "self-locked". Stable self-locking has been observed for a number of lasers [3,4]. However, for a large number of pulsed lasers the self-locked output tends to be eratic. Consequently, it is usually necessary to introduce an extra element into the laser cavity to achieve good mode-locking. When the element is controlled external to the laser cavity the laser is said to be "actively mode-

---

* The photographs are appropriate to non-mode-locked and partially mode-locked outputs from a pulsed TE CO_2 laser operating at a laser pressure of 1 atm and with a SF_6 saturable absorber.

Fig. 1-1

Typical non-mode-locked and partially mode-locked pulse outputs from a 1 atm TE CO_2 laser. The cavity round trip time is ~20 ns.

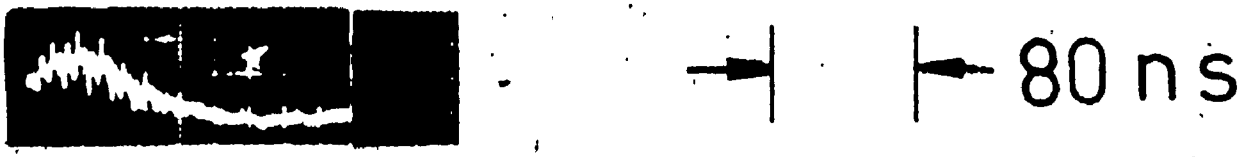
80 ns

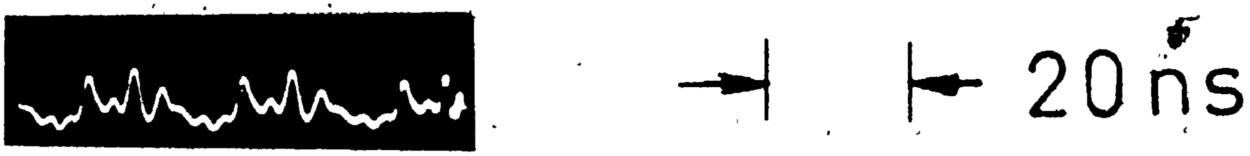
20 ns

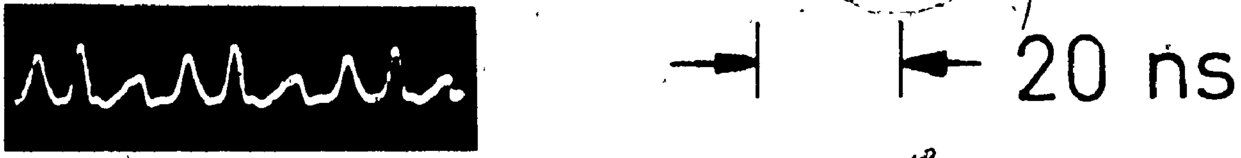
20 ns

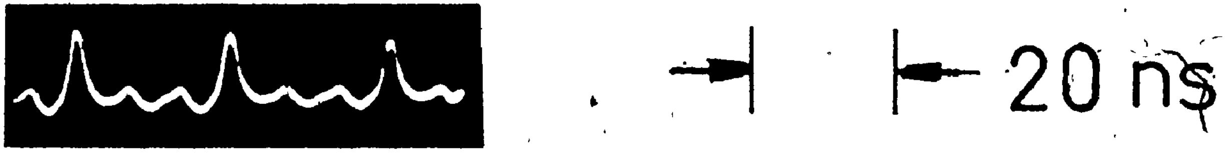
20 ns

locked". The externally driven device periodically modulates the cavity loss (amplitude modulation (am)) or the refractive index (phase modulation (pm)). The modulation is typically driven at a frequency which is equal to, or integrally related to, the laser cavity axial mode frequency difference (c/2L) and results in the production of a single pulse per 2L/c round trip time [5]. Such systems have the advantage that the mode-locking process can be electronically controlled. This control results in stable reproducible mode-locked pulses. An alternative technique is to insert a passive element called a saturable absorber inside the laser resonator. A saturable absorber is a material whose small-signal absorption is reduced as the incident light intensity is increased. For a 2-level homogeneously broadened absorber which possesses an absorption cross-section σ and an effective level recovery time T_1, saturation occurs when the stimulated absorption rate σI (where I is the input intensity at the absorber) approaches the rate at which the absorber populations can return to equilibrium (i.e., $1/T_1$). An intensity saturation parameter I_s for the homogeneous saturable absorber case is a measure of the intensity needed to reduce the small-signal absorption coefficient by a factor of 2 [6]. The production of a mode-locked "state" using a saturable absorber can best be understood in the time domain. Noise fluctuations are produced from spontaneous emission in the amplifying medium. The most intense fluctuation experiences the least loss on passage through the saturable absorber. After a considerable number of such passes, the filtering action of the absorber allows only a single high intensity pulse to propagate in the laser cavity. A necessary condition for these absorbers is that the effective recovery time of the absorption must be less than the cavity round trip time in order to produce a periodic set of pulses separated by 2L/c. The relationship between the absorber and gain medium saturation, and the relative amounts of saturable absorber loss to linear cavity loss, are also important consideration in the mode-locking process. Saturable absorbers have been successfully used to mode-lock a wide variety of laser systems. For example, mode-locking has been achieved with Nd:glass lasers [7], flashlamp-pumped dye lasers [8] and TE CO_2 gas lasers [9]. The mode-locked pulse durations obtained using passive mode-locking techniques are usually shorter than those obtained by active means [10]. It is also possible, with saturable absorbers, to produce reproducible mode-locked trains, on a laser pulse-to-pulse basis, without the use of an externally driven modulation system. Such modulation systems are often expensive and in many cases are subject to severe noise pick-up (for e.g., due to high voltage laser discharges).

1.2 CO_2 Lasers and Mode-Locking

In the early 1970's a dramatic range of pulsed CO_2 laser powers became available with the invention of the transversely excited atmospheric pressure (TEA) CO_2 laser [11]. In this system the electrical discharge occurs transversely (rather than longitudinally) to the laser axis. The reduced discharge length meant that high laser pressures could be used at easily attainable discharge voltages. The higher CO_2 laser pressure and therefore the increased gain bandwidth, allows for the possibility of obtaining very short mode-locked laser pulses [12].

An energy level diagram for the CO_2 molecule is shown in Fig. 1-2. The research in this thesis deals only with transitions in the 10.4 μm band. Mode-locking experiments were usually performed with the P(20) transition (10.59 μm), which has the most gain in the 10.4 μm band under normal operating conditions. A typical Q-switched TEA CO_2 laser pulse is shown in Fig. 1-3. When a fast risetime (i.e., <<2L/c) oscilloscope is used the pulse is not temporally smooth, but consists of a set of pulses of fluctuating intensity, similar to those shown in Fig. 1-1. Self-locking of CO_2 lasers to produce an output resembling the bottom photograph in Fig. 1-1 has been reported [13]. The stability of the output pulses can be improved by using active mode-locking techniques [14, 15] or by using saturable absorbers [16, 17, 18]. A typical mode-locked train, obtained with a saturable absorber, is shown in Fig. 1-4. Pulse durations, using both these techniques (with a TEA CO_2 laser), are usually ∿1 ns. The main application of such short duration CO_2 pulses is in the study of the interaction of laser radiation with plasmas. In particular there is interest in using CO_2 pulses as starting pulses for long chain amplifiers to initiate controlled thermonuclear fusion. Short pulses can also be used as probes to obtain information on the vibrational and rotational energy coupling rates of molecules which absorb CO_2 radiation.

Fig. 1-2

Detailed transition diagram of laser oscillations in the 10.4 μm and 9.4 μm bands of CO_2.

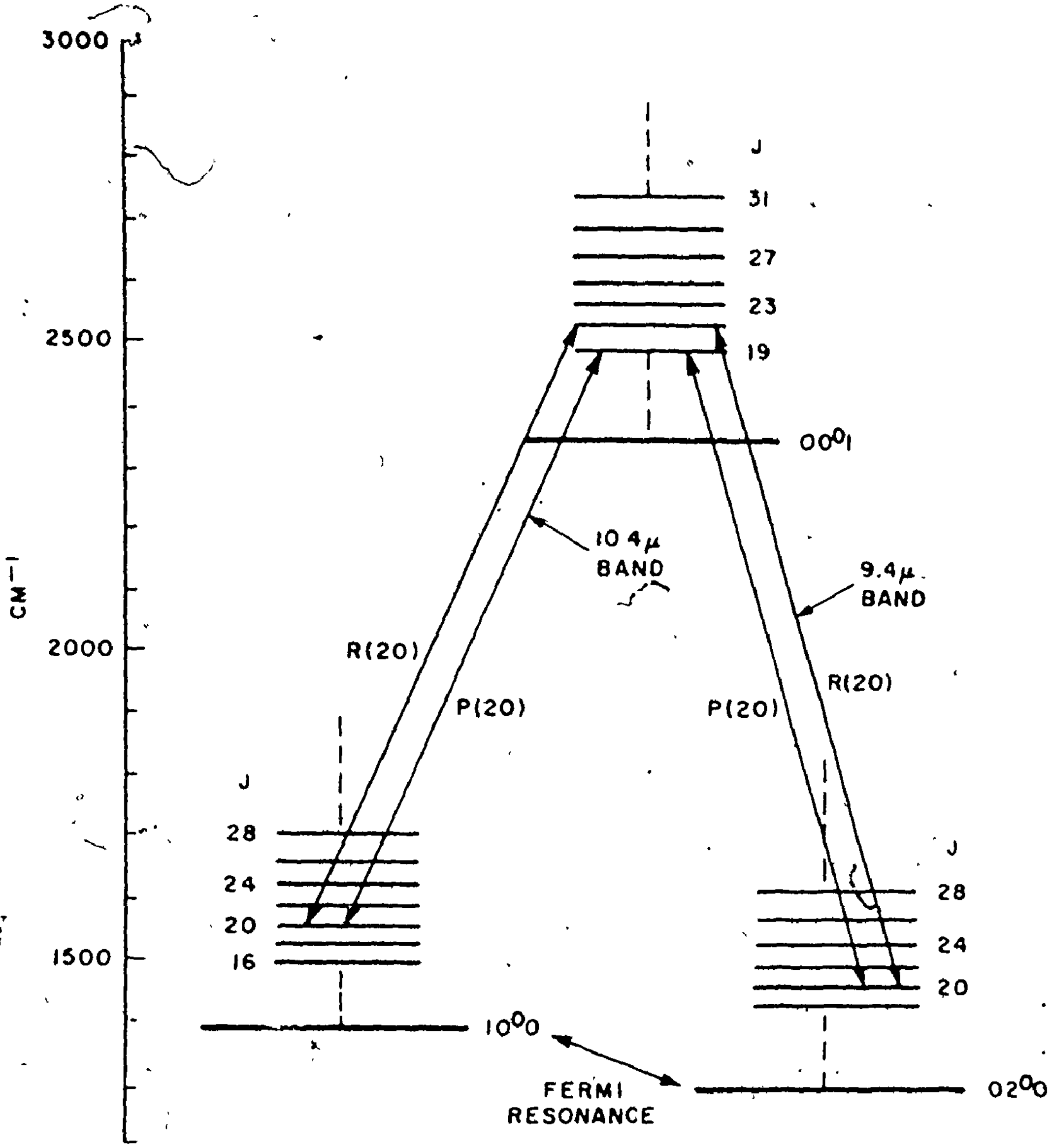
3000
2500
2000
1500
CM⁻¹
J
31
27
23
19
00^01
10.4μ BAND
9.4μ BAND
R(20)
P(20)
P(20)
R(20)
J
28
24
20
16
J
28
24
20
10^00
FERMI RESONANCE
02^00

Fig. 1-3

Oscilloscope display of a typical TE CO_2 laser pulse. The time scale is 100 ns per division. The pulse profile appears smooth, since the risetime of the oscilloscope (Tektronix 547) is nearly equal to the cavity round trip time (∿20 ns) and therefore intensity fluctuations are averaged out.

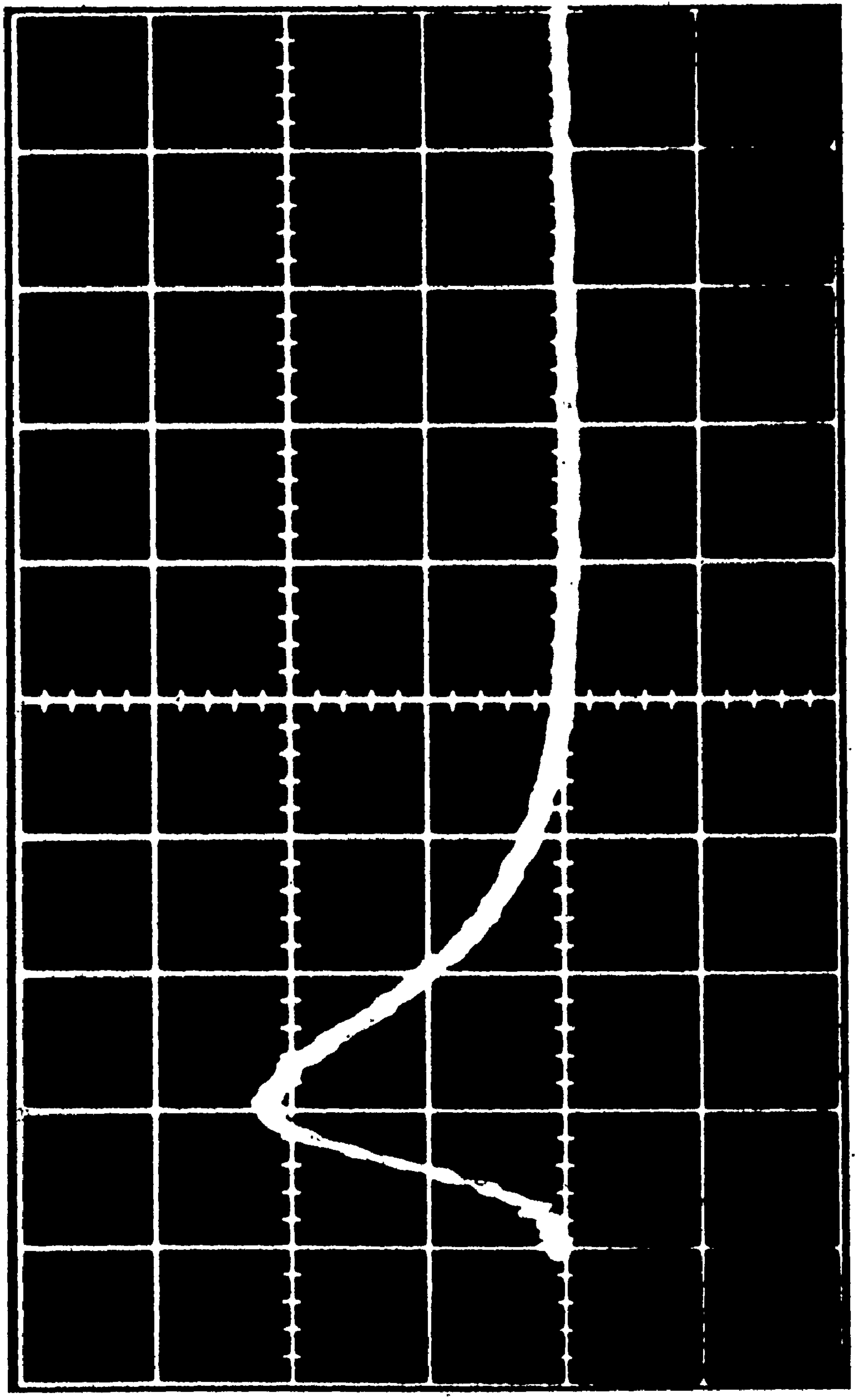

Fig. 1-4

Multiple exposure photograph of 10 consecutive mode-locked laser pulse trains. The pulse trains were obtained using a TE CO_2 laser and a SF_6 saturable absorber. The cavity round trip time is ∿20 ns.

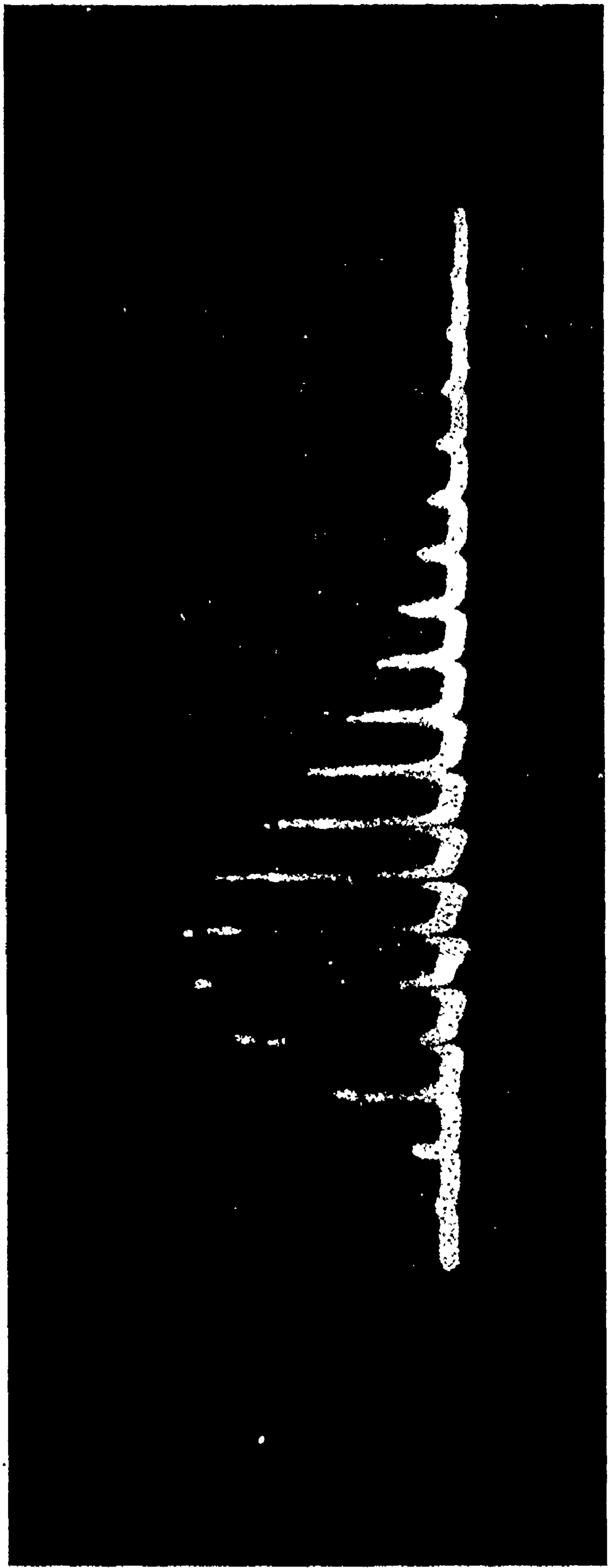

1.3 Saturable Absorbers for CO_2 Mode-Locking

The two saturable absorbers used for this thesis are solid p-type Ge and gaseous SF_6. Ge was selected for investigation since its very fast relaxation time (a few ps [19]) indicated that it had considerable potential for producing very short CO_2 laser pulses.* Although short pulses have been produced in recent years [12,21] the full potential of the absorber has not been utilized. SF_6** was selected as being representative of the class of gaseous saturable absorbers and it has previously been used to mode-lock CO_2 lasers [22]. Other gases, such as $BC\ell_3$ [18] and N_2F_4 [18], have also been used to mode-lock CO_2 lasers but not as frequently as SF_6. This is partly due to the fact that SF_6 is non-caustic, non-flammable, non-poisonous, relatively inexpensive, and readily available. It also possesses a very large absorption at the 10.4 μm band. In addition, the spectroscopy of the SF_6 molecule is well known [23].

1.4 Outline of the Contents of the Thesis

The primary purpose of this thesis is to understand the passive mode-locking behaviour of TE CO_2 lasers employing SF_6 and p-type Ge as saturable absorbers. SF_6 and Ge have both been used to mode-lock TE CO_2 lasers [17,24]. However, basic studies concerning their saturable absorber properties, and how they relate to the production of mode-locked pulses, were lacking. For example, there was very little reliable information on the two important saturable absorber parameters of SF_6, the small-signal absorption and the intensity saturation parameters. Furthermore, there was little known about the dynamics of the SF_6 absorption on a sub-ns to μs time scale, which is necessary to understand the mode-locking process. For Ge there was some debate as to whether the saturation behaviour was homogeneously or inhomogeneously broadened [20]. In addition, there had not been a study of the basic processes involved in the production of mode-locked pulses from spontaneous emission in CO_2 lasers. The effects of varying the laser, absorber and resonator parameters on the production of short laser pulses had not been demonstrated.

---

* The absorption of 10.4 μm radiation in p-type Ge results in the transition of holes from the heavy to the light hole band [20].

** SF_6 is a spherical top molecule (of O_h symmetry) which possesses 15 vibrational degrees of freedom. Due to level degeneracies it has 6 normal modes of vibration. Two of the modes (ν_3 and ν_4) are infrared active. The ν_3 fundamental vibration is triply degenerate and absorbs strongly at 10.4 μm.

In this thesis we present accurate measurements of the small-signal absorptions and saturation parameters for SF_6 and Ge over a wide range of CO_2 wavelengths. The dynamical behaviour of SF_6 is investigated on a ns to μs time scale for the wide range of SF_6 pressures used in mode-locking experiments (10-400 Torr). Finally the theoretical evolution of mode-locking from noise is described in detail and compared to experiments using a Ge saturable absorber.

The apparatus used for the above measurements, as well as for all the mode-locking experiments, is described in Chapter 2. The first part of Chapter 3 describes measurements of the small-signal absorption coefficient for SF_6 over a wide range of CO_2 rotational lines and SF_6 pressures. The second part describes large-signal transmission measurements using ∿200 ns TE CO_2 laser pulses. The data is interpreted in terms of a 4-level non-steady state absorption model to obtain information on the level recovery times, cross-sections, and hence on the saturation parameters. The absorption properties of SF_6 cannot be completely accounted for by this 4-level treatment. In Chapter 4 a multi-level vibrational bath model is presented, which provides much better agreement between theory and experiment. Infrared double-resonance experiments, outlined in Chapter 4, provide information on the energy coupling rates to the many vibrational and rotational levels. These experiments determine the range of validity (i.e., SF_6 pressures and pulse durations) of the vibrational bath model. Chapter 5 shows that the vibrational bath model can completely describe the high pressure transmission data for all the CO_2 rotational lines studied. In Chapter 6 it is demonstrated that a knowledge of the intensity saturation and vibrational bath heating effects can be used to predict the mode-locking behaviour of an SF_6-CO_2 mode-locking system.

The theoretical production of mode-locked pulses from noise had not been previously dealt with in any quantitative fashion. This is done in Chapter 7, which outlines a model that describes the development of mode-locked pulses from noise. The model uses density equations and includes rotational coupling to describe the CO_2 amplifier. In Chapter 8 the theoretical predictions are compared with experimental results obtained with a Ge saturable absorber. That chapter demonstrates that the theory can be used to predict reliably the quantitative effect of varying such parameters as the laser gain, cavity loss, linear and non-linear loss, and laser gas pressure, on the mode-locked output.

CHAPTER 2

EXPERIMENTAL APPARATUS

2.1 Introduction

This chapter outlines the main features of the experimental apparatus that were designed and constructed for the research described in this thesis. Section 2.2 discusses the different types of TE CO_2 amplifiers that were considered for use in a mode-locked laser system. That section also descibes in detail the particular laser system (Pearson and Lamberton double-discharge) that was finally chosen and constructed. In Section 2.3 the design parameters and operational details of a 3-mirror laser cavity are outlined. The 3-mirror arrangement provides a tightly focussed beam in one arm of the cavity while maintaining large beam areas at all 3 mirrors. This cavity configuration makes available a wide range of laser beam spot sizes, which are often necessary for optimizing the mode-locking operation. Section 2.4 describes a variable thickness gas cell, used in most of the transmission and mode-locking experiments involving SF_6. Finally, Section 2.5 describes the detection system and associated noise pick-up problems often encountered in the measurement of ns duration mode-locked pulses.

2.2(a) TE CO_2 Lasers

Since the development of the first TE CO_2 lasers in the early 1970's the trend has been to higher laser discharge voltages and increased discharge volumes in order to produce progressively higher output energies. Under these conditions, it is generally very difficult to obtain stable uniform glow discharges between two contoured electrodes, due to the formation of arcs. The presence of arcs prevents the efficient excitation of the upper laser level. In addition, the continual formation of arcs damages the electrode surfaces and therefore limits the lifetime of the laser. Arcs are more likely to occur between electrodes which have large electric field gradients associated with them and/or have poor surface properties (i.e., unpolished, dirty, etc.). There are two basic approaches, common to all TE CO_2 lasers, which are used to prevent the formation of arcs. The first technique is to limit the discharge current density. An example of this method is the frequently used resistor pin-to-pin electrode configuration in which rows of resistors limit the discharge current per pin [25]. The second approach involves producing the laser discharge in a time short compared to the time it takes to form an arc [26]. This can be accomplished by using low-inductance, fast-switching circuits, and high quality electrodes. The laser pulses obtained under such conditions are usually short duration ($\lesssim$ 200 ns FWHM) and of high power (multi-MW). An example of this approach is the double-discharge laser. The term "double" indicates that there are two discharges; a low energy preionization discharge which generates a uniform distribution of electrons between the main electrodes, followed by the main discharge. The uniform production of electrons shortens the time to complete the main discharge relative to the time needed to form an arc [27].

There are three main mechanisms for the production of electrons prior to the main discharge. Electrons can be produced by photoionization of the gas molecules* by hard ultraviolet (uv < 2000 Å) radiation [29] created by series of arc preionization discharges. Electrons can also result from photoemission from the electrode surface by soft uv radiation produced in a glow preionization discharge [30]. Finally, electrons can be produced directly by initiating a glow discharge between a third electrode and one of the main electrodes. The latter first serves as the anode to sweep the electrons into the main discharge region and then as the cathode in the main discharge [31].

Of the various systems described, the resistor pin-pin discharge laser, and the soft uv preionized double-discharge laser, were investigated in detail in order to satisfy the laser requirements for mode-locking.

2.2(b) Laser Requirements for Mode-Locking

It will be demonstrated in this thesis that the CO_2 mode-locking process occurs at near lasing threshold conditions. It is necessary to have very repeatable uniform laser discharges in order to achieve stable output intensities on a pulse-to-pulse basis for such near threshold operation. In addition, for convenience in tuning the laser cavity and obtaining sufficient output information for accurate data analysis, the laser should be able to operate at a minimum repetition rate of a few pulses per second. The laser gain should be sufficiently large to allow the use of low transmittance saturable absorbers. In mode-locking experiments the TEM_{00} fundamental transverse mode of the cavity is usually selected by means of an intra-cavity aperture. This is done to avoid coupling of the axial (longitudinal) modes with the transverse modes [32], and to avoid fluctuations in the laser output due to the different buildup times associated with various transverse modes. These result from the different diffraction losses experienced by each mode. Efficient coupling of the electrical input energy into the fundamental mode can best be achieved by reducing the electrode width to the minimum required for the lowest order mode. A properly reduced discharge volume allows the use of low input electrical energies, while still maintaining high gains. The use of low input energies avoids some of the problems associated with high voltage circuitry (i.e., >30 kV).

---

* Very often gases (e.g., xylene) with low ionization potentials are added to the gas mixture to increase the yield of electrons [28].

2.2(c) Helical and Double-Discharge Lasers

A schematic diagram of a typical excitation system for the lasers discussed in this section is shown in Fig. 2-1. A pulse generator (Datapulse) provides a short duration, low voltage pulse (5 μs, 5 V) to a trigger module (EG and G). A pulse from the trigger module (∿30 kV, 2 μs) then causes the spark gap to break down, allowing the capacitor to discharge through the laser tube. This circuit is both straightforward and very reliable for a wide range of capacitors (0.005 to 0.05 μF) and charging voltages (10 to 35 kV).* For the helical laser the preionization capa-

---

* The high voltage limit of this circuit was the ∿38 kV hold-off voltage of the spark gap.

Fig. 2-1

Schematic diagram of the discharge circuit used for the double-discharge laser.

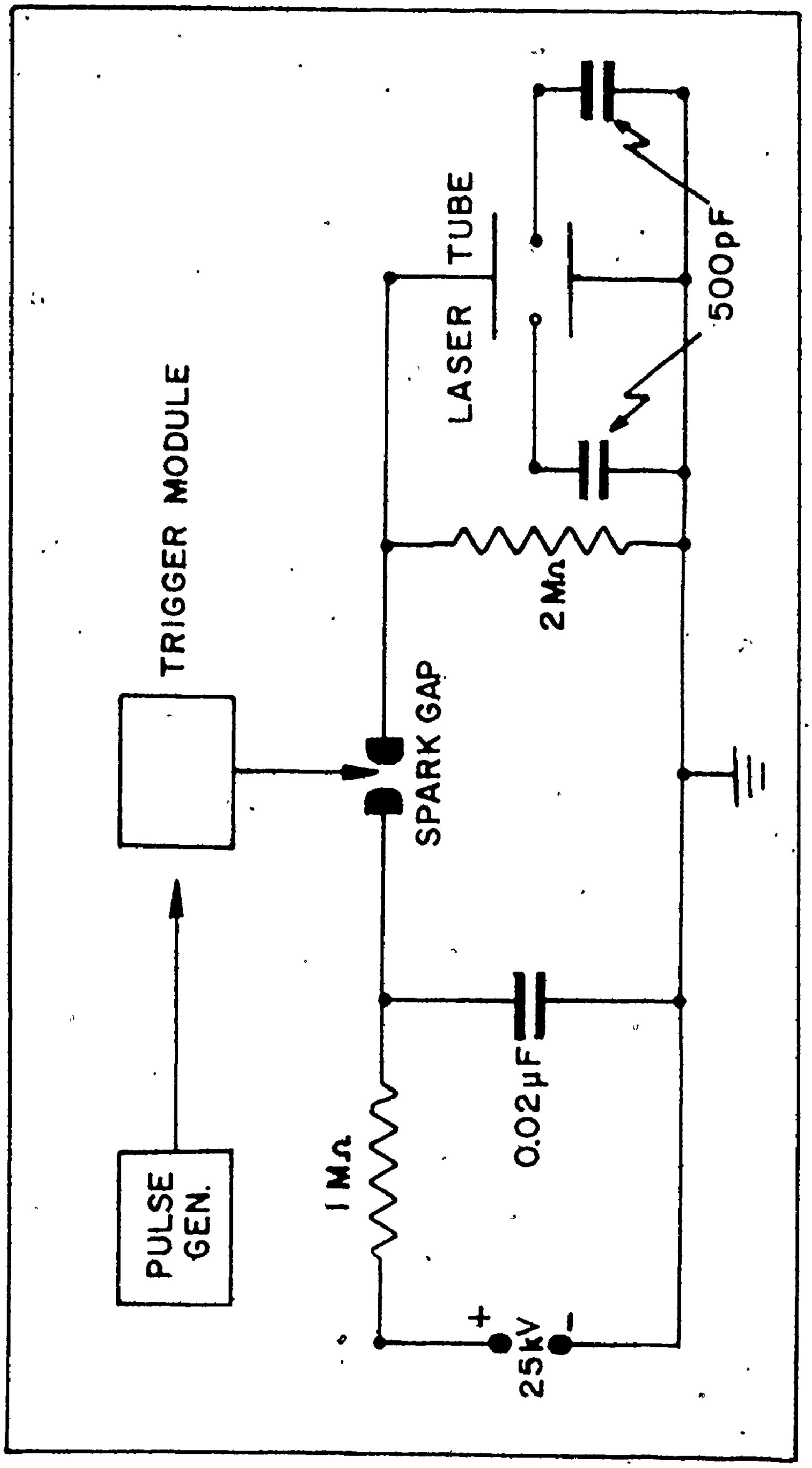
TRIGGER MODULE
LASER TUBE
500pF
2 MΩ
SPARK GAP
PULSE GEN.
1 MΩ
0.02μF
+
-
25kV

citors shown in Fig. 2-1 are not used.

The resistor pin-to-pin discharge system was one of the lasers investigated. The resistors* were wound in a helical array similar to the arrangement used in Ref. [25], and shown in Fig. 2-2. The helical array results in a gain medium which has cylindrical symmetry and which effectively couples the discharge energy into the TEM_{00} mode [25]. When these lasers ($\sim$1 m long) were operated at pressures $\lesssim$ 1/2 atm, they produced adequate gain for mode-locking, excellent coupling efficiency into the TEM_{00} mode, and had a reasonable repetition rate (10 pps). They were very stable ($\lesssim$ 5% variation in output intensity) both on a short and long term (several years) basis. This laser system was used in most of the sub-atmospheric mode-locking experiments (Chapter 6) and SF_6 transmission experiments (Chapters 3 to 5).

The second system investigated was the Pearson and Lamberton double-discharge laser [30]. In this laser the main discharge occured between an identical pair of solid electrodes separated by $\sim$2 cm. A tungsten wire was stretched parallel to the main electrodes,but offset from their centre line,and connected at either end to small coupling capacitors. When a high voltage pulse ($\sim$25 kV) was applied to the anode, field emission from the wire resulted in a sheet discharge between the anode and the wire followed by a similar discharge between the cathode and the wire. Soft uv radiation produced in these discharges "seeded"

---

* The resistors were 1 kΩ carbon composite manufactured by Allen Bradley. These were the only resistors that gave stable discharges at high currents (40 A/pin) for long periods of time.

Fig. 2-2

Photograph of a resistor pin-to-pin helical laser. Also shown in this photograph is a dual beam oscilloscope (Tektronix 556) and a portion of the laser gas flow system.

the main discharge with electrons resulting from photoemission from the cathode surface [30]. A uniform glow discharge then occured between the main electrodes. The appealing features of such a system were the narrow discharge width ($\sim$1.5 cm), the ruggedness and simplicity of the preionization system, and the ability of the laser to produce repeatable arc-free discharges.

The laser system developed in our laboratories differed from that of Pearson and Lamberton's in several ways. Two tungsten wires (rather than one) were suspended, one on each side of the main electrodes, by two 500 pF door-knob capcitors (Fig. 2-3). This achieved a more uniform and symmetric discharge across the electrode width compared to the original system. In addition, the electrode discharge width was reduced from 1.5 to 1 cm. As previously mentioned in Section 2.2(b), narrow widths allow efficient coupling of the excitation energy to the TEM_{00} mode. However, the narrower width meant that arc-free discharges were difficult to obtain due to the large field gradients associated with the sharper electrode profile. Considerable time was spent in order to obtain electrodes which were suitably shaped* to constrict the discharge width to $\sim$1 cm while preventing arc discharges. Cost was minimized by casting (in aluminum) rather than by machining each electrode shape. The electrodes were initially finished by milling a few thousandths of an inch from the aluminum casting to ensure a flat

---

* The electrode shapes did not conform to any of the ideal electrode profiles (e.g. Rogowski, Bruce) [33] due to the narrowness of the electrodes ($\sim$1 cm) and the electrode separation ($\sim$2 cm).

Fig. 2-3

Photograph of two double-discharge modules. This photograph shows the solid aluminum electrodes as well as the door-knob capacitors used in the preionization circuit.

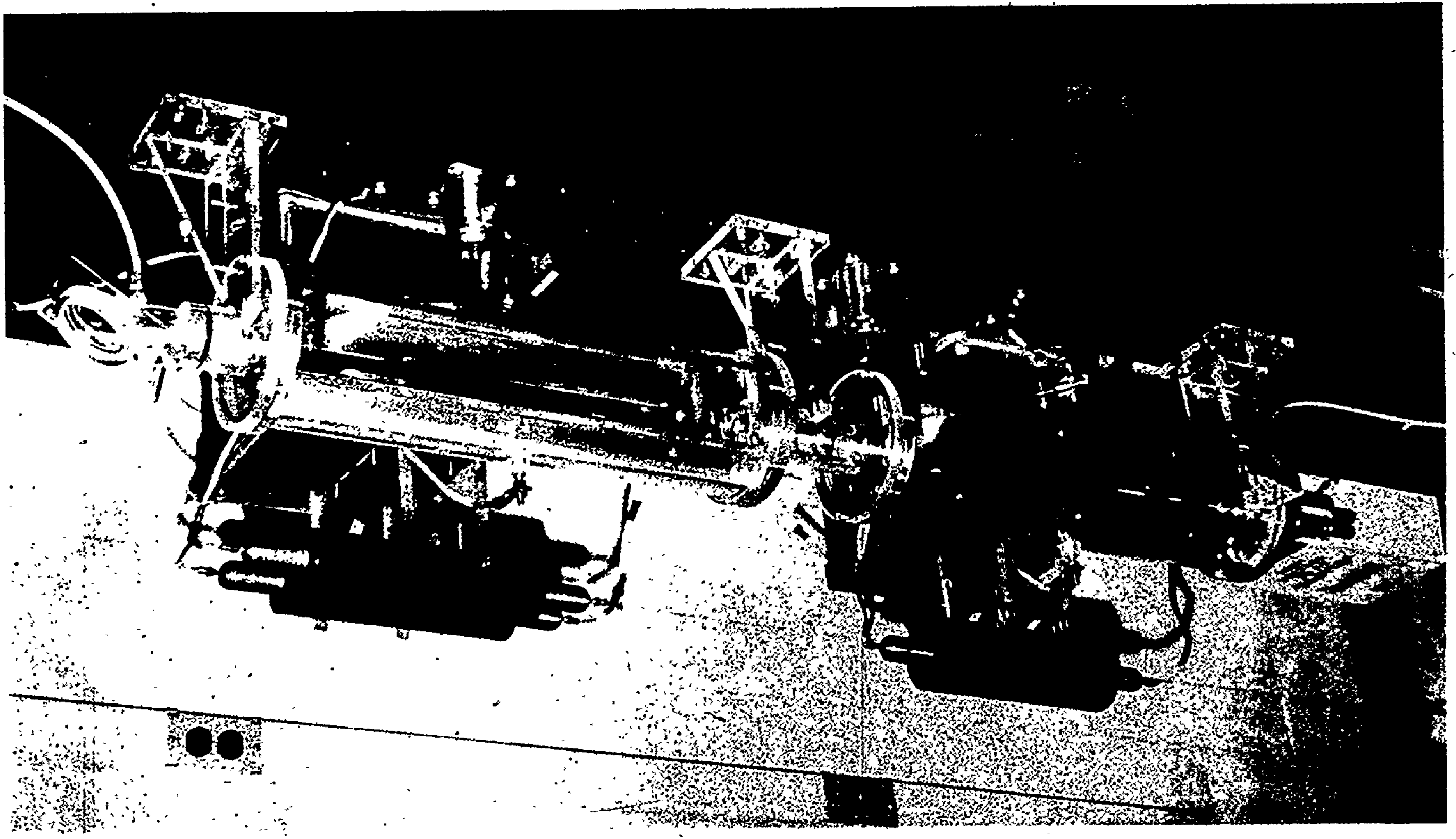

electrode surface. The surface was then polished to a near mirror finish. Aluminum was chosen for the electrode material since it has a larger photoelectric yield* than most other metals and is inexpensive and very easy to cast.

Once a suitable electrode profile had been obtained (Fig. 2-3) the electrode separation, the tungsten wire separation, the inductances, the resistances and the capacitances for the main and trigger circuits, were all adjusted to give the optimum discharge stability and uniformity. The optimum mechanical and electrical parameters are recorded in Table 2-1. In the first laser module constructed (not shown in Fig. 2-3) the coupling capacitors of the trigger circuit were mounted external to the laser tube, thereby decoupling the preionization circuit pathway to ground from that of the main discharge. The current pulse height (in A) and shape for both the main and auxillary discharges could therefore be monitored as the charging voltage was raised from below to above the main electrode breakdown threshold. The current pulses were measured by a current probe (Pearson model 411) in conjunction with an oscilloscope (Tektronix 547). Figure 2-4(a) shows the current pulse which accompanies the initial sheet discharge between the anode and the trigger wire.** The maximum current is limited to ∿120 A,

---

* The photoelectric yield is defined as the number of emitted electrons per number of incident ultra-violet photons on the metal surface. The yield depends on both the radiation wavelength and on the metal surface conditions [34].

** These results were obtained using a gas concentration of 85% He, 5% N_2 and 10% CO_2, a 0.005 μF main capacitor, and an overall circuit inductance of 1 μH.

TABLE 2-1

Double-Discharge Laser Parameters

Mechanical Specifications	
Discharge Length	30 cm
Discharge Width	1.0 cm
Electrode Separation	2.2 cm
Discharge Volume	66 cm^3
Trigger Wire to Anode Distance	1.1 cm
Trigger Wire Separation	4.8 cm
Electrical Specifications	
Main Capacitance	0.02 µF
Trigger Capacitance	4 x 500 pF
Charging Voltage	20-30 kV
Peak Currents	1000-2000 A
Current Pulse Duration	∿400 ns
Circuit Inductance	1 µH
E/N	4.1×10^{-16} $V\text{-}cm^2$
E/P	1.1×10^4 V/cm atm
Discharge Stability	∿0.01% arcs
Output Specifications	
Gas Composition	typically 85% He, 5% N_2, 10% CO_2
Laser Repetition Rate	up to 5 pps
Peak Gain per Pass	3%/cm
Input Electrical Energy	5 to 10 J
Output Energy Density	up to 8 J/ℓ
Pulse Duration	∿150 ns
Output Power	up to 3 MW
Laser Efficiency	∿5%
Fluctuations in Peak Power	<5% pulse-to-pulse

Fig. 2-4

Fig. 2-4 (a), (b), and (c) show displays of the preionization current pulse as the voltage across the main electrodes is progressively increased. The main discharge current pulse amplitude is zero for these three displays. Fig. 2-4(d) shows the main discharge current pulse obtained at a slightly higher voltage (∿22 kV) than used in (c). The preionization current pulse for this voltage setting would appear similar to that shown in (c).

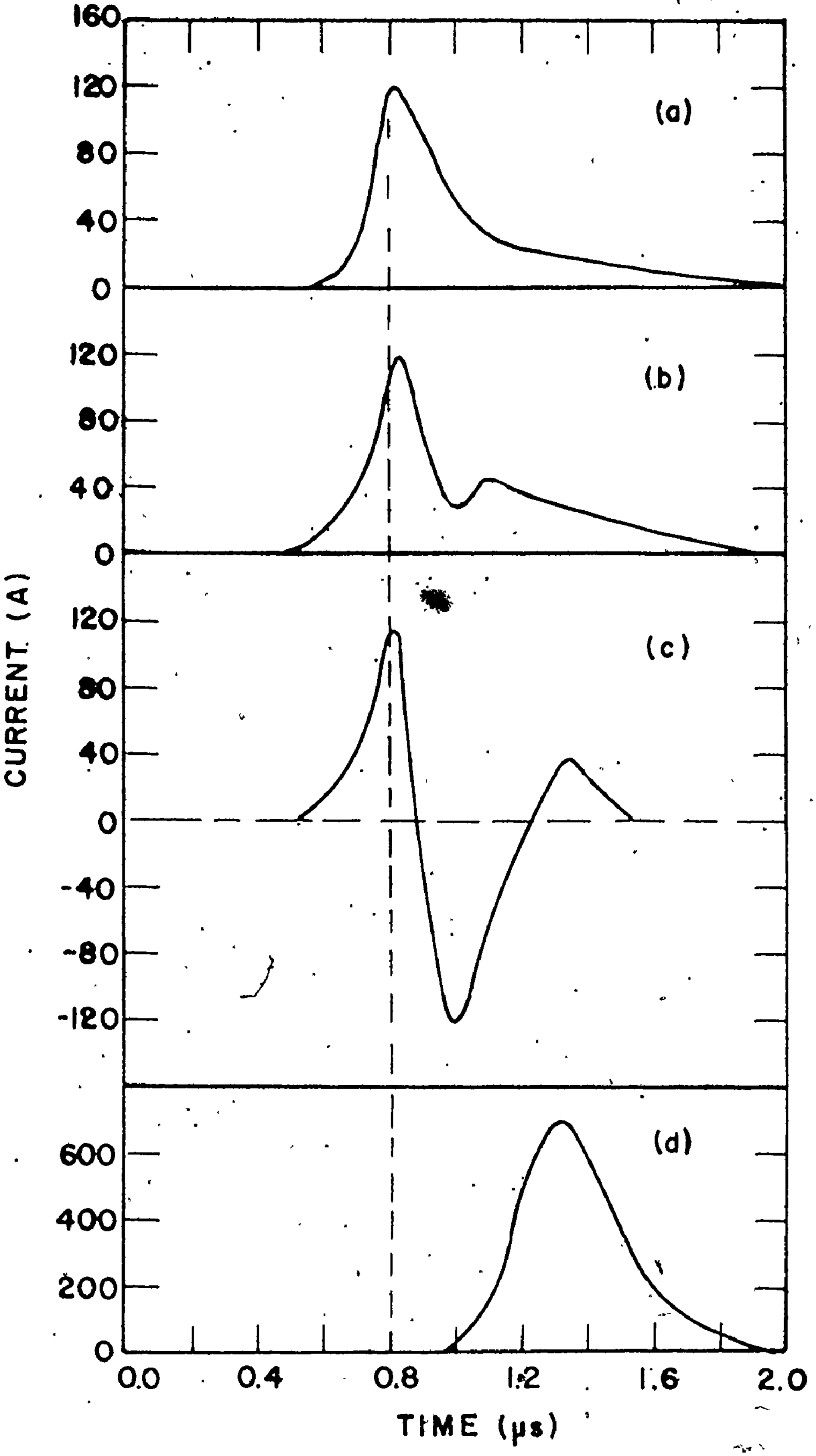
(a)
(b)
(c)
(d)
160
120
80
40
0
120
80
40
0
120
80
40
0
-40
-80
-120
600
400
200
0
CURRENT (A)
0.0
0.4
0.8
1.2
1.6
2.0
TIME (μs)

independent of the main capacitance values. Figure 2-4(b) (at slightly higher voltage) shows the beginning of a reversal in the current on the tail portion of the pulse. Fig. 2-4(c) indicates that addition of a few more kV across the main electrodes results in an oscillatory preionization current pulse with the negative going current pulse corresponding to the onset of the cathode to trigger wire discharge. For all of these voltage settings the main current pulse amplitude was zero. However, as shown in Fig. 2-4(d), above a certain critical voltage (∿22 kV for an electrode separation of ∿2 cm) the magnitude of the main current pulse rises very fast. This voltage threshold is accompanied by the onset of a visible glow discharge between the main electrodes. The amplitude of this current pulse depends on the value of the main capacitance, as expected. It is clear from this figure that there exists a delay between the preionization discharge and the main discharge which is sufficiently long to allow the production of an electron density between the main electrodes necessary for the production of stable discharges. Fig. 2-5 shows a typical discharge, as seen through the end window of the laser tube. This photograph illustrates the narrow but very uniform nature of the discharge. The percentage of arcs with this laser system was in the order of 0.01. However, after several hundred thousand discharges, the electrodes become coated with products of the discharge and the performance deteriorated somewhat. The long term electrode performance could probably be improved by replacing the aluminum electrodes with electrodes constructed from materials such as nickel or stainless steel. Nevertheless, the overall performance of this laser system was very good, as is indicated by the output specifi-

Fig. 2-5

Photograph of a typical laser discharge as seen through the laser tube end window. This photograph illustrates the uniformity and narrowness (~1 cm) of the laser discharge.

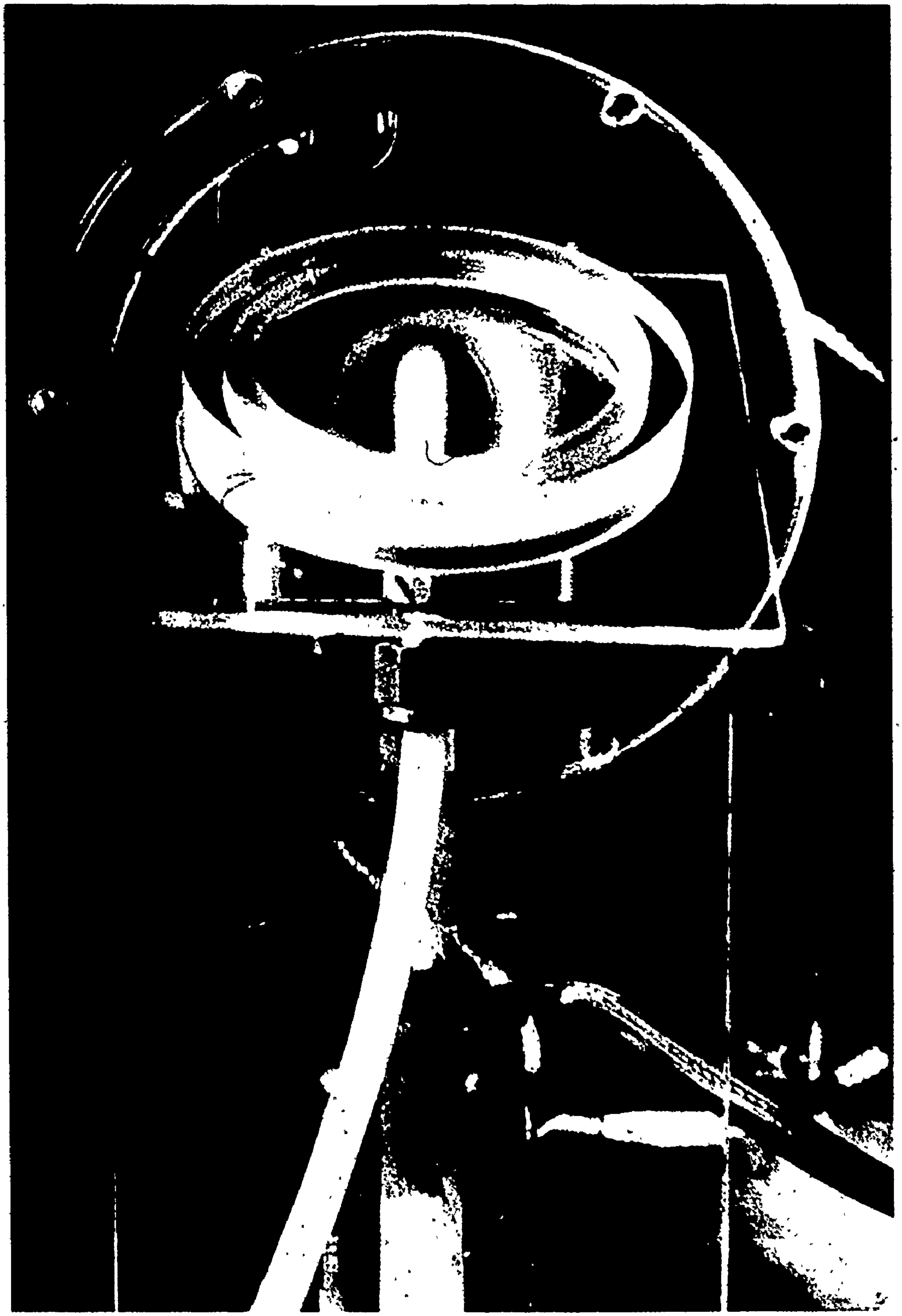

cations shown in Table 2-1, and it more than satisfies the laser requirements for mode-locking outlined in Section 2.2(b).

The gain measurement quoted in Table 2-1 was obtained using an oscillator-amplifier technique. The oscillator consisted of a short helical laser (∿30 cm long) which operated at a gas pressure of 150 Torr and in the TEM_{00} mode. The output had a low intensity and was very stable. The oscillator and double-discharge amplifier were aligned so that the oscillator beam passed through the centre of the amplifer and was incident on a Au:Ge detector. It was verified, by varying the oscillator pulse intensity, that saturation effects did not occur in the amplifier. The amplifier discharge could be delayed from that of the oscillator to ensure that the peak of the amplifier temporal gain was measured. The transmitted pulses were observed with thermal image plates, with and without the presence of the amplifier discharge, to determine if any beam deflection effects due to the amplifier discharge were occuring. Deflections were not observed. The gain was obtained from the ratio of the probe intensity at the exit of the amplifier to its intensity at the input of the amplifier. The peak gain (for stable discharges) was ∿3%/cm. Figure 2-6 shows the small-signal gain obtained as a function of discharge input energy using the oscillator amplifier technique. Note that the gain starts to plateau at high input energies. This behaviour was observed for a wide range of gas concentrations and discharge parameters, and was independent of the laser discharge stability. A detailed investigation of this effect in Ref. [35] indicated that such gain saturation is common to all TE CO_2 systems. However, the exact mechanism responsible for the saturation is not known.

Fig. 2-6

Plot of the small-signal gain as a function of the input electrical energy to the discharge. The data was obtained at the P(20) wavelength, with a laser gas concentration of 85% He, 5% N_2, and 10% CO_2, at a total gas pressure of 1 atm.

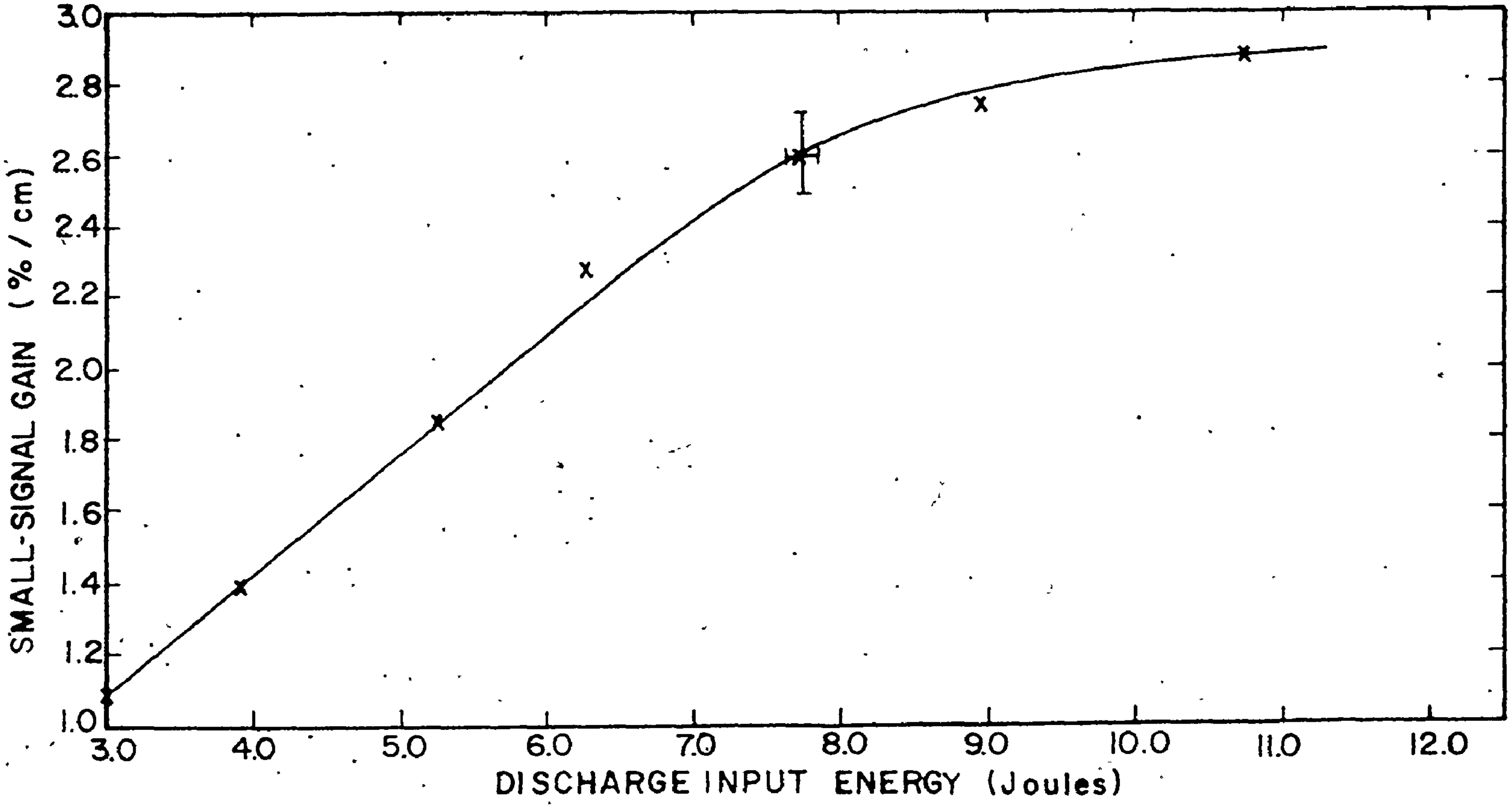
3.0
2.8
2.6
2.4
2.2
2.0
1.8
1.6
1.4
1.2
1.0
SMALL-SIGNAL GAIN (% / cm)
3.0
4.0
5.0
6.0
7.0
8.0
9.0
10.0
11.0
12.0
DISCHARGE INPUT ENERGY (Joules)

This saturation effect is exploited in some of the SF_6 mode-locking experiments of Chapter 6.

2.3 3-Mirror Laser Cavity

It is often necessary, in mode-locking experiments, to focus the laser beam at the saturable absorber in order to produce significant absorber saturation. The ratio of the largest beam area to the smallest beam area in a 2-mirror cavity is usually limited to values <20. As well, for the most frequently used plane-spherical laser cavity the focus occurs at the plane mirror, and therefore increases the possibility of mirror damage. A 3-mirror cavity was designed and tested in which the radiation is focussed well inside the laser resonator, while maintaining large beam areas at all 3 mirrors. Figure 2-7 shows a schematic diagram of such a cavity. The initial values for the cavity parameters were obtained from an analysis outlined by Kogelnik [36,37] and are described in Appendix A. The analysis in Ref. [36], developed for for an internal lens resonator, was extended to the 3-mirror resonator case. The parameter values were then optimized experimentally (changes were <10% from the theoretical predictions) to produce the minimum beam waist and largest spot sizes at the 3 mirrors.* In the mode-locking experiments either a gold-coated replica grating, or a 10% transmitting germanium flat, was used for M2. A 0.5 m radius of curvature

---

* It was calculated from Ref. [37] that astigmatism caused by tilting the central mirror should be negligible at the 10.4 μm wavelength, and for beam waists greater than a few tenths of a mm.

Fig. 2-7

Schematic diagram of the 3-mirror laser resonator. The curvature of mirrors M1 and M2 are referred to in the text by R_1 and R_2, respectively. The parameter f denotes the focal length of the central mirror, and ω_0 is the radius of the beam waist.

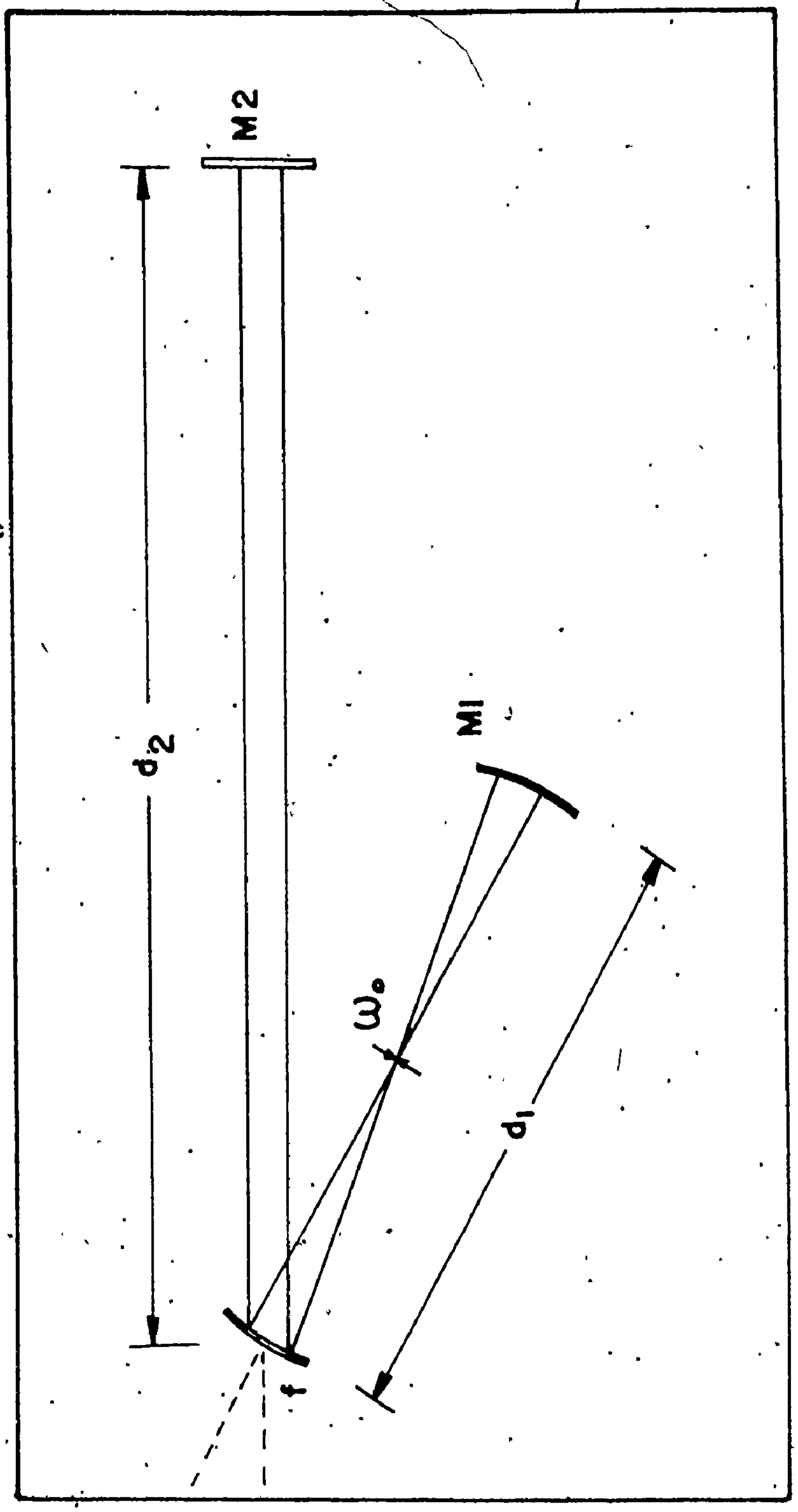
M2
d_2
M1
ω_o
d_1
f

14% transmitting mirror, or a 0.5 m gold-coated mirror*, was used for M1. The central mirror was always a 1 m radius of curvature gold-coated mirror. The maximum beam area ratio achieved experimentally (∿65) was somewhat less than that predicted theoretically in Appendix A (100). The discrepancy is probably due to the effect of the distributed gain medium, which was not included in the theoretical analysis. The 3-mirror system proved very easy to align and insensitive to small variations in the parameter values (such as d_1, d_2, f, etc.). Furthermore, the spatial output distribution for the lowest order mode was measured to be a Gaussian, indicating that no beam distortion effects were present.

2.4 Adjustable Thickness Gas Cell

A gas cell, constructed from brass, was made sufficiently large to employ ∿5 cm diameter NaCl or Kcl salt windows. It could therefore be used in conjunction with large laser beam diameters. An O-ring, situated in the main body of the cell, provided a seal to allow low pressure (a few Torr) operation. The cell was designed to ensure uniform gas flow over the entire window area by making use of large entrance and exit channels, which were suitably shaped to diverge the gas flow across the cell. The gas cell thickness could be varied from ∿0.0 to 0.3 cm by using a threaded component (containing one of the two salt windows) which could be screwed into the main body of the cell. At any separation the cell thickness was known to within 2 x 10^{-3} cm.

---

* The reflectivity of the gold-coated mirrors were measured to be better than 98% at 10.4 μm.

2.5 Detection Apparatus

A gold doped germanium (Au:Ge) detector, cooled with liquid nitrogen, was used for the detection of low intensity laser pulses. The detector sensitivity at 10.4 μm, using a 45 V bias supply and a 50 Ω load, was ∿25 mV for a 1 kW/cm^2 intensity. The detector risetime, also for a 50 Ω load, was ∿2.5 ns. The linearity of the detector was verified over the four orders of magnitude of input intensities for which the detector was used. Photon-drag detectors were used to detect the higher ranges of pulse intensity [38]. These detectors were constructed from single crystal, p-type germanium [(1,1,1) orientation]. They operated at room temperature, were very rugged and compact, and linear up to intensities as high as 10 MW/cm^2 [39]. Their risetimes (when matched to a 50 Ω load) were sub-ns. However, their sensitivity (a few hundred mV per MW/cm^2) was quite low; they were often used in conjunction with a fast risetime (0.9 ns) amplifier (Avantek AV-9T).

The photon-drag detectors were used in all absolute intensity measurements and were calibrated in the following manner. A very stable output pulse from a repetitively pulsed helical laser was made incident on the detector. The detector area was much less than the beam area, so that the intensity across the detector was approximately constant. The corresponding voltage deflection on an oscilloscope (Tektronix 547) was obtained by averaging over many such laser pulses. The laser pulse shape was then recorded photographically using an oscilloscope camera. The area of the detector was measured and an energy meter

(Scientech), with a quoted accuracy of better than 1%, was used to measure the portion of the pulse energy that was incident on the photon-drag detector. The measurements allowed calculation of a factor for converting from a photon-drag detector output voltage to an absolute intensity in W/cm^2. The overall accuracy associated with the above measurements produced approximately ± 20% uncertainty in the conversion.

A major concern in all the mode-locking experiments (discussed in later chapters) was the presence of high frequency noise pick-up in the detection apparatus. The noise resulted from the high voltage pulses in the trigger module, the spark gap, and in the laser discharge itself. This noise was present before, and sometimes during, the laser pulse, and made oscilloscope triggering of mode-locked pulse trains very difficult. The noise problem was reduced by moving the detection apparatus as far away from the noise source as possible, by mimimizing all coaxial cable lengths (e.g., between detectors and oscilloscopes), by shielding all such cables with tinned copper braiding, and finally by inserting the detection apparatus in a copper-mesh Faraday box. Employment of these techniques allowed stable triggering of individual pulses well down on the leading edge of the pulse train.

2.6 Summary

This chapter has outlined the basic features of the experimental apparatus that was used for the research reported in this thesis. The major portion of the chapter dealt with the successful design and operation of a double-discharge laser which was used for all the atmospheric pressure mode-locking experiments. A brief description was given of the helical laser, which proved to be excellent for sub-atmospheric mode-locking experiments. The latter part of the chapter dealt with the design and construction of a 3-mirror cavity, and a variable thickness gas cell to be used in transmission and mode-locking experiments. The detection equipment and associated noise problems were also described in this chapter.

CHAPTER 3

SMALL-SIGNAL AND LARGE-SIGNAL ABSORPTION IN SF_6

3.1 Introduction

To predict the mode-locking behaviour of an SF_6 saturable absorber, it is necessary to have an accurate knowledge of the small-signal absorption characteristics as a function of CO_2 wavelength for a range of pressures appropriate to SF_6 mode-locking (10-200 Torr). Values of the absorption coefficients obtained from the literature cover a limited range of wavelengths [40,41]. Where they were available, there was considerable variation from one reference to another. Therefore a study of the small-signal transmission behaviour for the SF_6 molecule was carried out and is reported in Section 3.2.

For mode-locking it is also necessary to understand the details of the dynamical processes on time scales varying from sub-ns to µs, which occur in SF_6 subject to pulsed CO_2 radiation. In addition, knowledge of the SF_6 dynamics is important in understanding other effects which involve the interaction of pulsed CO_2 radiation and SF_6, such as Q-switching [42], self-induced transparency [43], photon-echo effects [44], isotopic separation in SF_6 employing laser induced photodissociation [45], and optical pumping of SF_6 to obtain laser action at 16 µm [46]. For example, it is important to know which vibrational and rotational levels participate in the saturation of the absorption, and how fast and by what means energy is being coupled between these and other levels. One technique for studying the dynamical processes is to measure the pulse shaping and transmission behaviour of pulsed CO_2 radiation by SF_6 over a wide range of laser intensities. Information on the intensities needed to saturate the absorption for a given wavelength, the amount of residual absorption present at high intensities and the pressure dependence of the saturation intensities (and therefore of the absorber relaxation times), can be determined from such transmission experiments. Since there was virtually nothing known about the large-signal transmission properties of SF_6 it was decided to measure them for a wide range of CO_2 wavelengths P(12) to P(30) lines and SF_6 pressures (10-200 Torr). Section 3.3 describes such measurements. Information on the dynamical behaviour of SF_6 can also be obtained using well known infrared double-resonance techniques to measure the vibrational and rotational relaxation rates directly [47]. Chapter 4 outlines such double-resonance experiments.

3.2 Small-Signal Absorption Measurements

The initial step in this investigation was to determine the small-signal absorption of SF_6 for all the P-branch lines of CO_2 between P(12) and P(28) in the 10.4 μm band. In each case, the dependence of the absorption coefficient on SF_6 pressure was determined for pressures in the range 10-200 Torr, both with and without the presence of a buffer gas. As has been pointed out, it is very important to establish, for a given P-branch line, good values for the small-signal absorption and the associated pressure dependence in order to design optimal mode-locking or Q-switching configurations for the resonator and amplifier system. A number of investigators have reported values of the absorption coefficient of SF_6, determined either by standard spectroscopic techniques [48], or directly employing a CO_2 laser probe [49]. The latter method is more appropriate when the data is subsequently required to predict the interaction between the CO_2 radiation and SF_6. The values for small-signal absorption coefficients determined here are compared with previous work for those cases in which data is available. There has been little in the way of published data concerning the dependence of the absorption coefficients on SF_6 pressure, particularly in the important pressure range of 10-200 Torr reported on here.

3.2(a) Experimental Observations and Discussion

The pressure-dependent low-signal absorption was measured employing a pulsed TE CO_2 laser probe source. This source, which has been described in Chapter 2, consisted of a resistor-pin type TE CO_2 laser operated at low output power in a range of excitation, gas mixture and pressure where the output is very reproducible on a shot-to-shot basis. Apertures were employed in the laser to ensure that it operated in the TEM_{00} mode. The use of a pulsed helical laser permits absorption measurements to be made to high precision with a probe source having the same pulse characteristics as that to be employed for subsequent large-signal transmission measurements.

The attenuated laser output was incident on an absorption cell containing SF_6 gas at a temperature of 300 K and at pressures between 10 and 200 Torr. The windows of the cell were polished NaCl flats, oriented so that the TE CO_2 radiation was incident at Brewster's angle. The cell, described in detail in Chapter 2, was constructed so that the path length (L^{b}) could be easily adjusted over the range of 0.25 - 4 mm. The intensity of the radiation incident on the absorption cell could be varied over a range sufficient to ensure that the measured absorption coefficient was independent of the incident intensity. Measurements were made of the absorption coefficient of pure SF_6 as a function of gas pressure for all the P-branch lines of the pulsed CO_2 laser between P(12) and P(28). It was verified, by varying the total pressure of gas in the laser gain tube (and hence the width of the frequency spectrum of the probe laser), that the results were independent of the detailed shape of the probe laser pulse spectrum. The measurements were carried out employing a total gas pressure of 160 Torr in the helical gain tube, giving an output pulse length of approximately 260 ns. It is estimated that the spectral width at this pressure (160 Torr) is 800 MHz (FWHM).

The transmitted laser beam was collected by a one inch focal length anti-reflection-coated germanium lens and subsequently detected by a Au:Ge detector. Care was taken to eliminate any possible effects of beam distortion or deviation in passage through the absorption cell. The results of these measurements are displayed in Figs. 3-1 and 3-2, where $\alpha_0 L^B = -\ln(I_{out}/I_{in})$ is plotted as a function of SF_6 pressure for all the P-branch CO_2 lines investigated. Observe that, in every case, the absorption coefficient is a linearly increasing function of SF_6 pressure over the total range of pressures employed. This relationship between absorption coefficient and SF_6 pressure has been reported

Fig. 3-1

Absorption as a function of SF_6 pressure. The circles represent experimental data points. The number quoted under each CO_2 rotational line designation is the small-signal absorption coefficient, α_0, in units of $cm^{-1}Torr^{-1}$. These values are accurate to better than 5%.

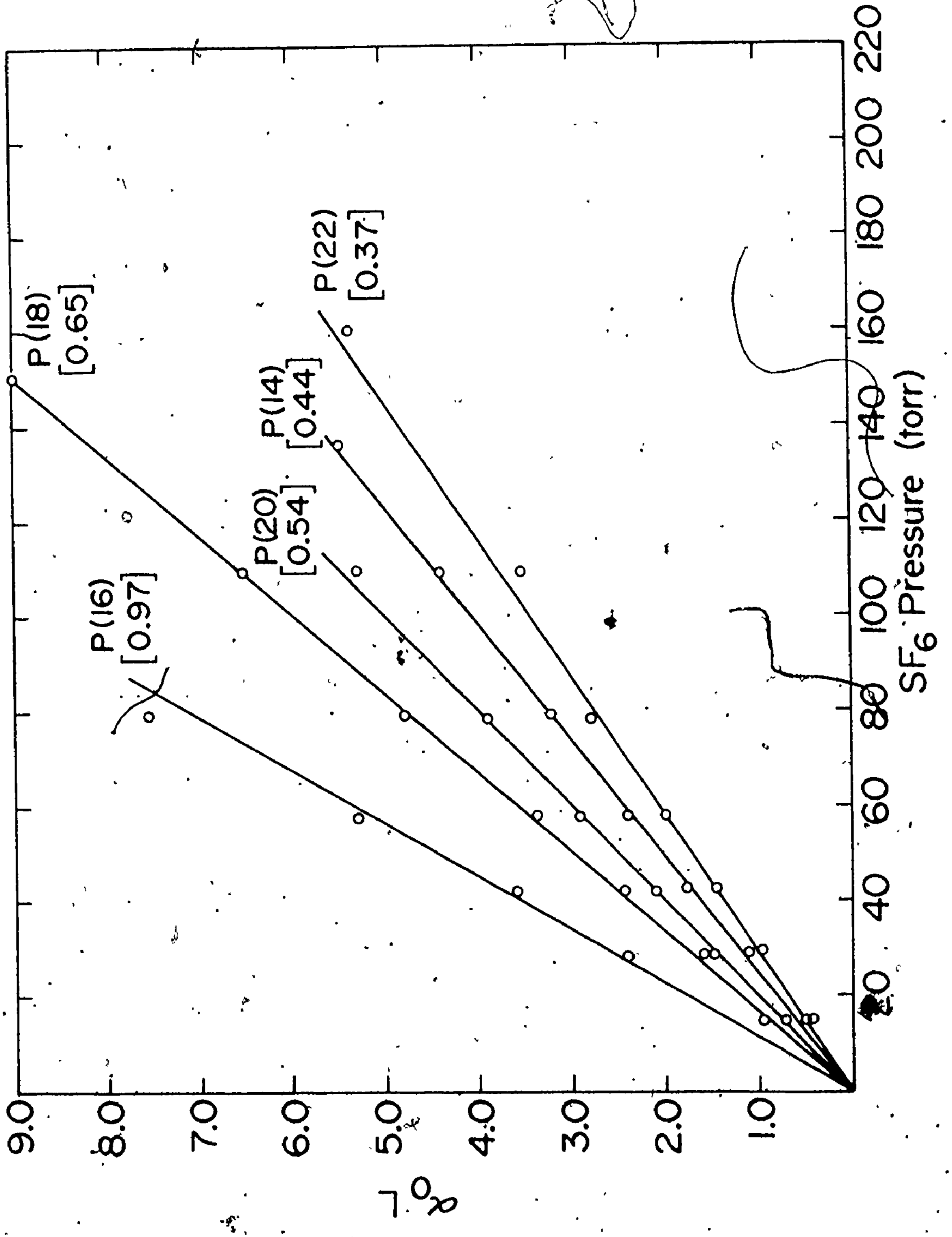
$\alpha_0 L$
9.0
8.0
7.0
6.0
5.0
4.0
3.0
2.0
1.0
20
40
60
80
100
120
140
160
180
200
220
SF_6 Pressure (torr)
P(16) [0.97]
P(18) [0.65]
P(20) [0.54]
P(14) [0.44]
P(22) [0.37]

Fig. 3-2

Absorption as a function of SF_6 pressure. The circles represent experimental data points. The number quoted under each CO_2 rotational line designation is the small-signal absorption coefficient, α_0, in units of $cm^{-1}Torr^{-1}$. These values are accurate to better than 5%.

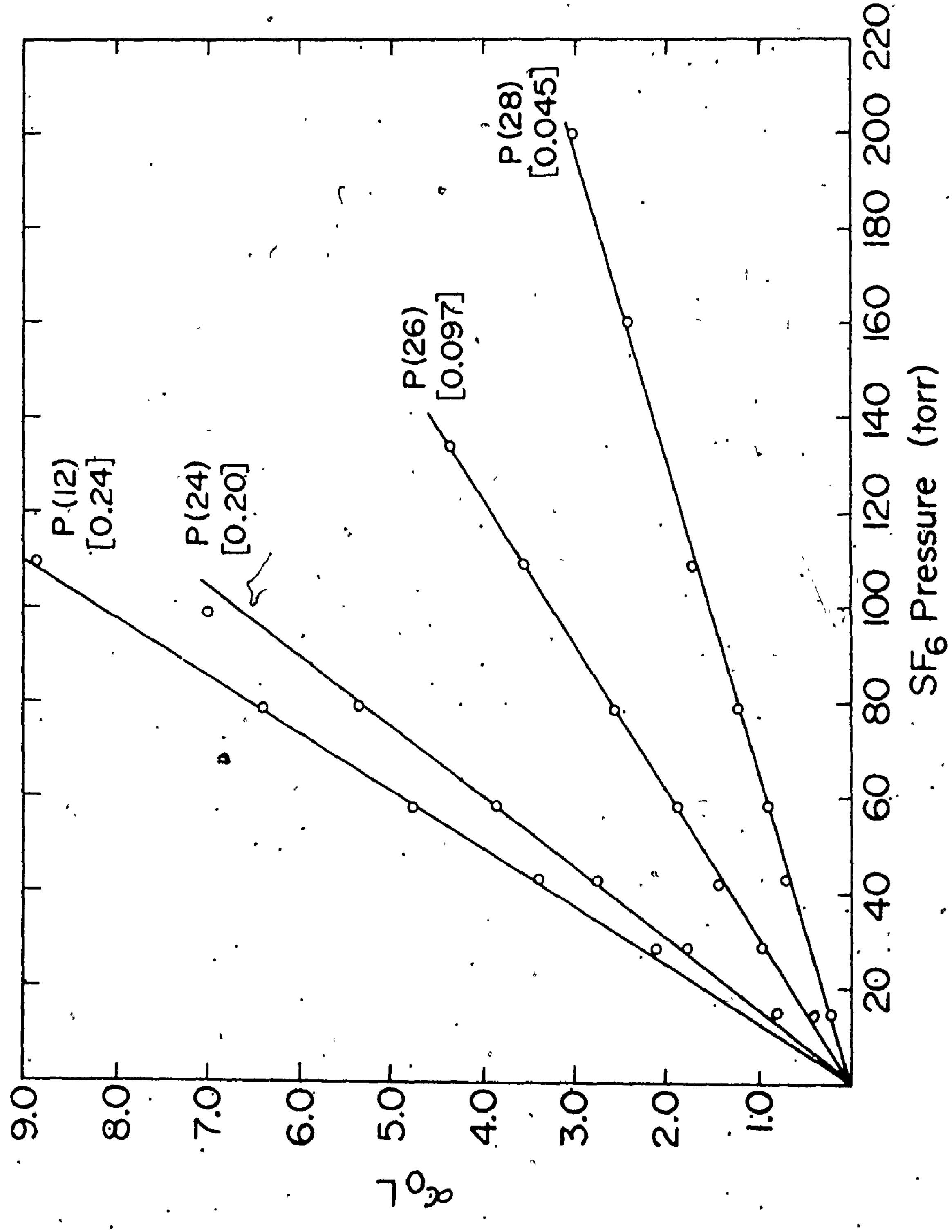
P(12)
[0.24]
P(24)
[0.20]
P(26)
[0.097]
P(28)
[0.045]
$\alpha_0 L$
9.0
8.0
7.0
6.0
5.0
4.0
3.0
2.0
1.0
SF_6 Pressure (torr)
20
40
60
80
100
120
140
160
180
200
220

earlier for some of these CO_2 laser lines in the considerably lower pressure range of 0.5-5 Torr [50]. At low pressure, a linear dependence of α_0 on gas pressure is generally observed even for a single resonance line absorption - it is a consequence of the inhomogeneous nature of the line-broadening at low enough pressure.* This might account for the results reported in Ref. [50], but will certainly not account for the persistence of a linear dependence on pressure up to values in excess of 100 Torr. However, it can easily be shown that the presence of a large number of overlapping resonance lines in the absorbing gas, each of which contributes to the total absorption at a given probe wavelength, can easily produce an absorption which increases monotonically with pressure. Recent very high resolution spectroscopic measurements, using tunable diode lasers and Lamb-dip techniques for a few of the CO_2 lines reported on here, are in general agreement with this conclusion [51]. An experimental observation which lends further support to this idea is that the addition of 200 Torr of He buffer gas to the SF_6 makes no detectable difference to any of the plots shown in Fig. 3-1 and Fig. 3-2. This again argues that a near-continuum of SF_6 levels must be contributing to the measured absorption over the whole pressure range investigated. The fact that the absorption coefficient has been shown experimentally to be linearly dependent on pressure in the range 10-200 Torr SF_6 pressure allows the absorption coefficients to be expressed in terms of the absorption coefficient per Torr of SF_6.

---

* For gases this occurs when the Doppler broadened linewidth is larger than that due to collision broadening.

for each CO_2 laser line. This permits intercomparison with measurements reported for various SF_6 and buffer gas pressures for certain CO_2 laser wavelengths.

Fig. 3-3 shows the values obtained in the present work for the SF_6 absorption as a function of wavenumber. Also shown are values obtained by Nowak et al., using a cw CO_2 laser and a SF_6-Ar mixture and a spectrum obtained using a continuum source and an infrared spectrometer having a 0.8 cm^{-1} spectral window [48]. The agreement between these measurements is surprisingly good considering the major differences in both experimental technique and SF_6 pressure range employed. Such close agreement is not generally found, even for the most frequently measured P(20) CO_2 line, as shown in Table 3-1. Since the SF_6 absorption frequency spectra in the region of the various CO_2 lines are not constant [53],some variation in α_0 is expected due to the different laser probe bandwidths used in the various experiments. Nevertheless, Table 3-1 indicates that there is substantial variation which is largely independent of the probe source and SF_6 pressure range employed.

3.3 Large-Signal Absorption Measurements

A number of studies of the saturation of SF_6 at moderately low pressures on some of the CO_2 P-branch laser-line wavelengths have been reported, in which cw CO_2 lasers were employed as probes [49,50]. However, it is essential to study the dynamic response of the SF_6 molecular system to obtain an understanding of the SF_6 mode-locking behaviour and any other applications involving the use of SF_6 and a pulsed TE CO_2 laser. Therefore, investigations were carried out on the dynamics

Fig. 3-3

SF_6 absorption as a function of wavenumber. The solid circles are values obtained in this work. The open circles are values obtained by Nowak et al. [48] using a cw CO_2 laser and low SF_6 pressures. The curve represents the absorption of SF_6 determined by using a continuum source [48].

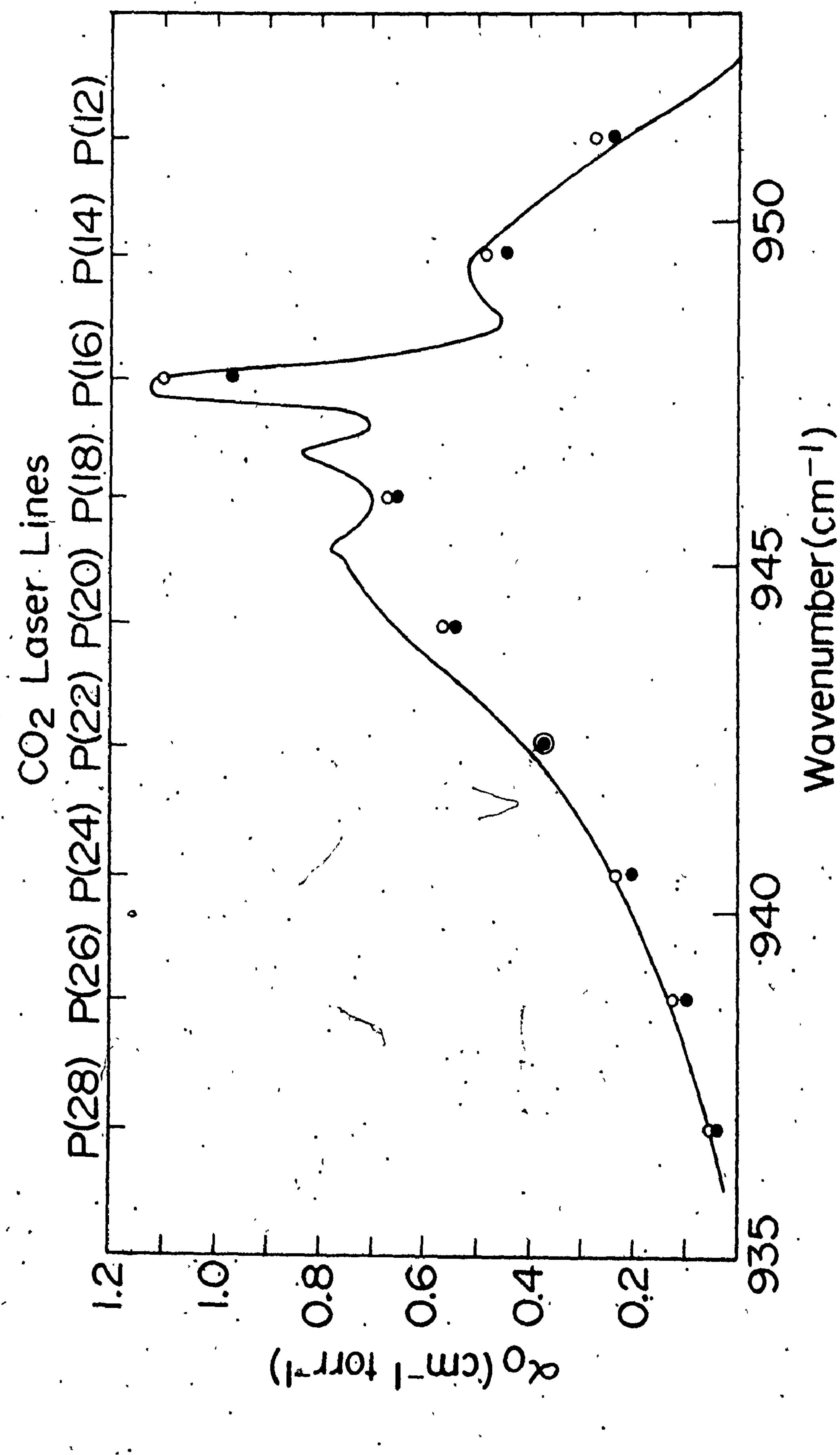
CO₂ Laser Lines
P(28)
P(26)
P(24)
P(22)
P(20)
P(18)
P(16)
P(14)
P(12)
935
940
945
950
Wavenumber (cm⁻¹)
1.2
1.0
0.8
0.6
0.4
0.2
α₀ (cm⁻¹ torr⁻¹)

TABLE 3-1

SF_6 Small-Signal Absorption Coefficient for the P(20) CO_2 Line.

α_0 ($cm^{-1}Torr^{-1}$)	Probe Source	SF_6 Pressure (Torr)	Reference
0.34	pulsed CO_2	$1\text{-}5 \times 10^{-2}$	Patel & Slusher [52]
0.43-0.66	cw CO_2	3×10^{-2}	Shimizu [53]
0.46	cw CO_2	0.1 - 0.4	Burak et al. [49]
0.40	cw CO_2	0.5 - 4	Wood et al. [50]
0.23	cw CO_2	3×10^{-2}	Abrams & Dienes [41]
0.46±0.02	cw CO_2	0.2 - 1	Brunet [40]
0.69	continuum and spectrometer	< 1 plus Ar buffer	Nowak & Lyman [48]
0.57	cw CO_2	< 1 plus Ar buffer	" "
0.54±0.03	pulsed CO_2	10 - 110	This work

of SF_6 at the P(12) to P(30) laser lines of the 10.4 μm band and are reported in this section and in Refs. [54,55]. Transmission data has been obtained using a pulsed TE CO_2 laser, in conjunction with an optical system providing four orders of magnitude intensity range at the SF_6 absorber. For ease of comparison of the transmission data, the small-signal absorption was kept constant for all lines. The observed non-linear absorption properties can be divided into three characteristic regions, namely P(12)-P(16), P(18)-P(22), and P(24)-P(30), each of which has distinctive features in the measured transmission as a function of incident radiation intensity. The first is characterised by a transmission which increases monotonically to very high transmissions with increasing laser probe intensity. The last is typified by a transmission which first decreases with increasing intensity, reaches a minimum, and then saturates to again give very high transmittances at sufficiently high intensity. The transmission behaviour at P(18)-P(22) corresponds to a transition region. The lines P(14), P(20) and P(26) have been chosen as representative of the three groups. Data is presented below for the pressure dependence of the SF_6 absorption at these three lines, for an order of magnitude variation in SF_6 pressure.

In each region, dynamical effects such as pulse shaping occur, indicating that analysis of the data with steady-state models cannot be employed*. Consequently, the transmission data is interpreted in terms of a 4-level non-steady-state representation. Such an analysis can provide information on the coupling times between levels, the contribution of excited-state absorption to the total absorption, and the values of the saturation parameters which characterize the intensity dependent transmission behaviour of SF_6. It will be shown that to determine the model parameters, it is necessary to obtain data on both the temporal behaviour of the transmitted pulse and the transmission for a wide range of input intensities at the absorber.

---

* A strictly steady-state model, in which the level cross-sections and the levels responsible for the absorption remain constant with time, cannot produce asymmetric pulse narrowing.

3.3(a) Experimental Procedure

The probe source was a helical TE CO_2 laser, used primarily because of its excellent short and long term pulse-to-pulse reproducibility (less than 5% variation, as noted in Chapter 2). The laser was operated at high He content and at a total gas pressure of 400 Torr. The output pulse duration was kept close to 210 ns (FWHM). A grating was employed to ensure that only the desired rotational line oscillated. An aperture, inserted within the laser resonator, ensured operation in the TEM_{00} mode.

The absorption cell, maintained at 300 K, was oriented at Brewster's angle to the incident radiation. This cell, as detailed in Chapter 2, was constructed so that the path-length could be adjusted from 0.25-4 mm, permitting the use of a wide range of SF_6 pressures whilst keeping the small-signal transmission constant. High purity SF_6 gas was employed (supplied by Matheson) and no additional purification was attempted. The intensity incident on the cell was varied over 4 decades by the use of attenuators and a 10 inch focal length germanium lens. The absolute intensity incident at the cell was determined by a calibrated photon-drag detector.* Any systematic error in the input intensity measurement was less than 20% (relative errors were less than 5%). Since the cell path-length was generally less than a few mm, the beam size did not vary significantly in passage through the cell, even when the lens was employed. Furthermore, the optical thickness of the absorption cell was such that the intensity variation of the beam along the path through the cell did not vary greatly. No significant dissociation effects are expected because the SF_6 cell was probed at a single CO_2 rotational line, and at intensities less than 10 MW/cm^2 [56].

3.3(b) Four-Level Non-Steady-State Absorption Model

The four-level non-steady-state model is shown schematically in Fig. 3-4. The rate equations governing the level population densities N_j (j = 1-4), in molecules/cm^3, are

$$\frac{dN_1}{dt} = A_{21}N_2 + A_{31}N_3 - \sigma_1 I(N_1 - N_3) - (N_1 - N_1^e)A_{vv}^1 , \tag{3-1}$$

$$\frac{dN_2}{dt} = -A_{21}N_2 - A_{23}N_2 + A_{32}N_3 + A_{42}N_4 - \sigma_2 I(N_2 - N_4) - (N_2 - N_2^e)A_{vv}^2 \tag{3-2}$$

$$\frac{dN_3}{dt} = A_{23}N_2 - A_{31}N_3 - A_{32}N_3 + \sigma_1 I(N_1 - N_3) , \tag{3-3}$$

---

* The detector calibration procedure is outlined in Section 2.5.

Fig. 3-4

Four energy-level scheme for absorption in SF_6. The A_{ij} terms represent collisional (relaxation rates. The absorption and stimulated rates are given by $\sigma_i I$, where σ_i is a cross-section in cm^2 and I is in photons-$cm^{-2}s^{-1}$. Saturation parameters are defined by $I_s^1 = h\nu A_{31}/\sigma_1$ and $I_s^2 = h\nu A_{42}/\sigma_2$.

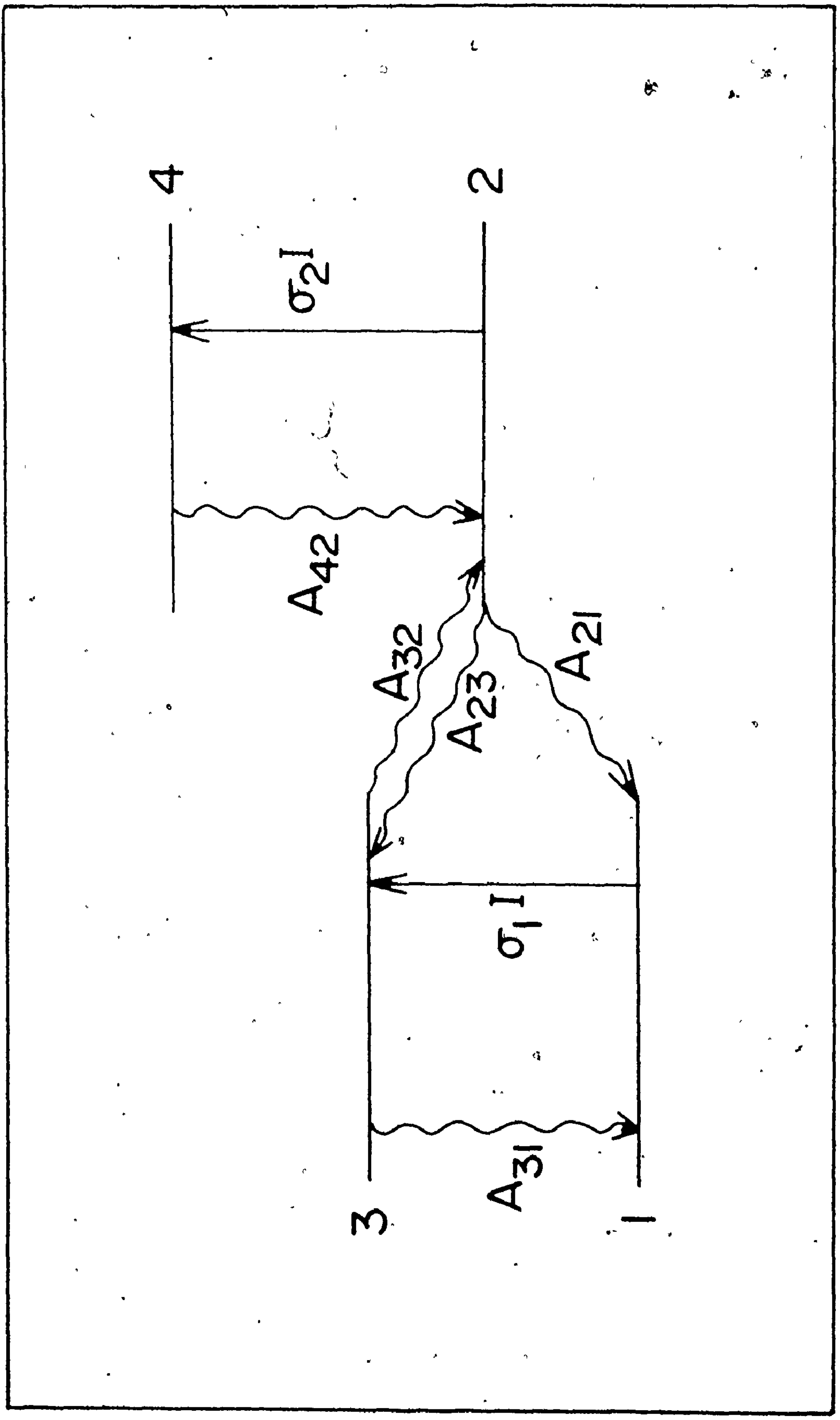
4
2
σ_2^I
A_{42}
A_{32}
A_{23}
A_{21}
σ_1^I
A_{31}
3
1

$$\frac{dN_4}{dt} = -A_{42}N_4 + \sigma_2 I(N_2 - N_4) \quad (3\text{-}4)$$

The A_{ij} terms represent collisional relaxation rates. Here σ_i is an optical cross-section for the i'th level, in cm^2, and I is in photons-$cm^{-2}s^{-1}$. The model allows for coupling between levels 2 and 3. In addition, the relaxation of levels 1 and 2 to their equilibrium mode population densities, N_1^e and N_2^e, has been allowed for by incorporation of the terms A_{vv}^1 and A_{vv}^2, respectively.

The rate equations were solved using a finite difference method outlined in Appendix B. The optically thick absorber case is treated, and account is taken of intensity and population density variation in the direction of pulse propagation. This is accomplished by dividing the absorber up into a number of sections (of optical length Δz) such that the intensity variation across each section is small. A step-by-step calculation of the intensity is used in a similar fashion to that employed in Huff and DeShazer [6]. The output intensity (I_1) from the first absorber increment is calculated from the cell input intensity (I_0), at time t, according to

$$I_1 = I_0 \exp -\Delta z[(N_1 - N_3)\sigma_1 + (N_2 - N_4)\sigma_2] \ . \quad (3\text{-}5)$$

I_1 then becomes the input for the second absorber section and the calculation is repeated to the end of the absorber. A sufficient number of steps were used to provide less than a 5% variation in the calculated quantities (usually six steps were sufficient). The next intensity increment (corresponding to a time $(t + \Delta t)$) is then fed into the absorber and the calculations repeated. This procedure is continued until the entire pulse has propagated through the absorber. The inverse of the time increment (Δt^{-1}) is chosen to be greater than the largest relaxation rate, or absorption and stimulated emission rate $\sigma_i I$ (typically >10^9 s^{-1}), whichever proved to be the largest for a given input intensity. The time dependence of the population densities and pulse transmission is calculated in each of the absorber increments and comparisons can therefore be made between the model and experimental pulse shaping.

The saturation parameters defined by $I_s^1 = h\nu A_{31}/\sigma_1$ and $I_s^2 = h\nu A_{42}/\sigma_2$, together with the cross-section ratio σ_2/σ_1, provide four important parameter groupings, which are: $\sigma_2/\sigma_1 > 1$, $I_s^2 > I_s^1$; $\sigma_2/\sigma_1 < 1$; $I_s^2 > I_s^1$; $\sigma_2/\sigma_1 < 1$, $I_s^2 < I_s^1$; and $\sigma_2/\sigma_1 > 1$, $I_s^2 < I_s^1$. The I_s^2/I_s^1 and σ_2/σ_1 ratios, together with the branching ratio of level 3 (A_{32}/A_{31}), are the key parameters varied in the model analysis. The equilibrium population densities of levels 2, 3 and 4 (relative to level 1) are obtained from spectroscopic data, where possible. In every case it proved necessary to have the A_{21} relaxation rate less than the inverse of the pulse duration.

3.3(c) Results and Discussion

Figure 3-5 shows the measured SF_6 transmission with input intensity for a number of CO_2 rotational lines, at a gas pressure of 50 Torr. Observe that the saturation intensity increases with increasing J-value. Furthermore, as we progress towards higher J-values the onset and deepening of a transmission minimum is apparent. The data for the P(12) and P(14) lines (not shown) lies close to the P(16)

Fig. 3-5

Transmission as a function of input intensity for the P(16), P(20), P(22), P(24) and P(26) CO_2 lines at an SF_6 pressure of 50 Torr. The input intensity is that of the elliptical beam cross-section at the front surface of the Brewster-angled cell.

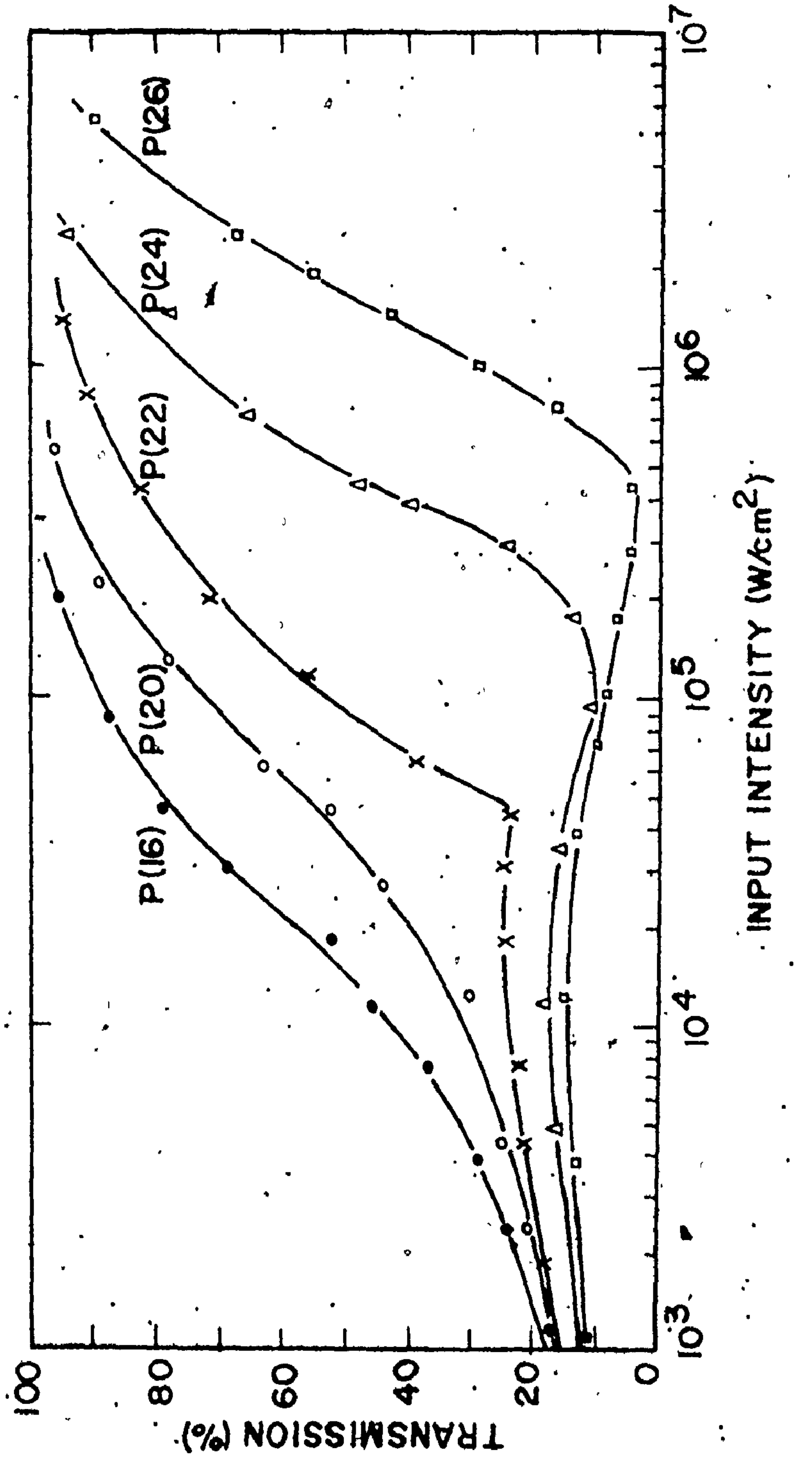
P(16)
P(20)
P(22)
P(24)
P(26)
TRANSMISSION (%)
100
80
60
40
20
0
10^3
10^4
10^5
10^6
10^7
INPUT INTENSITY (W/cm^2)

transmission curve, while the P(28) and P(30) lines (not shown) have a similar transmission curve to that of the P(26) line, but are shifted to higher input intensities. At high input intensities, the transmission approaches 100% for all the P-lines studied.

P(14) Saturation Behaviour

Figure 3-6 displays the transmission as a function of input intensity for the P(14) CO_2 line for SF_6 pressures in the range of 10 to 100 Torr. The solid curves indicate the transmissions predicted by the 4-level model. The important parameters for the fit at 50 Torr SF_6 are listed in Column 1 of Table 3-2. Figure 3-6 indicates that very good agreement can be obtained over the entire transmission range by pressure scaling of all collisional rate parameters obtained from the 50 Torr data. As well, the parameters in Table 3-2 predict the observed symmetric pulse narrowing (∿12% of input FWHM) at low input intensity, followed by a broadening to the input pulse FWHM at moderate input intensities.

An estimate of particular cross-sections can be obtained from the above analysis when some characteristic relaxation time (i.e., V-V or rotational) appropriate to our data is determined by independent means. It will be shown in Chapter 4 that reasonable time for the level 4 to level 2 relaxation is about 0.4 ns at 50 Torr of SF_6. This corresponds to a value of 50 $\mathring{A}^2$ for σ_1.

Fig. 3-6

Transmission as a function of input intensity for the P(14) CO_2 line at SF_6 pressures of 10 Torr (x), 25 Torr (Δ), 50 Torr (o), and 100 Torr (●). The curves represent the theoretical transmission predicted by the 4-level model.

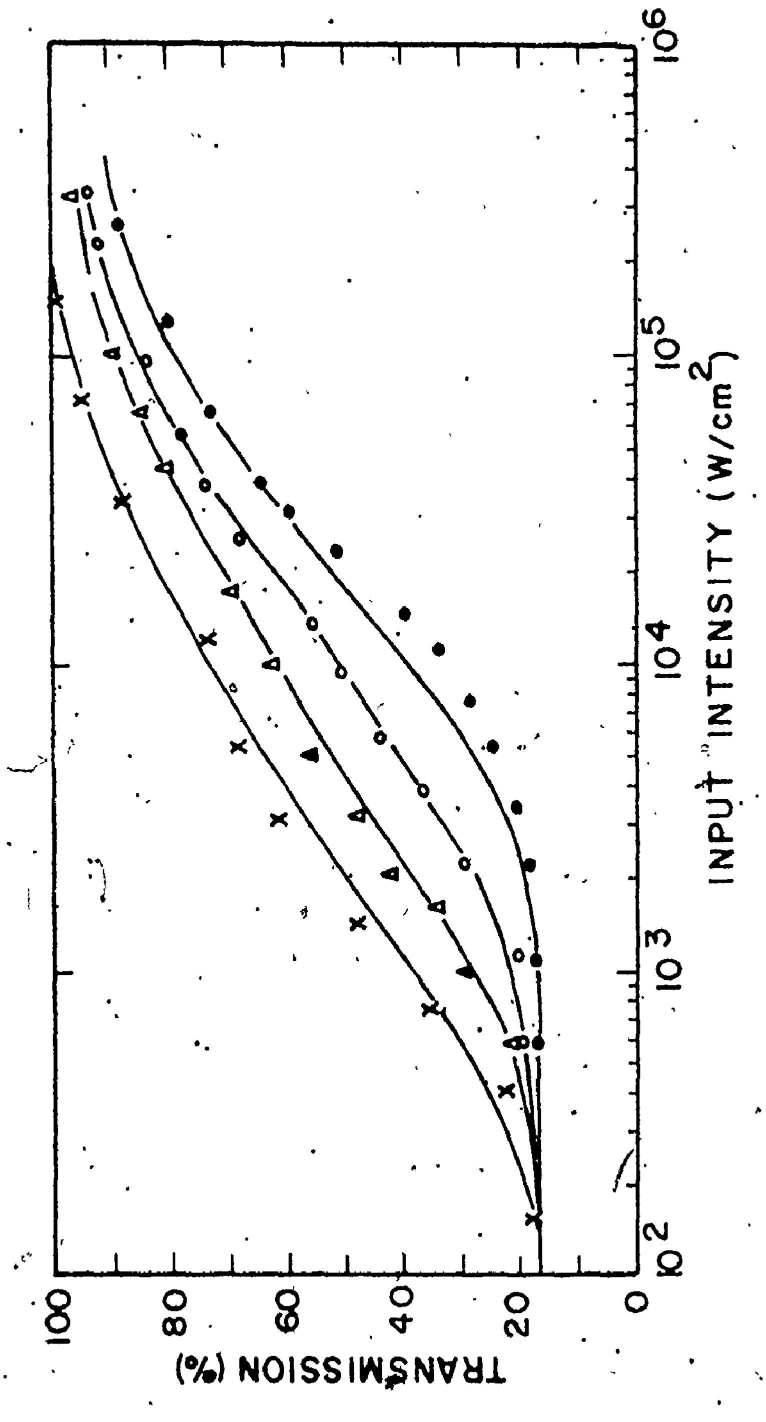
TRANSMISSION (%)
100
80
60
40
20
0
INPUT INTENSITY (W/cm^2)
10^2
10^3
10^4
10^5
10^6

TABLE 3-2

Four-Level Model Parameters Appropriate for 50 Torr of SF_6

	P(14)	P(20)	P(26)
σ_2/σ_1	3	1.5	5
I_s^2/I_s^1	0.02	7.5	6.2
I_s^1	79 kW/cm^2	7.4 kW/cm^2	53 kW/cm^2
A_{32}/A_{31}	0.03	0.35	0.5

P(20) Saturation Behaviour

Figure 3-7 shows the transmission as a function of input intensity over an SF_6 pressure range of 10 to 100 Torr. Pulse narrowing is observed at low transmissions; it is predominantly on the pulse tail and has a magnitude of 12 to 15% of the input FWHM. At moderate transmissions, the transmitted pulse exceeds the width of the input pulse. The particular transmission for which the maximum observed pulse broadening (∿15%) occurs increases as the SF_6 pressure is reduced. The magnitude of the broadening decreases with lower SF_6 pressures; in fact no broadening was observed at a pressure of 10 Torr. At higher input intensity, the pulse duration and shape return to that of the input pulse. Broadening to greater than the input pulse width has been noted previously [57] at lower SF_6 pressures (6-12 Torr). Much lower small-signal transmission was employed and the return of the transmitted pulse shape to that of the input was not observed. It was suggested that this broadening may be due to coherent effects such as self-induced transparency. The observed persistence of this broadening to at least 100 Torr SF_6 pressure makes this suggestion seem very unlikely. Pulse broadening has also been observed at the transmission minima of the P(22) to P(30) lines. This will be discussed in further detail in the section on P(26) saturation characteristics.

The parameters for the P(20) fit are recorded in column 2 of Table 3-2. The curve through the 50 Torr data in Fig. 3-7 was generated using these parameters, together with the assumptions that $N_2^e < N_1^e$ and that the A_{21}^{-1} relaxation time was longer than the input pulse duration. The remaining curves of Fig. 3-7 were generated by pressure-scaling

Fig. 3-7

Transmission as a function of input intensity for the P(20) CO_2 line at SF_6 pressures of 10 Torr (x), 25 Torr (Δ), 50 Torr (o), and 100 Torr (•). The curves represent the theoretical transmission predicted by the 4-level model.

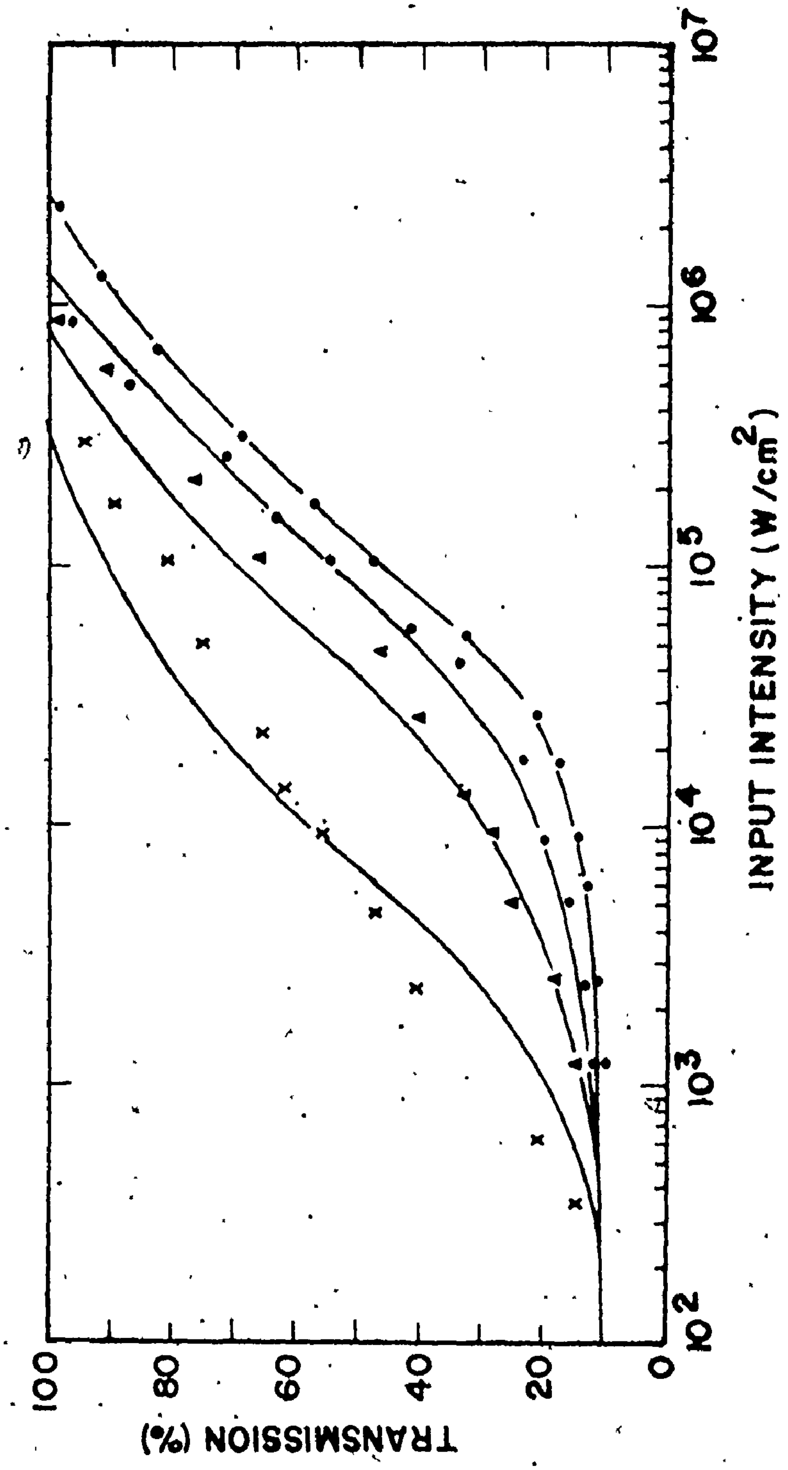
TRANSMISSION (%)
0
20
40
60
80
100
INPUT INTENSITY (W/cm^2)
10^2
10^3
10^4
10^5
10^6
10^7

the 50 Torr collisional rates. Very good agreement was obtained at 100 Torr; the agreement was somewhat poorer at the lower pressures. The pulse dynamics were reasonably well accounted for using the parameters of Table 3-2. However, no combination of parameters could accurately predict the observed pulse broadening. The σ_2/σ_1 ratio of 1.5 (Table 3-2) is in very good agreement with the value of 1.3 obtained from the infrared double-resonance experiments performed at ∿0.2 Torr of SF_6 [47]. For an effective relaxation time of ∿0.4 ns at 50 Torr SF_6, the cross-section values for the P(20) line are in the order of 10 $Å^2$.

P(26) Saturation Behaviour

Spectroscopic investigations of SF_6 at 300 K indicate that almost all of the absorption of the P(14) CO_2 line occurs from vibrational levels < 1000 cm^{-1} above the ground state; the converse is true for the lines P(20) to P(30) [48]. There are many absorbing levels for the P(26) line in SF_6, with each level making only a small contribution to the total absorption. Nevertheless, a four-level model, for which each level represents a group of absorbing vibrational and rotational levels, can give an adequate description of the saturation process. The curves in Fig. 3-8 represent the best visual fit to the data.† Furthermore, the curve through the 100 Torr SF_6 data also represents the theoretical fit employing the parameters of column 3 in Table 3-2.

---

† A similar curve to the 100 Torr case was obtained using 50 Torr of SF_6 and 200 Torr of He. Such behaviour has been noted for the P(14) and P(20) lines as well.

Fig. 3-8

Transmission as a function of input intensity for the P(26) CO_2 line at SF_6 pressures of 10 Torr (o), 50 Torr (x), 100 Torr (●), and 200 Torr (Δ). The curve through the 100 Torr data indicates the theoretical transmission predicted by the 4-level model at this pressure.

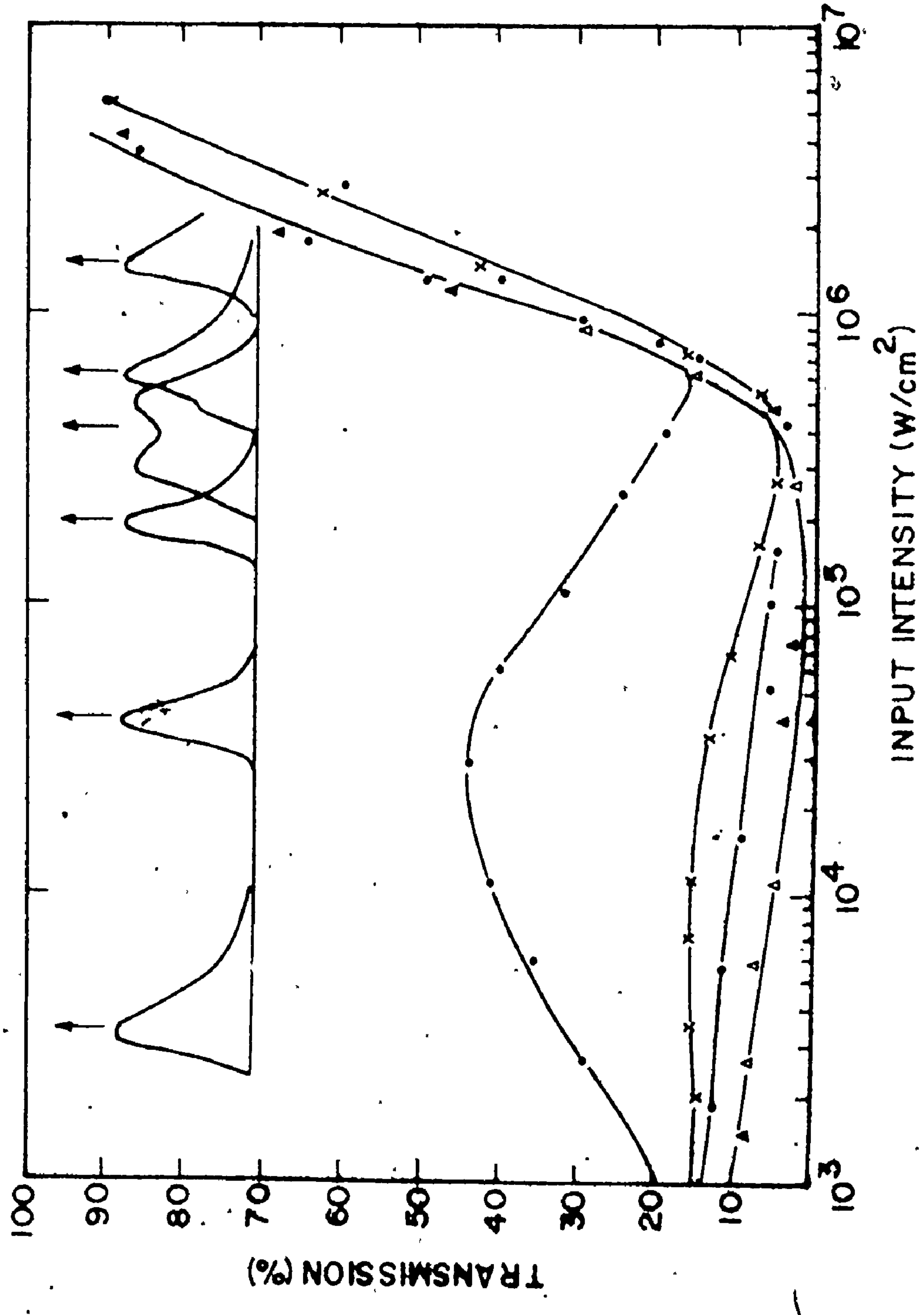
100
90
80
70
60
50
40
30
20
10
TRANSMISSION (%)
10^3
10^4
10^5
10^6
10^7
INPUT INTENSITY (W/cm^2)

The pulse shaping for the P(26) line, as a function of input intensity, consists of a region of very strong pulse narrowing on the pulse tail followed by a partial pulse break-up at the transmission minimum. The rather dramatic pulse shaping, which is typical of all the SF_6 pressures, is shown in Fig. 3-8 at the appropriate input intensities. The pulse shaping behaviour is also shown in the multiple exposure photograph in Fig. 3-9.* At high input intensities the pulse narrows to approach the input pulse duration, as expected.

Time delays, measured between the peaks of the incident and transmitted pulses, indicate that the transmitted pulse peak is first advanced by ∿20 ns in the pulse-narrowing region, goes through zero to delays of the order of 100 ns at the position of maximum pulse broadening, and finally returns to zero delay at higher intensity. The pulse dynamics and time delays are well accounted for by the 4-level model, except for an inability to predict accurately the pulse-broadening effect.

The σ_2 cross-section is determined to be ∿0.5 $\mathring{A}^2$ for an A_{42}^{-1} relaxation time of 0.5 ns at 50 Torr SF_6. The magnitudes of the σ_1 and σ_2 cross-sections indicate that participation of a large number of vibrational levels in the P(26) absorption is needed to account for the observed absorption saturation. It is estimated that 30% of the molecules are in states above 1000 cm^{-1} [23] from the ground state (at

---

* Further experiments verified that the pulse shaping effect was not due to intensity and therefore not to time-dependent index of refraction effects.

Fig. 3-9

Multiple exposure oscilloscope trace of four transmitted pulse shapes for the P(26) CO_2 line at an SF_6 pressure of 50 Torr. Pulses 1 to 4 indicate the progression to higher input intensities. The horizontal scale represents time (100 ns per division). The transmitted pulse peak time advancement (pulse No. 2) and delay (pulse No. 4) relative to the position of the input pulse (pulse No. 1) are shown in this photograph.

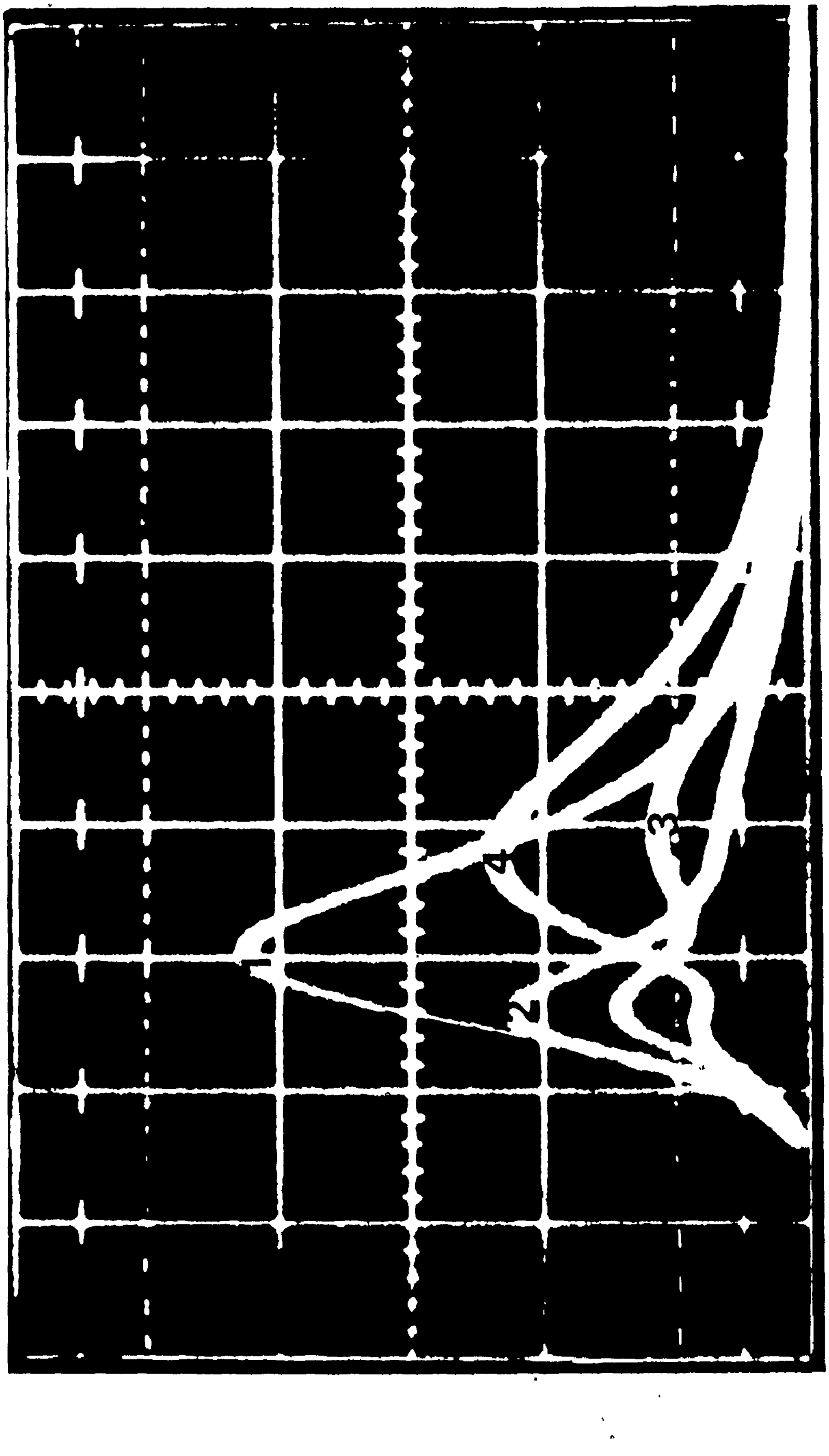
1
2
3
4

300 K. Roughly 1/3 of these must be strongly coupled to the absorbing states for the observed saturation intensity.

The cross-section ratio $\sigma_2/\sigma_1 = 5$ is also in very good agreement with the double-resonance experiments of Steinfeld, which gave a value of 4 [47].

The high-transmission data displayed in Fig. 3-8 indicates that the saturation parameter appropriate to this region ($I_s^2 = h\nu A_{42}/\sigma_2$) varies by at most 50% over a SF_6 pressure range of 10 to 200 Torr. Within the framework of the 4-level model, this either implies that σ_2 depends on pressure, or that A_{42}^{-1} does not. However, if σ_2 depends on pressure, then it is not possible to obtain good fits to the transmission data observed experimentally in the 10-200 Torr pressure range. It therefore seems, to the degree that a 4-level model is appropriate for the P(26) absorption saturation, that there must exist pressure-independent relaxation processes for levels 2 and 4.*

The four-level model gave good agreement to the data between 50 and 200 Torr over the entire transmission range. However, under no circumstances could the 4-level model (in which level 3 is directly coupled to level 2) predict the dramatic transmission rise, then fall to a transmission minimum which occurs for 10 Torr of SF_6. This, combined with the lack of complete agreement with the observed pulse-broadening effect for both the P(20) and P(26) lines, indicate that a more complicated model is necessary to account for all of the observations. Such a model must take into account the near continuum of rotational and vibrational levels above 1000 cm^{-1}. One approach is to treat the large number of vibrational levels as belonging to a single vibrational mode, characterised by an effective temperature. This model would allow for heating of the vibrational mode through absorption, followed by relaxation to a new distribution appropriate to a higher effective mode temperature. A detailed investigation of this model is given in the next chapter.

---

* Another interpretation of the lack of variation of I_s^2 with pressure (Fig. 3-8) will be presented in Chapter 5.

3.3(d) Summary

This section presents SF_6 transmission data in the pressure range of 10-200 Torr for the P(14), P(20), and P(26) CO_2 rotational lines. This data characterises the absorption saturation behaviour of SF_6 in the 10.4 μm band. The importance of knowing the pulse dynamics to obtain a reasonable set of 4-level model parameters has been emphasized. The 4-level modelling allowed a determination of the ratios σ_2/σ_1, I_s^2/I_s^1 and A_{32}/A_{31} for the P(14), P(20) and P(26) lines. These parameters are important for the understanding of Q-switching, mode-locking and optical-pumping experiments.

The 4-level model gave excellent agreement with the P(14) transmission data over a wide transmission and pressure range. However, it could not account for all the details of the SF_6 saturation at the P(20) and P(26) lines. An alternative multi-level absorption model is suggested, which is the subject of the next chapter.

CHAPTER 4

A VIBRATIONAL BATH MODEL FOR THE DYNAMICS OF SF_6 ABSORPTION NEAR 10.4 μm AS A FUNCTION OF WAVELENGTH AND ABSORBED ENERGY

4.1 Introduction

In the last chapter it was mentioned that a 4-level saturation model could account for much of the observed large-signal SF_6 transmission properties. However, there was a definite progression to poorer agreement at the longer CO_2 wavelengths. It will be shown in this chapter, and in the next, that excellent agreement is made possible by use of a multi-level vibrational bath model. The complete determination of the large-signal transmission behaviour of SF_6, for a large number of CO_2 wavelengths and SF_6 pressures, is of course important for the understanding of SF_6 mode-locking and Q-switching. This will be discussed in detail in Chapter 6.

There is much interest concerning the energy build-up processes in SF_6. At low SF_6 pressures ($\lesssim$ 1 Torr), interest is directed to the build-up mechanisms associated with the isotopic separation of SF_6 by laser-induced photodissociation [58]. Such photodissociation experiments on SF_6, as well as with other polyatomic molecules such as SiF_4 [59], $BC\ell_3$ [56], and CF_2 $C\ell_2$ [56], have demonstrated that the absorption mechanisms for vibrational energy build-up can lead to dissociation once a critical number of photons/molecule are absorbed. At low pressures there is evidence that the absorbed energy is transferred to a large number of vibrational levels via very rapid intramolecular, radiationless, collisionless, vibration-to-vibration (V-V) processes [60]. This chapter demonstrates that, at progressively higher gas pressures, very fast collision-dependent intermolecular V-V processes occur. The energy exchange processes are sufficiently short, compared to the duration of a Q-switched CO_2 pulse, to allow the construction of an absorption model for SF_6 in which the many vibrational and rotational levels are considered as belonging to a population distribution characterised by vibrational and rotational temperatures, T_V and T_R, respectively. Energy from an incident laser pulse is absorbed into the complex multilevel system and heats the entire vibrational mode, resulting in a new higher effective bath temperature. The absorption appropriate to this new temperature can be calculated for all the CO_2 P-lines once the SF_6 gas cell thickness, the gas pressure, the transmitted pulse intensity, and the input pulse duration are known. Provided that equilibrium conditions are met, the model can predict the time dependence of the absorption on all CO_2 P-lines during the input pulse duration. It will be shown in the next chapter that, at high SF_6 pressures, the model correctly predicts the entire transmission and pulse shaping behaviour of the input pulse itself from low to very high transmittances. The model is particularly applicable at high pressures since at these pressures (typically >200 Torr) the increase in pulse transmission due to vibrational heating dominates over the contribution by true intensity saturation processes. As was observed in Section 3.3, this is not necessarily correct at lower pressures.

Infrared double-resonance experiments using ∿200 ns and ∿3.5 ns pump pulses are reported in this chapter. These experiments demonstrate the effectiveness of the model as well as investigate the V-V and rotational recovery rates to ascertain the range of SF_6 pressures and input pulse durations for which the bath model applies. These experiments also supply information on the absorber recovery times, which will be useful in the discussion of mode-locking in Chapter 6.

4.2 Vibrational Bath Model

The band contour for the ν_3 fundamental of SF_6, as outlined by Nowak and Lyman [48], is modified to allow calculation of the absorption coefficients of the many vibrational and rotational states which interact with a CO_2 laser pulse (at 10.4 μm) when the energy is fed in through the vibrational degrees of freedom. The energy is stored as vibrational energy during the pump pulse when its duration is less than the vibration-to-translation (V-T) relaxation time of ∿120 μs-Torr [47]. This condition is satisfied for all the SF_6 pressures discussed in this chapter. In the model it is assumed that all the vibrational and rotational levels reach equilibrium in a time short compared to the input pulse duration and that they can be characterized by a Boltzmann temperature distribution. This assumption will be discussed further in the section on energy transfer rates. Its validity is primarily due to the high density of energy levels and the subsequent coupling between them, which is characteristic of large polyatomic molecules. Fig. 4-1 shows the vibrational energy diagram for SF_6. Absorption from the ground vibrational state to the ν_3 fundamental (10.55 μm) is indicated by the

Fig. 4-1

Energy level diagram for SF_6.

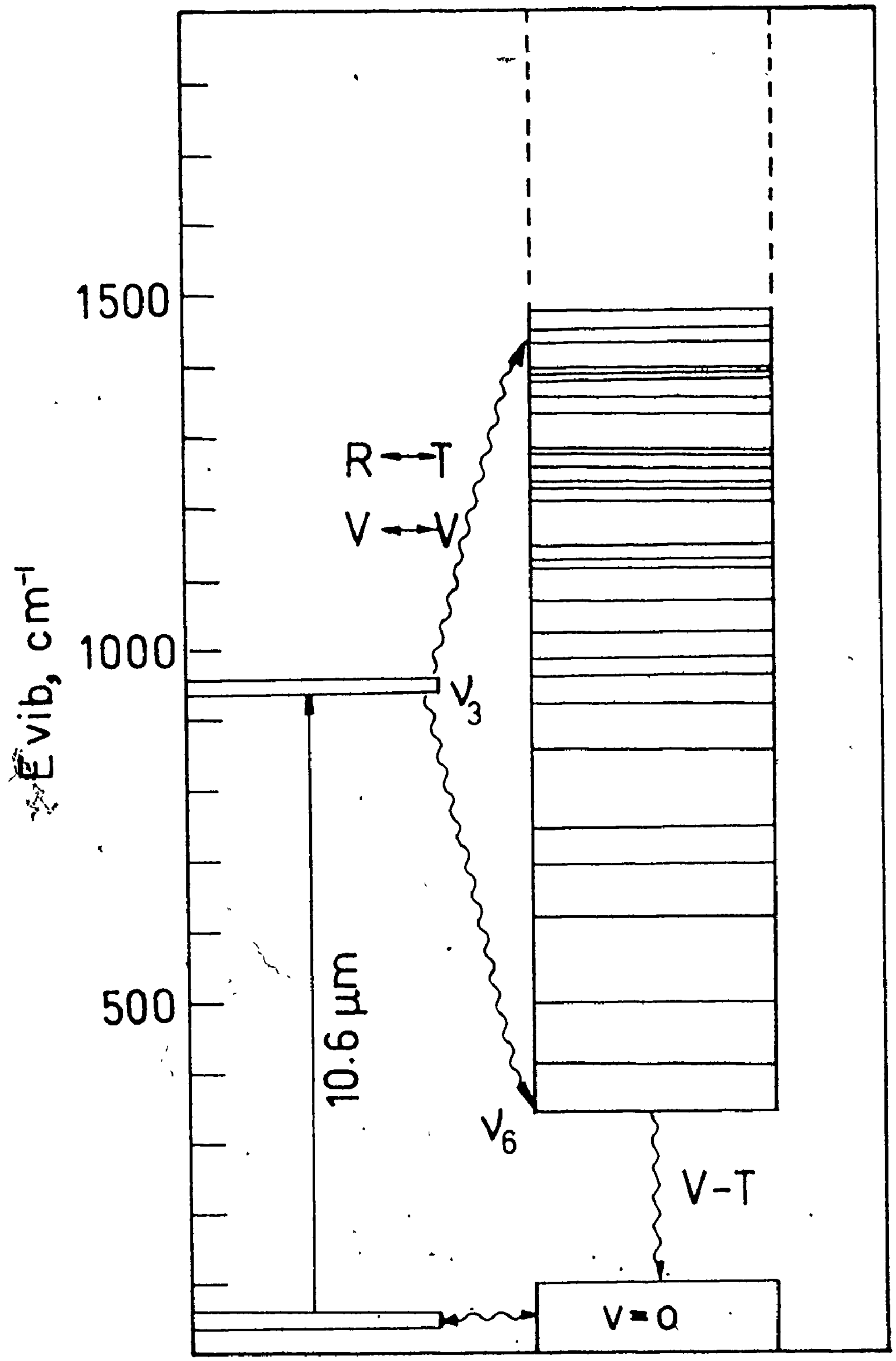
Evib, cm⁻¹
1500
1000
500
R ←→ T
V ←→ V
ν3
ν6
10.6 µm
V–T
V = 0

solid arrow. The subsequent V-V (vibration-to-vibration) and R-T (rotation-to-translation) processes transferring energy to a large bath of levels are indicated by wavy lines. Note that the density of vibrational levels starts to increase substantially above 1000 cm^{-1}.

Appendix C outlines the details of the model. All SF_6 energy levels less than 9000 cm^{-1} above the ground state were included in the calculations. It was found, however, that only levels below ∿5000 cm^{-1} contribute significantly to absorption near 10.4 μm.* The rotational temperature was kept at 300 K for all the calculations presented in this chapter because these calculations are relatively independent of the rotational temperature. This occurs for the following reasons: Although direct vibration-to-rotation (V-R) energy transfer processes are expected to be slow [67], heating of the rotational degrees of freedom may occur via V-T-R processes, but only at sufficiently high SF_6 pressures and at large absorbed energies. Under these conditions the V-T relaxation time becomes comparable to the typical ∿200 ns input pulse duration. However, even in these circumstances, the CO_2 absorptions at a given vibrational temperature are independent (to within 15%) of the rotational temperature chosen. This somewhat surprising prediction results from the fact that many vibration and rotation levels participate in the absorption at each CO_2 laser line. Raising T_R increases the rotational population for transitions which involve J-states with J above J^{max} (at 300 K, J^{max} ∿ 48) but at the expense of the population involving low J values.*

---

* The contribution to the absorption from the continuum of levels well above 5000 cm^{-1} can be significant for the very low J-lines, such as P(10), or for the very high J-lines, such as P(28).

The model also includes the contribution of the $S^{34}F_6$ isotope to the absorption spectrum. The ν_3 band contour is assumed to be identical to that of $S^{32}F_6$, but is shifted to a lower frequency by 17.4 cm^{-1} [64]. The contribution becomes significant for CO_2 lines beyond P(28). The anharmonicity coefficients, defined in Appendix C, and obtained from Ref. [64], were varied within their experimental errors to yield a good fit to the experimental 300 K absorption spectrum. These adjusted coefficients, and all other spectroscopic constants, were not allowed to vary for all the remaining experimental comparisons.

Fig. 4-2 displays the predicted absorption coefficient for various CO_2 P-lines against vibrational temperature. The decrease in absorption coefficient at the shorter wavelength lines and the initial increase at longer wavelengths is simply due to the shift in the vibrational population distribution to levels farther removed from the ground state, and to regions where anharmonicities favour the longer wavelength CO_2 lines. This is demonstrated in Fig. 4-3 which shows the calculated energy above the ground state for which the effective absorption cross-section (defined in Appendix C) is a maximum for a given CO_2 P-value. This figure indi-

---

* Exceptions to this rule are the shorter wavelength CO_2 lines for which the J numbers of absorbing states are predominantly above J^{max} at 300 K. However, even in this case the absorption coefficient changes only by a factor of 5 at T_R = 1000 K with respect to the T_R = 300 K absorption, while a corresponding change in T_V produces a change of over a factor of 350. These lines are generally not of great interest due to their small low-signal absorptions at 300 K, which are reduced even further by vibrational heating. The result is that the variation in the level populations with temperature are basically determined by the vibrational Boltzmann distribution only.

Fig. 4-2

Absorption coefficient as a function of vibrational temperature for selected CO_2 rotational lines.

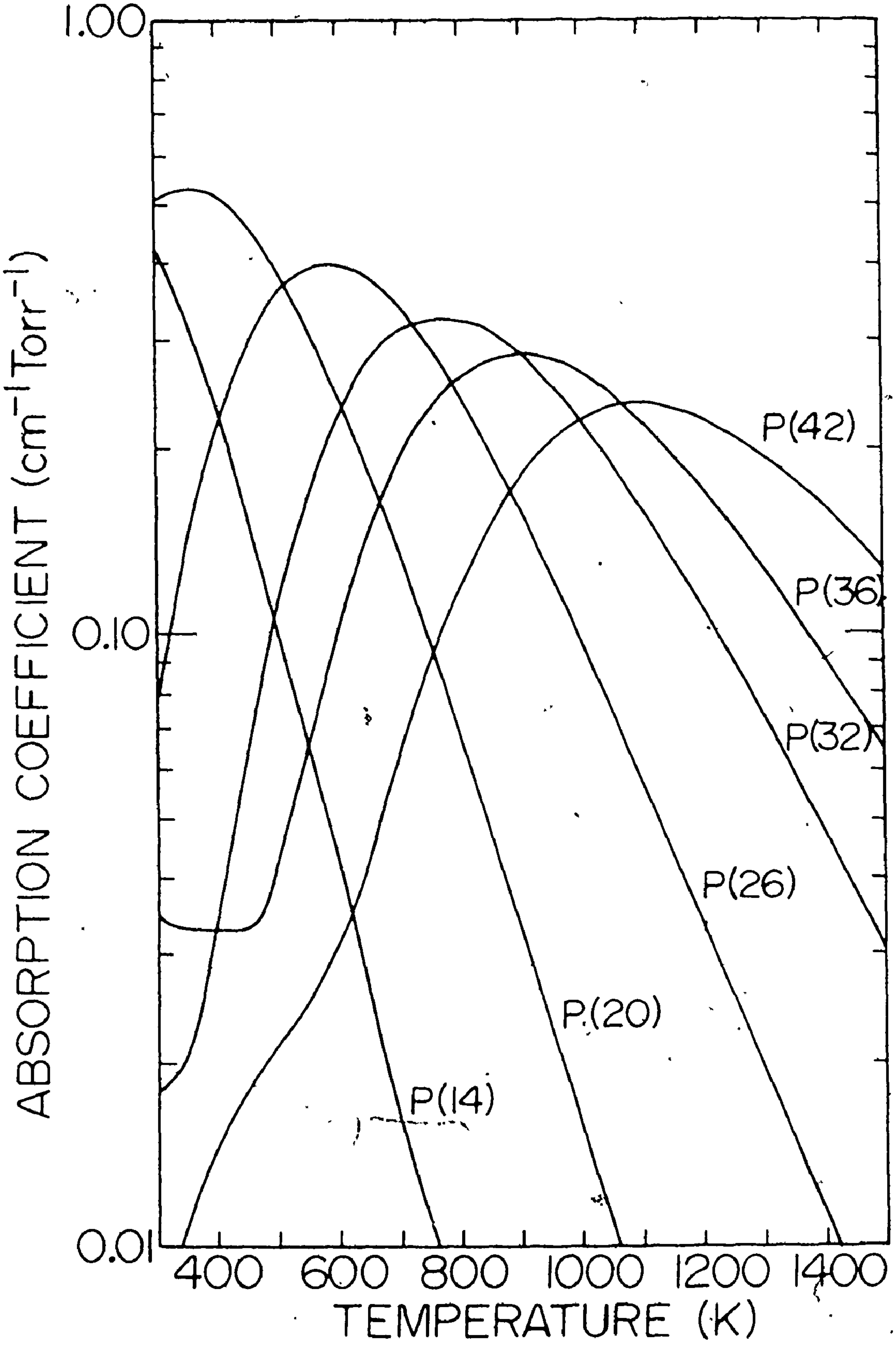
1.00
0.10
0.01
ABSORPTION COEFFICIENT (cm^{-1}Torr^{-1})
400
600
800
1000
1200
1400
TEMPERATURE (K)
P(42)
P(36)
P(32)
P(26)
P(20)
P(14)

Fig. 4-3

Vibrational energy (above the ground state) for P, Q and R cross-section maxima as a function of CO_2 wavenumber.

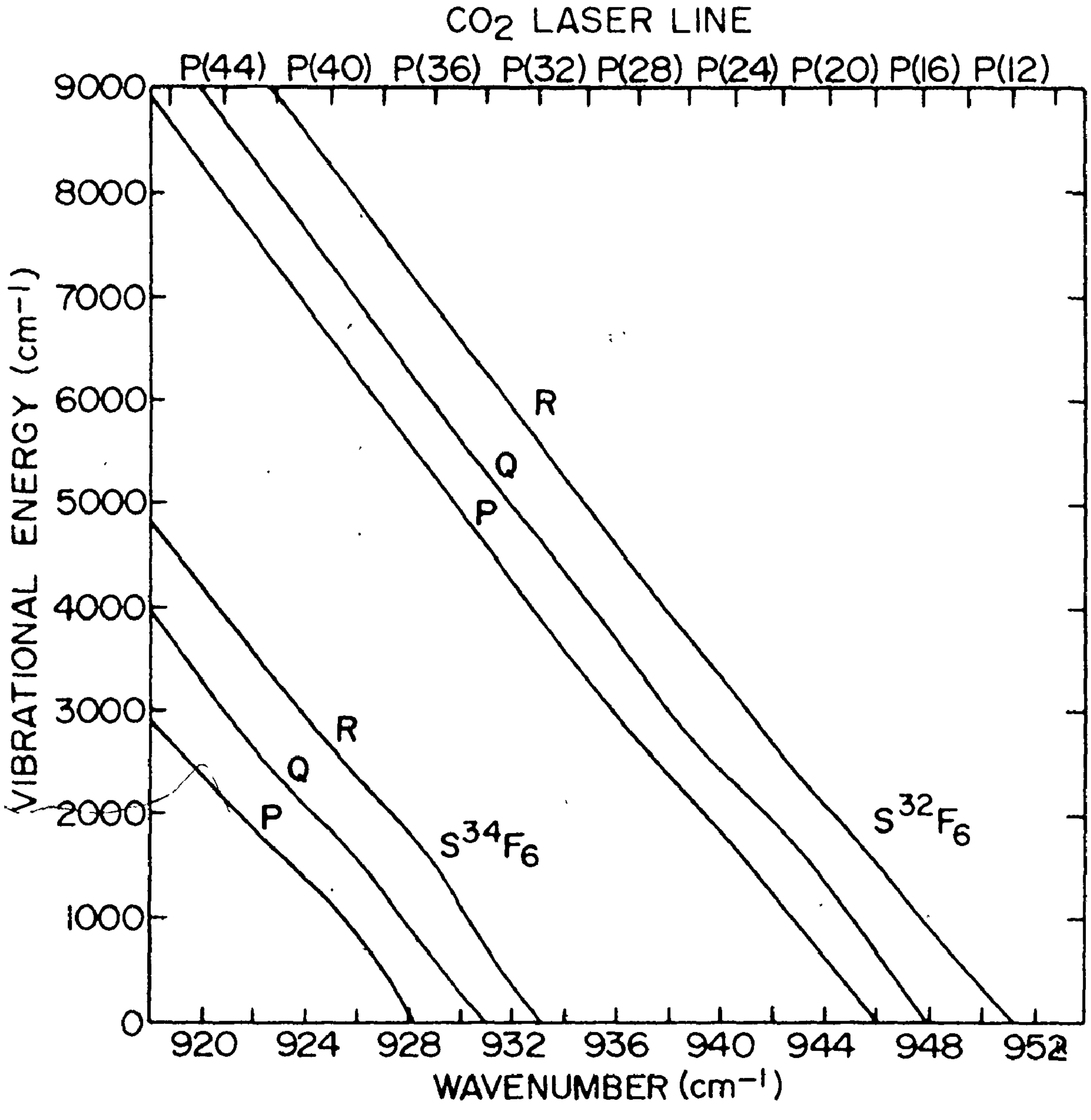
CO2 LASER LINE
P(44) P(40) P(36) P(32) P(28) P(24) P(20) P(16) P(12)
VIBRATIONAL ENERGY (cm⁻¹)
9000
8000
7000
6000
5000
4000
3000
2000
1000
0
R
Q
P
$S^{32}F_6$
R
Q
P
$S^{34}F_6$
920
924
928
932
936
940
944
948
952
WAVENUMBER (cm⁻¹)

cates the shift in the position for maximum cross-section to higher vibrational levels with progressively longer CO_2 wavelengths. Furthermore, it shows that there are two, and sometimes three maxima, for a given CO_2 P-line which are approximately separated in energy by the energy of a 10.4 μm photon, which correspond to P, Q and R branch rotational transitions. The widths of the P, Q and R cross-section maxima are quite large and can extend for many hundreds of cm^{-1}. These curves demonstrate the possibility of climbing the vibrational energy ladder employing multiple photon absorption processes. This is possible through a compensation for anharmonicities by proceeding through P to Q to R-branch rotational transitions. This mechanism has been discussed in Ref. [68]. It is evident that the P(16) CO_2 line should be able to reach E_{vib} ∿2000 cm^{-1} by a 2-photon process, i.e., a Q-branch followed by an R-branch transition. Lines with P number greater than P(18) that have P, Q and R branches allow for the possibility of 3-photon absorption processes.

Also shown in Fig. 4-3 are similar P, Q and R curves for $S^{34}F_6$ molecules. There is an interesting change in the number of multiple absorption steps possible for a P(30) compared to a P(32) CO_2 rotational line. The model-based absorption spectrum for the P(30) line at 300 K indicates that there is only a 10% absorption contribution from $S^{34}F_6$ molecules and that most of the absorption (∿70%) occurs from P-branch $S^{32}F_6$ transitions originating at ∿2000 cm^{-1} above the ground state. Therefore, for P(30) a possible multiple photon process would consist of a P-branch transition from ∿2000 cm^{-1} to ∿3000 cm^{-1}, followed by the P to Q to R sequence of transitions suggested by the $S^{32}F_6$ curves. The second P-branch transition is possible due to the large width of the P-branch cross-section maximum. This mechanism for the P(30) multiple photon absorption appears more appropriate than that proposed in Ref. [69].

For the P(32) line, however, 90% of the absorption at 300 K is due to $S^{34}F_6$ molecules in states <1000 cm^{-1}. Presumably, the P(32) absorption process can only consist of an R-branch transition which cannot connect with the region where there is significant P-branch $S^{32}F_6$ cross-section. This is true even when SF_6 pressures are high enough to allow effective collisional interaction between the two isotopic species. However, muliphoton transitions involving the stepping from excited $S^{34}F_6$ to $S^{32}F_6$ should be possible if the gas is vibrationally heated so that most of the $S^{34}F_6$ absorption occurs around 3000 cm^{-1}. This argument indicates the importance of considering vibrational heating effects when one speculates on multiphoton absorption processes for different CO_2 lines.

4.3 Experimental

Fig. 4-4 outlines a typical experimental arrangement for the ∿200 ns pump-pulse double-resonance experiments. The pump laser was the familiar helical-pin-discharge TE laser which operated at a total gas pressure of ∿1/2 atm. The output pulse duration was kept close to 200 ns (FWHM) and the laser was operated without N_2 to avoid long pulse tails. A grating was employed to select the desired rotational lines. An aperture inserted within the laser resonator ensured operation in the TEM_{00} mode. The intensity of the pump beam at the SF_6 cell could be varied from 10 kW/cm^2 to 1 MW/cm^2 by the use of transmitting mirrors

Fig. 4-4

Schematic diagram of the experimental double-resonance apparatus.

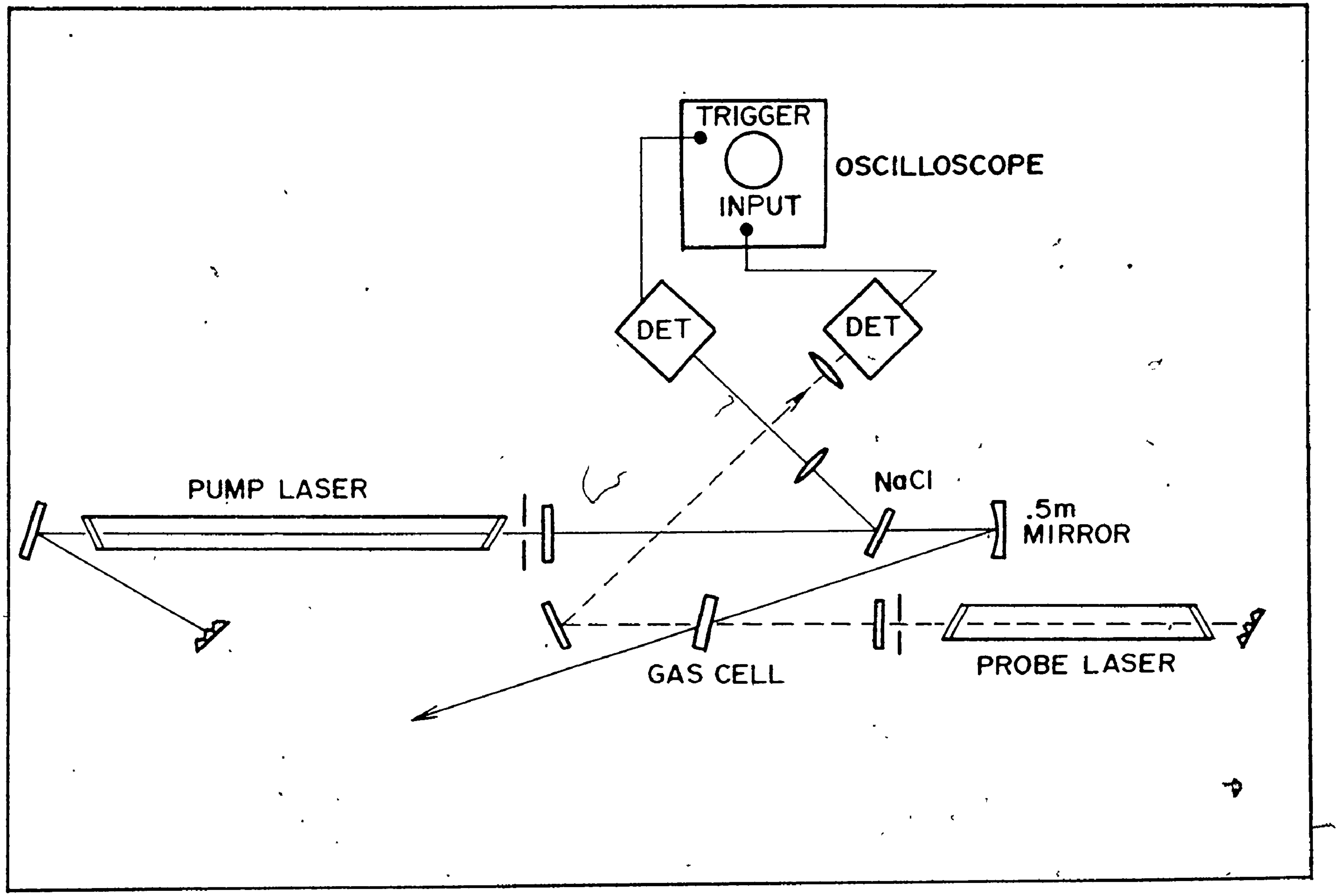
TRIGGER
OSCILLOSCOPE
INPUT
DET
DET
PUMP LASER
NaCl
.5m
MIRROR
GAS CELL
PROBE LASER

employed as attenuators and a 0.5 m radius of curvature gold mirror to vary the beam cross-section at the cell. A small portion of the pump pulse was selected by a NaCl flat and focussed onto a 2 ns risetime Au:Ge detector. The detected signal was used as an external trigger for measurements of time delays between the pump pulse and the start of the double-resonance signal. The remaining portion of the pump beam was sent to an SF_6 gas cell maintained at a gas temperature of 300 K. Where appropriate, all optical components were tilted slightly to avoid reflections from entering either the pump or probe lasers. All of the SF_6 gas used in these experiments was of high purity (obtained from Matheson) and no extra purification was attempted.

A helical TE CO_2 laser was used as a probe source instead of the more conventionally used cw CO_2 laser. This was done to avoid possible heating of the SF_6 gas by the probe beam and also to obtain a higher double-resonance signal, with consequent improvement in the signal-to-noise ratio. It was ascertained experimentally that restricting the probe laser output intensity to values below a kW/cm^2 obviated intensity saturation effects. This laser operated at a total gas pressure of between 100 and 150 Torr and with a very large N_2 concentration. The high N_2 concentration, together with the use of a low linear-loss cavity, produced a suitably low intensity laser pulse with a long fall time. The fall time was sufficiently large that the probe signal appears flat over the time scale of expected V-V relaxation times (∿ a μs-Torr) [70]. The pump pulse was always arranged to fall on this plateau region, as shown in Fig. 4-5(a). A grating selected the desired probe CO_2 rotational line and an aperture ensured operation in the TEM_{00} mode. The probe

Fig. 4-5

(a) Oscilloscope display of a CO_2 pump laser pulse superimposed on the plateau region of the probe pulse.

(b) Display of a P(16) pump, P(16) probe double-resonance signal obtained at an SF_6 pressure of 10 Torr. The top dashed curve represents the 100% transmission level; the bottom dashed curve represents the SF_6 transmission level in the absence of the pump pulse. The base line indicates zero transmission.

(c) Display of a P(16), P(16) mode-locked double-resonance signal at 10 Torr of SF_6 plus 150 Torr of air. The pulse-to-pulse separation is 24 ns and the pulse durations are ∿3.5 ns (FWHM). The top dashed curve represents the 100% transmission level; the bottom dashed curve represents the SF_6 transmission level in the absence of the pump pulse. The base line indicates zero transmission.

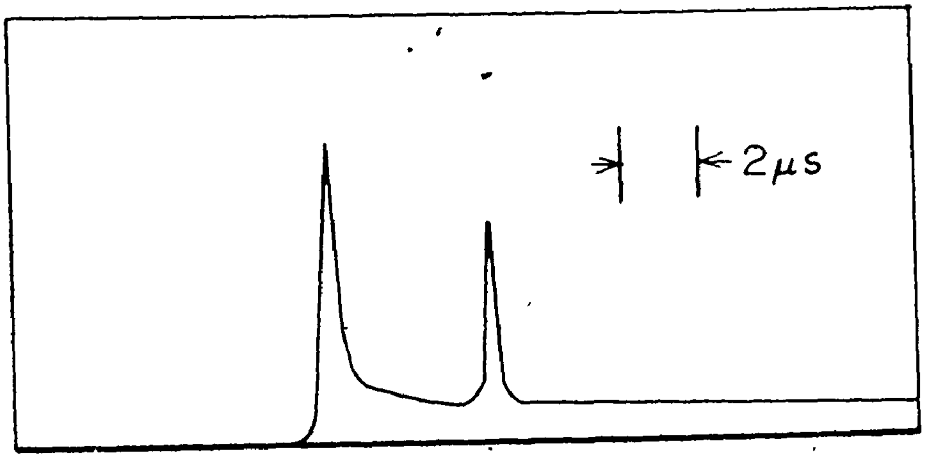

5(a)

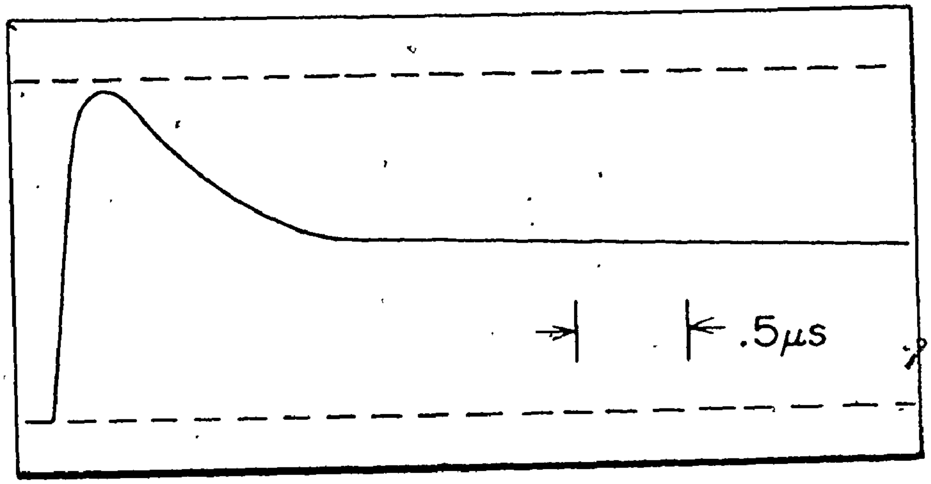

5(b)

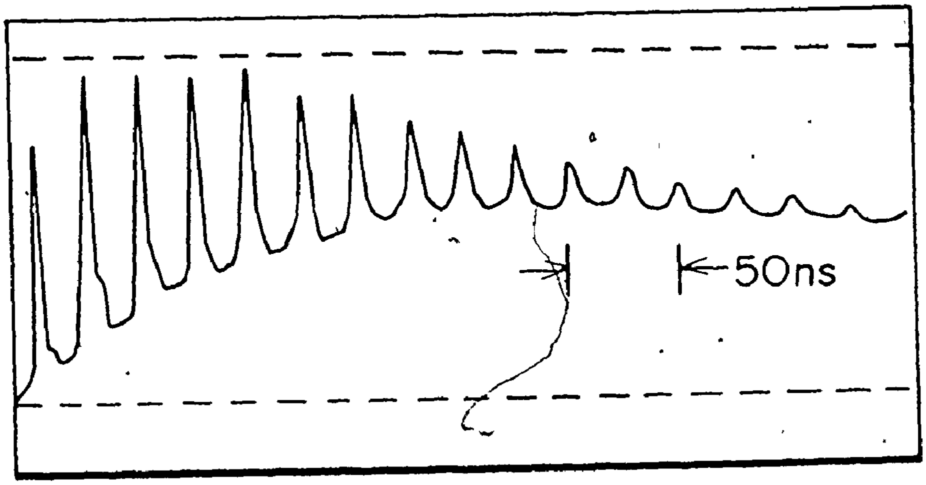

5(c)

laser beam, polarized in the same direction as the pump beam, was passed through the tilted SF_6 cell, collected by a gold mirror, and focussed onto a second 2 ns risetime Au:Ge detector. The detector output was amplified by a fast risetime amplifier (Avantek AV-9T) and displayed on an oscilloscope (Tektronix 547). The probe beam area at the SF_6 cell was always made smaller than that of the pump beam. Furthermore, the position of the pump beam on the gas cell could be adjusted to ensure maximum overlap and therefore maximum double-resonance signal. By variously blocking the probe and pump beams, and removing SF_6 from the gas cell, it was noted that no spurious signals were present.

The experimental setup for the mode-locked-pump,double-resonance experiments was very similar to the 200 ns arrangement, except that a Brewster-angled SF_6 gas cell was inserted near the grating for use as a saturable absorber. This produced a train of ∿3.5 ns (FWHM) mode-locked laser pulses. The cell was usually operated with 10-30 Torr of SF_6 plus ∿60 Torr of helium.* Since the entire mode-locked pulse train was incident on the SF_6 cell, the cavity length was made large to give a reasonable viewing range of ∿24 ns between successive mode-locked pulses. Also, use of a lower probe laser pressure (∿70 Torr) provided stable operation on a single longitudinal mode (SLM). The absence of the usual high-frequency modulation (with SLM) was necessary for ns detection of mode-locked double-resonance signals. The probe laser was not frequency locked and therefore some frequency variation may be expected over the gain bandwidth

---

* The SF_6 mode-locking apparatus will be dealt with in detail in Chapter 6.

($\sim$250 MHz). Such frequency variations will cause fluctuations in the SF_6 probe transmission from one laser pulse to another. However, it was observed that the fluctuations in the SF_6 probe transmission on a pulse-to-pulse basis were small. Furthermore, the existence of such effects are of secondary importance since these experiments were aimed at obtaining data on recovery times rather than data on double-resonance transmissions.

4.4 Results and Observations

Vibrational Bath Model

Fig. 4-7(a) and 4-7(e) are typical signals observed for P(14)-P(18) and P(24)-P(30) probe lines, respectively. The signals are integrals of the laser pulse (i.e., energy dependent) rather than following the pump pulse intensity profile. These types of signals are independent of the pump pulse wavelength used so long as it is not the same as the probe wavelength. The P(20)-P(22) double resonance signals are usually weaker than the other lines and very often resemble either of the above two groups in shape. Fig. 4-5(b) illustrates a typical double-resonance signal when the probe wavelength is the same as that of the pump. In this figure the pump and probe are at the P(16) line. The change in the transmission level after the pump pulse has passed through the cell is attributed to a vibrational bath heating effect which depopulates the ground state. The plateau finally decays in a V-T time which is typically greater than 2 μs for the pressures used in this paper (1-10 Torr). Fig. 4-5(c) shows a similar P(16) - P(16) double-resonance at 10 Torr of SF_6 plus 150 Torr of air, using a train of mode-locked pulses as a pump.

The sharp rise in transmission to near 100% over the duration of individual mode-locked pulses indicates that there are strong intensity saturation processes occurring. However, it can be observed that the double-resonance signals do not return to the initial transmission value (obtained in the absence of a pump pulse) after each pulse, but continue to rise to a much higher transmission level. Energy is therefore being absorbed from individual laser pulses. This leads to heating of the vibrational mode, which for the P(16) CO_2 line results in an increase in the dc level of the double-resonance transmission.

Fig. 4-6 shows the transmission measurement data obtained from a double-resonance experiment performed at 50 Torr of SF_6, at a cell thickness of 0.16 cm and with input intensities of 3.8×10^5, 1.2×10^5, and 3.8×10^4 W/cm^2, using a P(26) pump pulse of ∿220 ns duration (FWHM). The experimental absorption coefficients were obtained from the transmission data from the double-resonance experiments just after the laser pulse has passed through the absorber. Fig. 4-6 also shows the 300 K SF_6 experimental small-signal absorption coefficients measured using a low intensity TE CO_2 laser (as outlined in Section 3.2). Also shown in this figure (as solid lines) are the absorption predictions of the bath model for the four vibrational spatially-averaged temperatures* which gave the best fit to the experimental data. In every case these temperatures were within 15% of the temperatures calculated using the experimental pump pulse transmissions, cell thickness, input intensity, pulse duration, and

---

* Account was taken of the temperature gradient produced in the SF_6 gas cell by the pump pulse in determining the theoretical probe transmission.

Fig. 4-6

Absorption as a function of CO_2 wavenumber. The open circles represent 300K small-signal experimental data. The remaining data was obtained from double-resonance experiments using a P(26) pump pulse ($\sim$220 ns FWHM) at 50 Torr of SF_6, at a cell thickness of 0.16 cm and with pump input intensities of 3.8×10^4 W/cm^2 (Δ), 1.2×10^5 W/cm^2 (x), and 3.8×10^5 W/cm^2 (●). The solid curves represent the bath model predictions at 300K, together with those at the spatially-averaged temperatures of 470K, 800K, and 1250K.

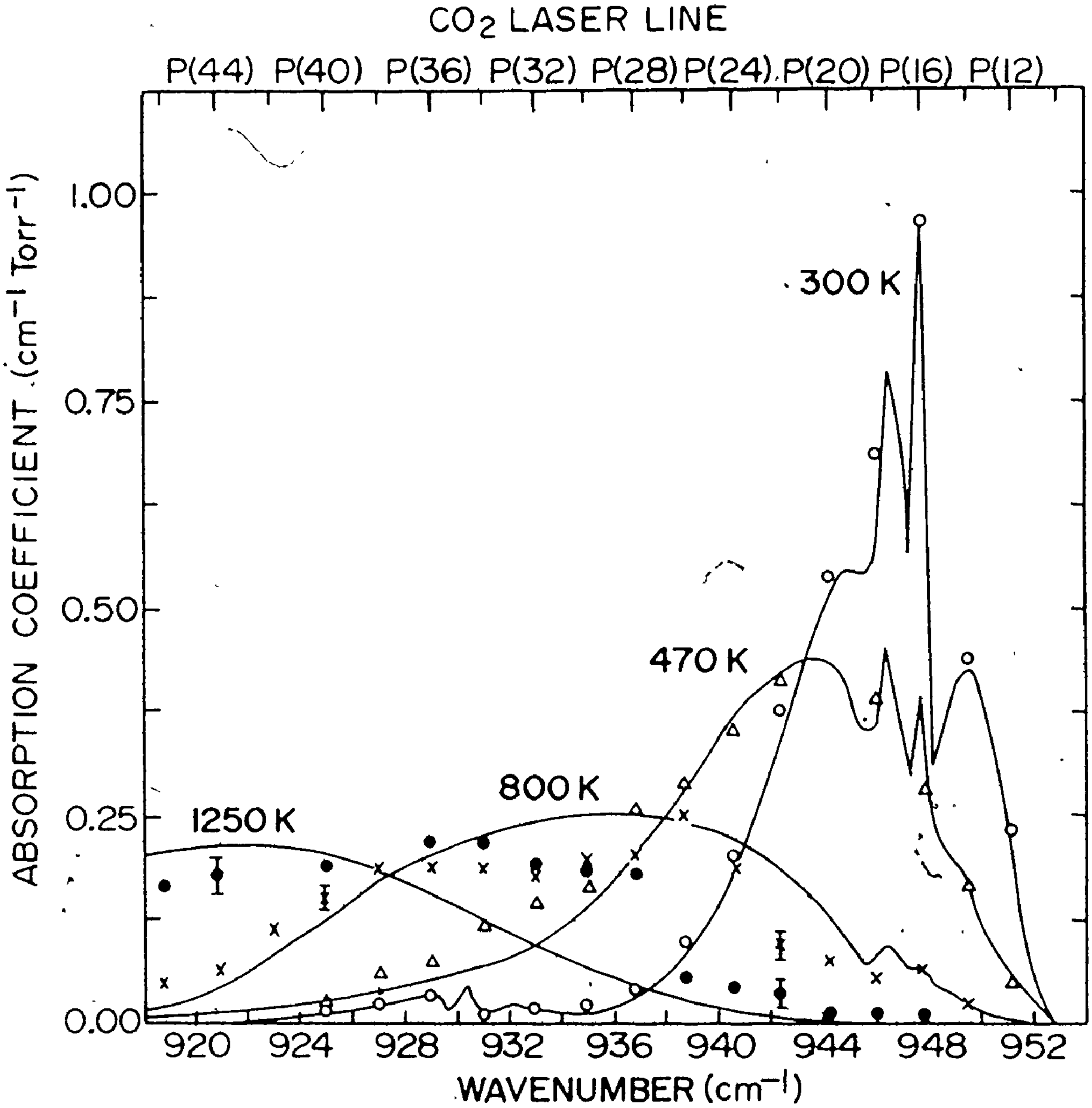
CO$_2$ LASER LINE
P(44) P(40) P(36) P(32) P(28) P(24) P(20) P(16) P(12)
ABSORPTION COEFFICIENT (cm^{-1} Torr^{-1})
1.00
0.75
0.50
0.25
0.00
300 K
470 K
800 K
1250 K
920
924
928
932
936
940
944
948
952
WAVENUMBER (cm^{-1})

SF_6 gas pressure. The experimental temperatures were calculated by dividing up the input pulse into energy increments and calculating a temperature change using the ideal gas law and the harmonic oscillator vibrational heat capacities for each successive energy increment.*

The generally good agreement between experimental data and the predictions supports the assumptions made in the model. Good agreement was also found in the high temperature case (1250 K) for the P(56) CO_2 rotational line at 907.8 cm^{-1}, where both absorption coefficients are ∿0.1 cm^{-1}-$Torr^{-1}$. Such agreement at a wavelength so far removed from the band center strongly supports the general applicability of the model.

Fig. 4-7 compares P(26) pump experimental double-resonance curves, obtained with 10 Torr of SF_6 and a cell thickness of 0.25 cm, with curves generated from the absorption against temperature data of Fig. 4-2 at a temperature of 700 K. The model temperature of 700 K represents the final vibrational temperature after the pump pulse has left the gas cell, and is within 25% of the temperature calculated using pump transmission data, input intensity, pulse duration, cell thickness, and SF_6 pressure.† The theoretical double-resonance curves were generated

---

* Significant deviations from the harmonic oscillator heat capacities due to anharmonicity corrections [62] and the onset of dissociation processes [71] can be expected to occur at temperatures above 1300 K.

† The temperature agreement to within 25% rather than the 15% mentioned earlier represents a decrease in the accuracy of obtaining the amount of energy absorbed in the SF_6 gas cell. This is due to the fact that the fraction of the pump energy absorbed in this case was ∿20% (compared to the ∿70% previously) and fluctuations in the transmission measurements (∿5%) can produce a 25% error in the estimated energy absorbed compared with an ∿7% error in the previous calculations.

Fig. 4-7

A comparison of experimental P(26) pump double-resonance curves at various CO_2 rotational lines with those predicted by the heating model. The gas pressure was 10 Torr, the cell thickness 0.25 cm, the input intensity 1.9 x 10^5 W/cm^2, and the pump transmission was 80%. The arrows indicate the position of the peak of the pump pulse.

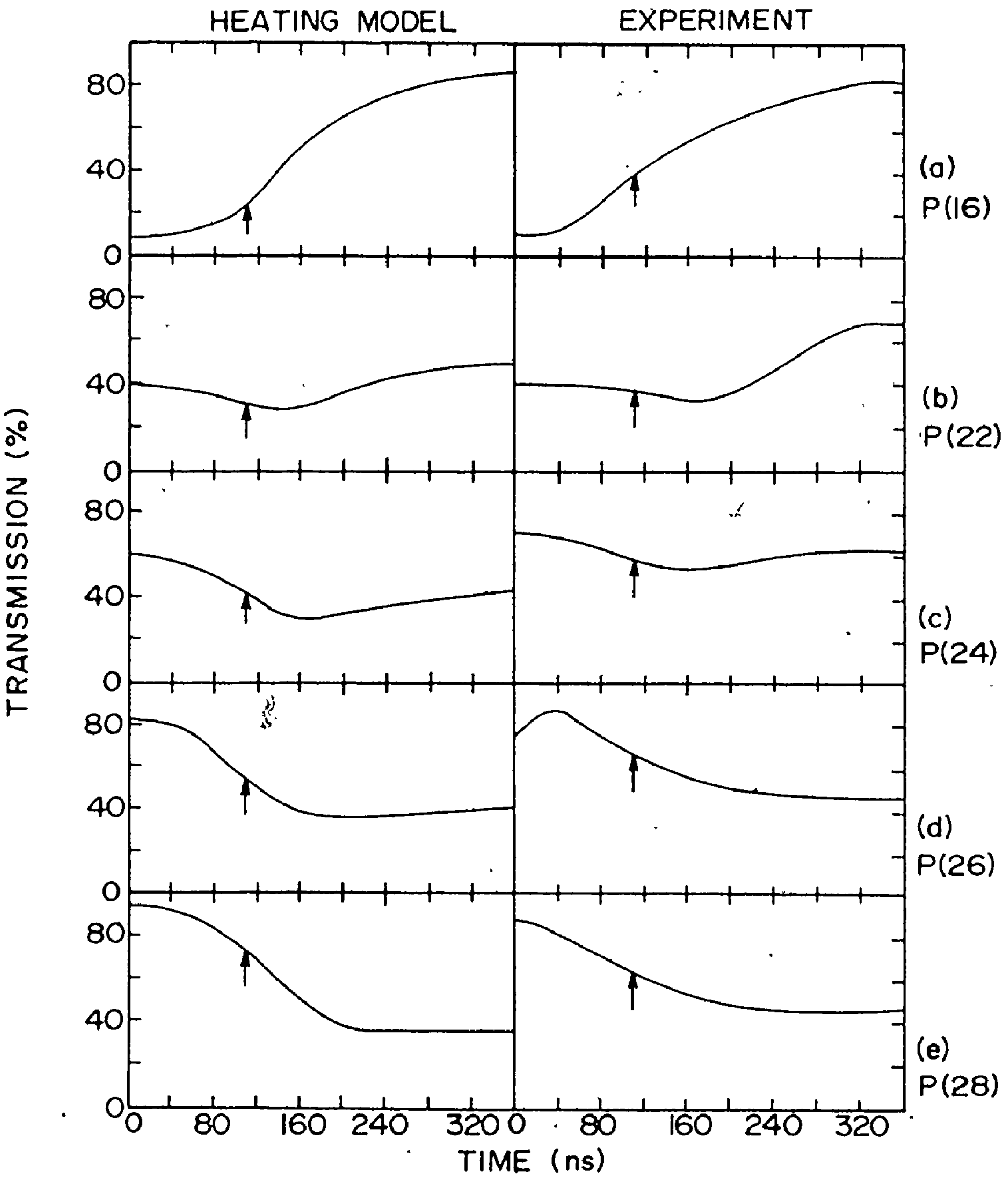
HEATING MODEL
EXPERIMENT
TRANSMISSION (%)
80
40
0
(a)
P(16)
(b)
P(22)
(c)
P(24)
(d)
P(26)
(e)
P(28)
0
80
160
240
320
TIME (ns)

by calculating the energy absorbed and the temperature change for each pump-pulse increment, and the obtaining a transmission for all the CO_2 probe lines from the curves of Fig. 4-2. The P(26) curve exhibits a fast rise in transmission, followed by a steady fall to a final transmission level lower than that at 300 K. The portion of the transmission rise not accounted for by the model is attributed to intensity saturation effects of the pump on vibrational and rotational levels common only to the P(26) absorption. In these experiments the transmitted pump pulse shape was consistent with the observed double-resonance signal at that line. Note that there is very good agreement on the shapes of these curves and also that there is quite good agreement in the actual transmission values and positions of the input pump peak with respect to the double-resonance signals. The agreement is remarkable when one considers that there were no adjustable parameters used in the model predictions and that the small-signal absopritons were not adjusted to agree with the experimental probe laser absorptions obtained in the absence of the pump beam. A similar experiment at 10 Torr of SF_6 but with a P(16) pump,* also gave good agreement with the calculated transmissions and double-resonance signal shapes. Double-resonance responses have also been observed at 1 Torr of SF_6. However, no attempt was made to obtain quantitative double-resonance data due to the small changes in transmission at this pressure.

---

* Most of the absorption on the P(16) line comes from the ground state whereas for P(26) the absorption occurs mainly at or greater than 1000 cm^{-1} above the ground state.

Energy Transfer Rates

In the last section, we demonstrated that a vibrational bath model can predict the transmission behaviour of a wide variety of P-lines from just a knowledge of the input pulse characteristics, pump-pulse transmission, cell thickness, and gas pressure. It also was noted that the behaviour of the double-resonance curves, even at 1 Torr of SF_6, seemed consistent with the double-resonance shapes predicted by the model. This agreement is somewhat surprising since the main assumption of the model is that a single Boltzmann temperature distribution must be established in a time typically less than 10% of the pump pulse duration. However, V-V transfer times obtained from fluorescence measurements (1.1 μs-Torr) [70] indicate that pressures greater than 50 Torr may be needed to satisfy the assumption for ∿200 ns input pulse widths.

This section will deal with how fast energy absorbed from a pump pulse is distributed to the various other levels that absorb CO_2 radiation. As Fig. 4-3 indicates, regions of maximum absorption cross-section move progressively to higher vibrational levels above the ground state as the CO_2 wavelength is increased. Therefore V-V transfer processes can be studied over widely separated energy levels by probing over a wide range of CO_2 lines. Time delays between the start of the laser pump pulse (∿10% point) and the start of the double-resonance signal (∿10% point) should be related to the V-V mixing time between levels associated with the absorption of the pump and probe laser pulses. The experiments were performed with ∿200 ns pulses and SF_6 pressures in the 1-10 Torr range. Two pump wavelengths were used, namely P(16) and P(26).

Probing at 10 Torr of SF_6 over the P(12)-P(30) CO_2 rotational lines, using both the P(16) and P(26) pumps, produced time delays of less than 20 ns, which was the lower limit of our measurements.

An experiment at 1 Torr of SF_6, with a P(16) pump, and P(12)-P(14) and P(24)-P(30) probe wavelengths, again yielded time delays <20 ns. Fig. 4-8 shows the P(26) probe double-resonance signal. The P(16) pump pulse is shown in Fig. 4-8(c). No extensive measurements were attempted with P(18)-P(22) probe lines since, as Fig. 4-2 illustrates for P(20), very little change in absorption is obtained as a function of temperature at the lower temperatures (T_V < 400 K).

An experiment at 1.5 Torr of SF_6 with a P(26) pump showed time delays <20 ns for P(24)-P(30) probe lines, but ∿100 ns delays on P(14) and P(16) lines. The 100 ns delay is shown in Fig. 4-8(a). Further work over a restricted range of pressures indicates that the delay is pressure dependent and of the order of 150 ns-Torr.

The P(16) pump data implies that energy must be transferred from the ground state via ν_3, and possibly $2\nu_3$, vibrational levels to a bath of levels above 1000 cm^{-1} in times <20 ns-Torr. The value of 20 ns is a factor of 55 less than the fluorescence data of Bates, Knudtson, and Flynn [70], but is much longer than the P(28) probe measurements of Frankel performed at low pressures of SF_6 (0.1-1 Torr) and with a 2 ns P(20) pump pulse [60].

Fig. 4-8

(a) Oscilloscope display of a P(26) pump, P(16) probe double-resonance signal obtained at 1.5 Torr of SF_6, indicating a 100 ns time delay between the pump peak (Fig. 4-8(c) and the start of the double-resonance signal.

(b) P(16) pump, P(26) probe double-resonance signal at 1.0 Torr of SF_6.

(c) Pump pulse appropriate to both the P(16) and P(26) lines.

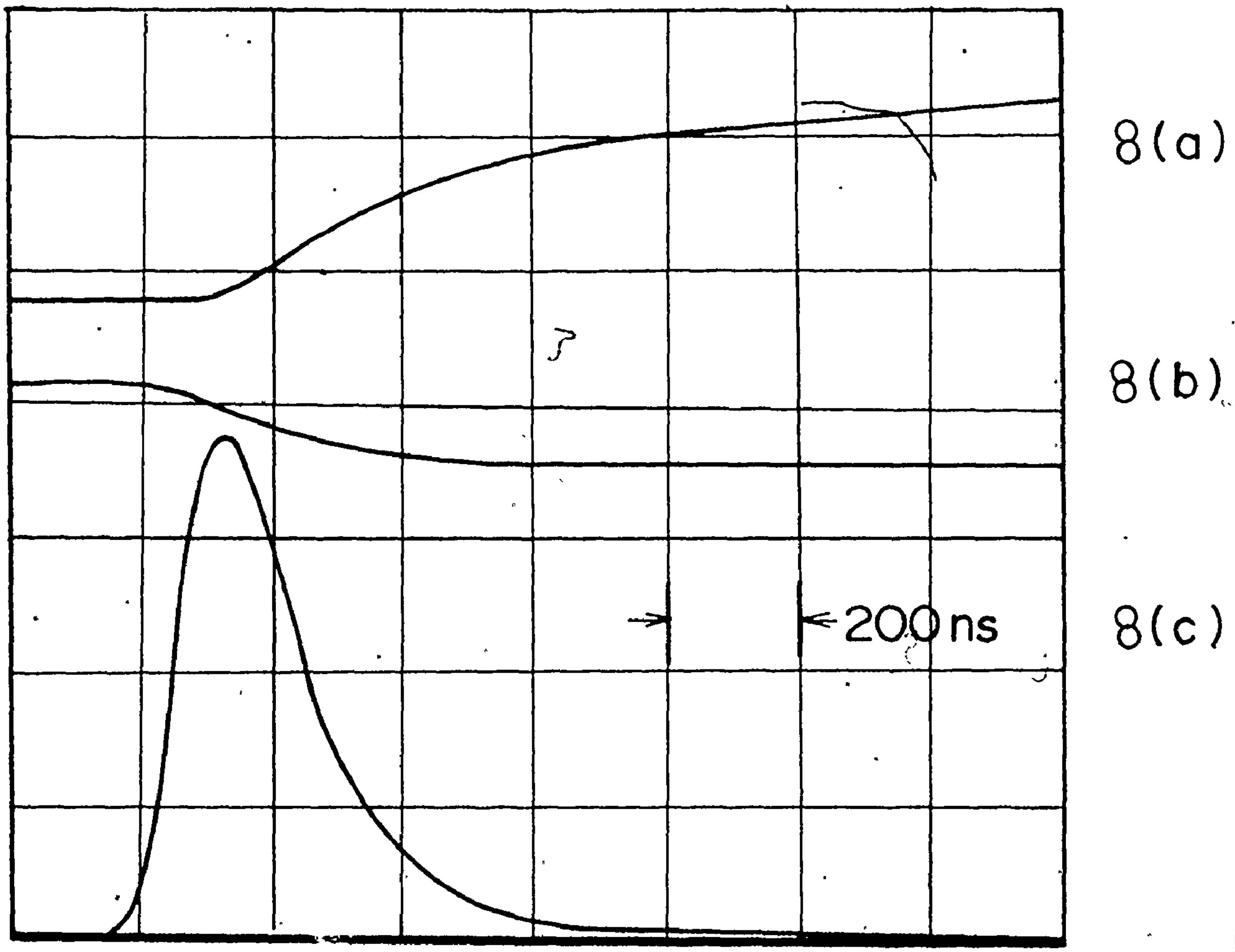
8(a)
8(b)
8(c)
200 ns

The observed time delay, using the P(26) pump and probing on P(14) and P(16) lines, may be explained as follows. Near-resonant collision processes such as

$$SF_6(2\nu_3) + SF_6 \rightarrow SF_6(\nu_3) + SF_6(\nu_3) \ , \ \Delta E = -5.2 \text{ cm}^{-1}$$

should be very efficient at removing molecules from the ground state and placing them in ν_3 vibrational levels, where rapid transfer to the bath can occur. However, since the low-pressure double-resonance experiments usually involve low vibrational bath temperatures there are simply very few molecules in the $2\nu_3$, $3\nu_3$ and higher vibrational states. Presumably then, it takes the order of the observed time delay to significantly deplete the ground state and produce a noticeable change in the P(26), P(16) double-resonance signal.

The following is a possible explanation for the disparity (a factor of 55) between the V-V transfer rates reported in this thesis and those of Bates et al. [70]. They have indicated that the rate controlling step for their observed V-V relaxation rates may be due to energy transfer processes between v = 1, ν_6 (346 cm^{-1} [64]) and v = 1, ν_3 (948 cm^{-1} [64]) vibrational levels. The bulk of the absorption for CO_2 wavelengths (reported in this chapter) occurs either from the ground state or from levels above 1000 cm^{-1} and, as mentioned above, the depletion of the ground state may occur primarily by means of collisions with molecules in states above 1000 cm^{-1}. It follows that the V-V rates given by Bates et al. may not be appropriate in describing transfer times between levels which absorb CO_2 radiation.

A further observation, at even lower SF_6 pressures (0.5-1 Torr), was the presence of small double-resonance signals with a shape similar to that of the input pulse (rather than being an integration of it). Most of these signals appeared as decreases in the transmission. They were observed more frequently at low SF_6 pressures, and at pump and probe combinations that differed by one CO_2 line. The signals were interpreted as induced absorptions of the type that might occur between a small number of overlapping vibration and rotation levels common to two CO_2 lines. Similar signals have been observed previously at very low SF_6 pressure (≤0.1 Torr) in Ref. [72]. Presumably these signals are more amenable to observation at these lower pressures because of the lower decay rate of the excess population induced in particular rotational and vibrational states by the pump pulse. In addition, at higher pressures the induced signal may be swamped by the more generally observed double-resonance signal because the latter sees contributions from so many more levels.

The last set of experiments was performed with a train of mode-locked pulses on the P(16), P(20), and P(26) CO_2 lines in order to investigate rotational (and possibly vibrational) recovery times of the particular levels being pumped by the laser. The above three CO_2 lines were chosen since they characterise (at $T_V \sim 300$ K) absorption from the ground state, near 1000 cm^{-1}, and beyond 1000 cm^{-1} above the ground state, respectively. Figures 4-9(a) and 4-9(b) show a typical mode-locked pulse train and corresponding double-resonance signal. Each mode-locked pulse gave a similar signal. There was no change in the dc transmission after the pulse train had passed, which is indicative of very little energy absorption during the pulse train. For all three

Fig. 4-9

(a) Oscilloscope display of a typical mode-locked pump pulse train used for double-resonance experiments performed at identical pump and probe wavelengths on the P(16), P(20), and P(26) CO_2 lines. The pulse separation is 24 ns.

(b) Corresponding double-resonance signals observed at 1 Torr of SF_6.

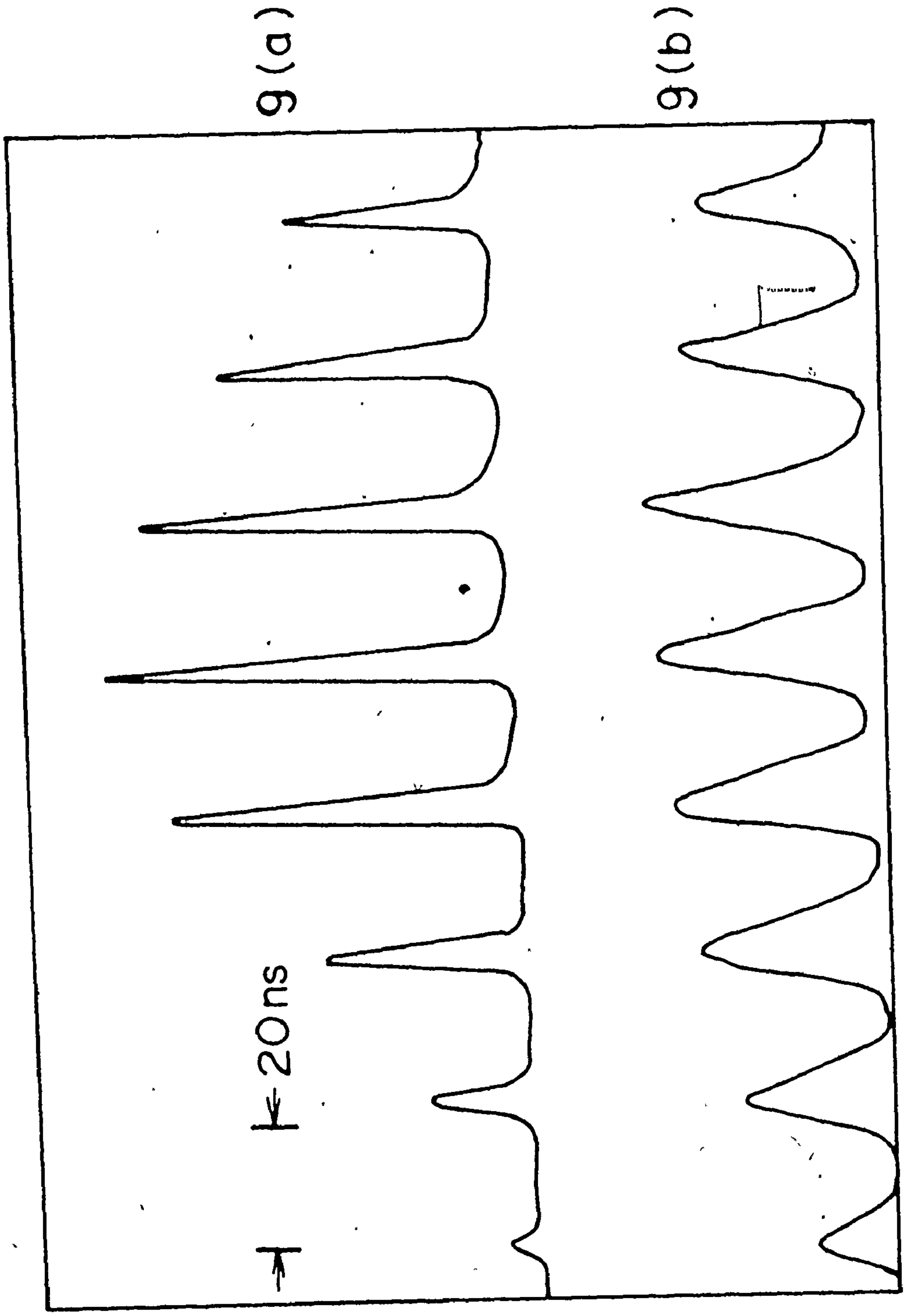
9(a)
9(b)
20ns

pump wave-lengths the double-resonance signals narrowed as the pump intensity was reduced. This is believed to result from intensities on the rise and fall of the mode-locked pulse having the ability to saturate particular rotational and vibrational levels as well as intensities just near the pulse peak.

For each probe wavelength the recovery times of the absorptions at 1 Torr of SF_6 were similar, and estimated to be approximately 6 ns.* This very fast recovery is 3-4 times shorter than the frequently quoted dipole dephasing time [52], but is comparable to Frankel's low pressure recovery results employing a P(20) pump and a P(20) probe [60].

The recovery time cannot be shown to be pressure dependent since it is already comparable to the pump pulse width of ∿3.5 ns. Further experiments, with sub-nanosecond resolution, and employing SF_6 pressures from a few tenths of a Torr to 10 Torr, are needed to establish the exact pressure dependence of the recovery times.

4.5 Summary

In this chapter, we have discussed the application of a simple vibrational bath model to describe the dynamics of the absorption of SF_6 in the region of 10.4 μm. The analysis is derived from a band contour model described by Nowak and Lyman [48]. They considered the case in which all the SF_6 degrees of freedom were in thermal equilibrium, characterised by a single temperature. Hence, the rates at which the energy is exchanged between the different molecular degrees of freedom was of no importance. The application of such a model to describe the response of SF_6 to a pulse of radiation is not generally possible if the pulse is sufficiently short and/or intense that the vibrational, rotational and translational degrees of freedom can no longer reach thermal equilibrium at a single temperature.

---

* This represents a 1/e decay time corrected for a finite laser pulse duration.

The CO_2 laser pump pulses employed in the experiments reported here were ∿200 ns long, a time which; for the SF_6 pressures studied, is much less than the V-T relaxation time. Consequently, equilibration between vibrational and translational degrees of freedom is prevented. The laser pulse energy is therefore absorbed solely into the vibrational degrees of freedom, thereby increasing the amount of energy stored in the vibrational modes. The rapidity with which this energy is redistributed determines whether thermal equilibrium is maintained within the vibrational bath for the duration of the pulse. Clearly, the vibrational temperature will not be the same as the translational-rotational temperature of the gas. The approach we have taken for analyzing the experimental results is to test first the general applicability of this dynamical model to the interaction of SF_6 with pulsed radiation. Next, we establish the range of validity (e.g., SF_6 pressures and pump pulse durations), the limits of which give information concerning both the vibrational and rotational equilibration times.

The major proportion of SF_6 absorption typically occurs from vibrational levels less than 5000 cm^{-1} above the ground state. The vibrational levels below 2000 cm^{-1} are well-separated and the appropriate V-V relaxation times for this region frequently quoted in the literature [47,70] are relatively long compared to the pump pulse duration. This should have the consequence that equilibration cannot be maintained on this time scale. However, good quantitative agreement is obtained between the theoretical and experimental temporal behaviour of double-resonance signals over a wide range of CO_2 pump- and probe-laser wavelengths (P(14) to P(30)) and SF_6 pressures (above a few Torr). Evidently, the agreement is a result of the existence of sufficiently fast V-V relaxation times. Our observed times (<20 ns-Torr) are much shorter than the previously reported values in Refs. [47] and [70] (0.3 μs-Torr and 1.1 μs-Torr, respectively). The existence of such very short V-V relaxation times is consistent with the low pressure measurements of Frankel [60], which were obtained over a restricted range of pump and probe wavelengths.

As will be shown in the next chapter, the vibrational bath model can also accurately describe the transmission of the pump itself over a wide range of pulse durations and intensities at high SF_6 pressures (>200 Torr).

A model similar to the one described in this chapter should be applicable to other polyatomic molecules that interact with pulsed laser radiation. This only requires a knowledge of the absorption band contour and the appropriate spectroscopic constants, together with the condition that the V-V relaxation rates are sufficiently fast.

CHAPTER 5

HIGH PRESSURE SF_6 PULSE TRANSMISSION NEAR 10.4 μm

5.1 Introduction

The SF_6 transmission characteristics obtained using a pulsed CO_2 laser operating in the 10.4 μm band have been described in Chapter 3. In that chapter, the intensity dependence of the SF_6 absorption on the three CO_2 rotational lines, P(14), P(20), and P(26), (which characterise the absorption saturation behaviour of the entire 10.4 μm band), was reported for over an order of magnitude variation in the SF_6 pressure. The saturation behaviour at these CO_2 lines was interpreted in terms of a 4-level, non-steady-state model. It was noted that good agreement was obtained between the model and the observed transmission characteristics for the P(14) line. The P(20) transmission curves could also be predicted over a large SF_6 pressure range. However, at increased SF_6 pressures, there was a small range of input intensities for which the observed transmitted pulse shape progressively broadened to durations beyond that of the input pulse. This behaviour could not be accounted for by the 4-level model. The deviation between theory and experiment became progressively worse at longer CO_2 wavelengths (increased P values). For example, the 4-level analysis for the P(26) CO_2 line could not fully reproduce the pulse broadening observed at the transmission minima of Fig. 5-1, or the unusual shape of the 10 Torr transmission curve in that figure. It was therefore suggested that a model

Fig. 5-1

Transmission of SF_6 as a function of input intensity at the P(26) CO_2 line. The dashed curves represent the experimental data obtained from Chapter 3 at 10 and 50 Torr of SF_6. The solid circles (●) denote 200 Torr data obtained from the same chapter. Solid curves 1 and 2 represent the theoretical calculations employing the vibrational and total heat capacities, respectively.

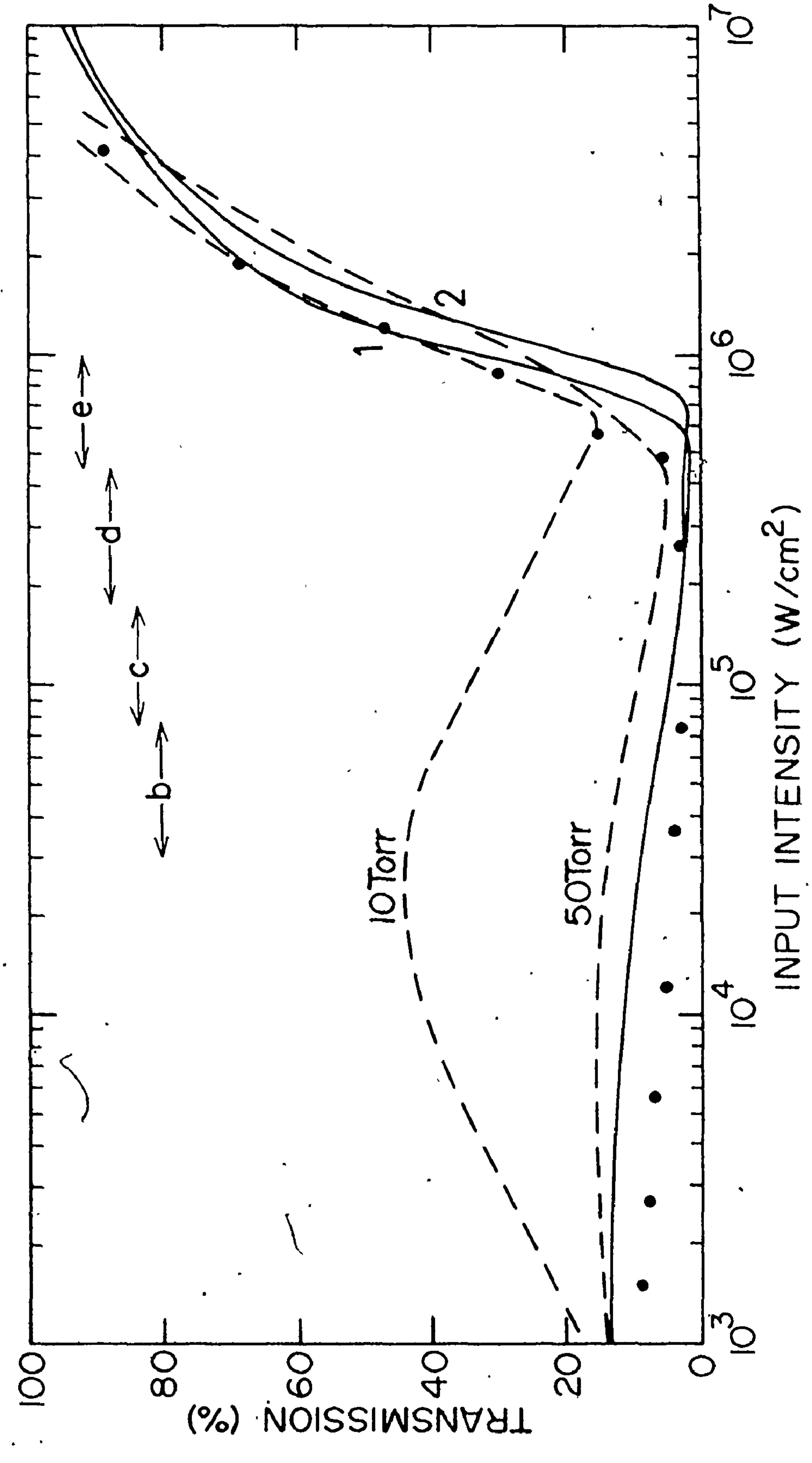
TRANSMISSION (%)
100
80
60
40
20
0
INPUT INTENSITY (W/cm^2)
10^3
10^4
10^5
10^6
10^7
10Torr
50Torr
1
2
b
c
d
e

which incorporated the multilevel nature of the SF_6 absorption was necessary to fully describe the transmission properties of all CO_2 lines. Such a model, based on the concept of a bath of vibrational levels, was outlined in Chapter 4 and in Ref. [73], and will be referred to throughout this chapter as the "vibrational bath model". Double-resonance experiments, described in the last chapter, verified that the model could account for the pump-induced SF_6 absorption dynamics over a wide range of CO_2 wavelengths and SF_6 pressures, when the pump and probe wavelengths were different. In this chapter, it is demonstrated that at high SF_6 pressures (typically $\gtrsim$200 Torr), the transmission behaviour of the pump pulse itself can entirely be accounted for by the vibrational bath model without requiring the inclusion of intensity saturation effects. It is also demonstrated that at high SF_6 pressures a train of short pulses also exhibits transmission behaviour consistent with the heating model. At lower SF_6 pressures, a combination of intensity saturation processes and increased pulse transmission due to vibrational heating are necessary to describe fully the absorption saturation behaviour of SF_6.

5.2 Experimental

The experimental apparatus used to obtain additional transmission data, employing ∿200 ns and ∿5 ns duration CO_2 laser pulses, is outlined in Chapters 3 and 4. Variation of the input intensity at the absorber was accomplished by the use of attenuators, and a 10-inch focal length germanium lens to vary the beam cross-section at the cell. The 200 ns pulse transmissions were measured using a 2 ns risetime

Au:Ge detector, with the output displayed on an oscilloscope (Textronix 547). The error in a transmission measurement is estimated to be ∿7%. The input intensities are known to better than 10% for low values and to within 15% for high values. All absolute intensities were measured with a calibrated photon drag detector. The mode-locked pulse durations and transmissions were measured using a photon drag detector in conjunction with a 1.5 ns risetime oscilloscope (Hewlett-Packard 183A).

5.3 Results and Discussion

The transmission behaviour at a given CO_2 line can be determined from the vibrational bath model. The input laser pulse is divided up into many small time increments (Δt) and each increment is fed into an absorber which is divided into spatial increments (Δz).* As energy is absorbed from the laser pulse, there is an increase in the vibrational temperature of each segment. An absorption coefficient appropriate to this new temperature is obtained from the absorption versus vibrational temperature curves of the type shown in Fig. 4-2. The above process is repeated for each successive increment until the entire pulse has passed through the absorber. This procedure allows calculation of both the shape and intensity of the transmitted pulse. The value of the temperature increase can be calculated from the expression which relates the energy (Q) added to n moles of an ideal gas to increase the temperature ΔT degrees at constant gas volume:

---

* Δz was chosen such that the product of Δz and the small-signal absorption coefficient α_0 was sufficiently small to ensure an optically thin absorbing medium. Typically $\Delta z \alpha_0 \sim 0.2$.

$$\Delta T = Q/nC_V^{tot}(T) \ . \tag{5-1}$$

In Eq. (5-1), $C_V^{tot}(T)$ is the total harmonic oscillator heat capacity at constant volume.* Deviations from the harmonic oscillator heat capacities, due to anharmonicity [62] and the onset of dissociation processes [71], can occur at vibrational temperatures >1300 K. This temperature is well above the values usually encountered in our work.

The solid curves in Fig. 5-1 show the predicted P(26) transmission obtained using either the vibrational heat capacity or the total heat capacity in Eq. (5-1). Note that there is very little difference between the two curves since at large temperatures the vibrational contribution to the heat capacity is much larger than the rotational and translational contributions.

Good agreement is obtained between the transmission predicted by the model and the 200 Torr experimental data obtained in Chapter 3. The agreement is quite remarkable when it is considered that the only parameters used in the model were the input pulse shape, the peak-pulse intensity, the cell thickness, and the gas pressure. These were all obtained from experimental measurements and no adjustable parameters were employed for the theoretical predictions. The small-signal absorption used in the modelling was generated directly from the band contour model rather than being normalized to an experimental small-signal value. This causes the discrepancy observed at low input intensities. It is clear, however, that the contribution of vibrational heating to the transmission behaviour at the P(26) line accounts for the sharp transmission increase over the wide range of SF_6 pressures observed in Fig. 3-8 and Fig. 5-1. The agreement between theory and experiment also extends to the shape of the transmitted pulse, as indicated in Fig. 5-2. For example, the approximate doubling of the input pulse duration shown in Fig. 5-2(d) (a result which could not be predicted by the 4-level treatment) is well accounted for by the vibrational bath model. An analysis employing this model for the P(20) CO_2 line predicted both the magnitude of the broadening observed experimentally at high SF_6 pressures and the approximate input intensity at which pulse broadening occurred.

---

* The total heat capacity is the sum of the vibrational, rotational and translational components. At a vibrational gas temperature of 300 K, the total heat capacity is 21 cal deg^{-1} $mole^{-1}$, while the vibrational contribution is 15 cal deg^{-1} $mole^{-1}$. The total heat capacity must be used in Eq. (5-1) at very high SF_6 pressures ($\gtrsim$400 Torr), where the vibration-to-translation (V-T) relaxation time becomes comparable to the 200 ns input pulse duration.

The model is most suitable for predicting the entire pulse transmission characteristics at high SF_6 pressures. At reduced pressures the lower coupling rate between levels allows for easier saturation of the absorption. At higher SF_6 pressures the effective level recovery times decrease, consequently making intensity saturation more difficult. However, at these higher pressures, substantial amounts of energy are coupled into the bath of levels, which can heat the entire vibrational mode sufficiently to change the mode population distribution in such a manner as to change the absorption on a given CO_2 line. For the P(12)-P(18) CO_2 wavelengths, the thermal change in population at the absorbing levels results in a decrease in absorption with increasing vibrational

Fig. 5-2

Columns I and II are the theoretical and experimental transmitted pulse shapes for the input pulse shape shown in Row (a). Rows (b) to (e) correspond to the intensity regions shown in Fig. 5-1. The dashed vertical lines indicate the peak of the input pulse.

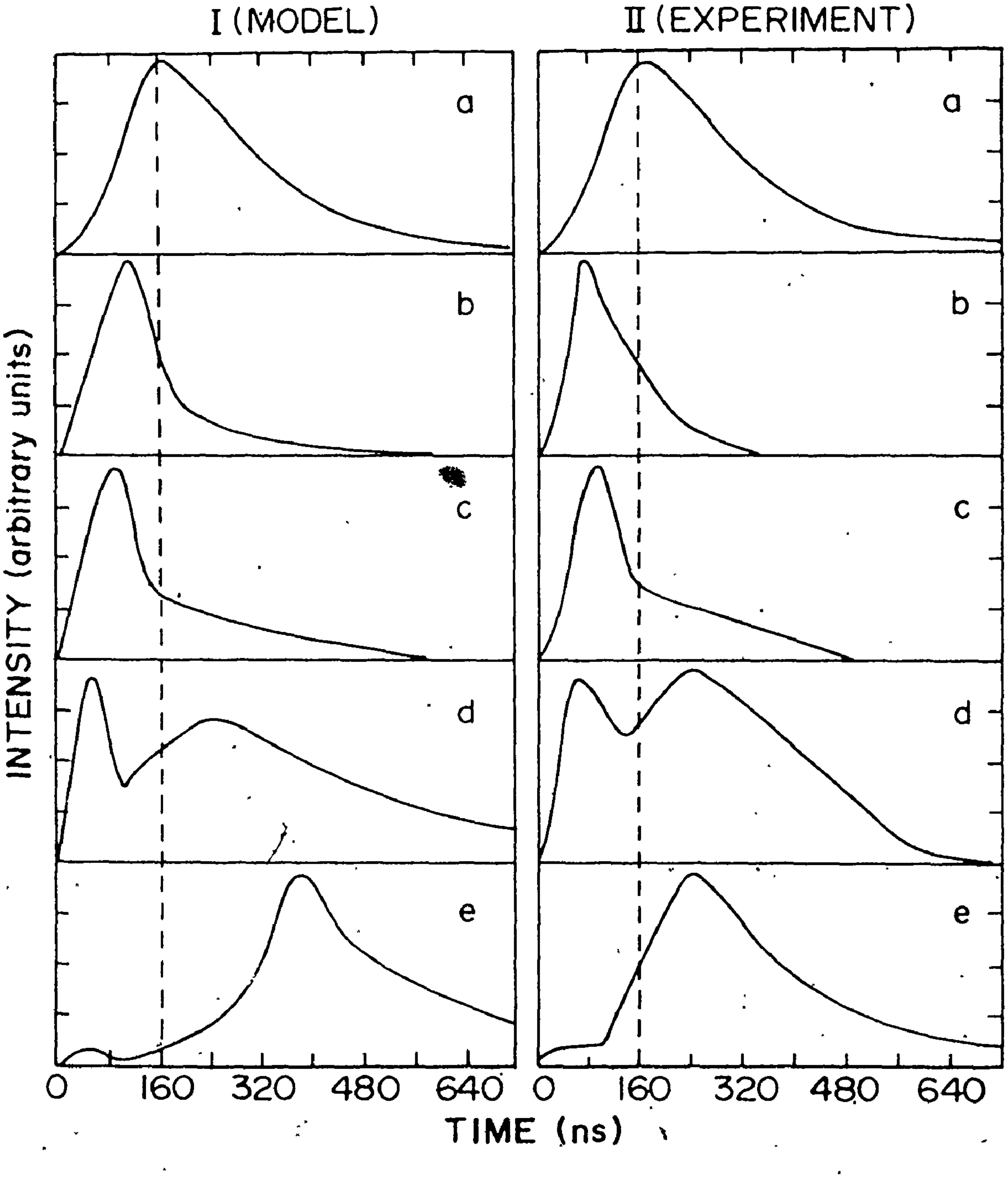
I (MODEL)
II (EXPERIMENT)
INTENSITY (arbitrary units)
a
b
c
d
e
a
b
c
d
e
0
160
320
480
640
0
160
320
480
640
TIME (ns)

mode temperature. At the P(24)-P(30) CO_2 wavelengths the absorption increases up to a certain vibrational temperature, reaches a maximum, and then decreases with increasing temperature.* The absorption maxima predicted for these rotational lines are shifted to higher vibrational temperatures for increasing wavelengths. This results from anharmonicities which cause the shift of absorption cross-section maxima to progressively higher energy levels at longer wavelengths. A maximum in the absorption occurs when the vibrational mode population distribution, which is also shifted to higher levels with increased vibrational temperature, is centered at the levels corresponding to the cross-section maxima. It is just the passage of the mode population distribution through regions where the P(26) line experiences a maximum absorption cross-section which accounts for the observed transmission minima in Fig. 5-1, and the observed pulseshaping on this line (Fig. 5-2). Note that even at low SF_6 pressures heating effects can contribute substantially to the overall transmission behaviour. This is evidenced by the presence of an absorption minimum in the 10 Torr P(26) transmission curve similar to that observed for high SF_6 pressures. The pulseshaping at 10 Torr is also very similar to that depicted in Fig. 5-2 for 200 Torr of SF_6.

At sufficiently high SF_6 pressures, the entire experimental transmission curves, and those predicted by the model, should be very similar for all CO_2 wavelengths. This is dramatically illustrated in Figs. 5-3 and 5-4 for the P(14) and P(20) CO_2 lines, respectively. The 100 Torr data in these figures shows that the agreement between the individual transmission curves (for a fixed pressure) exists for pressures greater than 100 Torr. Recent data has been published concerning experimental pulsed CO_2 transmission characteristics for the P(28) CO_2 line at high SF_6 pressure (100-500 Torr) [74]. This data was compared in Ref. [74] with a calculation using a 4-level model similar to the one outlined in Chapter 3. We have recently performed very similar measurements for the same P(28) line, as shown in Fig. 5-5 (for SF_6 pressures of 100 and 500 Torr).* The solid lines indicate the theoretical predictions of the vibrational bath model.† The P(28) pulse shaping which was similar to that observed for the P(26) line, is also in excellent agreement with that predicted by the model. Plainly, vibrational heating effects, rather than intensity saturation processes, account for the high pressure transmission on the P(28) CO_2 rotational line.

---

* The P(20) and P(22) lines have a behaviour which lies somewhere in between the other two sets of lines and display very little change in the absorption for the first 100 K temperature rise.

Pulse shaping effects can also occur when energy is absorbed from a train of ∿4.5 ns (FWHM) mode-locked pulses. Fig. 5-6 illustrates the strong asymmetric narrowing of the P(26) pulse train envelope after passage through 10 Torr of SF_6. This pulse shaping is similar to that

---

* The experimental curves shown in Fig. 5-5 are in good agreement with the data of Ref. [74] when the different small-signal absorptions are considered.

† The model included an absorption contribution from the quasi-continuum (above 5000 cm^{-1}) by incorporation of a quasi-continuum $\sigma = 4. \times 10^{-19}$ cm^2 [75]. The contribution becomes important for very low or high J-number lines.

Fig. 5-3

Transmittance at the P(14) CO_2 line through a path length L^B in SF_6, as a function of input intensity. Experimental data, denoted by (x), (o), and (●), was obtained at SF_6 pressures of 100, 400 and 760 Torr, respectively. The calculated small-signal transmittance at 760 Torr is ∿8. The dashed line represents the 100 Torr experimental data; the solid curves are the theoretical transmissions calculated using $C_v^{tot}(T)$.

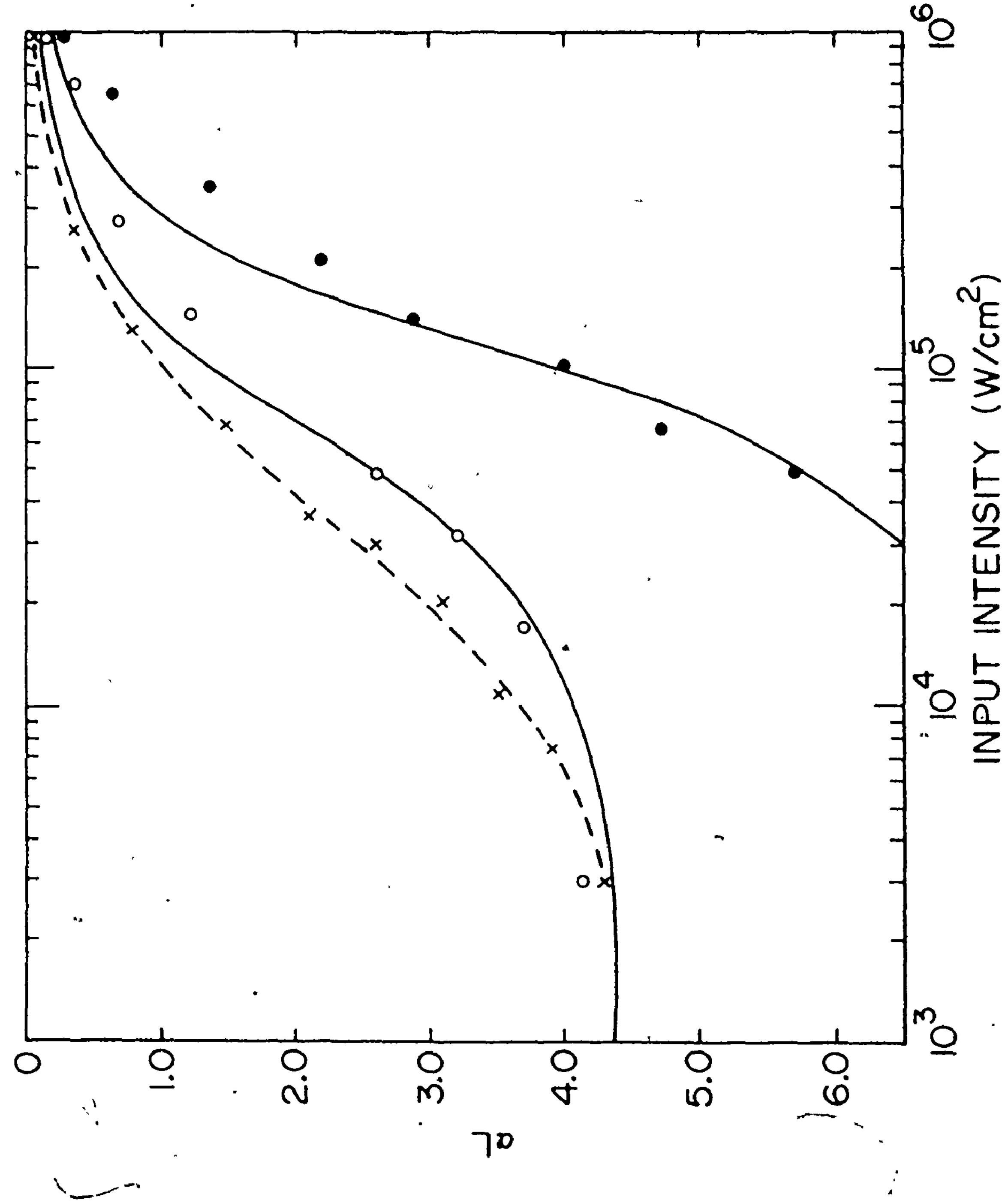
αL
0
1.0
2.0
3.0
4.0
5.0
6.0
10^3
10^4
10^5
10^6
INPUT INTENSITY (W/cm^2)

Fig. 5-4

Transmittance at the P(20) CO_2 line, through a path length L^B of SF_6, as a function of input intensity. Experimental data, denoted by (x), (o), and (●), was obtained at SF_6 pressures of 100, 400 and 760 Torr, respectively. The calculated small-signal transmittance at 760 Torr is ∿10. The dashed line represents the 100 Torr experimental data; the solid curves are the theoretical transmissions calculated using $C_v^{tot}(T)$.

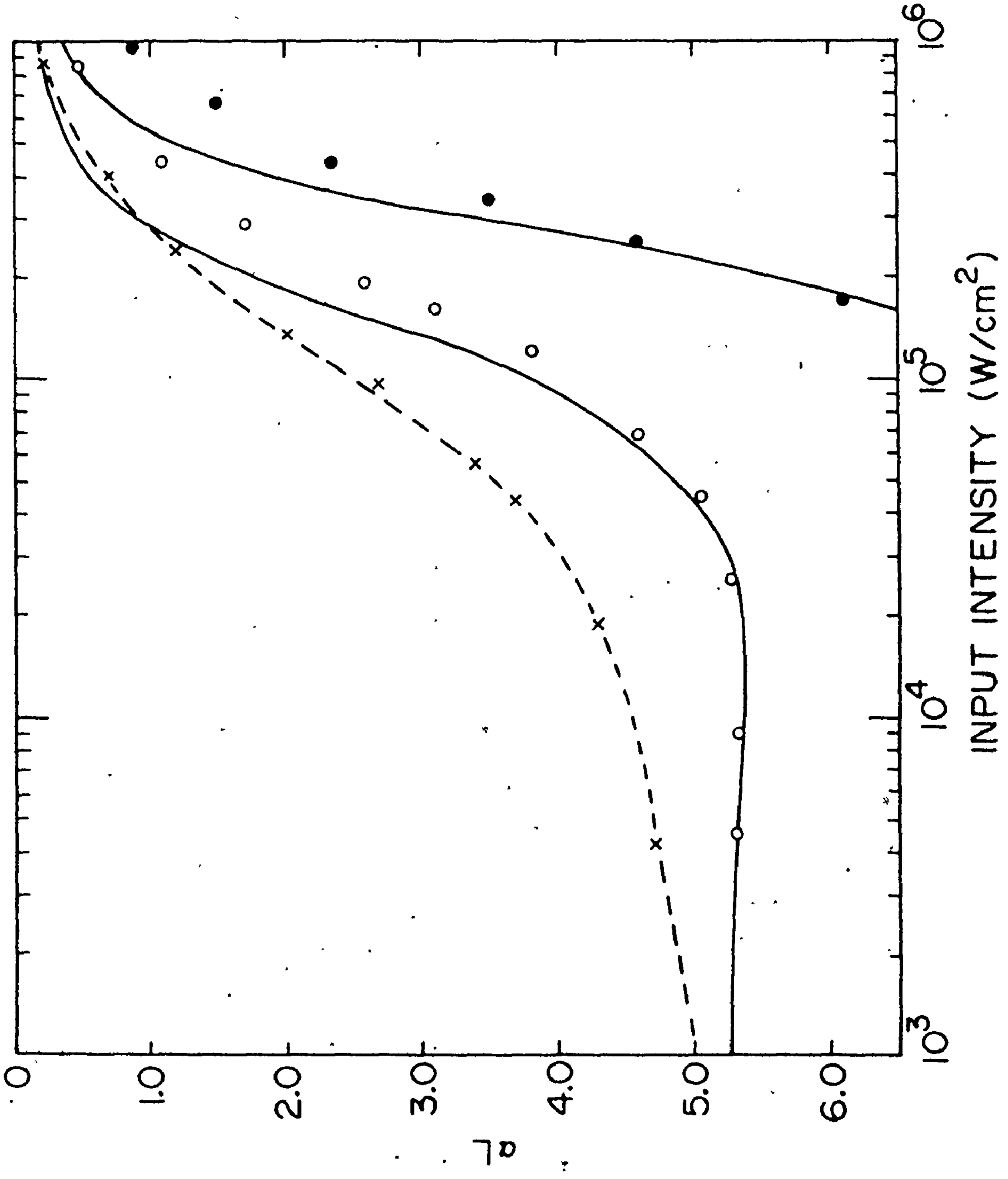
αL
0
1.0
2.0
3.0
4.0
5.0
6.0
10^3
10^4
10^5
10^6
INPUT INTENSITY (W/cm^2)

Fig. 5-5

Transmission of SF_6 as a function of input intensity at the P(28) CO_2 line. The solid curves represent the theoretical calculations employing the vibrational heat capacity. Experimental data denoted by (o), (●), was obtained at SF_6 pressures of 100 and 500 Torr, respectively. The gas cell thickness was 0.15 cm and the input pulse FWHM was 125 ns.

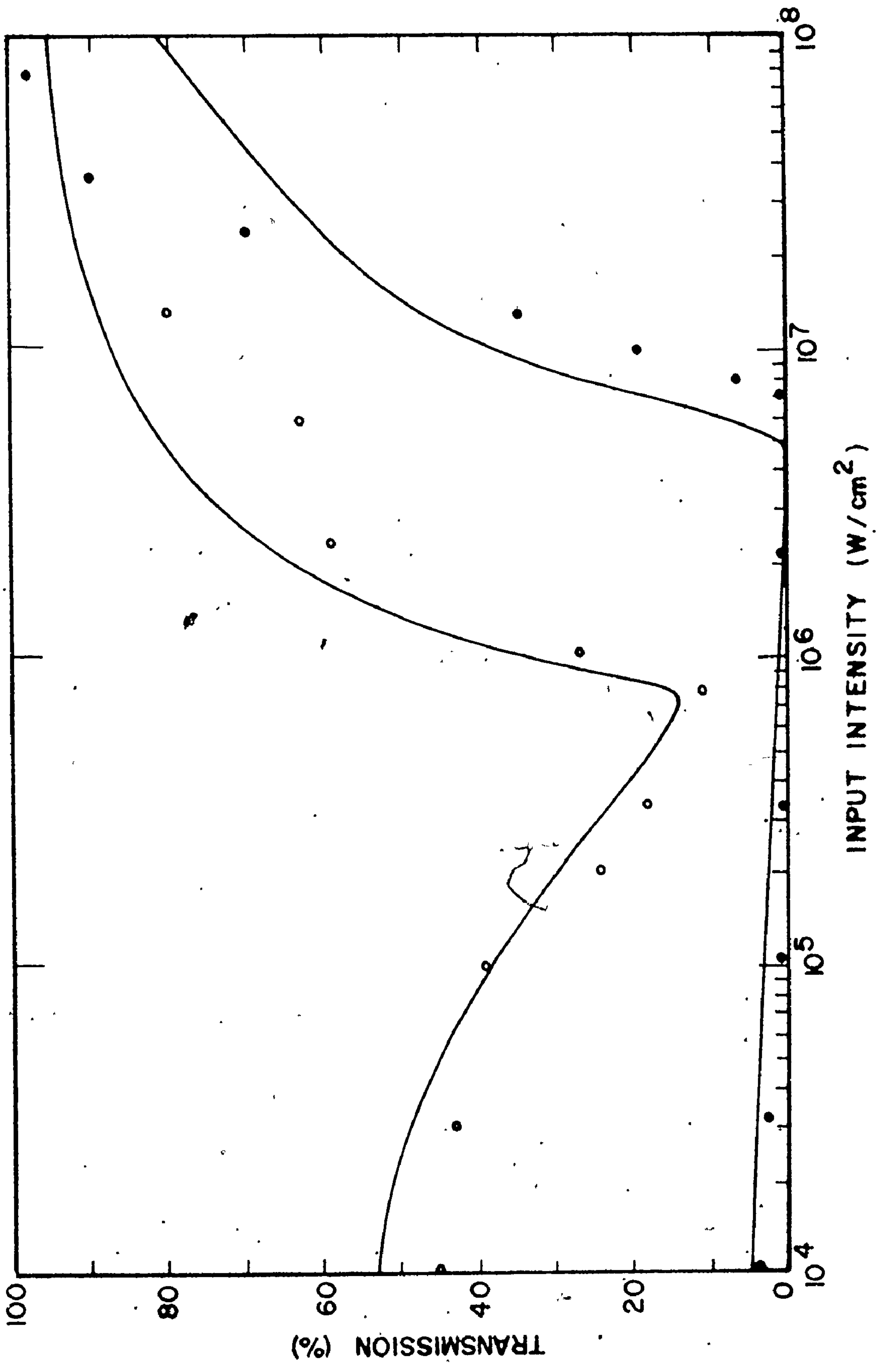
TRANSMISSION (%)
100
80
60
40
20
0
10^4
10^5
10^6
10^7
10^8
INPUT INTENSITY (W/cm^2)

Fig. 5-6

The top curve shows a mode-locked pulse train (at the P(26) CO_2 line) transmitted through an empty gas cell. The bottom curve represents the pulse train transmitted through the cell filled with 10 Torr of SF_6 (path length L^B = 2.5 cm).

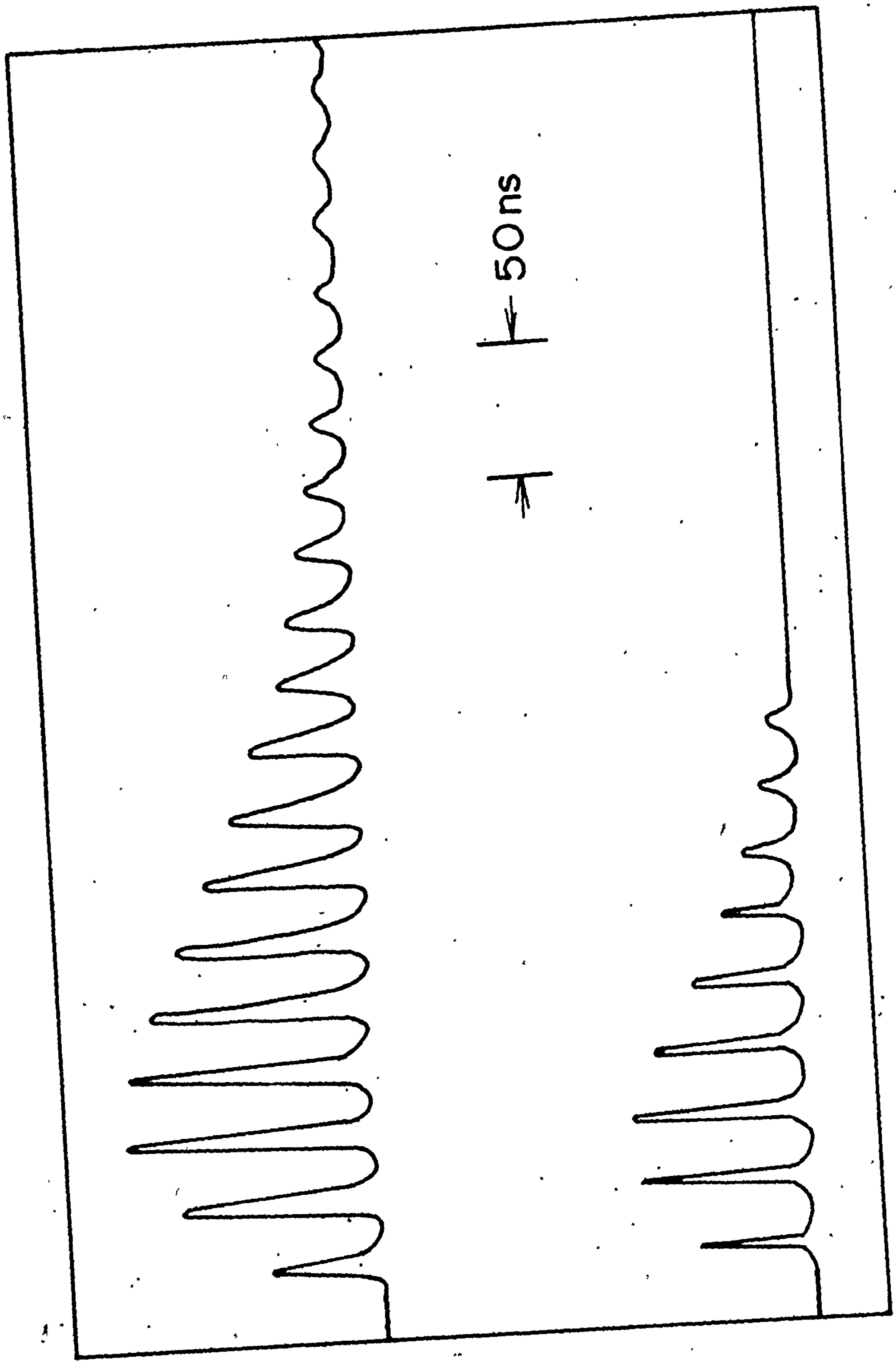
50ns

observed in Fig. 5-2(b) for a ~200 ns non-mode-locked input pulse. Fig. 5-7 illustrates the transmission behaviour of mode-locked pulse trains at the P(20) CO_2 line passing through 250 and 20 Torr of SF_6, respectively. The gas cell thickness for 250 Torr of SF_6 was reduced so as to give the same small-signal transmission as in the 20 Torr case (calculated to be $\sim 2 \times 10^{-12}$). A time delay between the input and transmitted pulse train peaks can be observed at 250 Torr of SF_6. Furthermore, there is very little narrowing of individual mode-locked pulses (<10% of the FWHM). Similar results were obtained at low SF_6 pressures (10-20 Torr) and approximately 1 atm of air. On the other hand, no time delay was observed for the 20 Torr SF_6 data, and substantial pulse-narrowing (4.5 ns to 2 ns in the FWHM) did occur.* Similar pulse narrowing at low SF_6 pressures has been observed recently by Nowak et al. [76]. These observations are again consistent with the vibrational bath model. At high SF_6 pressures (or SF_6 plus high buffer gas pressures) the transmission behaviour is dominated by vibrational heating, which tends to enhance the transmission on each individual pulse tail, and thus prevents pulse narrowing. Furthermore, the enhancement of the transmission on the mode-locked pulse train tail, due to vibrational heating on the pulse train rise, qualitatively accounts for the observable time delay.

At sufficiently high input intensities, vibrational anharmonicities can be compensated for by power broadening allowing multiple photon

---

* The 2 ns may represent an upper limit since the instrumentation risetime limits the minimum detectable pulsewidth to ~2 ns.

Fig. 5-7

The top curve shows the mode-locked pulse train (at the P(20) CO_2 line) transmitted through an empty gas cell. The maximum individual pulse intensity at the cell was ∿5 MW/cm^2. The middle and bottom curves show the transmission of the above pulse train through the cell containing SF_6 at 250 and 20 Torr, respectively. The low-signal transmission, calculated using $e^{-\alpha_0 L^B}$, was 2×10^{-12} for both 250 and 20 Torr. The transmissions for input pulse intensities shown in this figure were measured to be ∿2% (referred to the peaks of the pulse trains) for both pressures.

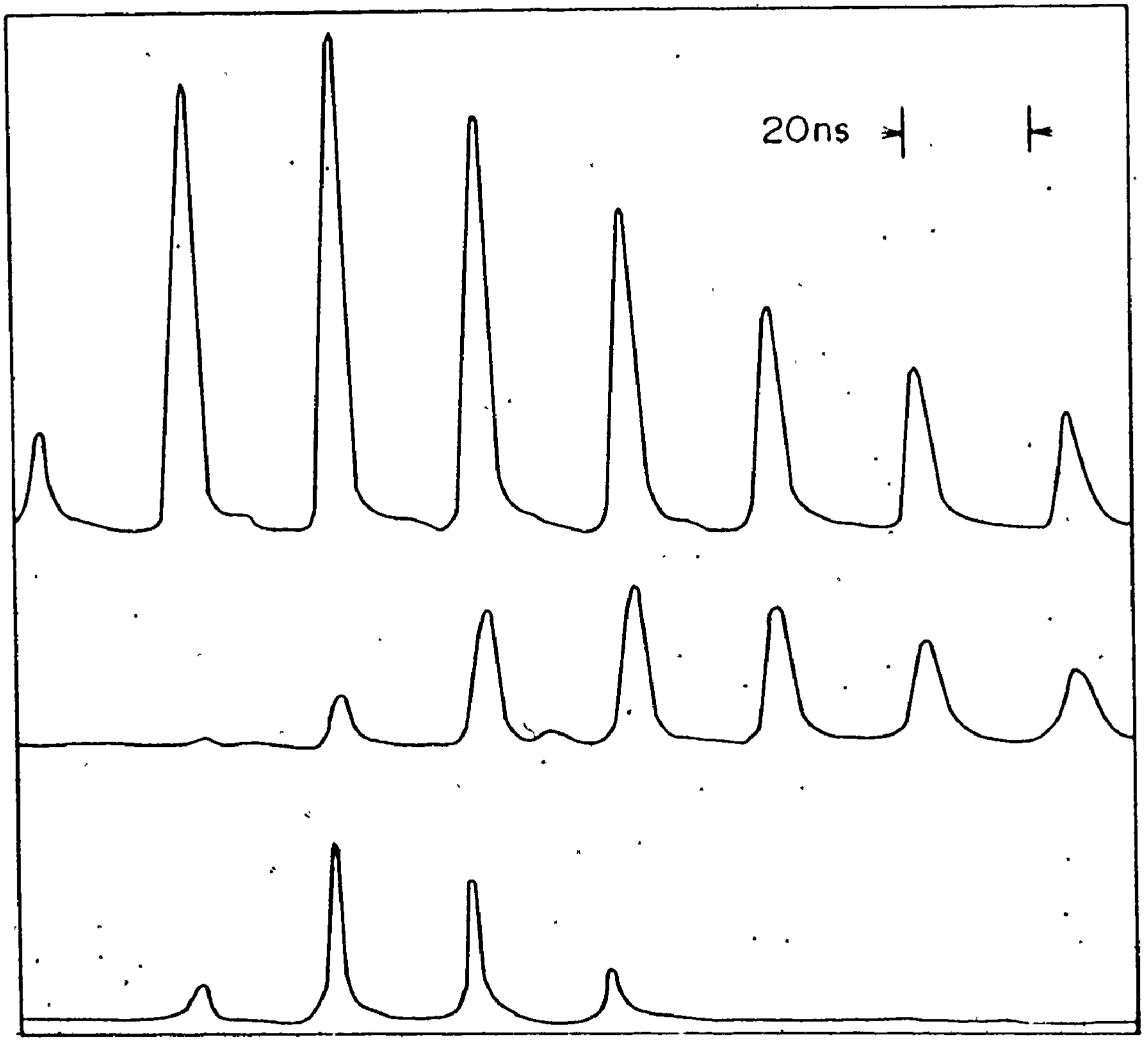
20ns

absorptions to occur up the ν_3 vibrational ladder [68]. Such an absorption process could be important in predicting the exact transmission behaviour of very high intensity (above a MW/cm^2) mode-locked pulses through SF_6. Furthermore, the onset of such a process may account for the discrepancy observed between the experimental transmissions at high input intensities (shown in Figs. 5-3 and 5-4) and those predicted by the vibrational bath model.

5.4 Summary

It has been demonstrated that a vibrational bath model, which takes into account the complex multi-level absorption spectrum of SF_6, can predict the entire transmission behaviour of CO_2 laser pulses through high pressure SF_6. This is valuable for the design of systems using SF_6 at atmospheric pressures to prevent parasitic lasing by, for example, the insertion of a flowing gas curtain between laser amplifiers.* It is particularly important to note that, although the absorption is strongly "saturated" at high intensity, no genuine intensity-dependent saturation process is involved. For high P-value CO_2 rotational lines, clear evidence is found for the persistence of heating effects down to low SF_6 pressures. This is consistent with previous indications in Chapter 4 that, for vibrational levels more than 1000 cm^{-1} above the ground state, very rapid vibrational energy exchange processes occur even at low pressures.

---

* Such a proposal is being considered by Avco Everett Research Laboratories and is outlined in the December 1976 issue of Laser Focus (page 34).

It is now possible to understand the entire pulse transmission behaviour for the P(12) to P(28) CO_2 rotational lines over a wide range of SF_6 pressures. The combination of the vibrational bath model with a 4-level intensity saturation model, accounts for the experimentally observed transmission characteristics for low as well as high SF_6 pressures and for all the J-value CO_2 lines studied. For low J-value lines the 4-level intensity saturation model alone (Chapter 3) provides a very adequate description of the transmission behaviour for SF_6 pressures less than 400 Torr. For pressures above ∿400 Torr the vibrational heating model must be used to determine the pulse transmission behaviour.

The importance of understanding the interaction of CO_2 radiation with the complex set of SF_6 vibrational and rotational levels will be further demonstrated in the next chapter which is concerned with the mode-locking properties of gaseous SF_6

CHAPTER 6

MODE-LOCKING PROPERTIES OF GASEOUS SF_6

6.1 Introduction

It has been shown (Chapters 3 and 4) that the absorption of CO_2 radiation by SF_6 is due to a large number of vibrational and rotational levels. Transmission measurements using a pulsed CO_2 laser further showed that "saturation" processes could occur which were different from those due to genuine intensity saturation effects. One such process, discussed in detail in Chapters 4 and 5 and in Refs. [73, 77], is vibrational bath heating. Clearly, SF_6 is a highly complex system. Nevertheless, extensive investigation is required because stable mode-locking has been achieved on a number of CO_2 rotational lines [17, 18].

This chapter outlines the mode-locking properties of gaseous SF_6. Section 6.2 describes typical experimental conditions necessary to obtain high intensity, stable, mode-locked laser pulses. This section also discusses the progression from single longitudinal mode (SLM) to mode-locked operation as the SF_6 and buffer (He) gas pressures are increased. Section 6.3 demonstrates that many of the mode-locking observations can be predicted from the transmission and double-resonance measurements of Chapter 3 to 5, thereby emphasizing the importance of these measurements for obtaining optimum mode-locking. This section also demonstrates the importance of the 3-mirror laser cavity (Fig. 2-7) in obtaining the first reported mode-locking on the

P(28) CO_2 rotational line. Experiments designed to obtain short (sub -ns) duration mode-locked pulses are outlined in Section 6.4.

6.2 Experimental Conditions for Stable Mode-Locking

To achieve optimum mode-locking, various cavity lengths (1.5 - 3.5 m) and cavity designs (2-mirror and 3-mirror) were tested. As well, a wide range of laser pressures (a helical laser was used for sub-atm operation, a double-discharge laser was used for 1 atm operation), gas cell pressures (SF_6 pressures in the range 10-400 Torr) and laser rotational lines (P(12) to P(28)) were investigated. A typical mode-locking arrangement consisted of a 2-mirror $\sim$3 m long cavity composed of a 92% reflecting gold-coated grating and a 10% transmitting Ge flat. The laser system was composed of two helical lasers (1 m) in tandem, operating at a total gas pressure of 1/2 atm, with typical gas concentrations of 85% He, 10% CO_2 and 5% N_2. An adjustable aperture placed in front of the grating ensured operation in the TEM_{00} mode. The adjustable thickness gas cell, described in Chapter 2, was placed at the Brewster angle and located as close as possible to the 10% transmitting mirror. Typically the gas cell thickness was $\sim$0.1 cm.

The procedure for mode-locking consisted of first tuning the grating to the desired wavelength (without SF_6 in the gas cell). For this the laser was operated just above threshold in order to achieve maximum tuning sensitivity. The wavelength was then verified by using a spectrum analyzer (Optical Engineering). The aperture was adjusted to introduce sufficient cavity loss to eliminate higher order modes and thus obtain the TEM_{00} mode. SF_6 was flowed slowly through the cell at a gas pressure which based on the small-signal measurements of Section 3.1 would just stop lasing action.* Small adjustments of the laser gain (by means of the power supply voltage) were made until lasing action was achieved. Under such conditions the laser pulse was delayed from the discharge current pulse by 3 to 4 μs. Additional increases in the laser gain produced an extremely large change of the output intensity, from a low intensity non-mode-locked state to a large intensity (x 10 to 15 increase) mode-locked state. Initially these large output intensities sometimes caused mirror damage. This problem was rectified by obtaining special gold coatings on the mirrors. The mode-locked outputs usually consisted of a train of 10 to 20 ($\sim$3 ns wide) pulses, as shown in Fig. 1-4 and Fig. 4.9(a). A He buffer gas was very often mixed with SF_6 to stabilize the gas flow characteristics and to obtain shorter duration pulses by reducing the absorber's recovery time.† The laser gain (usually $\sim$120% per amplifier pass) could be varied by ±5% before a significant deterioration was observed in the mode-locking stability. Lowering of the gain by much more than 5% either failed to produce a Q-switched output or stopped lasing action altogether. Raising the gain led to greater fluctuations in the peak mode-locked pulse intensity and to a greater probability of producing multiple pulses per round trip time. It was also observed that mode-locking could be obtained with non-linear to linear loss ratios as low as 2. However the output intensities were reduced compared to those at higher ratios.

---

* This procedure prevented the firing of the laser with too little loss in the cavity, thus avoiding the risk of mirror damage.

† Air was also used as a buffer gas with results similar to those with He.

Clean pulses (i.e., a mode-locked train with essentially a single pulse per round trip time) were observed > 85% of the time. The intensity stability on a laser shot-to-shot basis was better than ± 15%. The ratio of the intensity of the largest to the second largest pulse (contrast ratio) in a round trip time, and in the region about the maximum intensity pulse to the mode-locked train, was usually > 50.* The key factors in improving the mode-locked contrast-ratio and stability, aside from the gain and non-linear loss considerations mentioned above, were the use of stable laser discharges, a stable SF_6 gas flow system, and the use of large beam area at the grating. The laser stability was improved by sacrificing some gain in order to achieve very reproducible discharges. The optimum stability was determined by monitoring the fluctuations in both the time delays between the current and laser pulses, and the pulse output intensities at lasing threshold conditions (obtained by severely aperturing down the laser). The stabilities were tested over a wide range of gas concentrations, power supply voltages and discharge capacitances. It has been observed (Fig. 2-6) that, above certain input electrical energies, the laser gain becomes relatively independent of additional increases in the input energy. Such a levelling off in the gain at increased input energies has been investigated previously, and seems to be characteristic of all TE CO_2 lasers [35 ,78]. By operating near the start of the gain saturation region it is possible to exploit this effect to produce a situation where the fluctuations in the input electrical energy results in minimal variation in the small-signal gain. However, the laser cannot be operated too far from the start of the saturation region due to the onset of discharge instabilities. Reasonable control of the SF_6 flow and reduced pressure fluctuations were achieved by the choice of a suitable flowmeter (Matheson Tube #600). Furthermore, as was indicated in Chapter 2, the gas cell was designed to allow a smooth (laminar) flow across the entire cell diameter, and therefore to prevent the occurence of absorption gradients. It was noted that improper grating "tuning" resulted in a significant probability (up to 50%) of obtaining simultaneous mode-locking and Q-switching at two CO_2 wavelengths. Then the laser output consisted of two discrete pulse trains, usually separated in time by ∿ 1 μs. These two pulse trains most frequently occured where the grating loss experienced by the second wavelength was not ~~sufficient~~ to overcome the reduction in loss that this wavelength might experience due to the resonant nature of the SF_6 absorption (Fig. 3-3). The competition between neighbouring wavelengths was more likely to occur for lines such as P(14) and P(16), which possess a large difference in their small-signal absorption coefficients. The use of large beam areas at the grating (to ensure maximum discrimination between rotational lines), plus careful tuning of the grating, eliminated this problem.

---

* This value probably represents a lower limit due to noise pickup problems with the detection system.

The transition to mode-locking usually occurs from an initial state, which in the time domain is characterised by a collection of random intensity "spikes" (Fig. 1-1). However, a very interesting transition to mode-locking occurs at low SF_6 absorber pressures ($\leq$ 10 Torr). The laser output observed near lasing threshold (using a fast risetime oscilloscope) was temporarally "smooth", which is characteristic of single longitudinal mode (SLM) production [79]. The output was very reproducible on a pulse-to-pulse bases (i.e. >95% SLM). The addition of a few Torr of SF_6, and reducing the gas cell thickness to keep the absorber loss constant, produced a near-oscillatory output. This is characteristic of the beating of several axial modes. Further addition of SF_6 (up to $\sim$20 Torr) produced distinct 5 ns duration pulses, which narrowed to $\sim$2.5 ns as the SF_6 pressure was increased to $\sim$30 Torr. It was not possible to observe whether a lower SF_6 pressure limit existed for the production of SLM, since the gas cell thickness could not be increased to accomodate pressures less than 3-4 Torr and still maintain the same absorber loss. The transition from SLM to mode-locking has been observed when $\sim$10 Torr of He was added to a few tenths of Torr of SF_6 [80 ,81]. A proposed explanation for this is that the SF_6 absorption frequency spectrum is not completely flat over the gain bandwidth of a particular CO_2 transition, but possesses some structure. Consequently, modes under the gain bandwidth see different absorber losses. If the net gain (gain minus loss) on a particular axial mode is sufficiently greater than that of its neighbours, then,after a considerable number of passes in the absorber (typically 300), this mode will preferentially grow in intensity and eventually deplete the laser gain. The result is a large intensity "single frequency" laser pulse.* Ref. [81] was able to verify that all the observed SLM frequencies for different CO_2 wavelengths correlated to the measured SF_6 absorption minima. This explanation implies that there is still significant variation in the absorption spectrum at ∿10 Torr of SF_6 to cause SLM production despite the expected smoothing out of the absorption spectrum by the pressure broadening of the absorption lines.

6.3 Mode-Locking Observations and Discussions

Several aspects of SF_6 mode-locking can be predicted from the results of Chapters 3 to 5. For example, the transmission curves of Chapter 3 indicate little residual absorption (i.e., the absorption remaining at very high input intensities). Both the large Q-switching effect and the generally observed long fall times of the mode-locked trains (Fig. 1-4 and Fig. 5-6) are certainly consistent with an absorber which possesses a low residual absorption. In order to obtain simultaneous mode-locked and Q-switched pulses at the longer CO_2 wavelengths, it was necessary to use the 3-mirror cavity to produce sufficient focussing at the absorber. In contrast, the mode-locking stability for short wavelength lines such as P(12) to P(16), even with large buffer gas pressures (200-400 Torr), was improved by using a 2-mirror plane-plane cavity geometry. The above behaviour is entirely consistent with the transmission curves shown in Sections 3.3(c) and 5.3, which indicate a progressive increase in the intensities necessary to "bleach" the absorber as the CO_2 wavelength is increased. The very low saturation parameters (I_s) associated with short CO_2 wavelengths (e.g., for the P(14) line, I_s = 1.5 kW/cm^2 at 50 Torr SF_6 (Table 3-1)) indicates that the best cavity design for the rotational lines from P(12) to approximately P(18) is one that allows the laser beam to "diverge" at the absorber. On the other hand, much higher intensities (a few MW/cm^2 (Fig. 3-8)) are needed at the gas cell to greatly increase the absorber transmission for the P(26) and P(28) lines; a focussing cavity should be more suitable in this case. Experimentally, a factor of 15 to 20* in the ratio of the beam area at the amplifier to that at the absorber was needed for mode-locking at these lines employing a 1/2 atm CO_2 laser with an absorber pressure of 50 Torr of SF_6.**

---

* SLM can be produced in a short (< 1.5 m), low pressure (< 100 Torr), laser cavity without using an SF_6 absorber. This is due to the natural selection of the axial mode which is closest to the peak of the gain profile [82].

In Chapters 4 and 5 it was indicated that the combination of intensity saturation processes and vibrational heating effects could account for the transmission curves observed in Chapter 3. The contribution of vibrational heating was shown to be significant for the P(26) line, even at low SF_6 pressures. The mode-locking and Q-switching behaviour of this line is investigated in this section to assess the importance of vibrational heating in the production of mode-locked pulses. Experiments were performed using a 3-mirror cavity arrangement, as shown in Fig. 2-7. The output coupling from the cavity was provided by a 14% transmitting, 0.5 m radius of curvature, Ge mirror, denoted by M1 in Fig. 2-7. The gas cell, maintained at a pressure of 50 Torr of SF_6 and a temperature of 300 K,was placed at the Brewster angle and $\sim$10 cm from M1. The output observed at this position was mode-locked but of very modest intensity. Moving the gas cell 5 to 10 cm towards the beam waist actually reduced the output peak intensity, and caused a significant chopping of the mode-locked envelope tail. This behaviour is similar to that shown previously for the extra-cavity P(26) transmission experiments (Fig. 5-6). A further advance of the cell into the beam waist produced the dramatic switching to the high intensity outputs ($\sim$0.5 mW/cm^2) shown in Fig. 6-1. The most interesting observation concerning this figure is that the switching occurs from the tail portion of the first mode-locked train (i.e., after the first 6 round trips) rather than from the peak pulse intensity of that train. This observation indicates that a critical energy density, rather than intensity, is necessary to cause the sudden increase in the absorber transmission. It was also observed that there was no significant pulse narrowing across the pulse train, as might be expected if intensity saturation processes occur. The interpretation of these results is consistent with the transition from intensity saturation processes at the absorber at low laser fluxes to vibrational heating effects at larger fluxes. Mode-locked operation is obtained in the saturation

---

* The method for measuring the beam areas will be outlined in Section 8.2(c).

** The beam areas at the amplifier and the absorber are chosen to ensure that the gain and absorber bleaching occur nearly simultaneously. Since it becomes harder to saturate the gain at higher laser pressures less of a converging cavity is necessary for a 1 atm CO_2 laser.

Fig. 6-1

Simulataneous mode-locked and Q-switched output at the P(26) CO_2 wavelength obtained using a 3-mirror resonator and an SF_6 saturable absorber (50 Torr gas pressure). The peak output intensity is $\sim$0.5 MW/cm^2. The round trip time is 23 ns.

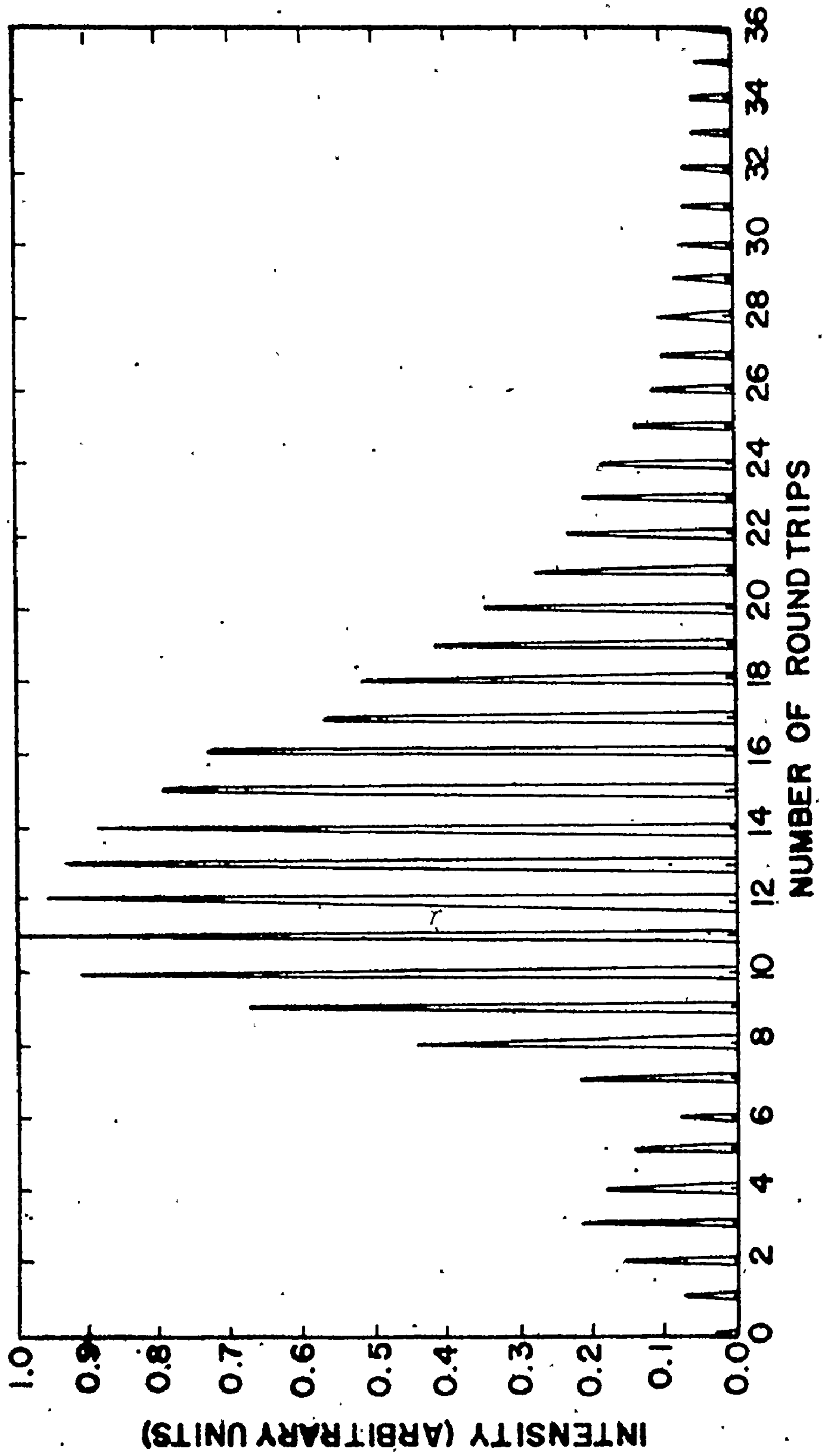
INTENSITY (ARBITRARY UNITS)
1.0
0.9
0.8
0.7
0.6
0.5
0.4
0.3
0.2
0.1
0.0
NUMBER OF ROUND TRIPS
0
2
4
6
8
10
12
14
16
18
20
22
24
26
28
30
32
34
36

regime, while Q-switching results from the dramatic increase in absorber transmission in the vibrational heating regime. The pressure dependence of the P(26) mode-locking, with gain and loss kept constant, provides further evidence of vibrational heating effects. Figure 6-2 shows the ratio of the laser beam area at the amplifier to that of the absorber necessary to obtain switching action. This was done for different SF_6 pressures and for 12 Torr of SF_6 plus various pressures of a He buffer gas. The small-signal absorption was kept constant for the different SF_6 pressures by appropriately changing the gas cell thickness. Figure 6-2 indicates that the ratio varies linearly with pressure at low SF_6 and buffer gas pressures, consistent with the linear scaling of the intensity saturation parameters with pressure (Chapter 3), but becomes very non-linear above ∿40 Torr of pure SF_6, and for 12 Torr of SF_6 with 150 Torr of He.* The pressure at which the linearity fails is very close to the pressure where the low intensity portions of the transmission against intensity curves of Fig. 3-8 are nearly flat. It appears that at higher SF_6 pressures the absorber transmission becomes progressively dominated by heating effects, which leads to an actual increase in the absorption (compared to the small-signal value) as the intensity builds up in the laser cavity. This type of behaviour prevents Q-switching from occurring at near lasing threshold conditions for the higher absorber pressures. Q-switching can be obtained by

---

* We have found in our experiments that the addition of He affects the mode-locking behaviour in a similar manner to SF_6, but requires considerably higher pressures (∿x5) to reach the equivalent effect of SF_6.

Fig. 6-2

Plot of gas cell pressure as a function of the ratio of the laser beam area at the amplifier to that at the absorber necessary to obtain Q-switched outputs. The data points denoted by (x) were obtained with pure SF_6. The SF_6 gas cell pressures are indicated by the scale on the left hand side of this diagram. The data points denoted by (●) were obtained at various He pressures with a fixed SF_6 pressure of 12 Torr. The He pressure scale is indicated on the right hand side of this diagram.

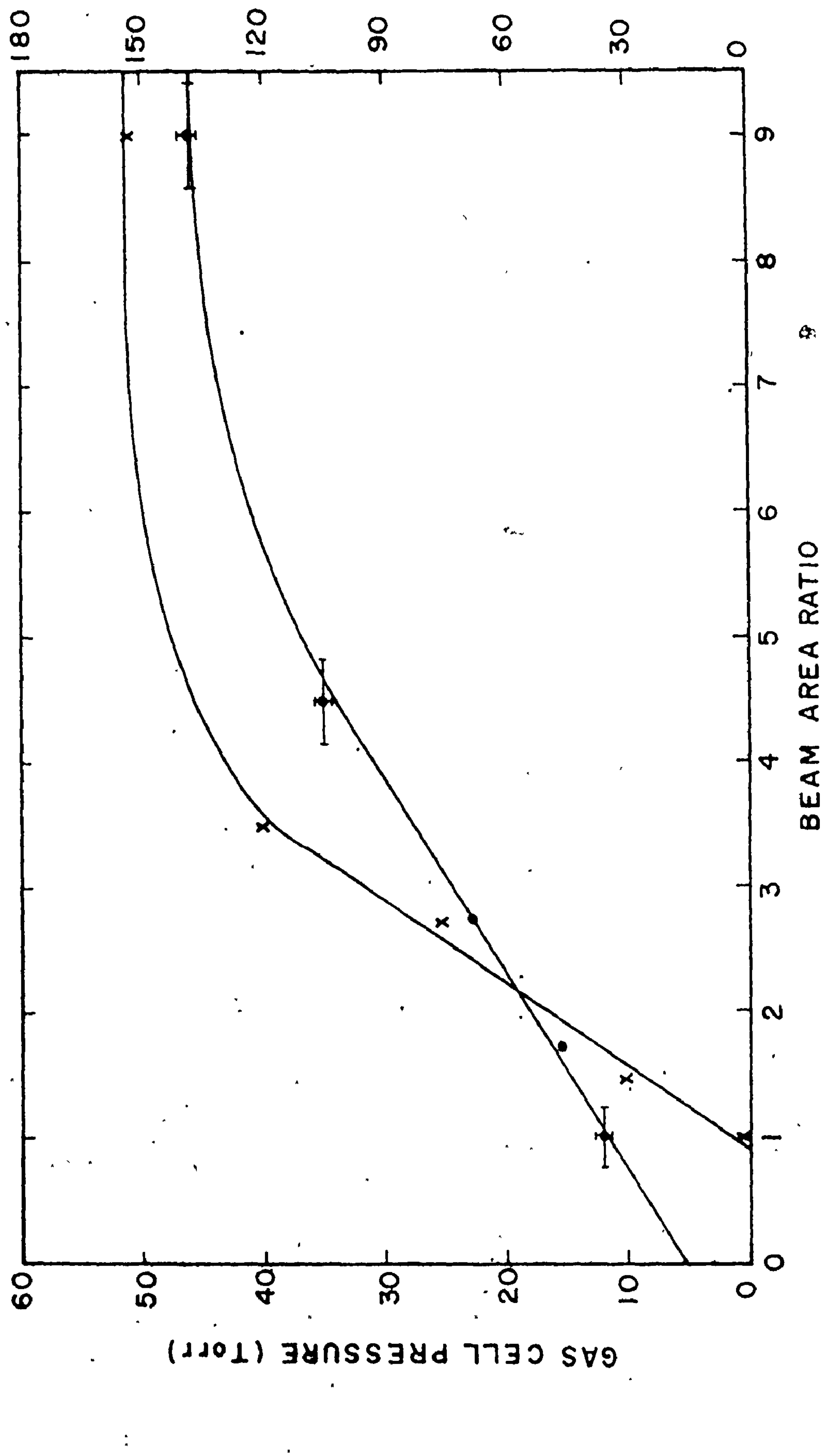
GAS CELL PRESSURE (Torr)
0
10
20
30
40
50
60
0
30
60
90
120
150
180
BEAM AREA RATIO
0
1
2
3
4
5
6
7
8
9

using much higher gains to conpensate for the increasing absorber loss.* A further observation on the P(26) line was that mode-locking could be obtained at pressures as low as 10 Torr, indicating that the frequency absorption spectrum was much flatter (over the gain bandwidth) at this pressure than that for the P(16) to P(22) lines. This behaviour undoubtedly results from the large number of absorbing levels at the P(26) wavelength.

Similar pulse shaping and mode-locked pulse switching behaviour was observed for the P(28) line. However, the SF_6 pressures had to be kept under ∿20 Torr for this rotational line and the gas cell had to be moved closer to the cavity beam waist. This behaviour is consistent with the shift of the P(28) transmission curve to higher intensities relative to the P(26) curve, as noted previously in Chapters 3 and 5

Once the correct beam area ratios and SF_6 pressures were found the mode-locking stability on the P(26) and P(28) lines was very good. The stable production of mode-locked pulses on these lines is contrary to some previous published theoretical mode-locking predictions employing a 4-level model [83]. These predictions indicate that it should be very difficult to obtain mode-locking for P-lines below P(16) and for P-lines at or above P(26). However, mode-locking has been obtained on the P(12), P(14) and P(28) rotational lines. It is therefore clear that a 4-level treatment for the P(26), and P(28) lines is inadequate for describing the mode-locking behaviour, and that the contribution of vibrational heating must be included in any analysis. The mode-locking stability for the P(12) to P(18) lines in a plane-plane cavity geometry was poorer than that obtained on the other lines but could probably be improved by using a diverging beam cavity, as suggested previously. Mode-locking was not obtained on the P(10) line; this may result from the fact that the major portion of the absorption on this line comes from the presence of a near continuum of vibrational levels. The high density of rapidly coupled levels makes intensity saturation, and therefore mode-locking, very difficult.

---

* The mode-locked stability was always poorer in these cases.

6.4 Sub-ns Pulse Generation

There are many applications in which many short infrared laser pulses are required. For example, there is a clear need for a source of stable sub-ns 10.4 μm pulses to be used as starting pulses in long chain CO_2 amplifiers designed for initiating controlled nuclear fusion [84]. As we have demonstrated in this thesis, short 10.4 μm wavelength pulses can also be used to measure very fast rotational and vibrational coupling times. However the shortest mode-locked pulse duration reported in the literature, for an SF_6 saturable absorber in conjunction with a 1 atm CO_2 laser, is ∿1.5 ns [17 , 18]. Therefore, considerable effort was expended in our research to obtain sub-ns mode-locked pulses. Such parameters as the CO_2 wavelengths, the SF_6 and He pressures, and different types of cavity configurations, were all investigated.

A typical mode-locked train observed in these experiments consisted of ∿15, 2 ns duration (FWHM), asymmetrically shaped pulses

(Fig. 6-3). Two interesting features of such mode-locked pulse trains are the lack of pulse narrowing across the train envelope and the enhancement of the pulse intensity on all of the pulse tails under the train envelope. This behaviour is contrary to the symmetric narrowing expected from repeated traversals through a fast 2-level absorber.* Fortin et al. [17] (using a TEA CO_2 laser) have observed that the mode-locked duration could be reduced from 5 ns to 2 ns by the addition of 400 Torr of He to $\sim$25 Torr of SF_6. Further addition of He did not reduce the pulse duration below 2 ns. This behaviour has also been observed by us. The SF_6 pressures in Ref. [17] could not be increased since the gas cell thickness was fixed. Similarly the laser gain for stable discharge operation could not be raised. Therefore a set of experiments at elevated SF_6 pressures (with and without a He buffer) were performed in our laboratory with the TEA CO_2 laser to investigate the effect of SF_6-SF_6 collision processes, rather than predominately SF_6-He processes, in reducing the mode-locked pulse duration. The majority of the experiments were performed with the variable thickness gas cell and the 3-mirror laser cavity. The minimum thickness (L^B) setting of the gas cell (0.015 cm) allowed mode-locking at SF_6 pressures up to 80 Torr for the P(20) line, while keeping the small-signal absorption at a reasonable level (i.e., $\alpha_0 L^B \sim 0.5$ to 0.8). The focussing capability of the 3-mirror cavity, which was not available in Ref. [17], ensured that at high SF_6 pressures a position could always be obtained in the cavity where Q-

---

* This will be discussed in detail in Chapters 7 and 8, which are concerned with germanium mode-locking.

Fig. 6-3

Photograph of two pulses from a mode-locked TEA CO_2 laser operating at the P(20) wavelength and with an SF_6 saturable absorber. The time scale is 5 ns per division. The risetime of the detection system is < 1 ns. The pulses were inverted by the detection system.

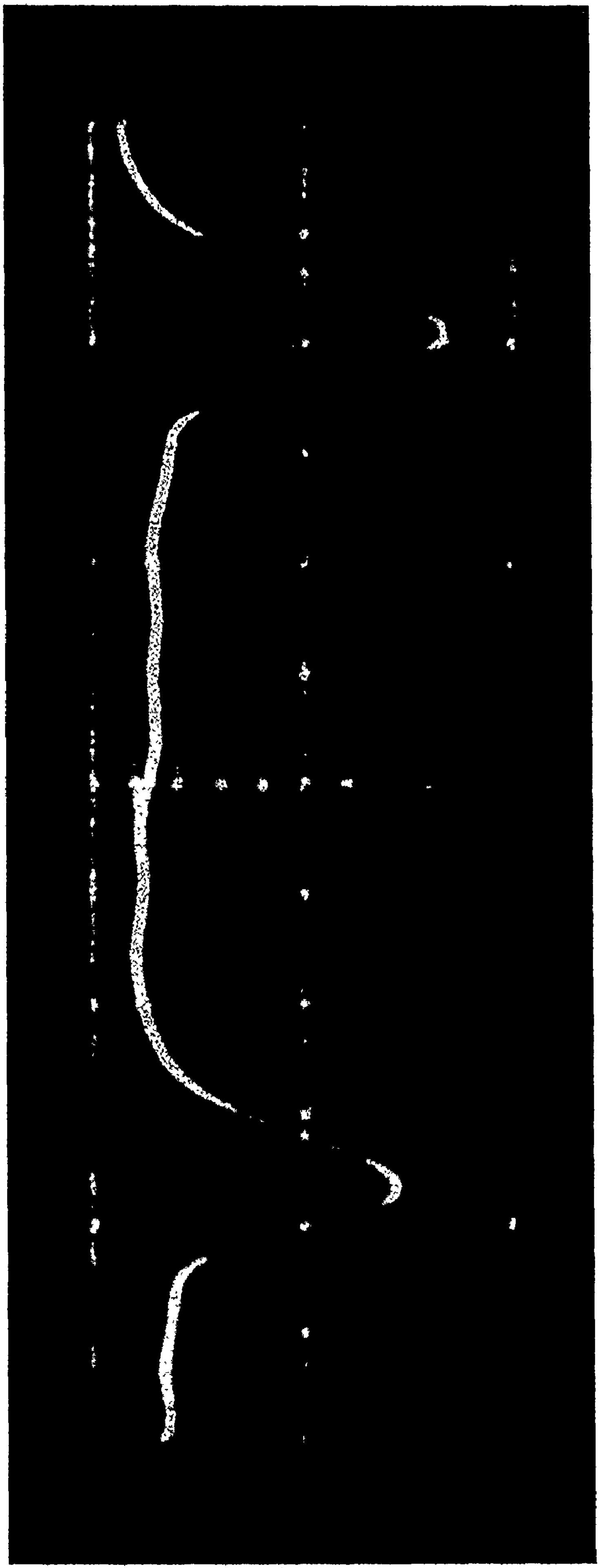

switching was observed. The pulses obtained in these experiments, for the P(14) - P(28) lines, and for both low and high (∿1 atm) buffer gas pressures, were always asymmetric and ≳ 1.5 ns* in duration throughout the mode-locked train envelope. Particular effort was made to obtain short pulses on the most frequently used P(20) CO_2 line. An experiment was performed with the TEA laser operating at the P(20) line and at moderate** SF_6 gas pressures (∿50 Torr). A plane-plane cavity† was used in the experiment, and special care was taken to place the absorber as close to the end mirror as possible.†† The pulse durations again were ≳ 1.5 ns.

There are many possible explanations for the lack of observed pulse narrowing and the enhancement of the intensity on the pulse tail. It is demonstrated in the next two chapters (dealing with Ge mode-locking) that pulse asymmetries, such as have been observed in the SF_6 mode-locking experiments, can result from the cumulative effect (due to a large number of passes in the amplifier) of rotational hole burning in the CO_2 amplifier. However, such a mechanism cannot account for the strongly asymmetric pulses observed on the rise of the pulse train envelope. Alternatively this pulse asymmetry, and lack of narrowing, might result if the absorber recovery time (at increased SF_6 or buffer gas pressures) fails to reduce to values less than ∿2 ns. This minimum value would result in a greater absorption on the pulse rise relative to that on the fall, as is observed experimentally. However, the experimental evidence obtained to date (Chapters 3 to 5) seems to support the existence of very short recovery times which do in fact scale with SF_6 pressure, at least up to several hundred Torr. It has also been pointed out in Chapter 4 that the SF_6 absorption, especially for the longer wavelength rotational lines, is due to a multitude of vibrational and rotational levels. No doubt the saturation behaviour on these lines involves a large number of absorbing levels with widely varying absorption cross-sections and with very complex level couplings. It is not at all obvious that such a system should produce pulse narrowing. It also appears that when vibrational heating effects start to dominate over intensity saturation processes (i.e., at high SF_6 pressures and high J CO_2 lines) pulse narrowing is again supressed (Chapter 5). Finally, recent work indicates that multiple-photon absorptions up the ν_3 vibrational manifold may occur at relatively low intensities which are easily achieved in mode-locked pulse operation (< 10 MW/cm^2) [66 ,85].* This absorption mechanism is theoretically possible at such low intensities due to the creation of many more absorption pathways resulting from anharmonic splittings of the vibrational degeneracies. Such a mechanism may in fact result in pulse broadening since the higher intensity portions of a mode-locked pulse may be more likely to experience multiple-photon absorptions than the lower intensity portions of the pulse. This is exactly the opposite behaviour to a fast 2-level saturable absorber. However, the multiple-photon absorption mechanism by itself would not account for the observed pulse asymmetry. The overall understanding of the pulse shaping problem is further complicated, since multi-level saturation, heating effects, and multiple-photon absorptions, are probably present to some degree for all the mode-locking conditions studied. These absorption processes should occur for other polyatomic molecules and may explain why Lavigne et al. [18] did not obtain mode-locked pulse durations shorter than 2 ns when employing BCl_3 and N_2F_4 as saturable absorbers in a TEA CO_2 laser cavity.

---

* A photon-drag detector and a Tektronix 7904 oscilloscope (625 ± 25 ps risetime) plus a Hewlett-Packard 183-A oscilloscope (1600 ± 50 ps risetime) were used for the pulse duration measurements.

** Moderate pressures were used to avoid heating effects.

† The plane-plane cavity is probably close to the optimum cavity configuration for the P(20) line.

†† The 2d/c time, where d is the distance of the gas cell to the end mirror, was 0.3 ns for this experiment and was much shorter than the observed ∿2 ns duration pulses. The importance of the absorber position in the laser cavity is discussed in Chapter 8.

---

* The probability of a multiple-photon absorption up the ν_3 vibrational ladder will be intensity dependent to the extent that power broadening of the absorption lines can compensate for level mismatch and thus keep the absorption essentially on resonance.

It may still be possible to obtain short pulses by reducing the contribution of these mechanisms relative to the contributions made by true intensity saturation effects by employing a suitable choice of cavity design, CO_2 wavelength, and SF_6 pressure. The most promising experiment that could be performed is one in which mode-locking is obtained for low J-number lines such as P(12) and at moderate SF_6 pressures (75-100 Torr). The low J-number line and the choice of SF_6 pressure should reduce the effect of vibrational heating while still giving a reasonably short absorber recovery time. In addition, the saturation of the absorption should be nearly 2-level since most of the

P(12) absorption comes from the ground state (88% at 300 K). A cavity which increases the beam area at the absorber relative to that of the amplifier should eliminate the problem of the switched intensity being so much greater than the absorber saturation intensity for these low J-lines (a factor of ∿10 may be necessary for 1 atm laser operation). Under these conditions the contribution of intensity saturation and multiple-photon absorption processes should dominate the absorber transmission behaviour and the significance of multiple-photon absorption processes in obtaining narrow pulses can then be assessed.

It may also be possible to obtain shorter pulses by using multi-atmospheric CO_2 lasers. Experiments performed at 1/2 atm to 1 atm laser pressures indicate that, although no narrowing occurs across the pulse train, the pulse durations scale inversely with the laser pressures.* Of course there will be an even greater need for using diverging beam areas at the absorber with multi-atmosphere CO_2 lasers.

6.5 Summary

This chapter has outlined the important features of passive mode-locking with an SF_6 saturable absorber. It has been demonstrated that stable, clean, high-intensity mode-locked pulses can be produced over a wide range of CO_2 wavelengths when stable laser operation and steady SF_6 flow conditions are achieved. The mode-locking behaviour was entirely consistent with the transmission curves obtained in Chapter 3. It was especially gratifying to observe experimentally the trend to greater focussing at the absorber with increased CO_2 wavelength, exactly as predicted by the transmission data. Work on the P(26) and P(28) lines demonstrated that intensity saturation effects accounted for the actual mode-locking on these lines, while vibrational heating effects accounted for the observed Q-switching, again in excellent agreement with the theoretical predictions of Chapters 3 to 5. However, it was not possible to obtain mode-locked pulse durations < 1.5 ns using a 1 atm CO_2 laser. It was therefore suggested that absorption processes such as multi-level saturation, multiple-photon absorption, and vibrational heating, may well account for the lack of narrowing across the pulse train. The choice of suitable mode-locking parameters should allow the isolation of the effect of multi-photon absorptions in pulse shaping and may result in a method to obtain narrower pulses. It was further suggested that short pulses can probably be obtained with multi-atmosphere lasers once the proper cavity geometry is found.

---

* This would be expected to occur if the absorber linewidth is flat with respect to the multi-atmospheric gain linewidth. In such a case the pulse broadening in the linear gain region will be proportional to the inverse of the gain linewidth and therefore inversely on pressure. The linear gain broadening mechanism is discussed in Chapter 7.

Although mode-locking has been achieved over a wide range of wavelengths, a single mode-locked train on several rotational lines is very difficult to obtain simultaneously due to the resonant nature of the SF_6 absorption. As well, SF_6 does not absorb 9.4 μm radiation, and thus prevents multi-band mode-locked laser operation. Multi-line and multi-band pulses are of great interest since the maximum energy that can be extracted from an amplifier by a short (∿1 ns) mode-locked laser pulse can be increased if the pulse is produced by many transitions

[86]. The inability to operate multi-line or multi-band also severely restricts the use of SF_6 as an isolator in short pulse multi-line, multi-band amplification systems. The use of SF_6 as a mode-locker does, however, have some distinct advantages. The gas cell for the mode-locking can be very easily scaled to accommodate large aperture laser systems. Furthermore, a gas cell employing NaCl windows has a high damage threshold ($\gtrsim 5$ J/cm^2 [87]) and can therefore be used in conjunction with high energy density laser cavities. One other appealing feature of the SF_6 system is the ability to adjust the SF_6 and buffer gas pressures to alter the small-signal absorption and saturation parameters. This ability allows one, for example, to produce variable pulse length laser pulses.

The next two chapters report investigations of the mode-locking behaviour of a very different kind of saturable absorber from SF_6, p-type germanium.

CHAPTER 7

INVESTIGATION OF PASSIVE MODE-LOCKING USING A GERMANIUM SATURABLE ABSORBER - PART I

7.1 Introduction

In the previous chapter we dealt with the mode-locking properties of gaseous SF_6. In this and the following chapter, we shall discuss a solid saturable absorber, p-type germanium. As mentioned in Chapter 1 the absorption of 10.4 μm radiation in germanium (Ge) is primarily due to the excitation of holes from the heavy to the light hole band. The excited hole distribution returns to equilibrium in a time of a few ps at room temperature due to lattice scattering of holes by optical and acoustical phonons [19]. Large intensity laser pulses are usually needed to saturate the absorption due to the short recovery time in solids such as Ge. Although the absorption saturation parameter of Ge is quite large (several MW/cm^2), it is considerably less than the material damage threshold (~ 100 MW/cm^2) [88]. However, this is not the case for materials such as silicon and gallium arsenide, and their use as saturable absorbers in CO_2 lasers is therefore prohibited [19]. The fast recovery times for Ge, combined with a moderate saturation parameter, make it a suitable candidate for the production of short high-intensity laser pulses.

Although Ge has been successfully used for several years in mode-locking CO_2 lasers [12, 24] no previous attempt has been made to quantitatively analyze the mode-locking process. For example, it was not clear from the literature which cavity, gain and absorber parameters were best suited to produce short, stable high-intensity mode-locked CO_2 laser pulses. Section 7-2 of this chapter outlines a detailed theoretical computer model for simulating the generation of short,high intensity mode-locked pulses from a spontaneous emission noise source. A comparison of the theoretical predictions with experimental results will be made in Chapter 8.

In the theoretical analysis, the amplifier is treated in terms of a 2-vibrational level dynamic gain model having a homogeneously broadened linewidth. The effect of rotational coupling within each vibrational level is also included in the model. The Ge absorber is treated in terms of a 2-level steady-state absorption model having a inhomogeneously broadened linewidth. A density matrix formalism, rather than an rate equation approach, is used to describe the interaction of the radiation field and the CO_2 amplifier medium. This approach was chosen since the generation of short CO_2 pulses often involves the production of pulses whose duration is comparable to the gain medium's phase memory time (T_2).

Section 7.3 outlines the basic principles behind the noise fluctuation model and describes the four important stages of pulse evolution-linear amplification, non-linear absorption, non-linear gain and the pulse decay region. Furthermore, the concept of "deterministic" mode-locking is introduced and its implications for the work of this thesis is discussed.

7.2 Theoretical Model of Passive Mode-Locking

(a) Amplifier

The equations used to describe the response of the CO_2 amplifier to propagating laser pulses are similar to those in Ref. [89], which were appropriate to a ring laser with a uni-directional mode of propagation. The equations were adapted to describe a regular cavity depicted in the upper half of Fig. 7-1. The analysis is generalized so that the amplifying medium can have a time-dependent small-signal gain coefficient g(t). The assumptions made in Ref. [89] , of a 2-level homogeneously broadened amplifying medium in resonance with the electromagnetic radiation in the cavity and uni-directional propagation of radiation, are also made for this analysis. The first assumption is justified for CO_2 amplifiers at pressures >20 Torr, where the linewidth is basically collision broadened. The second assumption avoids having to consider complicated standing-wave interactions and in addition requires only one space co-ordinate $(\hat{x})$ for the spatial propagation of laser pulses. Medium dispersion effects other than that due to the resonant gain are also ignored in this treatment.* An equivalent periodic optical system for the regular laser cavity is shown in the bottom half of Fig. 7-1. In this figure L_a and L_b refer to the optical path lengths in the amplifier and absorber, respectively. As well, all the linear loss of the cavity, including the output mirror coupling, is included as an effective mirror reflectivity denoted by R.

---

* The dielectric constant of the amplifier and absorber are assumed to be constant and hence the corresponding phase velocities are independent of frequency.

Fig. 7-1

Schematic diagrams of the laser cavity. The top diagram shows the layout of the 2-mirror laser cavity used in the experiments. The output intensity of this cavity is coupled through a partially transmitting mirror M2. The bottom diagram shows the equivalent periodic (2L/c) optical system as used in the computer simulations. In this figure L_a, L_b refer to the optical path lengths of the amplifier and absorber, respectively. The linear loss of the cavity is accounted for by an effective mirror reflectivity denoted by R.

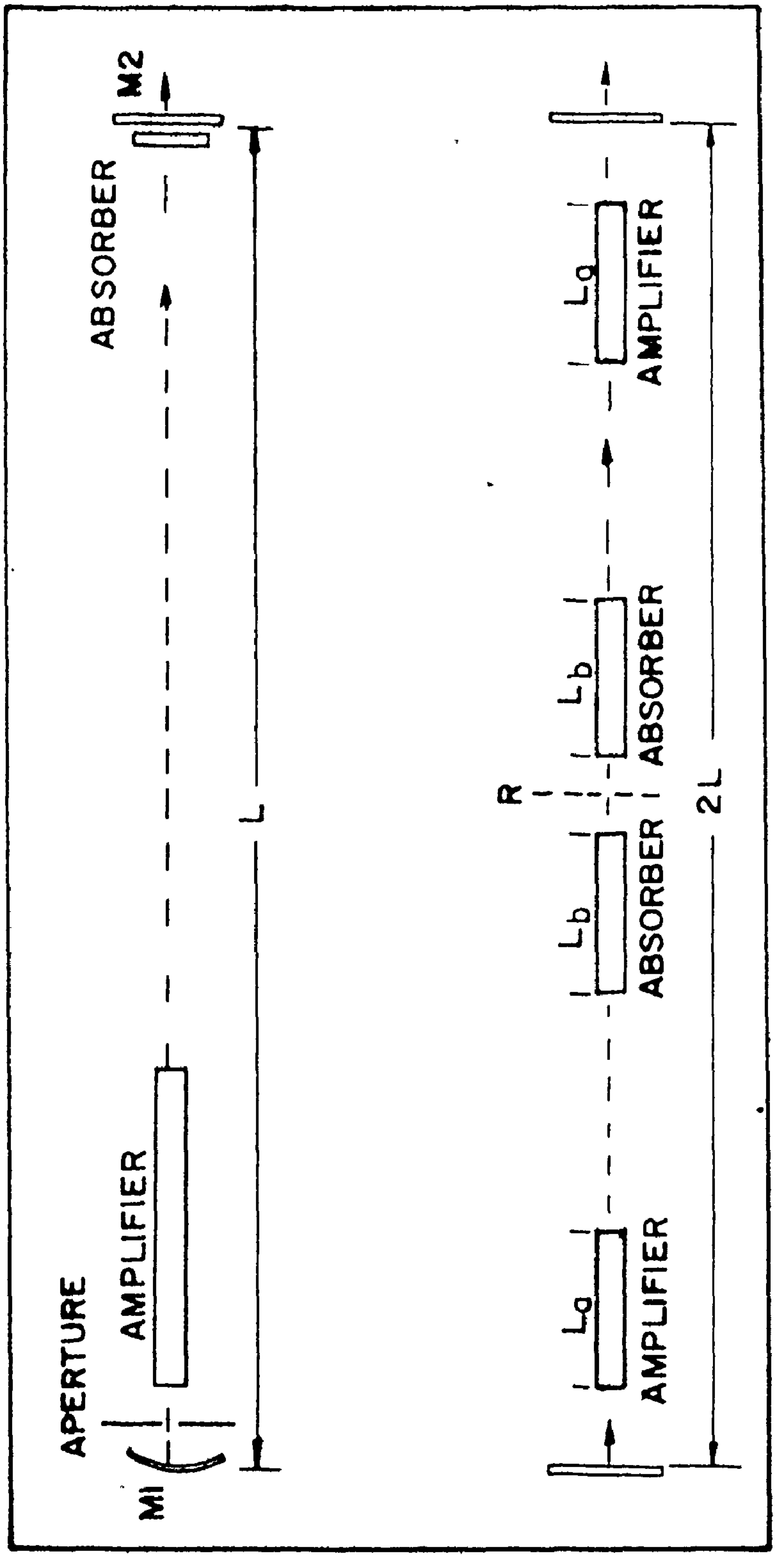
M2
ABSORBER
APERTURE
AMPLIFIER
MI
L
AMPLIFIER
La
ABSORBER
Lb
R
2L
ABSORBER
Lb
AMPLIFIER
La

The two-level gain medium consists of the upper CO_2 vibrational laser level (00°1) with a population N_2 and the lower vibrational laser level (10°0) with a population N_1. The time dependence of the upper and lower laser populations in the absence of radiation can be described by an exponential decay due to collisional relaxation [90]. Since the time dependent gain is proportional to the population difference between the upper and lower laser levels it can be written as

$$g(t) \propto N_2(t) - N_1(t) \tag{7-1}$$

and

$$g(t) = g_o(e^{-t/t_2} - e^{-t/t_1}) \ . \tag{7-2}$$

Here g(t) represents a small-signal intensity gain per unit-length defined, at any time (t), by

$$G = I_{OUT}/I_{IN} = e^{g(t)L_a} \ , \tag{7-3}$$

where I_{IN}, I_{OUT} represent the input and output intensities for an amplifier of length L_a. The times t_2 and t_1 represent the collisional decay times of the upper and lower vibrational levels respectively. The temporal gain profile is shown in Fig. 7-2 for t_2 and t_1 times appropriate to a 1 atm CO_2 amplifier (t_2 = 10 μs, t_1 = 0.4 μs) [91]. Note that the maximum small-signal gain g_{max} is not the same as g_o defined in Eq. (7-2),but is related to it by a constant.* Also shown in Fig.

---

* $g_{max} = g_o(e^{-t_{max}/t_2} - e^{-t_{max}/t_1})$, where t_{max} is given by $t_1 t_2 \ln(t_2/t_1)/(t_2 - t_1)$.

Fig. 7-2

Temporal gain profile for a 1 atm CO_2 laser. The t_1, t_2 times (defined in the text) are 0.4 μs and 10 μs, respectively. The time t_0 indicated in this diagram is the time at which the laser gain equals the total cavity small-signal loss, while t_d is the time measured from the peak of the current pulse to the 10% point on the rising edge of the laser pulse. The gain has been normalized to unity by dividing the expression for the gain (Eq. (7-1)) by g_{max}.

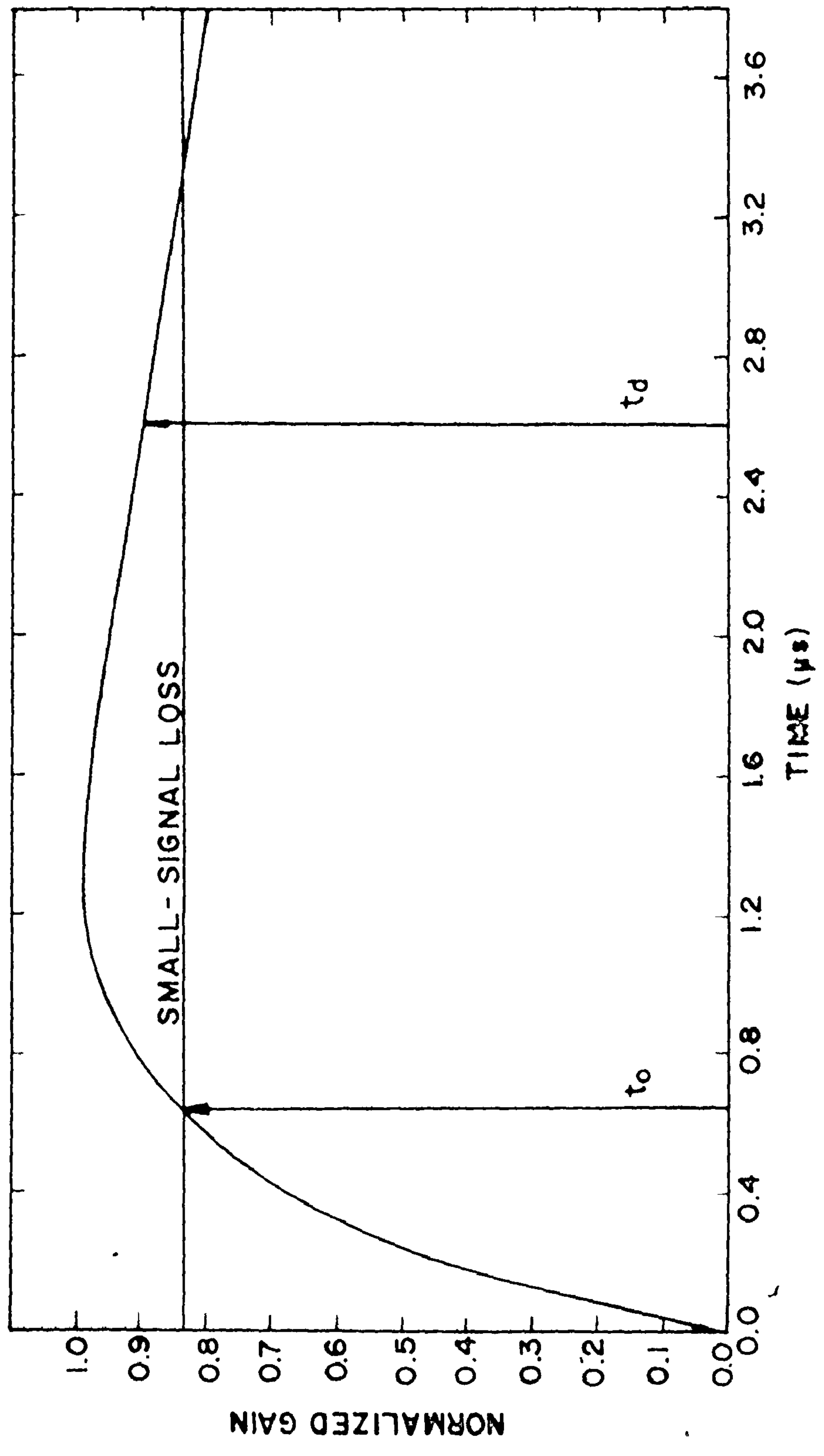
SMALL - SIGNAL LOSS
t_o
t_d
NORMALIZED GAIN
0.0
0.1
0.2
0.3
0.4
0.5
0.6
0.7
0.8
0.9
1.0
TIME (µs)
0.0
0.4
0.8
1.2
1.6
2.0
2.4
2.8
3.2
3.6

7-2 is the time, t_o, at which the laser gain equals the total cavity small-signal loss and the time delay, t_d, at which the laser pulse reaches sufficient intensity to cause a high rate of stimulated emission, thereby resulting in the reduction of the vibrational population inversion. Experimentally, the time delay t_d is measured from the peak of the current pulse to the 10% intensity point on the leading edge of the laser pulse.

It is not always possible to use the simple 2-level vibrational gain model at large photon densities. Most researchers believed that if the laser pulse duration was sufficiently long compared to the coupling time between rotational levels (denoted by τ_R), then all rotational levels belonging to the upper vibrational level could fully participate in supplying the inversion at a particular rotational line (e.g., J = 19 for the P(20) oscillation). However, Garside et al. [92] have shown that this is not always true and that the important consideration is the stimulated emission rate on a particular rotational line relative to the recovery rate of the rotational equilibrium at that line. Since the stimulated emission rate is intensity dependent, sufficiently intense long laser pulses can cause significant rotational saturation. Rotational coupling must be included in the model since the passive mode-locking process deals with pulses which are both short and intense. We shall follow the notation of Schappert [93] and define a rotational population inversion by

$$\delta^J(x,t) = N_2^J(x,t) - N_1^{J+1}(x,t) \tag{7-4}$$

and

$$\delta^{J}(x,t) = \kappa(J)D_2(x,t) - \kappa(J+1)D_1(x,t) \quad , \qquad (7\text{-}5)$$

where $\kappa(J)$ is defined as the fraction of the total rotational population that are in the rotational state J, at a temperature T, and is given by

$$\kappa(J) = g_J \exp\left(\frac{-\varepsilon(J)}{kT}\right)\left[\Sigma_J g_J \exp\left(\frac{-\varepsilon(J)}{kT}\right)\right]^{-1}, \qquad (7\text{-}6)$$

where $g_J = 2J + 1$ is a statistical weight, $\varepsilon(J)$ is the energy of the Jth sublevel and k is Boltzmann's constant. For the J = 19 state $\kappa(19) \sim \kappa(20) = 1/15$ at a temperature of 300 K.

In Eq. (7-5) we have normalized the vibrational populations by defining

$$D_2 = N_2/N_0 \text{ and } D_1 = N_1/N_0 \ , \qquad (7\text{-}7)$$

where N_0 is defined by the equation

$$N(t) = N_0(e^{-t/t_2} - e^{-t/t_1}) \ . \qquad (7\text{-}8)$$

The equation describing the rate at which the rotational population difference on a particular line J_0 returns to equilibrium is given by

$$\frac{\partial\delta^{J_0}}{\partial t} = - \frac{(\delta^{J_0} - (\kappa(J_0)D_2 - \kappa(J_0+1)D_1))}{\tau_R} \qquad (7\text{-}9)$$

We are now ready to introduce the full set of coupled non-linear amplifier density equations, following the notation of Ref. [89].

$$\frac{\partial D_2}{\partial t} = \frac{-EP}{2}\gamma_{\perp} - D_2/t_2 \qquad (7\text{-}10)$$

$$\frac{\partial D_1}{\partial t} = \frac{EP}{2}\gamma_\perp - D_1/t_1 \qquad (7\text{-}11)$$

$$\frac{\partial \delta^{Jo}}{\partial t} = \frac{-(\delta^{J_o} - (\kappa(J_o)D_2 - \kappa(J_o+1)D_1))}{\tau_R} - \gamma_\perp PE \qquad (7\text{-}12)$$

$$\frac{\partial P}{\partial t} = \gamma_\perp (\delta^{Jo}/\kappa(Jo))E - \gamma_\perp P \qquad (7\text{-}13)$$

$$c\,\frac{\partial E}{\partial x} + \frac{\partial E}{\partial t} = \gamma_\perp G_a P \qquad (7\text{-}14)$$

In these equations $\gamma_\perp = 1/T_2$, where T_2 is the dipole dephasing or phase interupt time, which, for a 2-level homogeneously broadened system such as CO_2, is related to the collision broadened linewidth $\Delta\nu$ by [94]

$$T_2 = \frac{1}{\pi\Delta\nu}\ . \qquad (7\text{-}15)$$

P is the amplitude of the polarization, c is the speed of light and G_a is related to the small-signal intensity gain coefficient (g_o) by

$$G_a = g_o c T_2/2\ . \qquad (7\text{-}16)$$

The two in the denominator of Eq. (7-16) indicates that G_a is appropriate to a field amplitude gain rather than an intensity gain. E is related to the amplitude of the electric field $\mathcal{E}$ by

$$E = \mu T_2/\hbar\,\mathcal{E}, \qquad (7\text{-}17)$$

where μ is the appropriate 2-level electric dipole moment. The value of $\mu T_2/\hbar$ is calculated in Appendix D. As well, the conversion from electric field amplitude to an absolute intensity, in W/cm^2, is outlined in Appendix D. Such a conversion allows a direct comparison between experimental and simulation generated pulse intensities.

The density equations are based on a semi-classical formalism of laser pulse propagation. The amplifying medium is treated quantum - mechanically by way of the time-dependent Schrödinger equation in which the perturbation component of the total Hamiltonian is $\tilde{P}E$, where $\tilde{P}$ is the dipole moment operator. The relaxation times t_1, t_2, τ_R and T_2 are inserted phenomenologically into the resulting equations in analogy to the Bloch equations in magnetic resonance.† The propagation of the electromagnetic radiation is treated using Maxwell's equations for a scalar, linearly polarized, real electric field given by

$$E(x,t) = \mathcal{E}(x,t) \cos (\omega t - kx) \tag{7-18}$$

The equations are simplified using the slowly varying envelope approximation (S.V.E.A.)* and the rotating wave approximation (R.W.A.).**

---

† Note that, even though the relaxation times were incorporated into the density equations in a similar manner to the Bloch equations for magnetic resonance, the equations should not be confused with those of Bloch since the Bloch equations are in fact rate equations. Equation (7-13), which describes the response of the medium to the incident electric field, is not present in the rate equation approach.

* The S.V.E.A. is valid if the propagation pulse duration is $< \omega_0^{-1}$, where ω_0 is the laser angular frequency. This condition is well satisfied for CO_2 lasers with pulse durations as short as 10 ps.

** The R.W.A. requires that $\omega_0 > T_2^{-1}$, which is satisfied even for 10 atm CO_2 laser pressures.

Numerical calculation of the propagation of the laser radiation in the laser cavity was accomplished by using the finite difference method. All calculations were performed on a CDC 6400 computer. The particulars of the method are outlined in Ref. [98] and in Appendix B. If the medium response is sufficiently fast to be considered steady-state with respect to changes in the radiation field, then the time dependence of Eq. (7-13) is removed. The polarization is then directly related to the electric field, via the level populations, by

$$P = (\delta^{J_0}/\kappa(J_0))E \ . \tag{7-19}$$

Substituting this expression for P in the density equations yields the set of rate equations

$$\frac{\partial D_2}{\partial t} = -\gamma_\perp I \delta^{J_0}/2\kappa(J_0) - D_2/t_2 \tag{7-20}$$

$$\frac{\partial D_1}{\partial t} = \gamma_\perp I \delta^{J_0}/2\kappa(J_0) - D_1/t_1 \tag{7-21}$$

$$\frac{\partial \delta^{J_0}}{\partial t} = \frac{-(\delta^{J_0} - (\kappa(J_0)D_2 - \kappa(J_0+1)D_1))}{\tau_R} \frac{-\gamma_\perp \delta^{J_0} I}{\kappa(J_0)} \tag{7-22}$$

$$c\frac{\partial I}{\partial x} + \frac{\partial I}{\partial t} = \frac{2\gamma_\perp G_a \delta^{J_0} I}{\kappa(J_0)} \tag{7-23}$$

The small-signal gain can be obtained from the time invariant solution of Eq. (7-23), evaluated at a time t,

$$\frac{c}{I}\frac{dI}{dx} = 2\gamma_\perp G_a \delta^{J_0}/\kappa(J_0) \ . \tag{7-24}$$

Substitution for $\gamma_\perp$ and G_a, and using the fact that at low radiation fluxes $\delta^{J_0}/\kappa(J_0)$ approaches $D_2(t) - D_1(t)$, results in the right hand side of Eq. (7-24) reducing to g(t), as expected.

(b) Saturable Absorber

Equations for the Ge absorber are much simpler than those for the amplifier since the absorber can be accurately described by a 2-level model with level recovery times that are considerably less than the shortest pulses possible from even a high pressure CO_2 laser* [19]. The absorber can therefore respond in a steady-state (cw) fashion over the entire incident pulse duration, i.e.,

$$\frac{1}{I}\frac{dI}{dx} = -\varepsilon(I)\alpha_0^B \, , \tag{7-25}$$

where α_0^B is the small-signal absorption coefficient (in cm^{-1}) and $\varepsilon(I)$ is a function which describes the absorber saturation behaviour. If the saturation response of Ge is homogeneous, as was first reported by A.F. Gibson et al. in 1972 [19], then

$$\varepsilon(I) = \frac{1}{1 + I/I_s^h} \, . \tag{7-26}$$

---

* Large intensity laser pulses are usually limited in durations to times $\sim T_2$ since the spectral width for pulses which are shorter than T_2 lie outside the gain bandwidth. The limiting duration is therefore reduced as the laser pressure is increased. At very high laser pressures ($\sim$10 atm) the CO_2 rotational lines overlap creating a very large effective gain bandwidth. In such cases, the absorber recovery time may not be much less than the laser pulse duration.

The parameter I_s^h is a homogeneous saturation parameter characteristic to Ge.* Equation (7-25) then becomes

$$\frac{1}{I}\frac{dI}{dx} = \frac{-\alpha_o^B}{1 + I/I_s^h} \tag{7-27}$$

or

$$(1 + I/I_s^h)\frac{dI}{I} = -\alpha_o^B\, dx\ . \tag{7-28}$$

Integrating the left hand side from I_{IN} (the input to the absorber) to I_{OUT} (the output intensity from the absorber) and the right hand side from zero to an absorber length L^B, results in

$$\ell n(I_{OUT}/I_{IN}) + \frac{I_{OUT} - I_{IN}}{I_s^h} = -\alpha_o L^B . \tag{7-29}$$

The quantities $\alpha_o L^B$ and I_s^h can be established from experiment and therefore I_{OUT} can be calculated if I_{IN} is known. The value of I_{IN} in the computer simulation is obtained from the instantaneous output electric field from the amplifier converted to an absolute intensity in W/cm^2 by Eq. (D-5). However, experimental work by F. Keilnmann (1976) [20], theoretical work by M. Sargeant III (1977) [99] and recent work reported by Los Alamos (June 1977) [100], indicate that the Ge saturation behaviour is in fact inhomogeneously broadened. In such a case the Ge atoms are characterised by a smooth distribution of resonant absorption frequencies rather than by a single frequency as in the homogeneous case. Consequently $\varepsilon(I)$ becomes

---

* The homogeneous saturation parameter can be expressed in terms of a 2-level absorption cross-section and a 2-level recovery time T_1 by $I_s = h\nu/\sigma T_1$.

$$\varepsilon(I) = \frac{1}{\sqrt{1 + I/I_s^i}} \tag{7-30}$$

Although the solution to Eq. (7-25) is now more complicated, it can still be obtained employing straightforward integration techniques. The resulting transcendental equation is

$$\ell n\left[\left(\frac{\sqrt{1 + I_{OUT}/I_s^i} - 1}{\sqrt{1 + I_{OUT}/I_s^i} + 1}\right)\left(\frac{\sqrt{1 + I_{IN}/I_s^i} + 1}{\sqrt{1 + I_{IN}/I_s^i} - 1}\right)\right] + 2\sqrt{1 + I_{OUT}/I_s^i}$$

$$- 2\sqrt{1 + I_{IN}/I_s^i} = -\alpha_0 L^B \tag{7-31}$$

This cumbersome looking equation can also be solved to give I_{OUT} once I_{IN}, I_s^i, $\alpha_0 L^B$ are known. Which saturation behaviour (homogeneous or inhomogeneous) is appropriate to the observed experimental results will be discussed in the next chapter.

The complete description of the laser system requires, in addition to the amplifier and absorber equations, the inclusion of two boundary conditions. As mentioned in the introduction to this chapter, the entire linear cavity loss is incorporated into the model as an effective mirror reflectivity. This reflectivity is comprised of two components. The first component is due to the linear loss (R^A) associated with the insertion of the aperture shown in Fig. 7-1; the second is associated with the transmission loss $(1-R^M)$ in the output mirror (M2) of Fig. 7-1. In addition, the ratio of the laser beam area at the amplifier compared to that at the absorber is incorporated directly into the pulse propagation model by the parameter m_0^2. The input intensity at the absorber is therefore related to the output intensity from the last slab of the amplifier by

$$I_{IN} \propto m_0^2 \, |E|^2 \, . \tag{7-32}$$

A m_0^2 value of unity corresponds to equal absorber and gain beam areas such as occurs in plane-plane mirror resonator geometries. Values of m_0^2 larger than unity corresponds to decreasing the diameter of the laser radiation at the absorber.

7.3 Noise Fluctuation Model

The noise fluctuation model has been discussed over the years by a number of authors [101,102]. A very good review of the subject is given in Ref. [103]. The noise fluctuation theory accounts for the production of ultrashort laser pulses, separated by the round-trip time 2L/c, by the selection and temporal shaping of fluctuations initially present as spontaneous emission noise in the laser. The build-up of short pulses from noise passes through four stages - linear amplification, non-linear absorption, non-linear gain, and finally a pulse decay stage.

(a) Linear Amplification Stage

In the linear stage of pulse development, fluctuations in intensity result from the interference of a large number (m_i) of axial laser modes having random phases. The absence of fixed phase relationships between axial modes results in a random intensity distribution of short pulses. The average number of such fluctuations in a round trip laser time 2L/c is the order of m_i, and the average fluctuation duration is given by

$$\ln(m_i)^{-1/2}(2L/c)/m_i \ , \tag{7-33}$$

provided $m_i > 1$ [102]* The intensity of these fluctuations can be obtained from the spontaneous emission calculation performed in Appendix E and are initially in the order of $\sim 10^{-11}$ W/cm^2. The linear gain region starts at the time t_0 shown in Fig. 7-2. Spontaneous radiation emitted at times earlier than t_0 will undergo an exponential decay given by

$$e^{-(\gamma - gLa)} \ , \tag{7-34}$$

where γ is the small-signal cavity loss. Radiation emitted well after t_0 cannot compete with radiation emitted at or near t_0 which has already undergone significant linear amplification. In this linear region, natural axial mode selection by the amplifying medium takes place because the collision-broadened Lorentzian gain spectrum gives preferential amplification to the modes near the centre of the gain profile. The mode selection causes the gain spectrum to narrow, which results in temporal broadening of the noise pulses. This broadening continues until the start of the non-linear absorption region at a time t_d. The broadening of noise pulses in N double passes of the amplifier, given by

---

* For a 1 atm CO_2 laser, $m_i \sim 43$. m_i must be large to enable the use of white noise (incoherent noise) statistics.

$$N = (t_d - t_0)/(2L/c) \, , \qquad (7\text{-}35)$$

is calculated in Appendix F. The calculation is performed for the largest intensity noise pulse, starting at t_0, and assumes that each noise pulse is statistically independent. The initial noise pulse and the medium gain are assumed to have Gaussian frequency distributions in order to simplify the calculation. The loss frequency variation is assumed flat over the gain bandwidth, which is in fact the case for germanium.* The calculation outlined in Appendix F was performed for the particular case in which the amplifier gain (g) was a constant as a function of time. The resulting pulse broadening expression appropriate to CO_2 amplifiers is given by

$$t_p(\mathrm{FWHM}) = T_2\sqrt{8\ell n2 g L_a N} \, . \qquad (7\text{-}36)$$

Notice that this expression is independent of the initial duration of the noise fluctuation. The final duration depends on the gain bandwidth through T_2, the small-signal single-pass intensity gain coefficient (gL_a), and the number of round trips (N) through the amplifier. N is a function of the gain and linear loss and is a measure of how close lasing operation is to threshold. The above expression can be generalized to account for the contribution due to the initial noise fluctuation duration ($\Delta t_{f\ell}$) and a 2-level time-dependent gain g(t) (Eq. (7-2)) by iterating the following expression, for the broadening due to the n^{th} double pass in the amplifier, until n = N.

---

* The effective absorption frequency width in germanium may be greater than 100 cm^{-1}. Note however that if the loss distribution had a similar shape and width to that of the gain medium and was centered at the same frequency, then it should be possible to prevent or at least to minimize pulse broadening.

$$t_p(\mathrm{FWHM}(n)) = \sqrt{8\ell n2 g_n(t) L_a T_2^2 + 2\ell n2 \Delta t_{f\ell}^2} \qquad (7\text{-}37)$$

In most cases this expression agrees with Eq. (7-36) to within 15% because the gain profile for most of the N passes is basically flat.

At the end of the linear amplification stage the number of axial modes decreases due to the process of natural mode selection. If the number of axial modes (m_f) at time t_d is sufficiently reduced, such that only one pulse can occupy the 2L/c cavity round trip time, then the transient evolution of passive mode-locking becomes deterministic rather than statistical. A theory for the deterministic evolution of mode-locked pulses has been outlined by C.P. Ausschnitt in June 1977 [105], Note that "deterministic" implies that a single pulse per 2L/c transit time has evolved well before substantial absorber and gain saturation occur. The non-linear gain and absorber regions primarily serve to determine the temporal pulse shape and the growth of the pulse intensity. Roughly speaking,a mode-locking system can be considered to be deterministic if the pulse spectral width, given by $1/\pi t_p$, is less than or equal to the axial mode separation (c/2L) at initial pulse durations t_p, as can exist in high gain lasers operating very close to threshold (large N), at low laser gas pressures (long T_2), and for short cavity lengths (L). In summary, there is a strong possibility of observing deterministic mode-locking when the laser is close to producing a single longitudinal mode output. However, calculations of the pulse broadening, for a 1 atm CO_2 laser, indicate that there will be 2, and possibly 3, pulses per 2L/c time at the start of the non-linear absorption region and therefore deterministic mode-locking is not expected to occur. Experimental observations of deterministic mode-locking will be given in the next chapter.

(b) Non-Linear Gain and Absorption Regions

In this region the noise fluctuation intensities are sufficiently high to start saturating the absorber and gain media. The degree of absorber saturation, which is determined by the ratio of the instantaneous fluctuation intensity to the absorber saturation parameter (I_s), can be calculated using Eqs. 7-29 and 7-31 for a homogeneously and inhomogeneously broadened saturable absorber, respectively. It follows that large intensity pulses incident on the Ge will see less absorption and therefore a greater net amplification per round trip, than low intensity pulses. Calculations performed using both homogeneous (7-29) and inhomogeneous saturation equations, (7-31) indicate that the discrimination between two nearly equal pulses, on a single pass through the Ge, is greatest if $I \sim I_s$. For example, when $\alpha_0 L^B = 0.8$ and $I_2/I_1 = 0.8$ in a homogeneous absorber, the transmission ratio of the largest to the second largest pulse is $\sim$1.04 at $I_1 = I_s$, 1.01 at $I_1 = 0.1\ I_s$ and 1.02 at $I_1 = 10\ I_s$. It is therefore beneficial, for good mode-locking, to hold the pulse intensity down to $I \sim I_s$ for as many round trips as possible.

There can be an interplay between the absorber and gain saturation if the cavity, and gain and loss parameters,are suitably chosen. When a large intensity pulse saturates the absorber, the cavity loss for that pulse is reduced. However,the gain may start to saturate due to this and other pulses in such a way as to keep the laser close to threshold for the large intensity pulses. Under such conditions pulses of low intensity decay rather than grow in intensity. Eventually the largest pulse is of sufficient intensity to significantly saturate both the absorber and the gain medium. Then the pulse intensity rises dramatically and the laser output is both Q-switched and mode-locked. Since the saturation of the gain medium will be a function of the number of propagating pulses per round trip time, a realistic value for this number is always used for the starting pulse distribution.

(c) Pulse Decay Region

In this region the population inversion has been significantly depleted and the pulse intensity has already reached its maximum value. The intensity then decays with a decay time that depends on the amount of residual gain present in the cavity and on the non-linear and linear cavity losses. The decaying pulses can still saturate the non-linear absorption, and further pulse discrimination is still possible. The discrimination can be substantial since the mode-locked pulse trains usually possess fall times which are much longer than the risetimes, thus affording a greater number of passes through the absorber.

Thus far we have mentioned the saturable absorber's ability to discriminate against all but the most intense noise pulses. However, since we are dealing with a fast recovery time absorber (a few ps for Ge), the absorber acts in a similar fashion over an individual pulse duration as it does to a distribution of noise pulses. That is to say low intensity portions of an individual mode-locked pulse see greater absorption than intensities at the pulse peak. This results in a symmetric narrowing of the overall pulse. It is therefore not surprising that we should find significant pulse narrowing, as well as pulse discrimination, across the mode-locked pulse train.

7.4 Summary

This chapter has outlined a model for the quantitative prediction of the passive mode-locking behaviour of a CO_2 laser containing a Ge saturable absorber. The particular features of this theoretical mode-locking treatment are:

(a) The model can be used without alteration to describe a TE CO_2 laser and any fast saturable absorber, provided that the effective absorption linewidth is considerably greater than the gain linewidth.

(b) The mode-locking analysis is appropriate to a regular (non-ring) laser cavity, but it does not allow for standing-wave effects.

(c) Amplifer density equations, rather than rate equations, allow us to treat the case where the pulse duration approaches the T_2 time. Furthermore, the model can easily be adopted for analysis of CO_2 injection-locking systems (with or without a saturable absorber)

[106].

(d) A 2-level homogeneously broadened time dependent gain g(t), which accurately describes the CO_2 gain temporal profile, in incorporated into the model.

(e) The model includes rotational coupling effects in the amplifier.

(f) Although the mode-locking occurs on only one rotational line, the model can be generalized to multi-line and even multi-band operation with careful gain bookkeeping.

(g) The non-linear and linear losses are treated in a straightforward and easily adjustable manner.

(h) The model can accomodate either a homogeneous or inhomogeneous 2-level steady-state treatment for the saturable absorber.

(i) The mode-locking simulation incorporates a parameter m_0^2 which allows variation in the ratio of the beam area at the amplifier relative to that of the absorber. This condition is very often necessary experimentally to allow the gain and absorber media to saturate at similar intensities.

(j) The number of starting pulses and pulse durations can be obtained directly from noise statistics and from a temporal broadening calculation in the linear gain region.

This chapter also discussed the four stages of pulse evolution: linear amplification, non-linear absorption, non-linear gain, and pulse decay. The conditions under which "deterministic" mode-locking might occur were also outlined in this chapter. The next chapter will deal with actual experiments performed with Ge to determine the basic absorber parameter values, followed by a comparison of theoretical and experimental mode-locking data.

CHAPTER 8

INVESTIGATION OF PASSIVE MODE-LOCKING USING A GERMANIUM SATURABLE ABSORBER - PART II

8.1 Introduction

The previous chapter outlined the theoretical treatment for the generation of short pulses, starting from noise, and on through the various stages of mode-locked pulse development. In this chapter measurements of the model parameters are reported. This chapter also provides a detailed comparison between theory and experimental measurements of Ge mode-locking.

Experiments with a TEA CO_2 laser, employing Ge at the Brewster angle, are reported in Section 8.2. These experiments provide values for the small-signal absorption ($\alpha_0 L^B$), the saturation parameter (I_s), and the beam area parameter (m_0^2). The latter quantity was obtained from experiments using a 3-mirror cavity similar to that described in Chapter 2. The observations of mode-locking experiments, employing anti-reflection (AR) coated Ge in a 1 atm laser utilizing a simple 2-mirror cavity, are reported in Section 8.3. These results are compared to theoretical predictions in order to assess the relative importance of varying parameters such as m_0^2 (Section 8.5), rotational coupling time τ_R (Section 8.6), gain above lasing threshold (Section 8.7), linear loss (Section 8.8), and non-linear loss (Section 8.9) in the production of short pulses. Section 8.10 demonstrates both the scaling of the theoretical parameters with pressure and the importance of noise statistics in the mode-locking of a 5 atm TE CO_2 laser. The computer simulations performed for the 5 atm laser also help to demonstrate the importance of the parameter m_0^2 in obtaining stable mode-locked pulse generation at high CO_2 laser pressures. Section 8.11 describes the pressure dependence of the mode-locked intensity, the energy, and the parameter m_0^2. In Section 8.12 it is shown that there should be some advantage in employing a short laser cavity for mode-locking. Finally, Section 8.13 compares the mode-locking properties of SF_6 and Ge.

8.2 Brewster Angle Experiments

The following experiments were carried out using p-type gallium-doped single crystal, germanium.* Ge possesses an index of refraction of 4.0 at the 10.4 μm band [107]. The corresponding Brewster angle is 76°. Alignment of the germanium at this angle, either inside or outside the laser cavity, was relatively simple because the Ge was parallel to within a 10.4 μm wavelength. Consequently, wedge and lens effects were insignificant in spite of the high refractive index for Ge. A relatively serious problem was damage to the Ge surfaces caused by high intensity laser pulses. Attempts made by us to polish the commercially obtained Ge, using standard polishing and chemical etching techniques met with only moderate success. It soon became apparent that to avoid surface damage to the Ge at intensities near $I = I_s$, a sub-micron finish was required over the entire active crystal surface. This had to be done commercially (by Interoptics). Subsequently, care was taken to keep the Ge surfaces clean to prevent the formation of oxide coatings and the deposition of particulate matter or grease on the Ge surface.

---

* The Ge was typically 5 cm long by 1.5 cm wide.

The absorption of Ge in the neighbourhood of 10.4 μm is very nearly constant with wavelength [108]. The absorption coefficient α_0^B for p-type Ge is a function of the resistivity ρ, and therefore of the doping concentration. An approximate relationship between α_0^B and ρ, obtained from Capron et al. [107], is $\alpha_0^B \rho \sim 2.3\ \Omega$. Greater absorption in p-type Ge is therefore obtained by decreasing the resistivity (i.e., increasing the doping concentrations). Phonon absorption (lattice vibrations) and absorption by electrons and holes constitute the total absorption. The contribution due to phonons is independent of the sample resistivity and has been estimated to have the value 0.013 cm^{-1} [109]. This value is negligible compared to the total absorption for the resistivities employed in this work. Electron absorption contributes $\sim$0.01 cm^{-1} at these resistivities. Therefore, the absorption at 10.4 μm is primarily due to holes, specifically involving a transition from the heavy to the light hole band in Ge.

(a) Small-Signal Absorption

The small-signal absorptions were measured using an unfocussed helical laser beam which was incident at the Brewster angle on polished Ge. The transmitted beam was detected by a photon-drag detector and observed with an oscilloscope (Tektronix 547). Ge possesses a large saturation parameter [19]. Therefore typical helical output laser intensities of 50 to 100 kW/cm^2 could be used and still be considered in the small-signal intensity regime. The values for $\alpha_0 L^B$, obtained for the 3 Ω-cm Ge employed in the experiments described in Section 8.3, were 0.69 ± 0.02 and 0.36 ± 0.01 for 0.85 and 0.49 cm thicknesses, respectively. It was also ascertained that the value of $\alpha_0 L^B$ varied by less than 5% over the entire crystal length.

(b) High-Signal Absorption

In this section results of measurements of the germanium saturation parameter (I_S) are given. This was a rather difficult experiment to perform since the large input intensities necessary to significantly saturate $\alpha_0 L^B$ frequently led to Ge damage. The possibility of damage was reduced by employing very good optical finishes on the Ge samples. As well, a train of mode-locked pulses,* rather than a conventional non-mode-locked laser, was used to probe the Ge. The mode-locked operation allowed high peak intensities while keeping the total pulse train energy lower than what would be needed to obtain a similar non-mode-locked laser intensity. The mode-locked pulse train provided another advantage. On a single passage through the Ge the variable set of input intensities allowed the simultaneous measurement of $\sim$10 pulse transmissions. The increased data improved the accuracy of the saturation parameter measurements. The experiment was performed with a 0.35

---

* A mode-locked pulse train can be used as a probe since the Ge obsorber can fully recover in a time much less than the round trip time.

cm piece of 0.7 Ω-cm Ge. The Ge was mounted at Brewster's angle to the incident laser beam since etalon effects and corrections due to Fresnel reflections made interpretation of transmission data for Ge oriented at ∿90° to the laser beam ambiguous. Unfortuantely, the 76° Brewster angle reduced the intensity of the laser beam at the tilted Ge surface relative to the input beam intensity by a factor of 4. Consequently, to obtain intensities of 25 MW/cm^2 at the Ge surface, beam intensities of 100 MW/cm^2 were needed. These high intensities were achieved by using a 25 cm focal length Ge lens to concentrate a 2 MW/cm^2* train of 3 ns pulses, obtained from an SF_6 helical laser, mode-locking configuration, which operated on the P(20), 10.4 μm CO_2 rotational line. The transmitted pulse train was detected by a calibrated** photon-drag detector situated in the diverging portion of the lens to avoid detector saturation effects. Since it was only possible to accurately obtain intensities of up to 25 MW/cm^2 at the tilted Ge surface, it could not be determined whether the absorption saturation was homogeneously (Eq. (7-29)) or inhomogeneously (Eq. (7-31)) broadened.† Figure 8-1 shows the plot of $\ell n(I_{IN}/I_{OUT})$ against $I_{IN}-I_{OUT}$, in MW/cm^2. The data falls on a straight line whose intercept represents the small-

---

* The intensity refers to the peak intensity of the mode-locked pulse train.

** The calibration procedure for the conversion of the oxcilloscope signal in volts to an intensity in MW/cm^2 has been outlined in Section 2.5.

† This is because one needs > 20 MW/cm^2 to observe a significant difference (> 10%) in transmission for the two cases.

Fig. 8-1

Plot of $\ell n\ (I_{IN}/I_{OUT})$ as a function of, $I_{IN} - I_{OUT}$. The solid line is the best fit to the data.

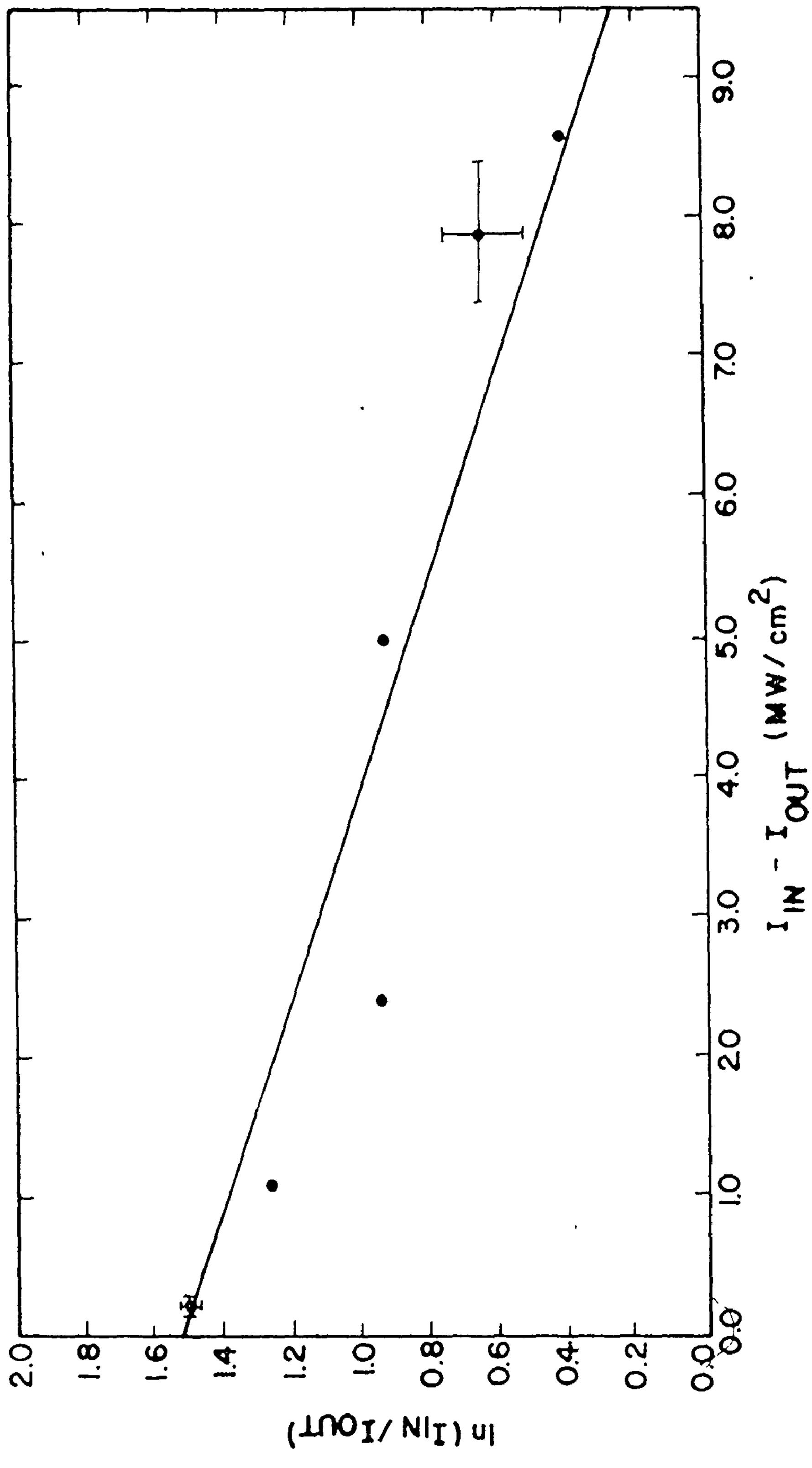
ln (I_{IN} / I_{OUT})
0.0
0.2
0.4
0.6
0.8
1.0
1.2
1.4
1.6
1.8
2.0
0.0
1.0
2.0
3.0
4.0
5.0
6.0
7.0
8.0
9.0
$I_{IN} - I_{OUT}$ (MW/cm^2)

signal absorption coefficient. The value of I_s^h obtained from the negative increase of the slope was 8 ± 2.5 MW/cm^2 (this is equivalent to an $I_s^i \sim 3.2$ MW/cm^2). This value is in good agreement with the value recently obtained at Los Alamos [100]. The uncertainty quoted in the saturation parameter reflects the uncertainty of obtaining the slope in Fig. 8-1. A similar saturation parameter (within experimental error) has been obtained for a 0.85 cm long, 3 Ω-cm piece of Ge, in agreement with the observations of A.F. Gibson et al. that the saturation parameter is not strongly dependent on the doping concentration [19].

(c) 3-Mirror Cavity Experiments

A set of measurements to determine the importance of the parameter m_0^2 were performed with the double-discharge lasers in the 3-mirror cavity shown in Fig. 2-7. The Ge, mounted at the Brewster angle could be moved away from M1 into the beam waist (ωo) while keeping all other parameters constant. It was observed that moving towards the beam waist resulted in a transition from a low intensity non-mode-locked output-state to a progressively higher intensity mode-locked state. The time delay between the peak of the current pulse and the rise of the laser pulse (t_d) changed by less than 100 ns under such a transition, consistent with the non-linear region being very short compared to the linear gain build-up region. Moving the Ge closer to the beam waist slowly increased the peak output intensity, rather than causing a dramatic switching effect as was observed when SF_6 was used as a saturable absorber (Chapter 6). Moving the germanium further into the beam waist resulted in surface damage. The parameter m_0^2 was measured by using internal variable apertures placed at various positions in the 3-mirror cavity and adjusted to just stop the lasing action of a low gain oscillator (i.e.,operated very close to threshold). The measurement of the beam diameters could quite accurately be used to obtain beam area ratios (m_0^2) for various positions in the laser cavity. The value of m_0^2 which resulted in the transition to mode-locking was ∿3.5.* The optimum mode-locking region was obtained for m_0^2 in the range 6 to 8 while the onset of damage occured for $m_0^2 > 12$. These experiments demonstrated that a minimum value of m_0^2 was necessary to saturate the absorber and obtain stable mode-locking. However, due to the onset of damage it could not be conclusively determined if there existed a maximum value of m_0^2 above which stable mode-locking could not be achieved.

In these experiments it was further observed that a large percentage of the mode-locked pulse trains contained 2 pulses per round trip rather than the expected single pulse. The second pulse, usually of slightly lower intensity,occured even with optimization of the laser parameters. It was noted that the second pulse was separated from the first by a time equal to 2d/c, where d was the distance of the Ge to mirror M1. Moving the Ge to the opposite side of the beam waist, but with the same m_0^2, gave a pulse separation in agreement with the increased value of d. It was therefore concluded that interference effects between noise pulses travelling in opposite directions through the Ge,in such a way that their overlapped intensities resulted in a smaller absorption coefficient than that would be obtained by independent passage through the Ge made two pulses production more likely. Double-pulses have been predicted theoretically [110] and observed experimentally for Nd:Glass lasers, [7] and for other laser systems [111]. The observation of double-pulses is of special significance since the theoretical model does not account for such interference effects. This will be discussed further in Section 8.5.

---

* The area at the absorber is the area of the elliptical beam cross-section at the front surface of the Brewster angled Ge.

8.3 2-Mirror Cavity Experiments

These experiments were conducted with 1 atm double-discharge laser tubes in the 2-mirror cavity shown in Fig. 7-1. The AR coated Ge was placed at 90° to the laser axis, and near M2. The laser cavity was composed of a 1.9 m radius of curvature gold mirror (M1, 98% reflecting) and a 10% transmitting Ge flat (M2). An aperture situated near M1 ensured operation in the TEM_{00} mode, while the oscillating wavelength (with the Ge present in the cavity) was determined,by using an optical spectrum analyzer,to be the P(20) line of the 10.4 μm CO_2 band.

The procedure for mode-locking proved to be quite straightforward. The AR coated Ge possessed no significant wedges and could simply be placed, to within a degree or two in alignment, in front of M2 without having to retune the laser cavity. The laser gas concentrations and voltage settings were chosen to just obtain lasing.* Fine adjustments to the power supply voltage and to the resonator aperture were made to obtain stable, clean, mode-locked pulses. The term "stable" refers to the shot-to-shot variation in intensity of the peak pulse in a mode-locked pulse train, while "clean" pulses refers to the contrast ratio or discrimination (D) between the largest pulse to the second largest pulse in the 2L/c time window around the peak intensity pulse. These terms will always be employed in this context. The mode-locked pulses were detected using a calibrated (∿50 Ω impedance) photon-drag detector and a fast risetime oscilloscope (Tektronix 7904). The risetime of the oscilloscope (10%-90% points) was measured to be 625 ± 25 ps using a 0.1 ns risetime calibration step generator (Tektronix 519). The risetime of the detector (<200 ps) is estimated to be much less than that of the oscilloscope so that the overall detection risetime is less than ∿650 ps.

---

* The laser parameters were also chosen to ensure that the laser operated in a very stable discharge region.

It was determined from preliminary experiments with the 2-mirror AR coated Ge system that very stable ($\lesssim$ 10% variation in peak intensity) and clean (D > 50)* mode-locked pulses could be obtained, over a wide range of laser and cavity parameters, on over 90% of the laser discharges. Pulse narrowing across the mode-locked pulse train was also observed for a wide range of mode-locking conditions. The mode-locked train energies were substantially less (factor of 3 to 4) than energies observed under similar conditions with SF_6 mode-locking. Finally there was a trend to slightly narrower (15 to 20%) pulses as the distance of the Ge to M2 was reduced from 5 cm to 0.5 cm. This last observation is consistent with previously mentioned interference effects observed in the 3-mirror Brewster angle experiments (Section 8-2(c)) However, in this case the mode-locked pulse reflects from M2 and overlaps with itself rather than with a discrete second pulse. If the 2d/c separation is comparable to the pulse risetime then the peak of the pulse may, for example,overlap with its tail. In such a case the saturable absorber transmission of the tail is enhanced relative to that of the pulse peak. In all the following 2-mirror experiments the Ge was placed as close ($\sim$0.5 cm) to the end mirror M2 as possible to minimize any pulse broadening effects.*

---

* This value represents a lower limit since the measurement is limited by noise pick-up.

8.4 Initial Conditions for the Comparison of Theory and Experiment

Sections 8.4 to 8.9 deal with the 2-mirror AR coated Ge experiments in which the laser gain, linear and non-linear losses and m_0^2 parameter are varied in a systematic fashion to allow comparison with theory. The quantities measured in the experiments were the pulse train output intensities and temporal shapes; the individual pulse durations across the pulse train; pulse stability,and pulse discrimination. The mode-locking parameters were obtained as follows.

(a) Experimental Initial Conditions

As outlined previously the m_0^2 values were obtained by using suitably placed apertures in the cavity to just stop lasing action when the laser was operated near threshold. The value of m_0^2 was varied by changing the 2-mirror cavity length. A length of 1.71 m gave an experimental m_0^2 of 4.5, wile a 1.81 m cavity gave an m_0^2 of 12. By replacing the 1.9 m radius of curvature gold-coated mirror with a 3.4 m one an m_0^2 of 2.2 was obtained with a 1.71 m cavity.

---

* The optical distance from the center of the Ge to M2 was 2.5 cm. This resulted in a 2d/c of 160 ps, which is significantly less than the detection risetime.

The non-linear losses $\alpha_0 L^B$, which will be used in Section 8.9, were measured in Section 8.2 to be 0.69 ± 0.02 and 0.36 ± 0.01 for 0.85 and 0.49 cm thickness of Ge, respectively. The laser gain for the mode-locking experiments was measured using an in-cavity attenuation technique [95]. The procedure involved inserting an accurately known loss (γ) into the laser cavity which would just extinguish laser oscillation. The small-signal insertion loss was comprised of the Ge absorber loss, the transmission loss at mirror M2, plus some small loss due to the Nacl laser tube windows and the gold mirror M1 (a few %). The technique was particularily appropriate for obtaining the gain since the mode-locking process also occured near lasing threshold and involved the same insertion loss. The laser gain was then obtained from the insertion loss value. The gain measured in this manner had to be corrected for the fact that the temporal gain profile (Fig. 7-2) was not constant and that the maximum gain, g_{max}, was greater than the insertion loss value. The correction involved find the suitable g_{max} which when inserted into Eq. (7-2), gave the correct growth in intensity from the initial spontaneous flux ($I_i \sim 10^{-11}$ W/cm^2,[Appendix E]) to a final intensity appropriate to the start of the non-linear absorber region

($I_f \sim 10^4$ W/cm^2) in N round trips,* i.e.,

$$I_f/I_i = \prod_{n=1}^{N} e^{[g(t_0 + n(2L/c))L_a - \gamma]} \sim 10^{15} \qquad (8\text{-}1)$$

The correction factor was usually 5-15%.** The g_{max} values obtained in this way were in good agreement (to within 15%) with the values predicted from the oscillator-amplifier gain measurements reported in Section 2.2 (c). All the gain measurements, reported in Section 8.7, were obtained in a region where the small-signal gain was directly proportional to the input electrical energy to the discharge (Fig. 2-6). As expected, ratios of the squares of the applied voltages for two lasing conditions gave a very good estimate of the corresponding gain ratios. Once the gain at a given voltage has been measured using the attenuation technique, gains close to this value were derived from the power supply voltage settings.

The values for the linear loss due to the insertion of an aperture near M1 were also obtained using the attenuator technique (measured with and without the aperture in the cavity).

(b) Theoretical Initial Conditions

Once the laser pressure and gas concentrations are known the gain bandwidth, and therefore the T_2 time, can be calculated using the expression given by Robinson [95].

---

* N was obtained from the maximum time delay for which lasing action was just observed.

** Since g is obtained from the natural logarithm of I_f/I_i it is not sensitive to the values of I_f and I_i.

$$\Delta\nu(\mathrm{FWHM}) = \frac{2C_{CO_2}}{(8\pi kT)^{1/2}}\left[P_{CO_2} + \frac{P_{He}}{1.69} + \frac{P_{N2}}{1.33}\right], \qquad (8\text{-}2)$$

where C_{CO_2} is a constant appropriate to CO_2 and is related to the optical broadening cross-section, P_i is the partial pressure of gas (i), T is the discharge gas temperature, and k is Boltzmann's constant. The total gas pressure for the experiments was 1 atm, while a typical gas concentration used was 85% He, 5% N_2, 10% CO_2. The discharge temperature was estimated at ∿320 K in accordance with the findings of Ref. [112]. Substitution of these values into Eq. 8-2 yields a value for $\Delta\nu$ of 3.76×10^9 Hz. The value of T_2 can then be obtained using Eq. (7-15), and is 0.085 ns.*

The average number of noise pulses (m_i) generated in a round trip about t_0 can be found by dividing the gain bandwidth $\Delta\nu$ by the axial mode separation c/2L. For a 1 atm laser with L = 1.71 m, c/2L = 0.88×10^8 Hz, and using a $\Delta\nu$ of 3.7×10^9 Hz, one obtains an m_i of 43. The initial fluctuation duration $\Delta t_{f\ell}$, given by Eq. (7-33), turns out to be 2.2×10^{-10}s, provided that $m_i \gg 1$. Knowledge of T_2, $\Delta t_{f\ell}$, the intensity gain coefficient $g_{max}La$, the number of round trips N, and use of Eq. (7-36), allows one to calculate the pulse duration just before the onset of the non-linear gain and absorber regions. The value obtained is ∿2.4 ns. This duration corresponds to a spectral width of 1.3×10^8 Hz which very nearly approaches 2 axial mode separations. At this point one can, in principle, calculate the statistical distribution of the random intensity noise pulses and obtain information, such as the ratio of the second largest pulse intensity I_2 to the largest intensity I_1, to obtain mode-locking within certain confidence limits. However, to perform such an analysis the number of pulses per round trip (m_f) must be large* to approach a white noise distribution [102]. Since the starting distribution for a 1 atm laser consists of 2, or possibly 3, starting fluctuations per round trip, such an analysis cannot be performed. It was therefore decided to run the mode-locking computer simulation with 2 input pulses per round trip time and with a high** starting intensity ratio of $I_2/I_1 = 0.6$. This high ratio allows the identification of a set of mode-locked parameters which will produce stable, clean mode-locking largely independent of the starting input pulse intensity ratios from one mode-locked train to another.

---

* Since the calculated T_2 values for other gas concentrations and discharge gas temperatures used in the experiments were within 3% of each other only one value of T_2 was used in the computer simulations.

Three further observations were made concerning the theoretical starting pulse distribution. The development of clean and stable mode-locked pulses was largely independent of the time separation between the starting pulses, since the separations were always much greater than the rotational recovery time and absorber recovery time. Secondly, the order of the pulses did turn out to be of some importance. The pulse which was propagated into the amplifier first always experienced more gain than the trailing pulse. The effect could be significant when the first pulse reached a sufficient intensity to reduce the gain in a few round trips. In high gain amplifiers this effect can actually cause significant pulse shaping over the pulse duration itself. However in our simulations the effect led only to an increase (x2) in pulse discrimination over the pulse train if the largest intensity pulse was fed first into the gain medium. This discrimination is much smaller than that typically achieved by the saturable absorber (10^2 to 10^4). Furthermore, pulse shaping effects due to the order of the input pulses amounted to <10% changes in the pulse FWHM, compared to factors of 5 to 10 in narrowing due to the Ge absorber. For consistency, the largest pulse was fed second into the amplifier in all the simulations performed in this chapter.

---

* M_f may actually be as low as 5 for a reasonable approximation to a white noise statistical distribution [113].

** It will be shown in Section 8.10 that the probability of observing two pulses with intensity ratios ≥ 0.6 (on the rise of the pulse train) was small (∿10%).

The third observation was that the final pulse intensities generated by the model were very insensitive to the starting intensities at t_d. This proved useful since these intensities could not accurately be predicted due to the large uncertainties in calculating the intensity of spontaneous emission at t_0. The starting intensities used ($\sim$10 kW/cm^2). were typically 1/500 of the Ge saturation intensity.

8.5 Influence of the Beam Area Parameter (m_0^2) on Mode-Locking

In the following sections the theoretical predictions of mode-locking are compared to experimental data where possible. The theoretical predictions are given over a much wider intensity range than can accurately be measured experimentally and thus the region for which experimental and theoretical predictions can be compared is somewhat restricted. For example, experimental observations in regions where the laser intensity causes damage to the AR coatings is prohibited.

Fig. 8-2 shows the theoretical predictions for the output intensity (at M2, Fig. 7-1), of the largest pulse of the 2 input pulses, as a function of the number of round trips from the starting time t_d and for three different m_0^2 parameters. The curves are continuous for appearance sake, since each round trip contributes one intensity data point to the curve. The intensity of the second pulse is not included in these curves. However, the effectiveness of the pulse discrimination is indicated by using the parameter D defined previously. The values for the other laser and cavity parameters for these three curves are outlined in Table 8-1. Notice that the output intensities for the three m_0^2 parameters at low round trip numbers are different since the reduction in the beam area at the absorber also increases the output intensity just outside mirror M2.

The $m_0^2 = 4.5$ curve illustrates the inability of the laser intensity to significantly saturate the absorber. At higher m_0^2 values there is a progression to very fast changes in intensity risetimes. It was found that the discrimination parameter, measured at the output peak intensity of each mode-locked pulse train, is actually optimum for the $m_0^2 = 9.0$ case (D = 60) compared to the $m_0^2 = 18.0$ case (D = 6.0) and the $m_0^2 = 4.5$ case (D = 5.0). The poorer discrimination at high m_0^2 (i.e., laser cavities which focus the laser radiation at the absorber) is due to the fewer number of passes in the absorber. As well, the large majority of the passes are at intensities much higher than the absorber saturation parameter I_s, resulting in less than the optimum

Fig. 8-2

Variation of the theoretical output peak intensity as a function of the number of round trips for different m_0^2 values indicated in the figure.

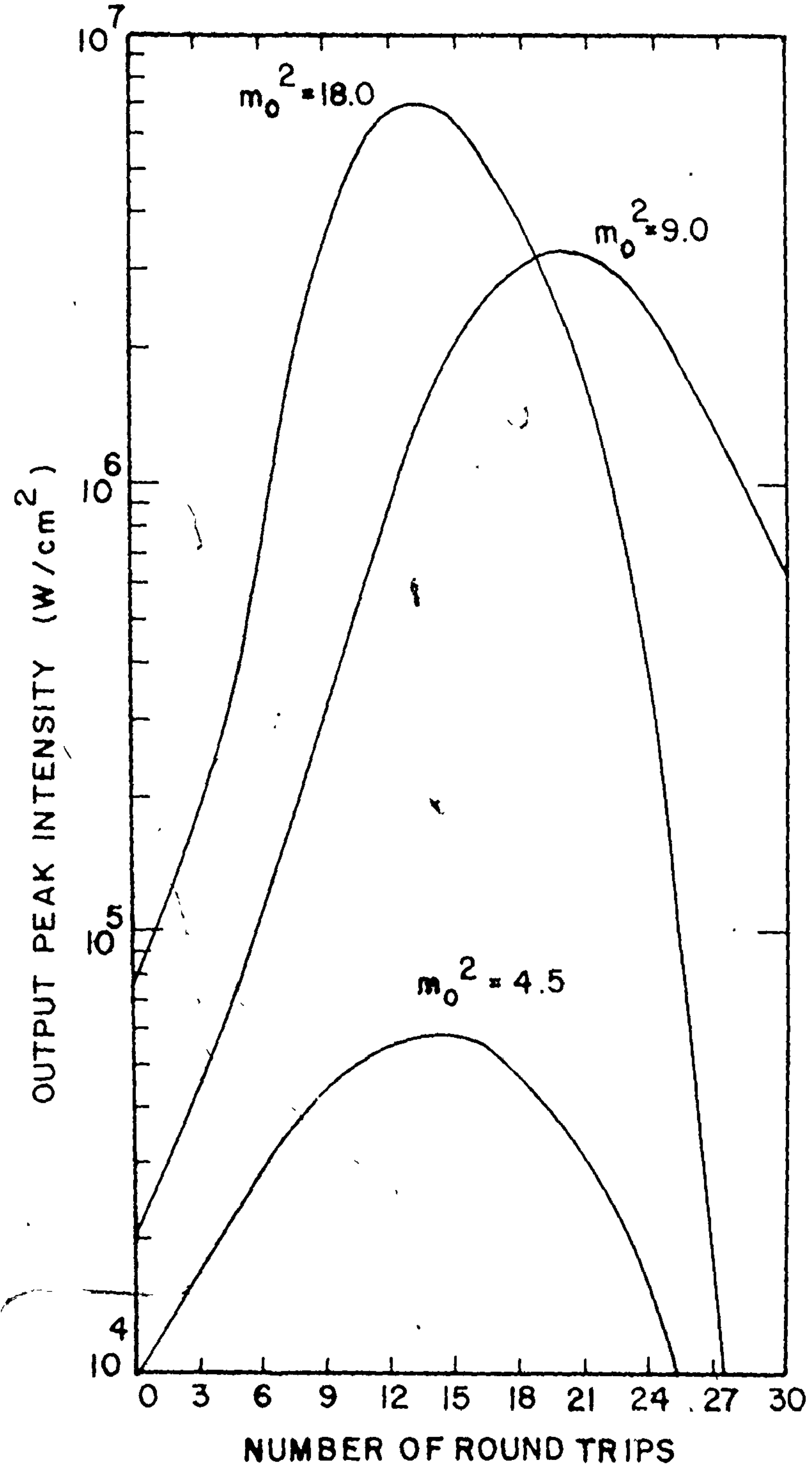
$m_0^2 = 18.0$
$m_0^2 = 9.0$
$m_0^2 = 4.5$
10^7
10^6
10^5
10^4
OUTPUT PEAK INTENSITY (W/cm^2)
0
3
6
9
12
15
18
21
24
27
30
NUMBER OF ROUND TRIPS

TABLE 8-1

Mode-Locking Parameters

L	1.71 m
$2L/c$	11.4 ns
R^M	0.87
R^A	0.88
$\alpha_o L^B$	0.69
$g_{max} L^a$	0.99
t_d	2.5 μs
t_1	0.4 μs
t_2	10.0 μs
τ_R	0.2 ns
T_2	0.085 ns

discrimination per pass. Experimentally, an m_0^2 parameter of 4.5 gave better agreement with the theoretical predictions employing $m_0^2 = 9.0$. The discrepancy of a factor of 2 may result from the fact that the pulse overlap mechanism mentioned in Section 8.3(c) creates effectively higher intensities in the Ge (equivalent to a x 2 change in m_0^2).* An m_0^2 of 9.0 produced experimental mode-locking of somewhat poorer stability than that observed for the $m_0^2 = 4.5$ value and also resulted in damage to the AR coatings after 10 to 30 laser "shots". An experiment with $m_0^2 = 2.2$ produced low intensity pulse trains similar to the theoretical $m_0^2 = 4.5$ predictions. It should be emphasized that these m_0^2 curves were all obtained using the same gain, and linear and non-linear losses. Increasing the gain, from that given in Table 8-1 for the $m_0^2 = 2.2$ cavity, caused significant saturation of the absorber, with a subsequent large increase in the observed output pulse intensity. However, increasing the gain from threshold to allow saturation of the absorber also resulted in poorer discrimination and eratic pulse intensities.

Figure 8-3 shows the pulse narrowing with round trip number (N) for the three cases described above. The arrows indicate the round trip number at which the peak intensity of the mode-locked train occurs. For both $m_0^2 = 9.0$ and 18.0 the pulse narrowing reaches durations which are the order of the rotational relaxation time $\tau_R \sim 0.2$ ns. There is, however,

---

* The time averaged intensity due to standing waves in the Ge gives a factor of 2 over the sum of single independent travelling wave intensities. In future sections, unless stated otherwise, we shall refer to experimental values of m_0^2 whenever the m_0^2 parameter is used.

Fig. 8-3

Comparison of theoretical and experimental pulse narrowing (FWHM) as a function of the number of round trips for different m_0^2 values. The (x), (●) denote experimental data points for m_0^2 of 2.2 and 4.5, respectively. The arrows indicate the round trip numbers at which the output intensity peaks for each of the m_0^2 values.

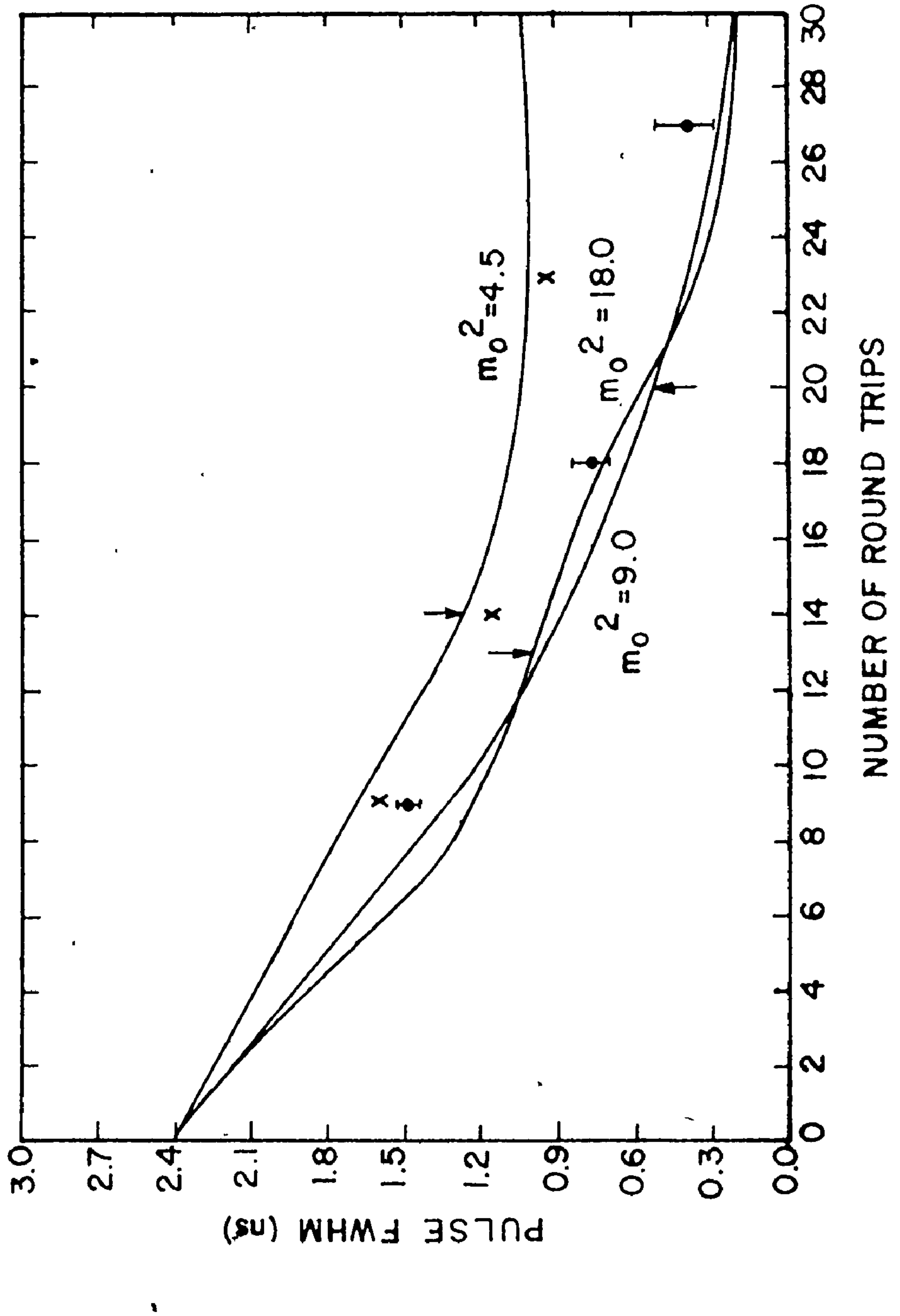
PULSE FWHM (ns)
3.0
2.7
2.4
2.1
1.8
1.5
1.2
0.9
0.6
0.3
0.0
NUMBER OF ROUND TRIPS
0
2
4
6
8
10
12
14
16
18
20
22
24
26
28
30
$m_o^2=4.5$
$m_o^2=18.0$
$m_o^2=9.0$

a distinct plateau for the $m_0^2 = 4.5$ curve which again reflects the inability to saturate the absorber under these conditions. The $m_0^2 = 18.0$ curve shows rapid narrowing at low values of N due to the very fast intensity build-up for this case. However, narrowing for the $m_0^2 = 9.0$ case soon catches up (by N = 12) since the intensities at the absorber are now close to I_s. Finally as the large intensities at the absorber for the $m_0^2 = 18.0$ case decay, to approach I_s ($N \geq 14$), the rate of narrowing again increases. The data points denoted by crosses and solid circles were obtained for $m_0^2 = 2.2$ and 4.5, respectively. The agreement with theory is satisfactory. Unfortunately, it was not possible to obtain data for $N < 8$ since the experimental intensities were too low in this region for accurate pulse duration measurements. Figure 8-4 shows a single mode-locked pulse obtained using a fast risetime oscilloscope (Tektronix 7904, 625 ± 25 ps risetime). The pulse was selected from the mode-locked pulse tail for an m_0^2 setting of 4.5. The experimentally observed duration was corrected for the oscilloscope risetime to give a true pulse duration of 350 ± 100 ps.** The error bars shown in Fig. 8-3 indicate the uncertainty in obtaining the pulse durations using the correction technique.

---

*The round trip number for a measured pulse duration was obtained by counting pulses from the experimental peak intensity, using the assumption that the theoretical and experimental peak positions coincide.

** A FWHM detector plus oscilloscope response τ_{det} (650 ps) was used together with the formula $\tau_{real} = \sqrt{\tau_{exp}^2 - \tau_{det}^2}$ to obtain the real pulse FWHM from the experimentally observed duration.

Fig. 8-4

An experimentally observed mode-locked pulse obtained from the pulse train tail for an $m_o^2 = 4.5$ and using a Tektronix 7904 oscilloscope (.625 ± 25 ps risetime).

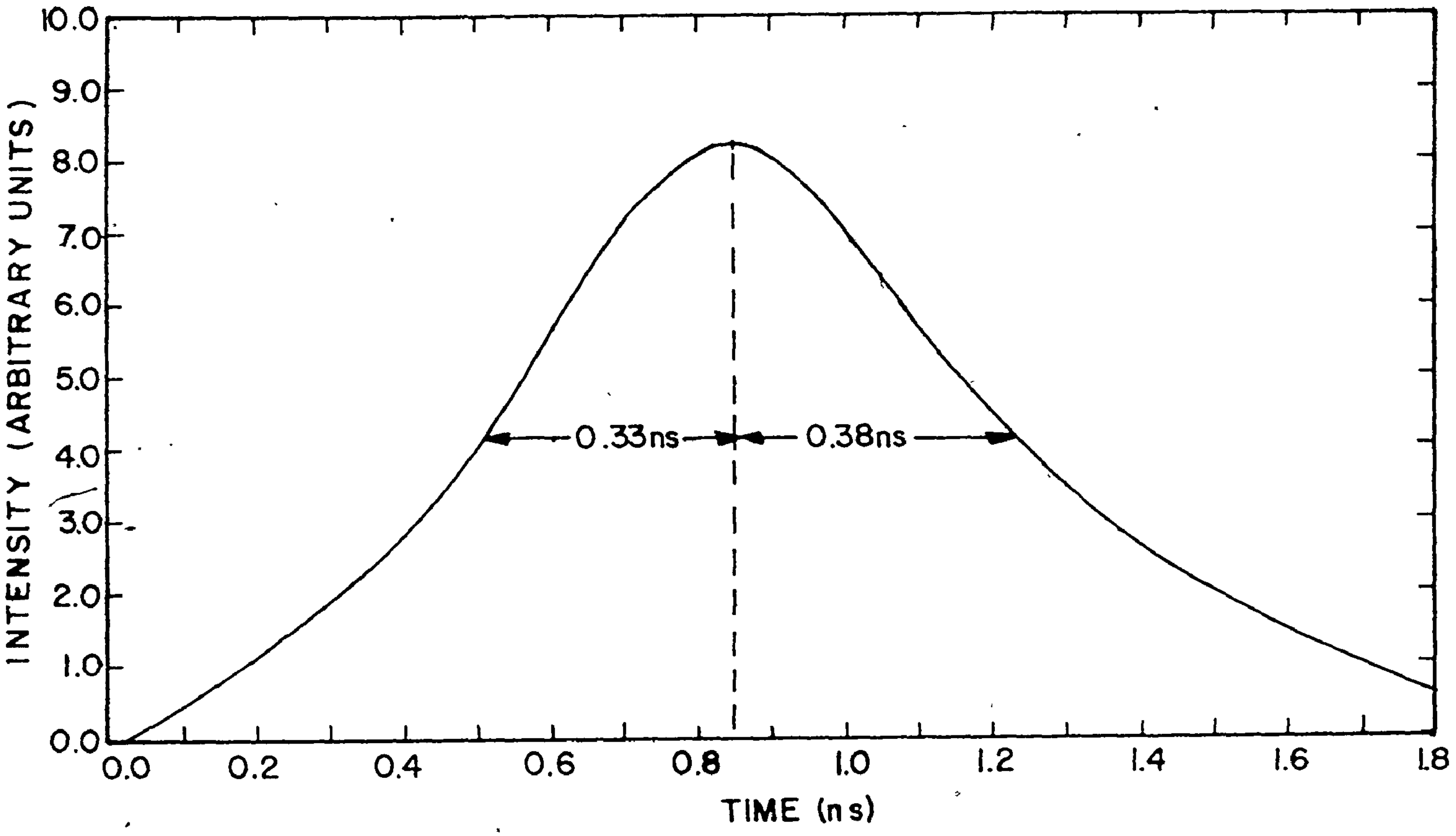
10.0
9.0
8.0
7.0
6.0
5.0
4.0
3.0
2.0
1.0
0.0
INTENSITY (ARBITRARY UNITS)
0.33ns
0.38ns
0.0
0.2
0.4
0.6
0.8
1.0
1.2
1.4
1.6
1.8
TIME (ns)

This section has demonstrated that, both theoretically and experimentally, there is an optimum value of m_0^2 necessary to achieve stable, clean, narrow, high-intensity laser pulses. Experimentally, however, mode-locking at high m_0^2 values is likely to be prohibited due to Ge damage rather than the onset of poorer mode-locking stability.

8.6 Influence of Rotational Coupling on Mode-Locking

It has been mentioned previously that depletion of the rotational population inversion on a particular rotational line, and the subsequent collisionally induced return to equilibrium in a time τ_R, has been included in the theoretical mode-locking treatments. It will be demonstrated in this section that the inclusion of rotational coupling into the mode-locking analysis actually aids in the theoretical production of stable, clean mode-locked pulses. This is accomplished by holding down the laser pulse intensities to produce a larger number of passes in the absorber at intensities near I_s. It will also be shown in this section that the cumulative effect of the passage of high intensity pulses in the amplifier can lead to substantial asymmetric pulse shaping.

Figure 8-5 shows the normalized vibrational population inversion $D_2 - D_1$, for the three m_0^2 cases of Section 8.5.* It was determined over the course of the mode-locking simulation work that the optimum mode-locked regimes usually possessed inversion profiles similar to that shown for the $m_0^2 = 9.0$ curve of this figure. The $m_0^2 = 4.5$ case barely depletes the gain while the $m_0^2 = 18.0$ curve depletes it too fast.

---

* The population inversion is appropriate to the last of the 5 spatial increments in the amplifier (Appendix B).

Fig. 8-5

Plot of the normalized vibrational population inversion, D_2-D_1, as a function of time, relative to t_d, for m_o^2 values of 4.5, 9.0, 18.0. The arrows indicate the round trip numbers at which the output intensity peaks for each of the m_o^2 values.

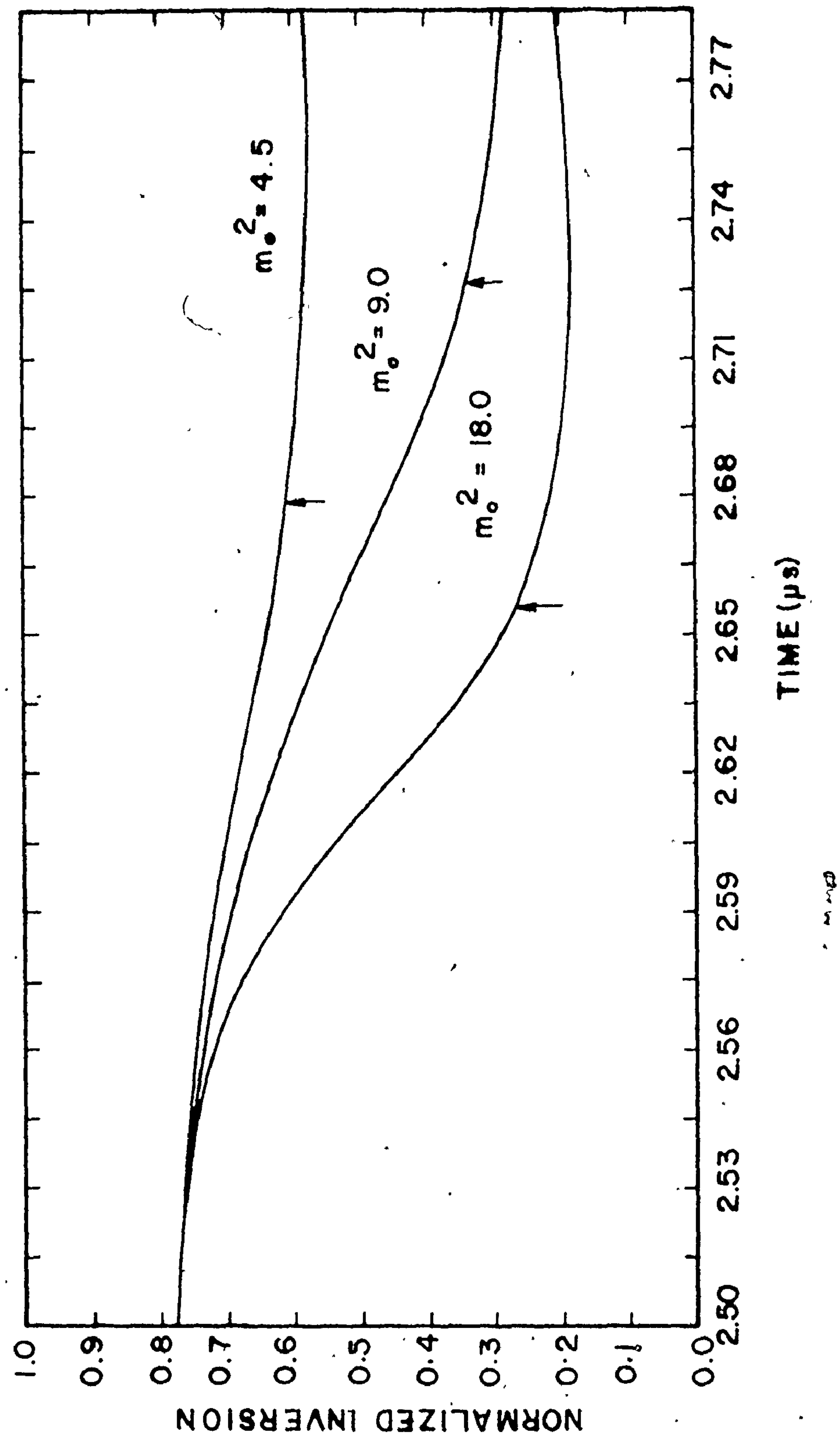
$m_o^2 = 4.5$
$m_o^2 = 9.0$
$m_o^2 = 18.0$
NORMALIZED INVERSION
1.0
0.9
0.8
0.7
0.6
0.5
0.4
0.3
0.2
0.1
0.0
2.50
2.53
2.56
2.59
2.62
2.65
2.68
2.71
2.74
2.77
TIME (μs)

Figure 8-6 shows the normalized vibrational $((D_2-D_1)$, top curve) and normalized rotational inversion $(\delta^{J_0}/\kappa(J_0))$ for a 3 ns time slice about the peak intensity of the mode-locked pulse train with $m_0^2 = 18.0$. The arrow indicates the position in time where the peak of the mode-locked pulse occurred. This figure illustrates the hole that is burnt in the rotational population distribution by the mode-locked pulse. The hole then recovers to approach the vibrational population inversion after the pulse has passed through the amplifier. The width of such holes is proportional to the mode-locked pulse duration, provided the duration is $> \tau_R$. For durations less than τ_R the holes recover exponentially in a 1/e time given by τ_R. The depth of the holes increases with the pulse intensity but does not follow it in any linear fashion. Due to the rotational hole-burning effect the leading edge of a symmetric mode-locked pulse propagating in the amplifier sees a greater gain than that of the trailing edge. This results in a faster risetime pulse which, on repeated propagation in the amplifier, further increases the pulse asymmetry.* Figure 8-7 illustrates the result of the cumulative pulse shaping on the peak intensity pulse $(m_0^2 = 18.0)$. The cumulative aspect of the pulse shaping is emphasized since on a single-pass basis the mode-locked intensities in the amplifier (1-5 MW/cm^2) are insufficient to fully deplete the population on a given rotational line.**

---

* If rotational coupling were not included in the analysis, completely symmetric narrowing by the Ge absorber would be expected.

** It has been estimated that for a 1 ns pulse $\sim$100 MW/cm^2 intensities are necessary (for a 1 atm laser) to significantly deplete the rotational population [114].

Fig. 8-6

Plot of the normalized vibrational population inversion, D_2-D_1, (top curve) and the normalized rotational population inversion, $\delta^{J_0}/\kappa(J_0)$, as a function of time for a ∿3 ns time interval about the peak intensity of the mode-locked pulse train. The population inversions are appropriate to the last section of the amplifier (Appendix B). The value of m_0^2 is 18.0. The arrow indicates the time at which the peak of the mode-locked pulse passes through the last amplifier section.

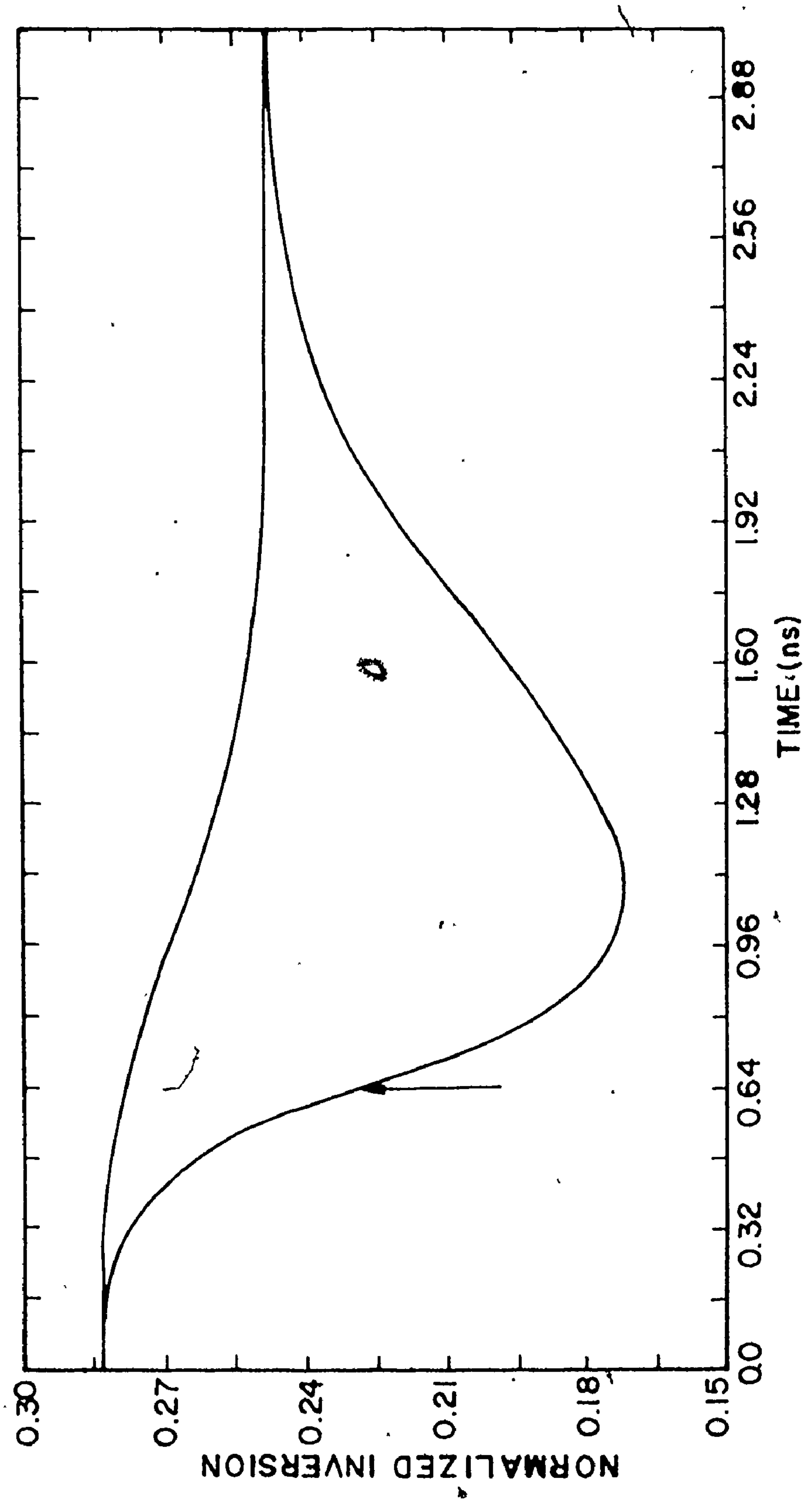
NORMALIZED INVERSION
0.30
0.27
0.24
0.21
0.18
0.15
TIME (ns)
0.0
0.32
0.64
0.96
1.28
1.60
1.92
2.24
2.56
2.88

Fig. 8-7

Theoretical prediction for the output pulse at the peak of the mode-locked train for the $m_0^2 = 18.0$ case.

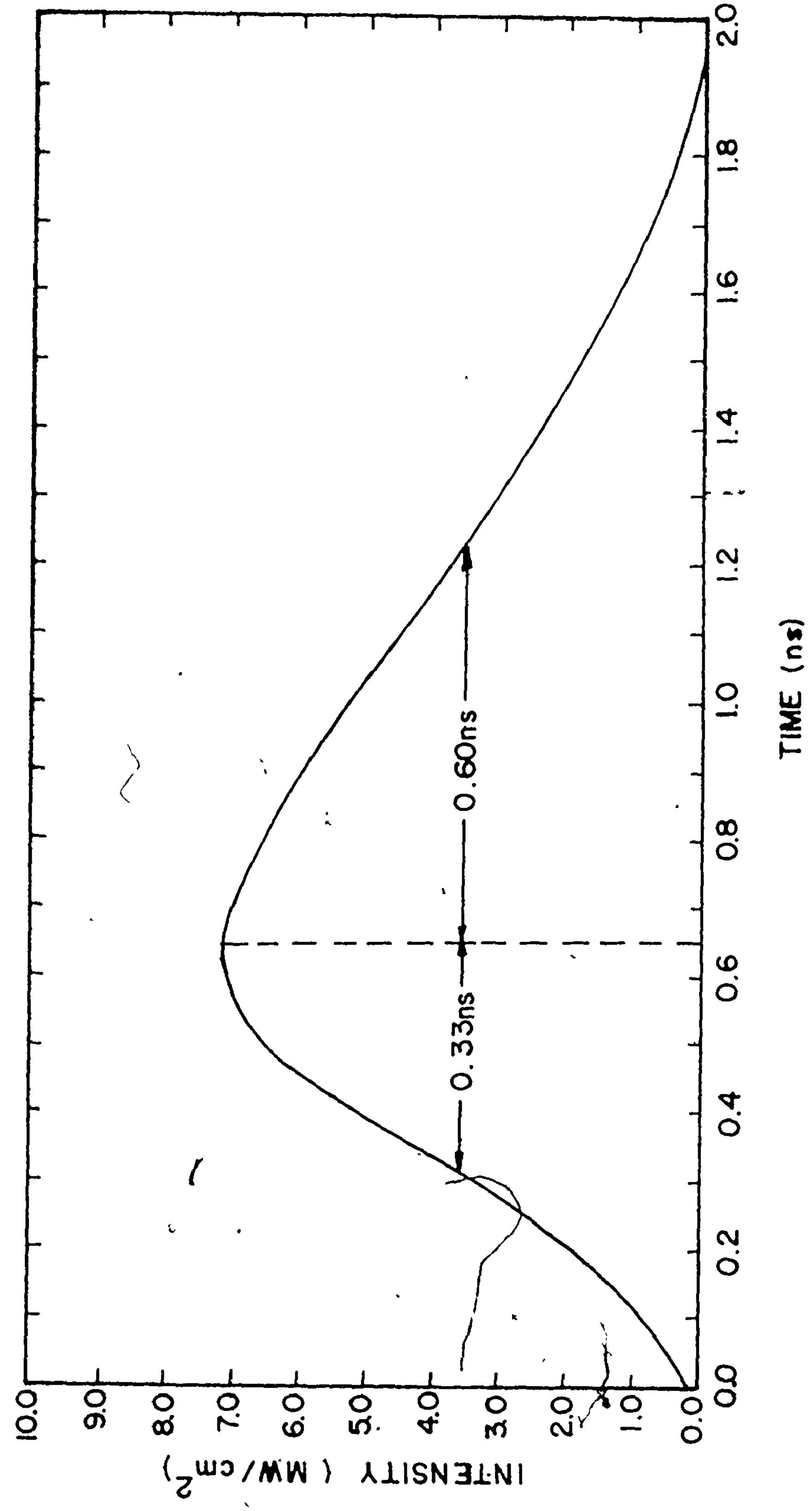
INTENSITY (MW/cm^2)
0.0
1.0
2.0
3.0
4.0
5.0
6.0
7.0
8.0
9.0
10.0
TIME (ns)
0.0
0.2
0.4
0.6
0.8
1.0
1.2
1.4
1.6
1.8
2.0
0.33ns
0.60ns

The effect of varying the rotational coupling time τ_R on the individual mode-locked pulse energies (keeping all other parameters fixed) is illustrated in Fig. 8-8.* The curves are appropriate to a single starting pulse in a 250 Torr amplifier with $g_{max}L_a = 0.6$, $\alpha_0 L^B = 0.4$, $R^M = 0.95$, $R^A = 1.0$, $m_0^2 = 12.0$ and $T_2 = 0.3$ ns. The figure shows that the effect of rotational coupling is to lower the mode-locked pulse energy, thereby resulting in longer envelope risetimes and FWHM. The longer risetimes and reduced pulse energies allow a greater number of passes in the absorber at intensities near I_s. The net result is better discrimination and pulse narrowing. Rotational hole-burning prevents the immediate use of the gain on the envelope rise, but makes the stored gain available on the envelope tail in such a way that the total mode-locked train energy extracted with and without rotational coupling is similar. It is clear from the observations made in this section that rotational coupling is important to correctly describe the mode-locked train output intensity, temporal profile of the train envelope and individual pulse shape and duration.

8.7 Influence of Gain on Mode-Locking

The next set of curves illustrate the dependence of the mode-

---

* The continuous nature of the curves is for appearance sake only.

Fig. 8-8

Plot of mode-locked pulse energy as a function of the number of round trips for a 250 Torr CO_2 amplifier. The curves (a), (b), (c) corresponds to rotational coupling times (τ_R) of 0.0, 0.6, and 1.2 ns, respectively. The curves are continuous for appearance sake only.

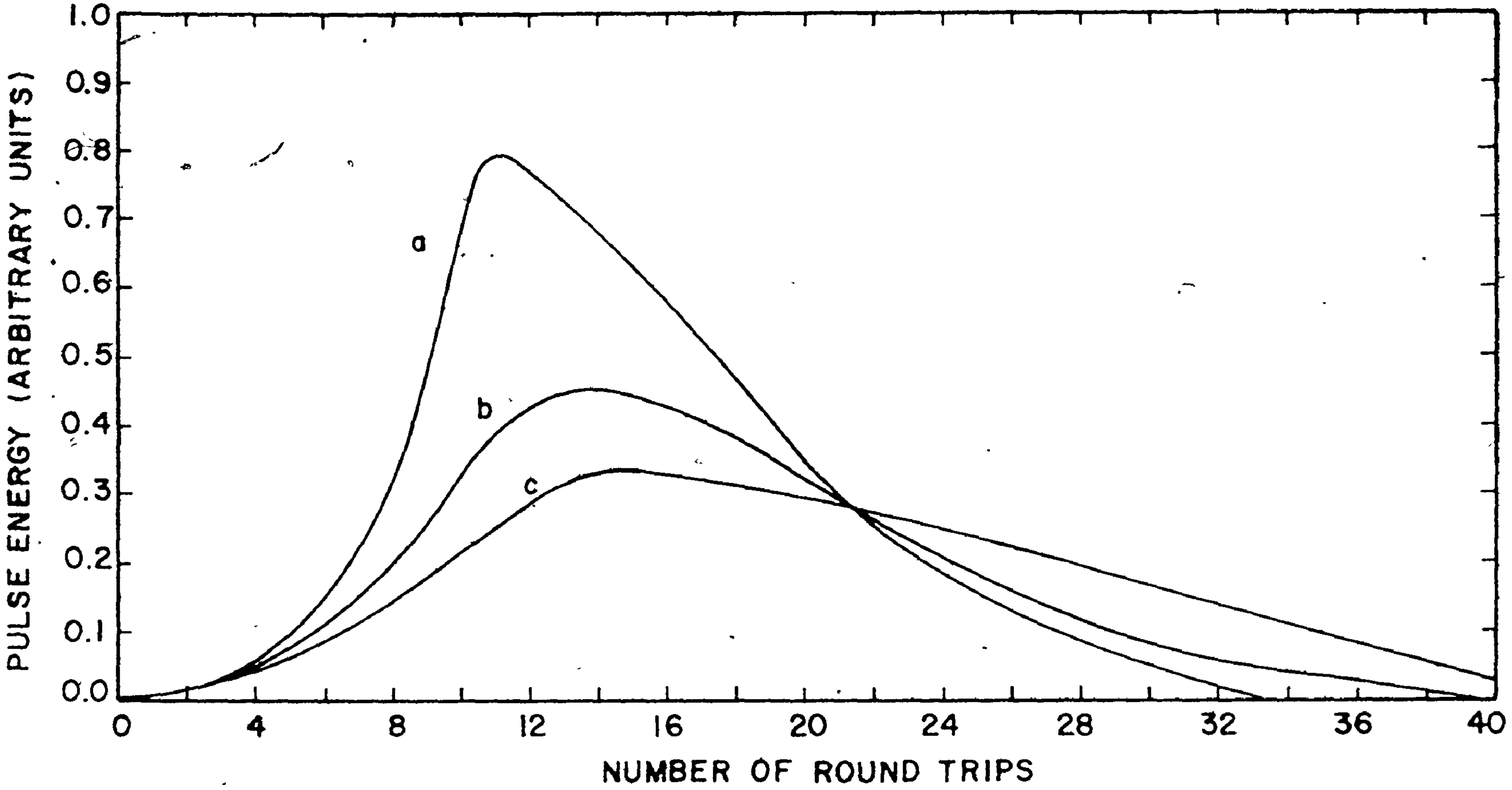
PULSE ENERGY (ARBITRARY UNITS)
1.0
0.9
0.8
0.7
0.6
0.5
0.4
0.3
0.2
0.1
0.0
a
b
c
0
4
8
12
16
20
24
28
32
36
40
NUMBER OF ROUND TRIPS

locking behaviour on the small-signal gain coefficient $g_{max}L_a$. This section demonstrates that there exists an optimum value in how close to lasing threshold one can operate in order to obtain clean dependable pulses.

The experiments and simulations were performed with the parameter values recorded in Table 8-1. The experimental m_o^2 value was kept at 4.5. Figure 8-9 shows the variation in output intensity with the number of round trips (relative to the time t_d). The $g_{max}L_a$ value of 0.9 represents the gain value just sufficient to observe lasing. The corresponding experimental time delay was $\sim$3.7 μs. At the higher gains (farther away from lasing threshold) the intensity rises very fast. Note that the intensity (1.8 MW/cm^2 at N $\sim$8) for $g_{max}L_a$ = 1.17 is actually less than that of the lower gain (0.99) case (3.3 MW/cm^2 at N $\sim$20). However, due to poorer pulse discrimination the simulation with the gain of 1.17 possesses a significant contribution from the second inserted pulse (D = 1.8 compared to a D = 60 for the 0.99 gain case). Furthermore the pulse duration for this gain setting (1.5 ns) is three times greater than the corresponding durations for the 0.99 case. Consequently, the mode-locked pulse energy is actually 2.3 times the energy of the pulse at the lower gain setting. However, since the envelope of the mode-locked gain for the 1.17 case rises and falls quite fast, the total energy of the pulse trains for the two cases are in fact very nearly equal. The time scale for the energy extraction from the amplifier is the main difference between the two cases. If the initial input pulse ratio (0.6) was much lower (say $\lesssim$ 0.2), then the theoretical peak intensity of the two cases would be within 20 to 30% of each other. It was in fact observed experi-

Fig. 8-9

Theoretical predictions for the output peak intensity with the number of round trips for values of the paramter $g_{max}L_a$ indicated in the figure.

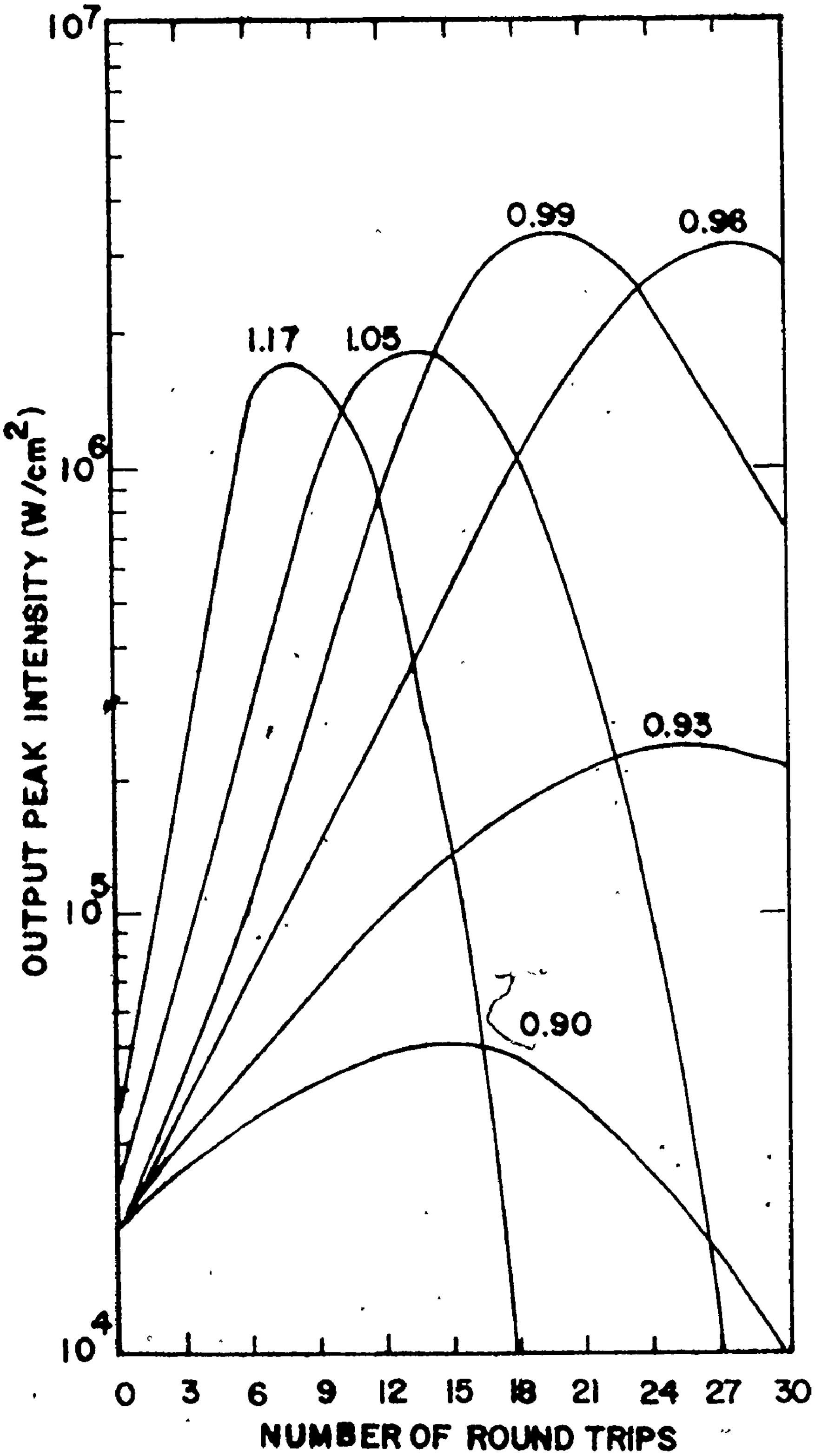
10^7
10^6
10^5
10^4
OUTPUT PEAK INTENSITY (W/cm^2)
0.99
0.96
1.17
1.05
0.93
0.90
0
3
6
9
12
15
18
21
24
27
30
NUMBER OF ROUND TRIPS

mentally that the peak output intensities (~ 2 MW/cm^2) were not particularily sensitive to the variation in gain from threshold once the experimental gain was greater than or equal to $\sim$0.96. Stable and clean mode-locking ($\lesssim$ 10% intensity variation, $D > 50$) was obtained experimentally on 95% of the laser discharges in a gain range of 0.96 to 1.05.* On either side of this range there was a progression to poorer mode-locking. Figure 8-10 indicates that the computer simulations predict a very sharp maximum in pulse discrimination (D)** as a function of small-signal gain. Knowledge of the parameter settings to obtain very large values of D (typically $\gtrsim 10^3$) is valuable if one plans to switch out a single pulse from the mode-locked train and cannot avoid switching out a secondary pulse in the 2L/c time window.

Figure 8-11 illustrates the pulse narrowing for the different gain cases. Poor narrowing occurs when the laser is operated so close to lasing threshold that the intensity at the absorber is insufficient to cause a Q-switching action. Note, however, that there is also a plateau at $\sim$0.8 ns for the high gain value of 1.17. In this case the gain is depleted too rapidly, thus preventing the large number of passes in the absorber necessary for pulse narrowing. It is clear from these curves that the region for best narrowing is also the region for best pulse discrimination, indicative of the mode-locking behaviour of a fast

---

* On the gain variation experiments, as with all subsequent parameter variations, the stability of the laser discharge was excellent and did not preferentially influence the mode-locking stability of certain gain settings.

** D is appropriate to the round trip number corresponding to the peak intensity of each mode-locked pulse train.

Fig. 8-10

Plot of the theoretical prediction of pulse discrimination (D) as a function of the value of the small-signal gain $g_{max}L_a$. The value of m_o^2 was 9.0. All other parameters were obtained from Table 8-1.

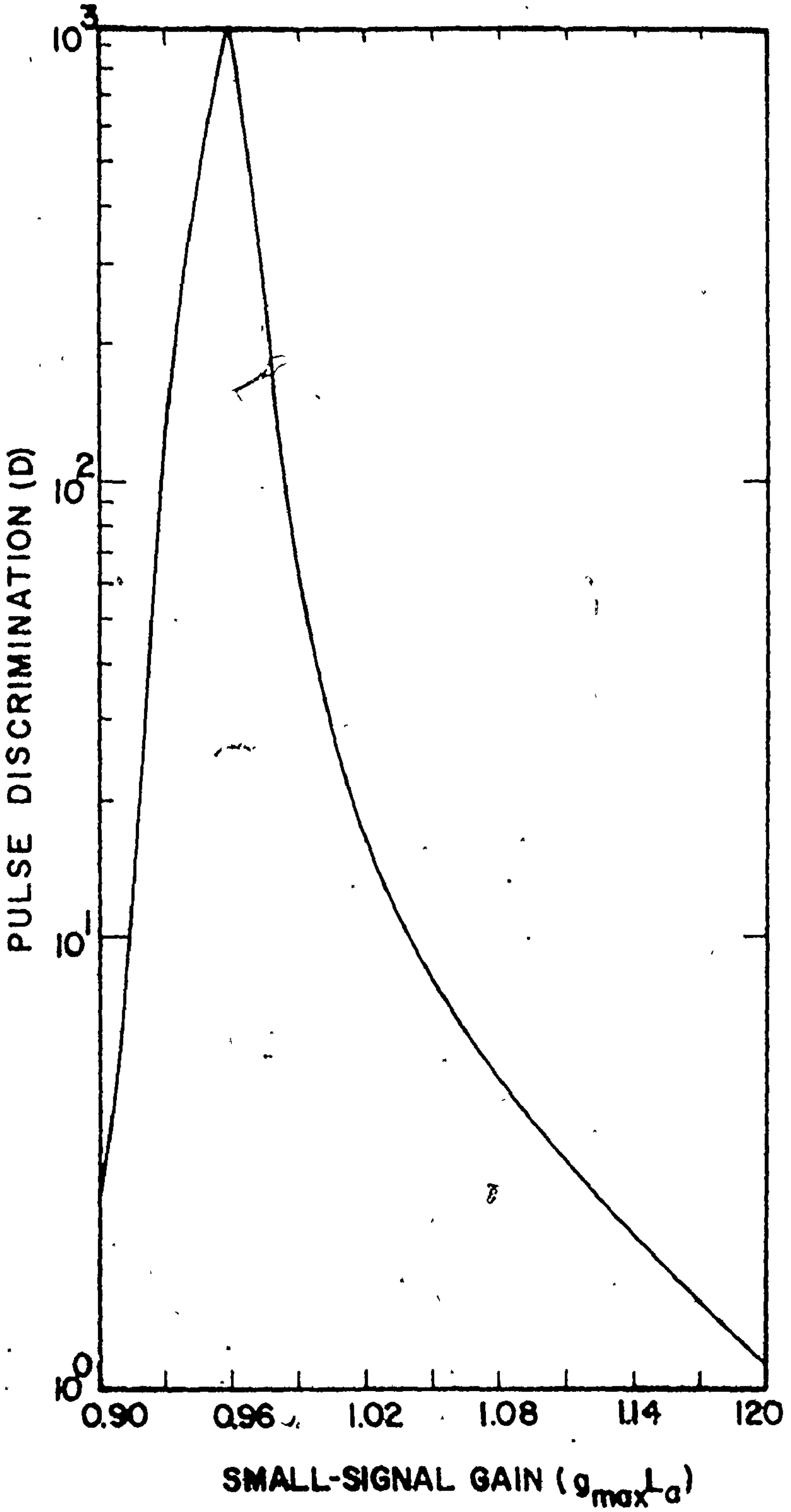
PULSE DISCRIMINATION (D)
10^3
10^2
10^1
10^0
0.90
0.96
1.02
1.08
1.14
1.20
SMALL-SIGNAL GAIN ($g_{max}L_a$)

Fig. 8-11

Theoretical and experimental pulse narrowing (FWHM) as a function of the number of round trips for the values of the parameter $g_{max}L_a$ shown in the diagram. The solid circles (●) represent experimental data points for the 0.99 gain case. The value of m_0^2 was 9.0. All other relevant parameters were obtained from Table 8-1.

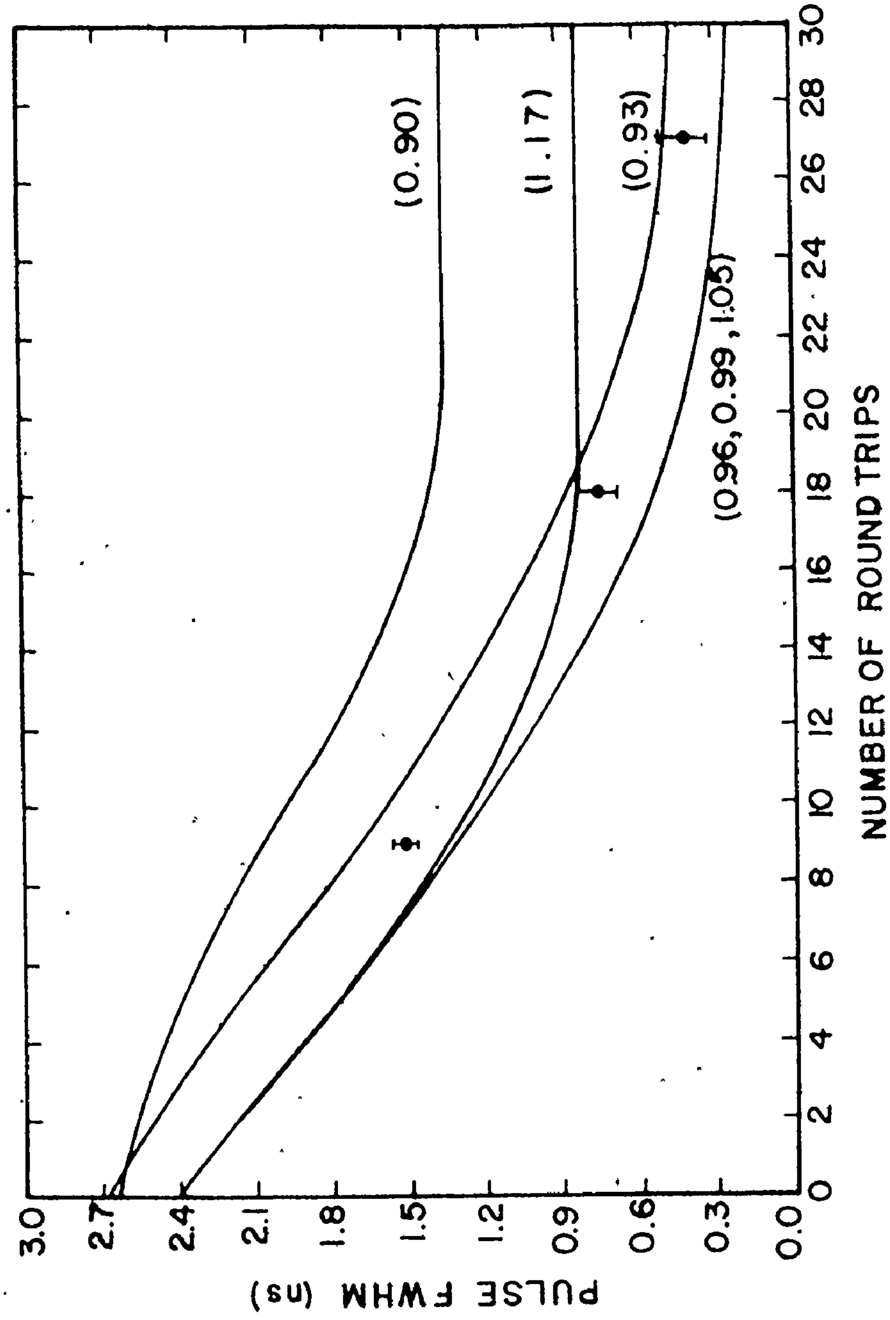
PULSE FWHM (ns)
0.0
0.3
0.6
0.9
1.2
1.5
1.8
2.1
2.4
2.7
3.0
NUMBER OF ROUND TRIPS
0
2
4
6
8
10
12
14
16
18
20
22
24
26
28
30
(0.90)
(1.17)
(0.93)
(0.96, 0.99, 1.05)

response time absorber such as Ge. The data points denoted by solid circles are appropriate to the 0.99 gain case and fall in reasonable agreement with the theoretical predictions. One further observation can be made from this figure. Since the 0.96 peak intensity (at $N \approx 27$) corresponds to a very narrow pulse duration (0.25 ns), high intensity as well as very short pulses should be possible for this setting. However, it appears that in order to obtain large-intensity very short pulses one must sacrifice pulse-to-pulse stability, since the optimum gain for such pulses is very close to the gains where the intensity is just sufficient to saturate the absorber (i.e., 0.90 to 0.93). A compromise of reasonably short pulses (0.45 ns) of large intensity, and good discrimination and stability, can be obtained by operating very close to $g_{max}L_a$ = 0.99 (i.e. ∿10% above the lasing threshold value of 0.90).

8.8 Influence of Linear Loss on Mode-Locking

The linear loss is comprised of an aperture insertion loss R^A and a lumped cavity loss R^M. In this section we demonstrate the effect of varying R^A to change the total linear loss, while keeping the non-linear loss constant (at $\alpha_0 L^B = 0.69$). The experimental value of m_0^2 is again 4.5. The laser gain is appropriately adjusted to give the same ratio of gain to total loss (linear plus non-linear) for the different values of R^A tested. Experimentally, this corresponds to adjusting the gain to keep the time delay constant. Figure 8-12 illustrates the output intensity against round trip number for 3 values of R^A; 0.88, 0.55 and 0.35. It is observed that the lowering of the linear loss increases the peak output intensities, as one might expect. Note however, that the

Fig. 8-12

Theoretical predictions for the output peak intensity with round trip number as a function of the linear loss (R^A). The solid and dashed curves for $R^A = 0.55$ were obtained using an inhomogeneous and homogeneous saturation parameter, respectively.

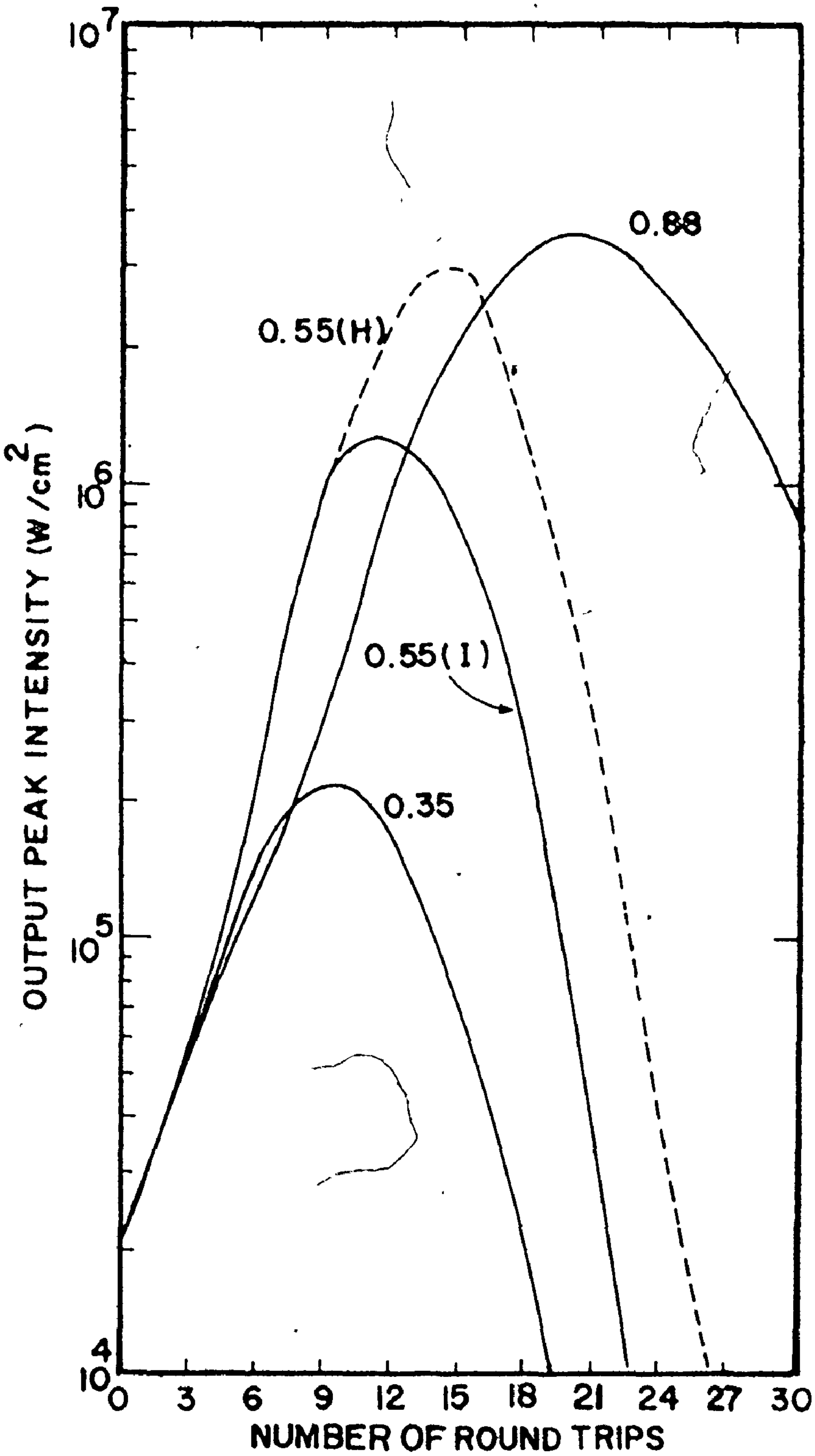
0.88
0.55(H)
0.55(I)
0.35
OUTPUT PEAK INTENSITY (W/cm^2)
NUMBER OF ROUND TRIPS
10^7
10^6
10^5
10^4
0
3
6
9
12
15
18
21
24
27
30

peak intensity is shifted to a higher value of N at lower loss due to the increased effect of rotational coupling. The discrimination (D) at the peak pulse intensity is 2.2, 7.0 and 6.0 for the progression to lower loss. Experimentally,reasonably clean mode-locking was achieved even for the high linear loss case. This indicates that the initial input pulse ratio of 0.6 used in the simulations is larger on average than that which is observed experimentally. Figure 8-13 illustrates the theoretically predicted mode-locked output pulse train together with the experimentally observed output for the $R^A = 0.55$ case. The theoretical output peak intensity (exit from mirror M2 of Fig. 8-1) indicated in Fig. 8-12 is 1.2 MW/cm^2. The experimental value is 1.3 ± 0.3 MW/cm^2. The agreement in absolute intensity and output pulse shape is excellent.

Figure 8-14 shows the pulse narrowing for the three values of R^A. The experimental data points are denoted by crosses, open circles, and solid circles, for $R^A = 0.35$, 0.55, and 0.88, respectively. It is observed that the greater the linear cavity loss the broader the final pulse durations.

The dashed curve of Fig. 8-12 and Fig. 8-14 represent the model predictions using the homogeneous saturation parameter for the $R^A = 0.55$ case. The homogeneous treatment predicted output intensities that were twice those observed experimentally. It also predicted ∿35% narrower pulses than were observed experimentally. This is in contrast to the inhomogeneous saturation case which gave good agreement in both intensity and pulse narrowing. This provides further evidence that Ge is in fact an inhomogeneously broadened saturable absorber.

Fig. 8-13

Comparison of an experimentally observed mode-locked pulse train (a) and the theoretically predicted output (b) for the case $R^A = 0.55$. The peak output intensities are 1.3 and 1.2 MW/cm^2 for the experimental and theoretical predictions, respectively. The cavity round trip time is 11.4 ns.

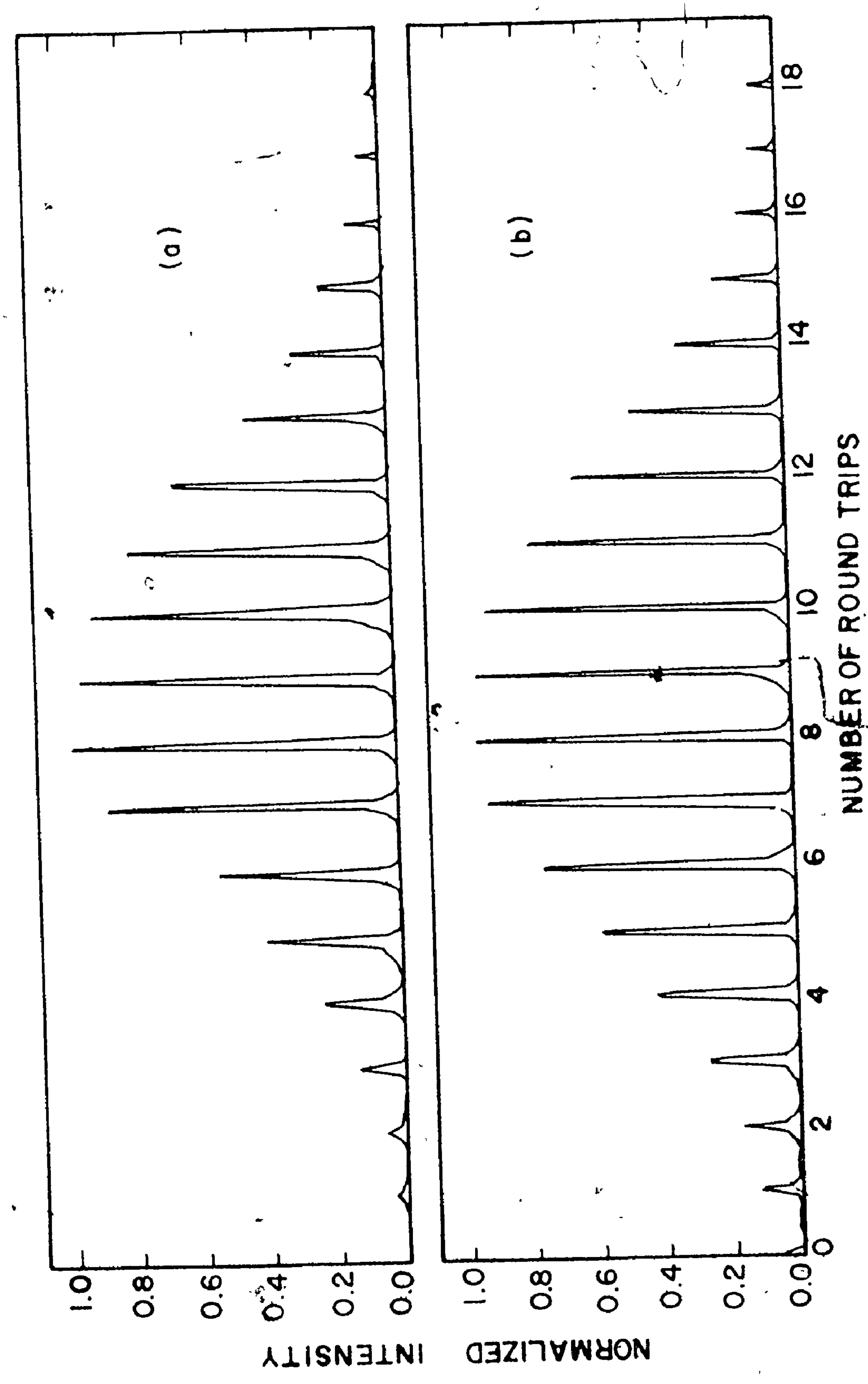
(a)
(b)
1.0
0.8
0.6
0.4
0.2
0.0
1.0
0.8
0.6
0.4
0.2
0.0
NORMALIZED INTENSITY
0
2
4
6
8
10
12
14
16
18
NUMBER OF ROUND TRIPS

Fig. 8-14

Theoretical and experimental pulse narrowing (FWHM) as a function of the number of round trips for various values of R^A. The experimental data points denoted by (x), (o), (•) correspond to values of $R^A = 0.35, 0.55, 0.88$, respectively. The dashed curve represents the predictions for $R^A = 0.55$, but with a homogeneously broadened saturation parameter.

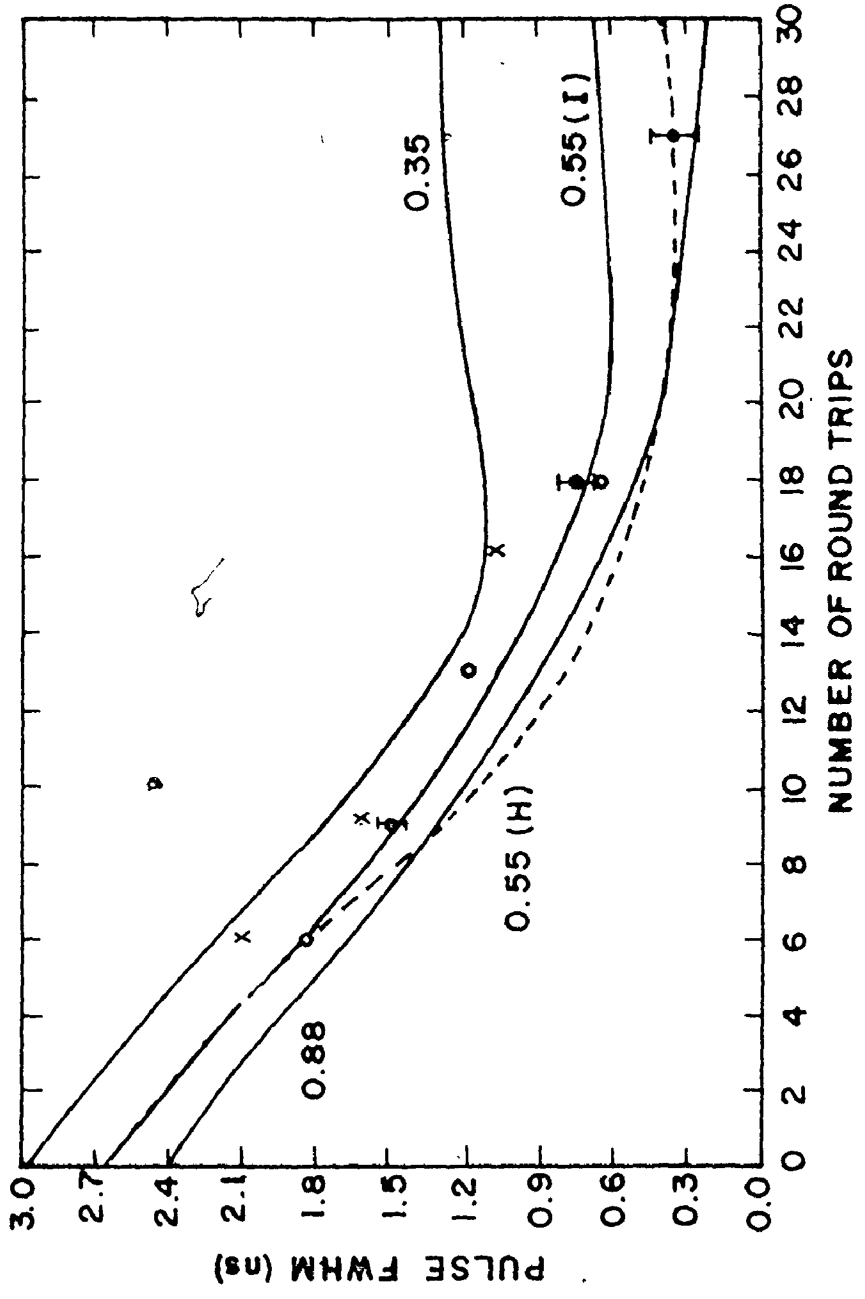
PULSE FWHM (ns)
3.0
2.7
2.4
2.1
1.8
1.5
1.2
0.9
0.6
0.3
0.0
NUMBER OF ROUND TRIPS
0
2
4
6
8
10
12
14
16
18
20
22
24
26
28
30
0.35
0.55 (I)
0.55 (H)
0.88

8.9 Influence of Non-Linear Loss on Mode-Locking

The non-linear loss was varied while keeping the linear loss constant (at $R^A = 0.88$, $R^M = 0.87$). The experimental m_o^2 value used was 4.5. The laser gain was adjusted to obtain a 2.5 μs time delay (t_d) in order to ensure a similar gain minus loss value to that used in the previous sections. The mode-locking behaviour was observed experimentally for two non-linear to linear loss ratios, 5.3 and 2.8, which corresponded to $\alpha_o L^B$'s of 0.64 and 0.36, respectively. The ratio of 7.7 ($\alpha_o L^B$ of 1.0) was also tested theoretically.

The curves of Fig. 8-15 indicate a sharp rise in intensity, at low round trip numbers, with increased $\alpha_o L^B$. The discrimination at the peak of the pulse train again favours the parameter setting whose curves take time to reach their peak intensity. The D values were 10.0, 60.0, 4.5 for $\alpha_o L^B$ of 1.0, 0.69 and 0.36, respectively. Figure 8-16 shows the pulse narrowing for the three cases. The wide discrepancy in starting durations is due to the variation in $g_{max} L_a$ for the three cases (i.e., in Eq. 7-36). These curves illustrate that the fast rise in intensity, due to the large non-linear to linear loss ratio obtained using $\alpha_o L^B$ = 1.0, does not in this case prevent substantial pulse narrowing. In fact, the duration predicted at 24 round trips is very close to the gain medium's T_2 time. The experimental data points denoted by crosses and closed circles refer to $\alpha_o L^B$ of 0.36 and 0.69, respectively. Once again there is reasonable agreement with the observed durations and those predicted by the mode-locking model.

Fig. 8-15

Variation of the theoretical output peak intensity as a function of the number of round trips for non-linear loss values ($\alpha_0 L^B$) indicated in the diagram.

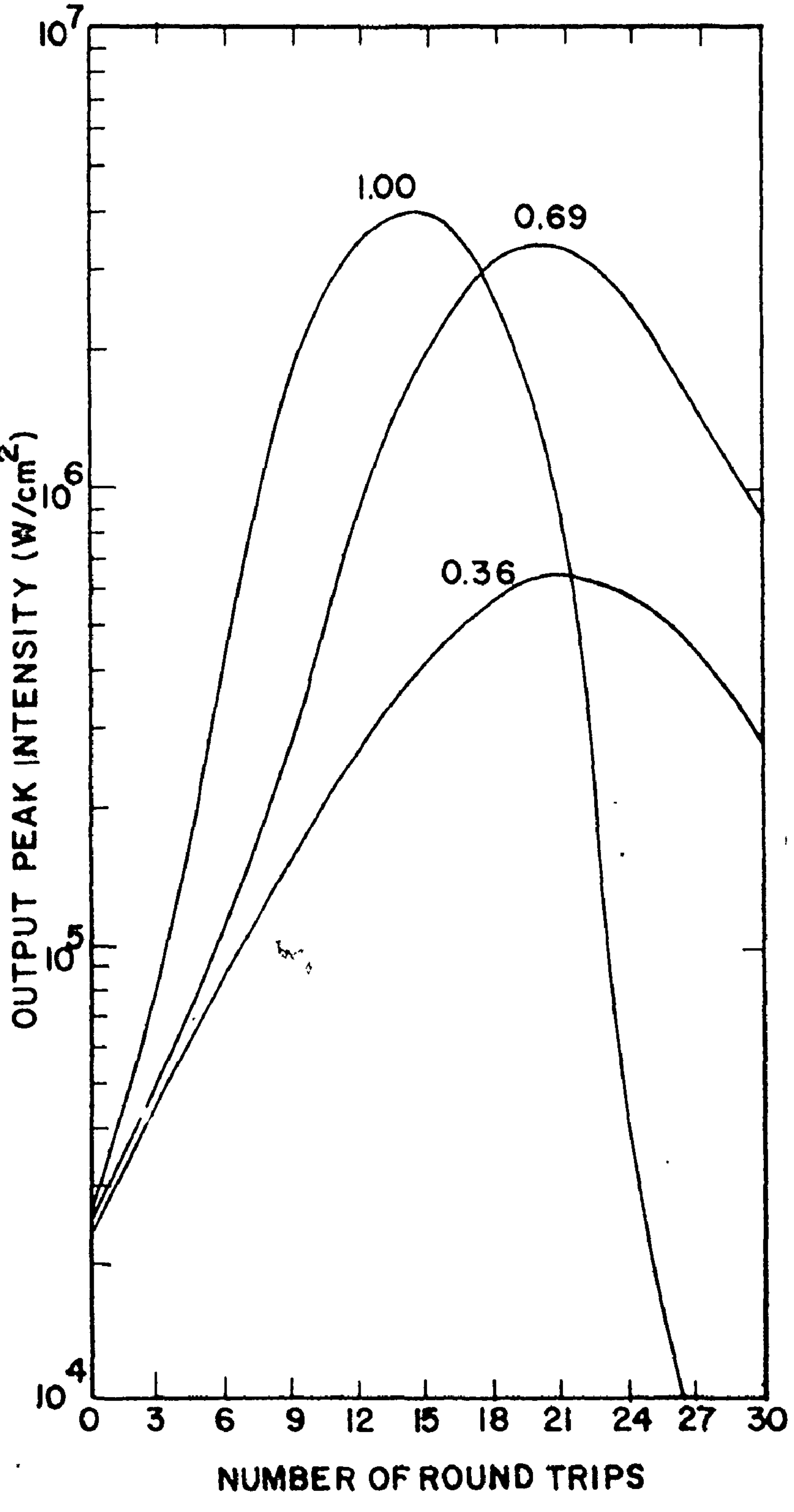
10^7
10^6
10^5
10^4
OUTPUT PEAK INTENSITY (W/cm^2)
1.00
0.69
0.36
0
3
6
9
12
15
18
21
24
27
30
NUMBER OF ROUND TRIPS

Fig. 8-16

Theoretical and experimental pulse narrowing (FWHM) as a function of the number of round trips for non-linear loss values ($\alpha_0 L^B$) indicated in the diagram. The experimental data points (x), (●) correspond to $\alpha_0 L^B$ values of 0.36, 0.69, respectively.

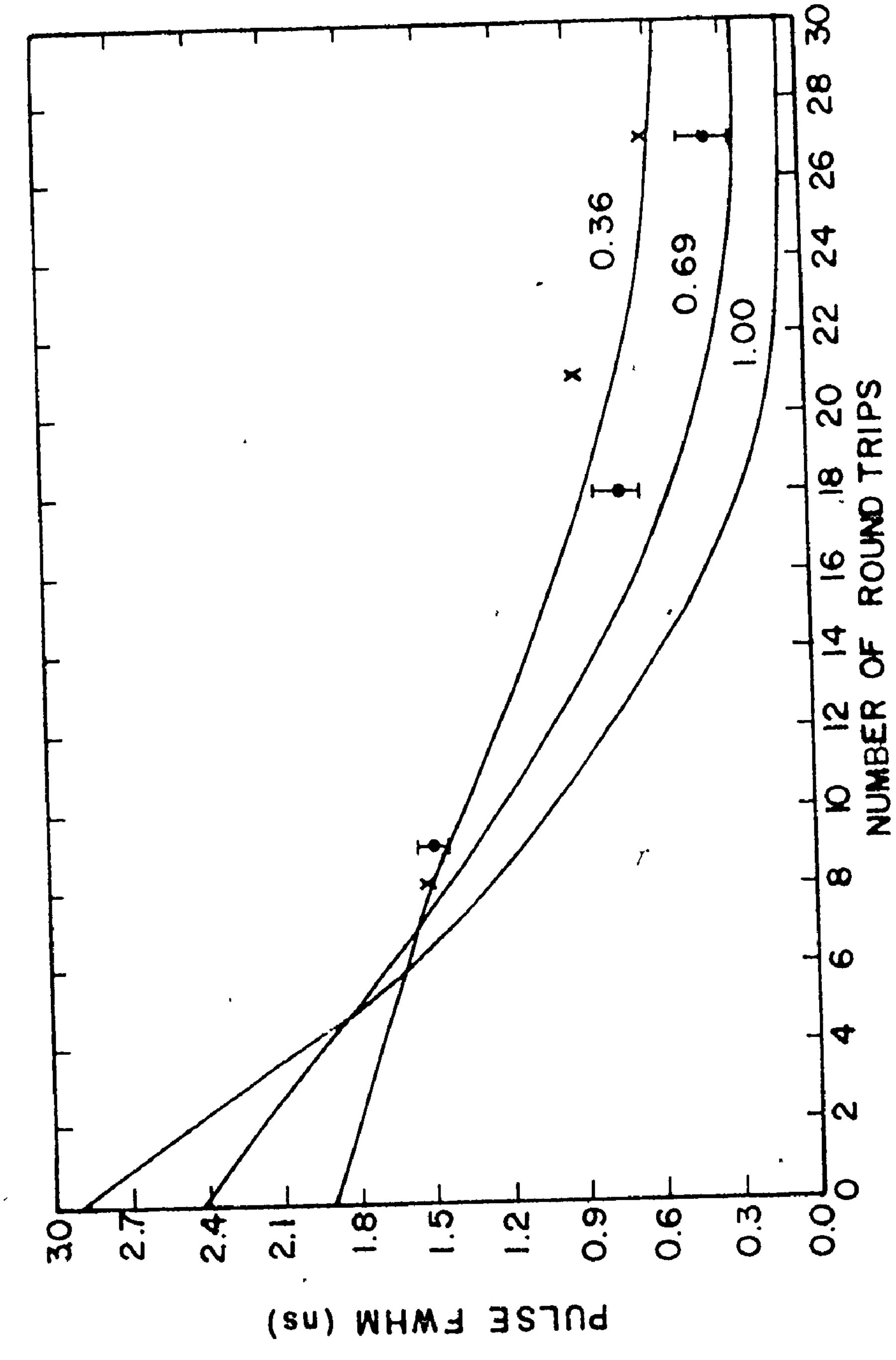
PULSE FWHM (ns)
3.0
2.7
2.4
2.1
1.8
1.5
1.2
0.9
0.6
0.3
0.0
NUMBER OF ROUND TRIPS
0
2
4
6
8
10
12
14
16
18
20
22
24
26
28
30
0.36
0.69
1.00

8.10 Mode-Locking as a Function of Laser Gas Pressure

We have mentioned that the starting pulse ratio of 0.6 in the simulations was chosen to test the theoretical parameters, relatively independent of the pulse-to-pulse variation in the noise distribution. Experimentally, clean mode-locking has been observed over a much wider range of conditions. It was attempted experimentally to ascertain whether the clean mode-locking was simply a result of a reduced number of starting pulses (2 or 3) per round trip time or due to the fact that we were in a deterministic mode-locking regime (defined in Section 7.3(a)) with a single starting pulse per 2L/c time. By sending 65% of the output beam to a Au:Ge detector (2.5 ns risetime) to set the oscilloscope time base for the observed mode-locked pulse trains, we were able to look at pulses on the train rise with intensities as low as ∿1/40 of the peak pulse intensity. It was observed that the pulse durations did not exceed 2 ns (FWHM). Furthermore, there was a much greater probability of observing double-pulses in this early time region with the intensity of the second pulse typically being 20 to 40% that of the main pulse. These secondary pulses were usually significantly suppressed at the 10% rise point of the mode-locked train, which accounted for the clean mode-locking generally observed. The question still arises as to how low in intensity one should check to see if the starting distribution consists of 1 or more pulses. The analysis by Ausschnitt [105] indicates that a single pulse output per 2L/c makes a transition to a series of discrete narrow pulses when the initial pulse begins to saturate the absorber. For our case this is close to the region in which measurements were made. Equation (7-36) predicts that if $g_{max}L_a$ and N are kept constant, then the starting pulse duration should be proportional to T_2 and therefore be longer at lower laser pressures. The formula predicts that only a single pulse should occupy the round trip time at laser gas pressures somewhere between 1/3 and 1/2 atm.* The laser pressure was therefore lowered keeping the linear and non-linear losses and gain the same as for the 1 atm mode-locked operation. The value of m_0^2 was increased to 12.0 by slightly increasing the cavity length to 1.81 m. The increase in m_0^2 ensured substantial saturation of the absorber to allow comparison with 1 atm results. At a laser pressure of 1/2 atm there was $\sim$20% probability of obtaining a single pulse whose width occupied the entire round trip time. Decreasing the pressure to 250 Torr produced mode-locked trains similar to that shown in Fig. 8-17. There was a large probability ($\gtrsim$ 70%) of obtaining a starting pulse which occupied the round trip time. It was concluded that deterministic mode-locking occurs for pressures near 1/3 atm but does not occur for 1 atm laser operation. Therefore the excellent mode-locking observed at 1 atm is due to the reduced number of starting pulses (but still $\geq$ 2). It was also observed for the pressures tested that the initial pulse duration scaled with T_2 and therefore inversely with pressure, as expected from Eq. (7-36).

There is considerable interest in understanding the mode-locking processes of multi-atm CO_2 lasers in order to produce very short (ps) laser pulses. The good agreement between theoretical and experimental predictions for the 1 atm laser pressure indicates that the

---

* The uncertainty is largely due to not knowing the exact pulse shape in the calculation of pulse broadening in the linear gain region.

Fig. 8-17

Experimentally observed mode-locked train output from a 250 Torr amplifier. The value of m_0^2 is 12.0. All the other relevant parameters were obtained from Table 8-1. The round trip time is 12 ns.

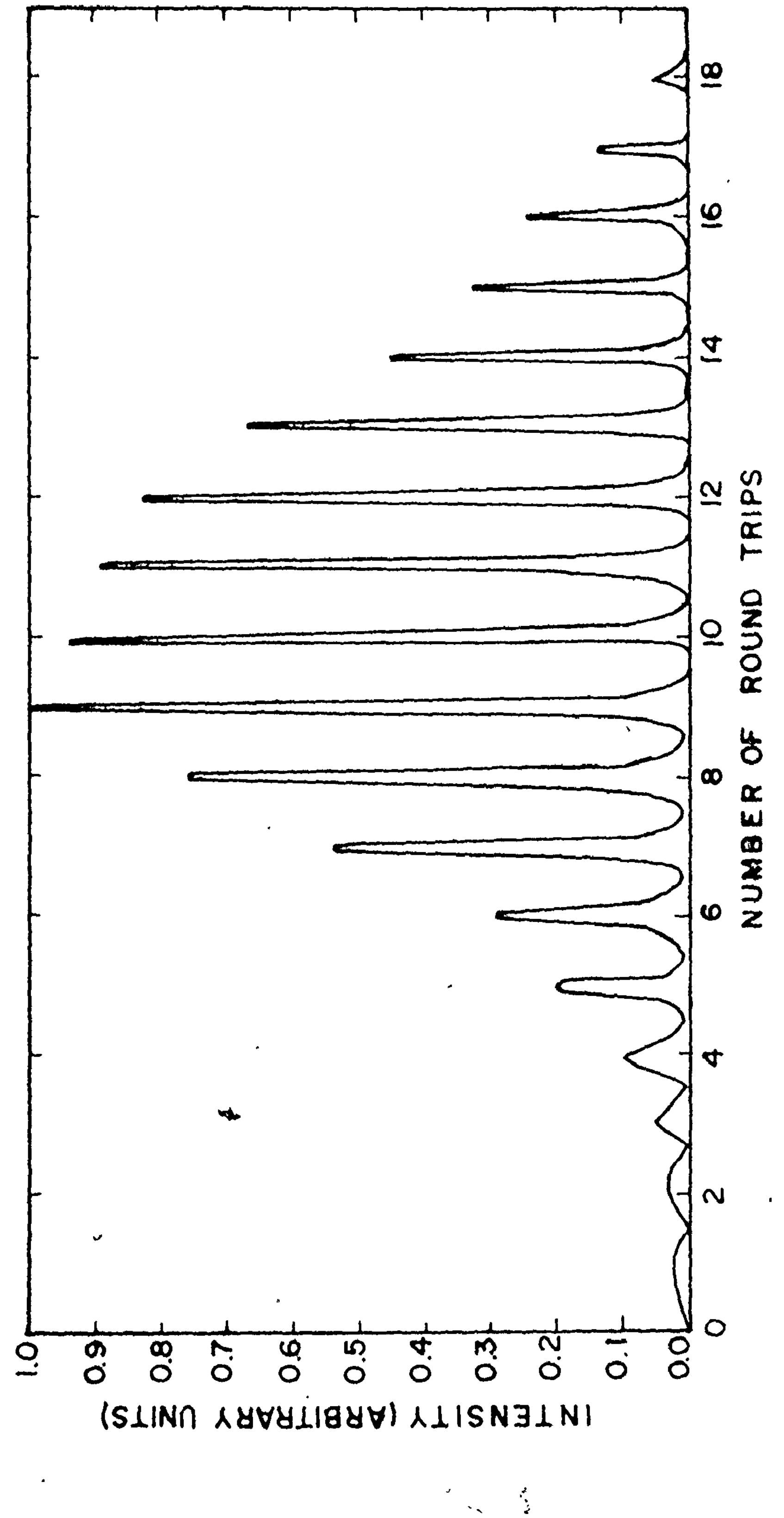
INTENSITY (ARBITRARY UNITS)
0.0
0.1
0.2
0.3
0.4
0.5
0.6
0.7
0.8
0.9
1.0
NUMBER OF ROUND TRIPS
0
2
4
6
8
10
12
14
16
18

theory is well established and can be used to predict, with some confidence, the mode-locking behaviour at high CO_2 pressures. The mode-locking behaviour at 5 atm, for example, although very similar to that at 1 atm, has some important differences. For the same cavity length (1.71 m) ~217 axial modes (m_i) lie under the 5 atm gain bandwidth. The resulting random beating of these modes produces fluctuations (at t_0) of roughly 20 ps duration. The final calculated duration at t_d is the order of 300 ps. Since it is now possible to fit 15 to 20 of these pulses into a 2L/c time, white noise or incoherent noise statistics can be used to predict the ratio of all the fluctuation intensities relative to the peak fluctuation intensity for a certain probability of mode-locking. Clean mode-locking will most crucially depend on the ratio of the largest to the second largest pulse intensity. The probability (V) that the largest pulse is C times larger than the second largest pulse is given by [103]

$$V(m_f, C) \sim \frac{C}{(m_f + 1)^{C - 1}} \cdot \qquad (8\text{-}3)$$

For example, at $m_f \simeq 20$, if one can arrange the laser parameters to obtain adequate pulse discrimination for the ratio $I_2/I_1 = 0.8$, then Eq. (8-3) predicts that clean mode-locking should also be obtained in ~60% of the subsequent laser shots, since in these shots I_2 is $\lesssim 0.8\ I_1$. The value of 0.8 for I_2/I_1, plus the ratio of each pulse intensity to I_1 and the average fluctuation durations, are used to generate the starting noise distribution. The 5 atm theoretical simulation parameters were obtained using the parameters recorded in Table 8-1, together with the pressure scaling of all relaxation times t_1, t_2. τ_R, and T_2.* Figure 8-18(a) shows the mode-locking predictions when the m_0^2 parameter results in a slight focus at the absorber (m_0^2 = 1.8). The peak intensity predicted at the CO_2 amplifier is ∿140 MW/cm^2. Very poor discrimination and relatively little pulse narrowing (from 300 to 100 ps (FWHM)) occurs across the pulse train. Fig. 8-18(b) indicates that one can do much better if the laser beam is expanded, rather than contracted, at the Ge absorber (m_0^2 = 0.36). The peak intensity at the amplifer in this case is 80 MW/cm^2. The pulse FWHM narrows from ∿300 ps to 120 ps at the pulse train peak, to 70 ps for the last pulse shown in Fig. 8-18(b) and to ∿30 ps farther down on the mode-locked pulse tail. m_0^2 values significantly less than 0.36 failed to saturate the absorber, and poor mode-locking was obtained.

This section has demonstrated that deterministic mode-locking occurs at laser pressure of ∿1/3 atm. The excellent mode-locking stability at 1 atm is therefore due to a reduced set of starting pulses. This section has also indicated that it will be harder to obtain clean mode-locking at high laser gas pressures due to the increased statistical nature of the starting pulse distribution. A further problem at high laser pressures (e.g., 10 atm) will be the rapid decay of the upper vibrational level, thereby preventing sustained operation near lasing threshold. This section has also demonstrated the importance of selecting the correct amplifier-to-absorber beam area ratio parameter m_0^2 in producing stable, clean, narrow mode-locked pulses.

---

* The scaling should be possible for pressures up to ∿5 atm. Care must be taken for higher pressures due to the significant overlap of rotational lines and the inclusion of sequence band lines [115].

Fig. 8-18

Theoretical predictions for the output intensity of a 5 atm CO_2 laser for m_0^2 values of 1.8(a) and 0.36(b). The round trip time is 11.4 ns. Each horizontal division corresponds to 2.2 ns.

(a)

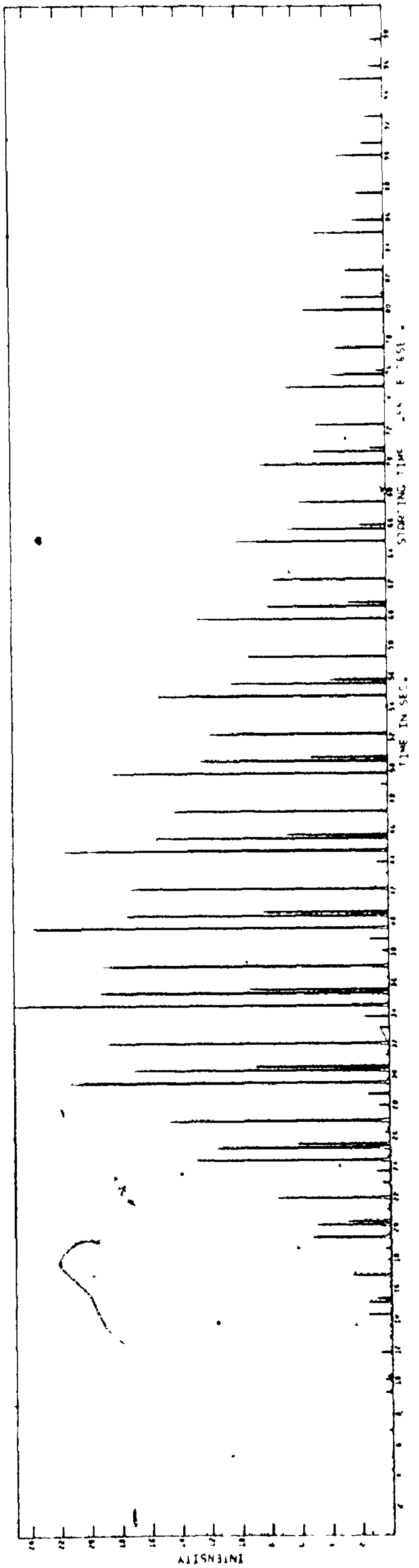
INTENSITY
TIME IN SEC.
STARTING TIME

(b)

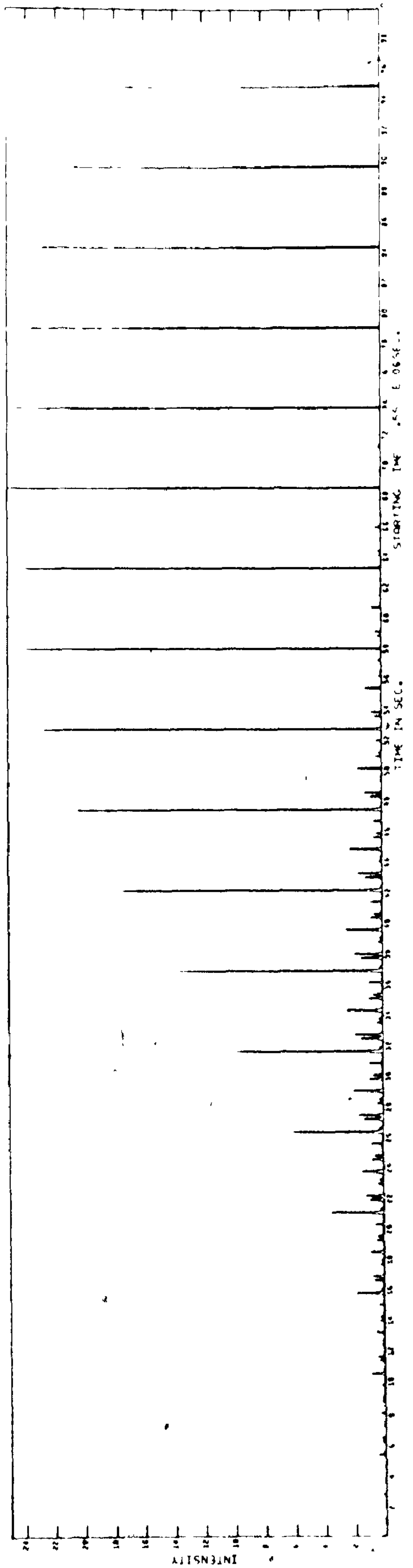
INTENSITY
TIME IN SEC.
STARTING TIME

8.11 Pressure Scalability of the Mode-Locked Output Characteristics

In this chapter we have described mode-locking simulations at gas pressures of 1/3 to 5 atm and have obtained experimental mode-locking data at pressures of 1/3 to 1 atm. It is therefore appropriate to comment on the pressure scalability of the various parameters such as peak pulse intensity, pulse energy, pulse duration, and total energy in a mode-locked pulse train,as well as the scaling of m_0^2.

The gain parameter g_{max} is independent of pressure for pressures >50 Torr and pressures ≤ 5 atm.* Since the Ge saturation intensity is obviously independent of CO_2 laser pressure the quantity m_0^2 must be scaled inversely with the square of the pressure to achieve optimum mode-locking. At fixed linear and non-linear losses and gain,and scaling m_0^2 in such a manner,one finds that the peak pulse intensities at the amplifier scale proportional to the pressure squared, the pulse energy proportional to pressure, and therefore the pulse duration inversely proportional to pressure.** Since the mode-locked train envelope durations are very similar at the different pressures the total energy in the mode-locked train also scales with pressures.

8.12 Influence of Cavity Length on Mode-Locking

Long laser cavities possess small axial mode separations (c/2L).

---

* At pressures >50 Torr the increased number density in the upper and lower lasing levels is compensated by a reduced radiative cross-section. Above 5 atm overlap of rotational lines and sequence band lines must be taken into account.

** This arguement strictly refers to the initial pulse durations but can apply to other pulse durations as well since similar narrowing factors across the pulse train are obtained for all the pressures studied.

The increase in the number of axial modes under the gain bandwidth leads to a corresponding increase in the number of initial noise fluctuations of slightly shorter initial duration $\Delta t_{f\ell}$. It was pointed out in Section 7.3 that under most circumstances the linear pulse broadening in nearly independent of $\Delta t_{f\ell}$, but depends on T_2, g_{max}, La and N, all quantities which have no explicit dependence on cavity length. In this case the starting pulses at t_d, for long laser cavities, will have similar durations to those of much shorter cavities. However, the longer cavity can accomodate many more starting fluctuations, thereby increasing the statistical nature of the input pulse distribution. When one is dealing with only 2 to 3 initial pulses per round trip an increase in cavity length by a factor of two can be significant. It has been observed experimentally that there was a greater occurence of a large number of pulses per round trip time in mode-locking with the 3 m long 3-mirror cavity as opposed to the 1.71 m 2-mirror cavity (with all other parameters constant). Therefore, a short cavity length may be suitable for further optimizing the mode-locking once the optimum values for the other parameters (gain, loss etc.) have been found.*

8.13 Comparison of SF_6 and Ge as Passive Mode-Lockers

Although there are a number of candidates for passive mode-locking at 10.4 μm, SF_6 and Ge are certainly the most widely used. In order to compare the SF_6 and Ge mode-locking capabilities it is of course necessary to establish suitable selection criteria. For example, if one is interested in obtaining sub-ns pulses operating on multi-rotational line or multi-vibrational band wavelengths, then Ge is the only possibility. Los Alamos Laboratories have in fact been keenly interested in the short pulse, multi-line (band) operation of a Ge mode-locked oscillator for their large CO_2 amplifier systems [24]. However, if one only requires ∿2 ns pulses on one rotational line, then the comparison between saturable absorbers is much closer. Table 8-2 outlines such a comparison between Ge and SF_6. The outstanding features of each absorber have been underlined in this table; however, one or two of the features deserve some clarification. The Ge saturation parameter varies very slowly with CO_2 wavelength.* This is an advantage since it is not necessary to change the cavity design to obtain the optimum m_0^2 setting when one changes the lasing wavelength. On the other hand, the SF_6 system can be quite easily scaled to accomodate large aperture lasers and can be very easily scaled to be used with both low and high gain lasers by simple variation of the SF_6 and buffer gas pressures. Furthermore, variable mode-locked pulse durations in the range 2 to 7 ns can be obtained with an SF_6 absorber, again by changing only the SF_6 and buffer gas pressures.

---

* Once the cavity length is shortened to the point that the initial number of axial modes at t_d is small, (say < 10) one begins to sacrifice the ability to get short pulses due to the increased starting pulse duration at t_d.

---

* Los Alamos have recently reported a factor of 2 increase in I_S for the 9.4 μm band compared to the 10.4 μm band value (June 1977 CLEA conference in Washington D.C.)

TABLE 8-2

Comparison of Ge and SF_6 Mode-Lockers

	Ge	SF_6
Wavelength Range	Multi-line Multi-band	Single line
Damage Threshold (for a 1 ns pulse)	~ 1 J/cm^2*	$\gtrsim 5$ J/cm^2†
Min. Pulse Duration††	350 ps (exp)	$\gtrsim 1.5$ ns (exp)
Saturation Parameter (I_s)	$I_s^i \sim 3$ MW/cm^2	Function of wavelength, typically << 1 MW/cm^2
Scalability of $\alpha_o L^B$	Vary Ge thickness and/or Ge doping (expensive)	Vary cell thickness or SF_6 pressure
Pulse Discrimination (D)	D > 50**	D > 50**
Number of Variable Elements	Laser discharge only	Laser plus gas flow system
M.L. Intensity Stability	Excellent, $\lesssim 10\%$	Good, $\lesssim 15\%$
Variability of Pulse Length††	0.3 to 2 ns	1.5 to 6 ns (by changing SF_6 and/or buffer gas pressures)

---

* The value may be as low as 0.2 J/cm^2 for AR coated Ge.

† Refers to the damage threshold of the salt windows (NaCℓ or KCℓ).

†† Values are appropriate for a TEA CO_2 laser.

** This value was limited by detector noise pick-up.

8.14 Summary

This chapter has described the measurement of the basic mode-locking parameters for p-type Ge. The major portion of the chapter described the quantitative theoretical and experimental comparison of the mode-locking process for a TE CO_2 laser and a Ge saturable absorber. The purpose of such a treatment was to define the regions for which stable, clean mode-locking could be obtained. Furthermore, the regions for which large intensity, short duration pulses occur could also be determined. The understanding of the mode-locking process should facilitate predicting the effect of variation of any of the mode-locking parameters on the output characteristics, as well as predicting the scalability of the system to larger CO_2 laser pressures. The conclusions of this chapter are as follows.

(a) The theory can successfully predict the experimentally observed pulse narrowing, output intensities, and mode-locked train temporal profiles, for a wide range of parameters.

(b) Standing wave effects do occur in TE CO_2-Ge mode-locking systems and can either lead to double-pulse production or to pulse broadening.

(c) The inclusion of rotational coupling in the theoretical analysis is important in obtaining good mode-locking and in predicting the pulse shaping of individual mode-locked pulses.

(d) The ratio of the laser beam area at the amplifier to that of the absorber is an important parameter for optimum mode-locking. Experimental values of m_0^2 of 4 to 6 are acceptable for a TEA CO_2 laser.

(e) The m_0^2 parameter is of even greater significance for high pressure CO_2 lasers since one is more severely restricted in the ability to vary the other mode-locking parameters to compensate for a non-ideal m_0^2. An expanded beam area at the absorber should be used for multi-atm mode-locking.

(f) One can operate neither too close nor too far from lasing threshold to obtain stable, clean mode-locking. Gain coefficient values ∿10% above the $g_{max}L_a$ to just obtain lasing action should prove near optimum.

(g) Better discrimination and pulse narrowing can be achieved at lower linear losses. Equivalent reflectivities $\gtrsim 0.65$ should be satisfactory.

(h) Large values of the non-linear loss ($\alpha_0 L^B$) ultimately produce the shortest pulses. However, non-linear to linear loss ratios $\gtrsim$ 5 should be adequate for short pulse production.

(i) Experimental evidence of deterministic mode-locking occurs at laser pressures of 200 to 250 Torr, in reasonable agreement with the theoretical prediction of ∿300 Torr. The excellent experimental mode-locking stability ($\lesssim$10% intensity variation) and discrimination ($D \gtrsim 50$) observed at 1 atm laser pressures is due primarily to the small number of starting pulses at the beginning of the non-linear gain and loss regions.

(j) All other parameters considered equal, a short cavity length may improve the mode-locking stability and discrimination.

To date Ge has produced the shortest pulses of any saturable absorber at the 10.4 μm CO_2 band. Pulses in the order of 350 ps for a

TEA CO_2 laser have been obtained by several different research groups [21], including the group here at McMaster University. Pulses as short as 150 ps have been obtained at N.R.C. (Ottawa) using a 12 atm CO_2 laser [12]. The fast absorber recovery time of Ge should allow the generation of 10 to 50 ps pulses in the future. Such pulses are of extreme interest for their used as starting pulses in long chain or multi-pass CO_2 amplification systems. The aim of such a system is to produce high energy, high power pulses to initiate controlled nuclear fusion. The interest will undoubtedly be intensified since it was announced at the 1977 CLEA conference in Washington D.C. that the CO_2 laser must now be considered the prime laser candidate for controlled nuclear fusion. The major drawback of Ge at this moment, whether it is used as a mode-locker or as an isolator in large multi-pass amplifier systems, is its low damage threshold. If this problem can be alleviated then Ge would be the CO_2 saturable absorber par excellence!

CHAPTER 9

CONCLUSIONS

The research in this thesis has provided, for the first time, an understanding of the passive mode-locking behaviour of TE CO_2 lasers employing the saturable absorbers SF_6 and Ge. This chapter outlines the important conclusions that can be drawn from our work and discusses the overall significance of the research.

It has been emphasized on several occasions throughout the thesis that, in order to predict the mode-locking process, it is important to know the dynamical behaviour of the saturable absorber on a sub-ns to μs time scale. In the case of SF_6 the dynamical behaviour was simply not known previous to our research. Chapters 3 to 5 of this thesis discuss in detail the saturation and dynamical processes involved in the SF_6 absorption of pulsed radiation, using such powerful investigative tools as non-linear transmission and infra-red double-resonance spectroscopy. The non-linear behaviour of SF_6 was measured for the first time, over a range of CO_2 wavelengths that characterized the entire SF_6 absorption at 10.4 μm (P(12) to P(28)) and over a range of gas pressures used in mode-locking experiments (10-400 Torr). The transmission curves, as well as the details of the associated pulse shaping, could be accounted for over this wide range of CO_2 wavelengths and SF_6 gas pressures using intensity saturation and vibrational bath heating effects. Chapter 6 demonstrates that the mode-locking behaviour of a TE CO_2 laser, used in conjunction with an SF_6 saturable absorber, could also be predicted from a knowledge of the saturation and vibrational heating effects. In the case of Ge, it was initially not clear whether a homogeneous or an inhomogeneous treatment of the saturation process was appropriate. The evidence accumulated in this thesis indicates that an inhomogeneous treatment best describes the saturation behaviour. In addition, the dynamical behaviour associated with the evolution of mode-locked pulses in a Ge-CO_2 mode-locking system was not well known. For example, the conditions necessary to produce very short, stable, high intensity mode-locked pulses, and the quantitative effect of varying the laser and cavity parameters in the production of such pulses, have not been discussed in the literature. Chapter 7 describes the development of mode-locked pulses from a noise source. In Chapter 8, it is shown that the theoretical predictions are in excellent quantitative agreement with mode-locking experiments. Such agreement allows accurate prediction of the quantitative effects of varying the laser, absorber and resonator parameters.

The main conclusions of each chapter are summarized below. Section 3.2 presents accurate measurements of the small-signal absorption coefficients of SF_6 for a wide range of CO_2 wavelengths (P(12) - P(28)). The measurements were performed with a laser probe source having the same pulse characteristics as that employed in all the large-signal transmission measurements. It is observed that the absorption coefficients are linearly dependent on pressure in the range 10 to 200 Torr, consistent with the absorption being due to a large number of overlapping resonance lines. Section 3.3 outlines the first complete study of the saturation behaviour (to pulsed radiation) of SF_6 over a wide range of wavelengths (P(12) - P(28)) and gas pressures (10 - 200 Torr). The 4-level analysis presented in that section provides information on the contribution of excited-state absorption to the total absorption, and provides values of the saturation parameters which characterize the intensity saturation behaviour of SF_6. The scalability of the level relaxation times with SF_6 pressure is also demonstrated in Section 3.3. Particular emphasis is placed on obtaining measurements of both the transmission behaviour (at the peak intensity) and the entire pulse shaping characteristics to obtain a restricted set of 4-level parameters. It is concluded that a 4-level intensity saturation model is adequate for the description of the transmission behaviour of low J-value CO_2 rotational lines. Agreement between theory and experiment becomes progressively poorer at the longer CO_2 wavelengths.

In Chapter 4 a vibrational bath model is proposed to account for the discrepancies at the longer wavelength lines. The model has remarkable success in predicting the transmission behaviour of double-resonance experiments performed at low SF_6 pressures. This is particularly impressive since previous publications predicted that a vibrational equilibrium could not be maintained over the pulse duration at those low pressures. Infrared double-resonance experiments detailed in Chapter 4 indicate that V-V and rotational relaxation times (<20 ns-Torr, 6 ns at 1 Torr, respectively) are much faster than indicated in the literature and explain the success of the model at the low pressures. It is also suggested that such a model has wider applicability than to the case of SF_6 and should apply to other polyatomic molecules such as $BC\ell_3$, N_2F_4, $CF_2C\ell_2$, SiF_4 which interact with pulsed CO_2 radiation.

Chapter 5 demonstrates the success of the vibrational bath model in predicting the transmission and pulse shaping behaviour for all the CO_2 lines at high SF_6 pressures. This chapter indicates that, although the SF_6 absorption was strongly "saturated" at these high pressures, no genuine intensity dependent saturation effects occur. It is further concluded that the contribution of vibrational heating is significant at low SF_6 pressures for the high J-value CO_2 lines such as P(26). In these cases, genuine intensity saturation of the absorption becomes more difficult since the saturation involves a greater number of tightly coupled levels than for the lower J-value CO_2 lines. In most of the transmission experiments reported in this thesis, the incident pulse durations were ∿200 ns. Since vibrational heating effects are energy rather than intensity dependent the exact behaviour of the transmission curves for the longer wavelength CO_2 lines will depend on the laser pulse duration used. However, the range of pulse durations for which the vibrational bath model is expected to apply is very large due to the short V-V and rotational relaxation times observed at even moderate SF_6 pressures.

It is concluded in Chapter 6 that the observed mode-locking with an SF_6 saturable absorber can be predicted from a combination of the intensity saturation processes outlined in Chapter 3 and the heating effects described in Chapters 4 and 5. This agreement emphasizes the importance of knowing the exact dynamical characteristics of the saturable absorber in order to fully understand its mode-locking behaviour. Chapter 6 also reported the first record of mode-locking on the P(12), P(14), and P(28) CO_2 rotational lines. The choice of the proper value of the beam area parameter m_0^2 was the important consideration in obtaining mode-locking on these lines. The mode-locked pulse durations obtained are on a par with the shortest durations recorded in the literature (1.5 ns). It was not possible, however, to obtain sub-ns duration pulses. Mechanisms such as multi-level saturation, vibrational heating and multiple-photon absorption are proposed as possible explanations for this apparent minimum pulse duration.

In Chapters 7 and 8, dealing with Ge mode-locking, it is shown that a relatively straightforward computer model incorporating proper allowance for rotational coupling successfully describes the Ge-CO_2 mode-locking behaviour. It is concluded that as the TE CO_2 laser pressure is raised, there is a progression from deterministic mode-locking (at ∿300 Torr) to mode-locking whose starting pulse distribution consists of 2 to 3 pulses per round trip time (at ∿1 atm) and then to mode-locking from a progressively more statistical starting pulse distribution (at ∿5 atm). The mode-locking experiments and computer simulations demonstrate that there are optimum parameter settings necessary to obtain narrow, high intensity mode-locked pulses. Estimates of how close to lasing threshold, the range of linear and non-linear losses, and which cavity configuration and m_0^2 are best suited for optimum mode-locking are given in those chapters (7 and 8)

In conclusion, this thesis demonstrates the importance of understanding the dynamical properties of both the saturable absorber and the gain medium in predicting the mode-locked behaviour of TE CO_2 lasers incorporating SF_6 and Ge saturable absorbers. The results of this thesis should be very useful in enabling researchers not only to understand and be able to optimize CO_2-Ge and CO_2-SF_6 mode-locking systems, but also to understand the mode-locking characteristics of other pulsed laser systems using saturable absorbers.

APPENDIX A

CALCULATION OF 3-MIRROR CAVITY PARAMETERS

In this appendix the beam radii (ω_i) and resonator stability criteria are calculated using the formulae in Ref. [36]. The formulae are appropriate for Gaussian (TEM_{oo}) beams propagating in an empty (no gain) laser cavity, such as shown in Fig. 2-7.

The fundamental mode of the electric field in any beam cross-section varies as

$$\exp\left(-r^2/\omega_i^2 - j\left(\frac{r^2}{\lambda R}\right)\right) \quad . \tag{A-1}$$

In Eq. (A-1), R represents the radius of curvature of the phase front. The 1/e beam intensity diameter is defined by Eq. (A-1) as $\sqrt{2}\,\omega_i$. The analysis of the 3-mirror cavity is treated in a similar fashion to a 2-mirror cavity with an internal lens of focal length f. A 3-mirror equivalent resonator is constructed with the cavity parameters defined in Fig. 2-7. The laser stability criteria are defined in terms of G_1 and G_2 by [36]

$$0 \leq G_1 G_2 \leq 1 \quad , \tag{A-2}$$

where

$$G_1 = [1 - d_2/f - \frac{1}{R_1}(d_1 + d_2 - d_1 d_2/f)] \tag{A-3}$$

and

$$G_2 = [1 - d_1/f - \frac{1}{R_2}(d_1 + d_2 - d_1 d_2/f)]. \tag{A-4}$$

The expression in round brackets can be replaced by a parameter d_o. The beam radii at mirrors M1 and M2 can be determined from

$$\omega_1\omega_2 = \frac{\lambda do}{\pi}(1 - G_1G_2)^{-1/2} \tag{A-5}$$

and

$$\omega_1/\omega_2 = (G_2/G_1)^{1/2} . \tag{A-6}$$

Different values for d_2, d_1, R_1, R_2, and f were tried in the above equations to maximize ω_1, ω_2 (and minimize ω_o, the minimum beam radius) while still keeping within the stable lasing regions. The values for the parameters obtained for our cavity were $d_2 = 1.95$ m, $d_1 = 1.05$ m, $f = 0.52$ m, $R_1 = 0.52$ m, and $R_2 = \infty$. Using these values in Eqs. (A-3) and (A-4) we obtain $G_1 = -0.95$ and $G_2 = -1.02$,or $G_1G_2 = 0.97$, which satisfies the stability condition (Eq. (A-2)) for a low diffraction loss cavity. Substitution of these values in Eqs. (A-5) and (A-6) yields values of 0.42, and 0.41 cm for ω_1 and ω_2, respectively. The beam diameters at mirrors 1 and 2 are therefore 0.60, and 0.58 cm,respectively. In order to calculate the beam radius ω_o one must define an equivalent radius of curvature R_2' by [37]

$$R_2' = \frac{R_2 f^2}{(d_2 - f)(d_2 - R_2 - f)} , \tag{A-7}$$

which for our cavity values reduces to

$$R_2' \sim \frac{-f^2}{(d_2 - f)} = -0.19 \text{ m} \quad . \tag{A-8}$$

An effective resonator separation, defined by

$$d = d_1 - \frac{d_2 f}{d_2 - f} = 0.34 \text{ m} \quad , \tag{A-9}$$

is also necessary to calculate ω_0 using the formula

$$\omega_0^4 = \frac{\lambda^2 d(R_1 - d)(R_2' - d)(R_1 + R_2' - d)}{\pi^2(R_1 + R_2' - 2d)^2} \tag{A-10}$$

obtained from Ref. [37]. On substitution of the appropriate values we determine that $\omega_0 = 0.042$ cm. These formulae therefore predict that there should be a factor of 10 reduction in the beam diameter (100 in beam area) at the position of the minimum beam waist relative to that of the beam diameters at mirrors M1 and M2.

APPENDIX B

FINITE DIFFERENCE METHOD

The (x,t) plane is divided into a 2-dimensional array of points A(m,n) in which the space and time points (m and n, respectively) are separated by Δx, Δt increments, where $\Delta x = c\Delta t$. A Taylor expansion is carried out about (m,n) for each differential equation. For example,

$$\frac{\partial E(m,n)}{\partial t} = \frac{E(m,n+1) - E(m,n)}{\Delta t} - \frac{\Delta t}{2}\frac{\partial^2 E(m,n)}{\partial t^2}, \qquad \text{(B-1)}$$

and

$$\frac{\partial E(m,n)}{\partial x} = \frac{E(m,n) - E(m-1,n)}{\Delta x} + \frac{\Delta x}{2}\frac{\partial^2 E(m,n)}{\partial t^2} \qquad \text{(B-2)}$$

with similar expressions for P, D_1, D_2 and δ^{J_o}. The second order derivatives can be removed from these equations by differentiating the original density equations and substituting in the first order derivative expressions. Summation of Eqs. (B-1) and (B-2) yields the electric field density equation ((7-14)). Substitution of Eq. (7-14) eliminates the left hand side of the above summation. Further substitutions to eliminate all first order derivatives results in the following expressions.

$$E(m,n+1) = d_1 E(m-1,n) + d_2 P(m,n) + d_3 \delta^{J_o}(m,n) + d_4 P(m-1,n)$$

$$d_1 = 1.0$$

$$d_2 = \frac{\Delta t \gamma_\perp G_a}{2} [1 - \gamma_\perp \Delta t] \qquad \text{(B-3)}$$

$$d_3 = \frac{\Delta t^2}{2} \gamma_\perp^2 G_a / \kappa(J_o)$$

$$d_4 = \frac{\Delta t}{2} \gamma_\perp G_a$$

Similarly one obtains

$$D_1(m, n + 1) = a_1 D_1(m,n) + a_2 P(m,n)E(m,n) + a_3 P^2(m,n) + a_4$$

$$P(m,n)E(m - 1,n) + a_5 \delta^{Jo}(m,n)E^2(m,n)$$

$$a_1 = 1.0 - [1.0 - \frac{\Delta t}{2t_1}] \Delta t/t_1$$

$$a_2 = \frac{\Delta t \gamma_\perp}{4} [1 - \gamma_\perp \Delta t - \Delta t/t_1] \qquad \text{(B-4)}$$

$$a_3 = \frac{\gamma_\perp^2 \Delta t^2 G_a}{4}$$

$$a_4 = \frac{\gamma_\perp \Delta t}{4}$$

$$a_5 = \frac{\gamma_\perp^2 \Delta t^2}{4\kappa(J_o)}$$

$$D_2(m,n + 1) = b_1 D_2(m,n) + b_2 P(m,n)E(m,n) + b_3 P^2(m,n) + b_4$$

$$P(m,n)E(m - 1,n) + b_5 \delta^{Jo}(m,n)E^2(m,n)$$

$$b_1 = 1.0 - [1.0 - \frac{\Delta t}{2t_2}]\Delta t/t_2$$

$$b_2 = \frac{-\Delta t \gamma_\perp}{4} [1.0 - \gamma_\perp \Delta t - \Delta t/t_2] \qquad \text{(B-5)}$$

$$b_3 = \frac{-\gamma_\perp^2 \Delta t^2 G_a}{4}$$

$$b_4 = \frac{-\gamma_\perp \Delta t}{4}$$

$$b_5 = \frac{-\gamma_\perp^2 \Delta t^2}{4\kappa(J_o)}$$

$$\begin{aligned} P(m,n+1) = {} & C_1 P(m,n) + C_2 E^2(m,n) P(m,n) + C_3 E(m,n) D_2(m,n) \\ & + C_4 E(m,n) D_1(m,n) + C_5 E(m,n) \delta^{Jo}(m,n) + C_6 E(m-1,n) \\ & \delta^{Jo}(m,n) + C_7 \delta^{Jo}(m,n) P(m,n) \end{aligned}$$

$$C_1 = 1.0 - \left(1.0 - \frac{\gamma_\perp \Delta t}{2}\right) \Delta t \gamma_\perp$$

$$C_2 = \frac{-\Delta t^2 \gamma_\perp^2}{2\kappa(Jo)}$$

$$C_3 = \frac{\Delta t^2 \gamma_\perp}{2\tau_R} \qquad \text{(B-6)}$$

$$C_4 = \frac{-\Delta t^2 \gamma_\perp}{2\tau_R}$$

$$C_5 = \frac{\Delta t \gamma_\perp}{2\kappa(Jo)} \left[1.0 - \gamma_\perp \Delta t - \Delta t/\tau_R\right]$$

$$C_6 = \frac{\Delta t \gamma_\perp}{2\kappa(Jo)}$$

$$C_7 = \frac{\Delta t^2}{2} \gamma_\perp^2 G_a/\kappa(J_o)$$

$$\begin{aligned} \delta^{Jo}(m,n+1) = {} & e_1 \delta^{Jo}(m,n) + e_2 E(m,n) P(m,n) + e_3 P^2(m,n) \\ & + e_4 P(m,n)\, E(m-1,n) + e_5 \delta^{Jo}(m,n)\, E^2(m,n) \\ & + e_6 D_2(m,n) + e_7 D_1(m,n) \end{aligned}$$

$$e_1 = 1.0 \frac{-\Delta t}{\tau_R} + \frac{\Delta t^2}{2\tau_R^2}$$

$$
\begin{aligned}
e_2 &= \frac{-\Delta t \gamma_\perp}{2} \left(1.0 - \gamma_\perp \Delta t - \frac{\Delta t}{\tau_R} + \frac{\kappa(J_o)\Delta t}{\tau_R}\right) \\
e_3 &= \frac{-\gamma_\perp^2 \Delta t^2 G_a}{2} \\
e_4 &= \frac{-\gamma_\perp \Delta t}{2} \\
e_5 &= \frac{-\gamma_\perp^2 \Delta t^2}{2\kappa(J_o)} \\
e_6 &= \frac{\kappa(J_o)\Delta t}{\tau_R} \left[1.0 \; \frac{-\Delta t}{2t_2} \quad \frac{-\Delta t}{2\tau_R}\right] \\
e_7 &= \frac{-\kappa(J_o)\Delta t}{\tau_R} \left[1.0 - \frac{\Delta t}{2t_1} - \frac{\Delta t}{2\tau_R}\right]
\end{aligned}
\tag{B-7}
$$

In the above expressions $\gamma_\perp = 1/T_2$, $G_a = g_o c T_2/2$ and $\kappa(J_o)$ is defined by Eq. (7-6). At a time t the input flux to the amplifier is propagated through a number of amplifier segments, establishing new values for E,P, D, etc. The calculation is then carried out for the next time interval $(t + \Delta t)$ and input intensity increment (ΔI). This is repeated until all the time intervals have been used for a complete round trip time 2L/c. The whole process is repeated with the resulting transformed input pulse for each of the N round trips. The time interval Δt must be shorter than either the dipole dephasing time (T_2) or the inverse of the stimulated emission rate (which is intensity dependent) in order to obtain stable and accurate pulse progagation. Only five amplifier spatial increments were used in order to reduce computer costs. Twice as many increments changed the final parameters by less than 5%. It should be mentioned that the finite difference equations given above must be modified at the input to the amplifier to correct for the spatial discontinuity at the amplifer input. This can be done by redefining Eq. (B-1) as

$$\frac{\partial E(m,n)}{\partial t} = \frac{E(m,n+1) - E(m,n)}{\Delta t} \qquad \text{(B-8)}$$

and repeating the procedure to determine E(m,n + 1), etc. The use of Eq. (B-8) changes the finite difference equations. In the equations for D_1, D_2, δ^{Jo}, a_3, b_3, e_3 are set to zero and the P(m,n) E(m - 1,n) term is replaced by P(m,n) E(m,n + 1). For the equation involving P, $C_2 = 0$ and E(m - 1,n) $\delta^{Jo}(m,n)$ is replaced by E(m,n + 1) $\delta^{Jo}(m,n)$.

APPENDIX C

BAND CONTOUR MODEL

The intensity of an absorption from a lower molecular state ℓ to an upper state u can be expressed as [61]

$$k_{\ell u}(\nu) = \frac{8\pi^3 \nu_{\ell u}}{3hc} |\langle \ell|\mu|u\rangle|^2 [1 - \exp(\frac{-h\nu_{\ell u}}{KT_V})] N_\ell f(J,T_R) \ , \qquad \text{(C-1)}$$

where N_ℓ refers to the population of the lower state. Here the quantity $f(J,T_R)$ involves the rotational dependence and has the form [62]

$$f(J,T_R) = A_{J,\nu} g_J Q_J^{-1} \exp(\frac{-BJ(J+1)hc}{KT_R}) \ , \qquad \text{(C-2)}$$

where Q_J is the rotational partition function, g_J the degeneracy of the rotational level, and $A_{J,\nu}$ the transition amplitude, which for octrahedral molecules has the value [63]

$$A_{J,\nu} = \frac{2J-1}{2J+1} \qquad \text{P-branch}$$

$$A_{J,\nu} = 1 \qquad \text{Q-branch} \qquad \text{(C-3)}$$

$$A_{J,\nu} = \frac{2J+3}{2J+1} . \qquad \text{R-branch}$$

The contribution of all the rotational lines that can absorb within a line-width $\Delta\nu$ is included by means of a scale factor $\Delta\nu/|\Delta\nu_J|$, where $\Delta\nu_J$ is the spacing between adjacent rotational lines in the neighbourhood of a given J. The product of this scale factor and $f(J,T_R)$ can be considered as an effective rotational cross-section. For the case of SF_6 it is found to be a slowly varying function of rotational temperature as is discussed further in the text.

By regarding the ν_3 mode as an independent harmonic oscillator, it can be shown that

$$|\langle \ell|\mu|u\rangle|^2 = \frac{h}{8\pi^2 c\nu_{\ell u}}\left(1+\frac{v_3}{3}\right)\left(\frac{d\mu}{dQ_3}\right)^2 , \tag{C-4}$$

where v_3 is the number of ν_3 quanta present in the lower level. The factor 1/3 accounts for the 3-fold degeneracy of the ν_3 mode.

Using the value of $d\mu/dQ_3$ given in Ref. [64] and setting $\nu_{\ell u}$ equal to the ν_3 fundamental, results in

$$|\langle \ell|\mu|u\rangle|^2 = (1.50 \pm 0.15) \times 10^{-37}\ (\text{esu-cm})^2 . \tag{C-5}$$

Substituting in the standard Boltzmann expression for N_ℓ and summing the contributions from the vibrational (E_v) and rotational (J) levels involved, as given by Eq. (C-1), yields the total absorption coefficient

$$\alpha(\nu)\Delta\nu = (1.91 \pm 0.20)\sum_{E_v}\left[1-\exp\left(-\frac{h\nu}{KT_v}\right)\right]\left(1+\frac{v_3}{3}\right)g(E_v)Q_v^{-1}\exp\left(-\frac{E_v}{KT_v}\right)$$

$$\times \sum_J Q_J^{-1}A_{J,\nu}(2J+1)^2\,\frac{\Delta\nu}{|\Delta\nu_J|}\exp\left[-\frac{BJ(J+1)hc}{KT_R}\right] , \tag{C-6}$$

in units of cm^{-1}-Torr^{-1}. The summation is to be evaluated for all J values at each value of E_v.

The values of J to be summed over at any vibrational level can be obtained in the following manner. The frequency of a ν_3 transition from a particular vibrational level represented by a set of quantum numbers $\{v_i\}$, is [62]

$$\nu\{v_i\} = \nu_0 + 2X_{33}v_3 + \sum_{i\neq 3} X_{3i}v_i \ , \qquad \text{(C-7)}$$

where ν_0 is the ground state transition frequency and the x_{3i} the anharmonicity coefficients.

The transition frequencies for the various branches are then obtained from

$$\nu(P) = \nu\{v_i\} - (B_3 + B_0 - 2B\zeta_3)J + (B_3 - B_0)J^2 \ ,$$

$$\nu(Q) = \nu\{v_i\} - (B_3 - B_0)J(J + 1) \ , \text{ and}$$

$$\nu(R) = \nu\{v_i\} + (B_3 + B_0 - 2B\zeta_3)(J + 1) + (B_3 - B_0)(J + 1)^2 \ . \qquad \text{(C-8)}$$

SF_6 has a very small rotational constant B. Therefore, the separation of rotational levels is such that, within the limits of the model, J can be considered as a continuous variable. Hence the summation over J in Eq. (C-6) is over all the positive real solutions of Eq. (C-8) when the frequency for the particular branch is set equal to that of the laser line.

The summation over all the vibrational levels would be a formidable task due to the high density of states in SF_6. However, application of the Whitten-Rabinovitch method [65] has been successful in obtaining both the proper density of states and the average values of the quantum numbers in those states [48]. The levels were considered as discrete up to 2000 cm^{-1} as the number of states in this region is still sufficiently low for practical calculation of the absorption coefficient as given by Eq. (C-6).

Values for the spectroscopic constants were taken from Ref. [64]. A best fit to the 300 K absorption spectrum for the CO_2 laser lines ranging from P(14) to P(32) was used to determine the optimum values of the anharmonicity coefficients. These are (in cm^{-1}) X_{31} = -2.1, X_{32} = -1.4, X_{33} = -2.6, X_{34} = -1.5, X_{35} = -1.5 and X_{36} = -1.0. Similarly, a value of 1.76 for the constant in Eq. (C-6) was found to give the best fit to the experimental data over the range specified above.

Jensen et al. [66] have recently calculated the anharmonic splittings for SF_6. Including such splittings in our model may provide a small improvement in the already good agreement between theory and experiment, but at the cost of considerably increased calculational complexity.

APPENDIX D

CONVERSION OF ELECTRIC FIELD AMPLITUDE TO INTENSITY

A two-level dipole moment can be defined in terms of the spontaneous emission rate by [95].

$$|\mu|^2 = \frac{3\hbar c^3 \varepsilon_0 A_{sp}}{16\pi^3 \nu^3} \text{ (mks units) ,} \tag{D-1}$$

where ε_0 is the permitivity of free space, h is Planck's constant, c is the speed of light, and ν is the CO_2 laser frequency. Using A_{sp}^{-1} = 5s [96], one obtains

$$|\mu| = 9.2 \times 10^{-32} \text{ C-m ,} \tag{D-2}$$

or

$$|\mu| = 9.2 \times 10^{-30} \text{ C-cm .} \tag{D-3}$$

For a real field amplitude $\mathcal{E}$ defined in Eq. (7-18) the intensity can be found using [97]

$$I = 1/2\ \varepsilon_0 c\ \mathcal{E}^2 \text{ (mks units),} \tag{D-4}$$

or

$$I = 1/2\ \frac{\varepsilon_0 c \hbar^2 E^2}{|\mu|^2 T_2^2} , \tag{D-5}$$

where we have used the electric field normalization defined in Eq.

(7-17). $|\mu|$ refers to the dipole moment between two rotational levels. However, since our equations are appropriate to the coupling of the radiation to two vibrational levels, it is therefore necessary to use $\kappa(J)|\mu|^2$ in Eq. (D-5), where $\kappa(J)$ is defined by Eq. (7-6) as the fraction of rotational levels, in equilibrium at a temperature T, that are in the rotational state J. For J = 19, $\kappa(19) \sim 1/15$. Substitution of $\kappa(J)|\mu|^2$ in Eq. (D-5) yields

$$I(\mathrm{W/cm^2}) = \left(\frac{2.6 \times 10^{-12}}{T_2^2}\right) E^2 \ , \tag{D-6}$$

where T_2 is in seconds. For $T_2 = 8.5 \times 10^{-11}$s (1 atm case) the conversion from normalized intensity E^2 to an intensity in W/cm^2 is given by

$$I = 3.6 \times 10^8 \, E^2 \ . \tag{D-7}$$

APPENDIX E

CALCULATION OF THE INTENSITY OF SPONTANEOUS EMISSION

The calculation of the spontaneous emission intensity for a single axial mode, near the peak of the vibrational-rotational emission line (P(20); 10.4 μm band) in a region about t_o, can be determined using the formula from Ref. [104].

$$I^{sp}(W/cm^2) = n_2 Lh\nu \left(\frac{\lambda^2\kappa(J)}{A}\right)\left(\frac{d\nu}{\pi\Delta\nu_c}\right) t_{sp}^{-1} , \qquad \text{(E-1)}$$

where

$$d\nu = (2\pi T_o)^{-1} , \qquad \text{(E-2)}$$

and

$$T_o = 2L/c\ (\ell n 1/R)^{-1} , \qquad \text{(E-3)}$$

and where

n_2 is the number of molecules/cc in the upper (00°1) vibrational level (typically 1.5 x 10^{17}/cc).

L is the length of the laser cavity (1.71 m).

$\kappa(J)$ is the fraction of the total rotational population in the J = 19 rotational state ($\kappa(19) \sim 0.066$).

A is the reflecting area of the smallest cavity mirror ($\sim 2.5 \times 10^{-5}$ m^2).

T_o is the cavity photon population decay time ($\sim 5 \times 10^{-8}$ s).

R is the equivalent mirror reflectivity which represents the total cavity losses ($R \sim 0.2$).

$\Delta\nu_c$ is the HWHM of the collision broadened linewidth (1.9×10^9 Hz, refer to Section 8.4(b)).

t_{sp}^{-1} is the spontaneous emission rate ($0.2 s^{-1}$,[96]).

h is Planck's constant (6.6×10^{-34} J-s).

$\nu(\lambda)$ is the CO_2 laser frequency (wavelength)(2.83×10^{13} Hz ($10.4\ \mu m$)).

On substitution of these values one obtains

$$I^{sp}(W/cm^2) \sim 5 \times 10^{-11}\ W/cm^2 \quad . \tag{E-4}$$

APPENDIX F

CALCULATION OF NOISE PULSE BROADENING IN THE LINEAR AMPLIFICATION REGION

In this appendix we shall calculate the pulse broadening of a single noise fluctuation having an initial duration $\Delta t_{f\ell}$. The calculation can be performed for a single pulse since the ensemble of noise pulses can be considered statistically independent in the linear gain region ($t \leq t_d$), where the stimulated emission processes do not cause significant gain depletion. As mentioned in Section 7.3 the calculation starts at a time (t_0) for which gain equals loss and continues to the start of the non-linear gain region (t_d). The frequency distribution of the noise pulse, assumed to be Gaussian and of amplitude E_0, is given by

$$N(\omega) = \Delta t_{f\ell}\ e^{\frac{-(\Delta t_{f\ell}^2)}{4}(\omega - \omega_0)^2} \qquad \text{(F-1)}$$

For ease of calculation the collision broadened Lorentzian gain distribution centered at a frequency ω_0 is also approximated by a Gaussian distribution.*

---

* This approximation results in at most a few percent error.

$$G(\omega) = G_o\, e^{\frac{-gLa}{2}(\omega - \omega_o)^2 T_2^2} . \qquad \text{(F-2)}$$

Here g is a single-pass intensity gain per unit length of gain medium of length L_a. T_2 is the dipole dephasing time, and G_o is defined by

$$G_o = e^{gL_a/2} . \qquad \text{(F-3)}$$

In the above equation the gain (g) is assumed constant as a function of time. Since the effective 2-level absorption bandwidth of ∼ 10^{13}Hz for a germanium saturable absorber, is much larger than the 3.8 x 10^9Hz/atm CO_2 gain bandwidth, it can be considered a constant over the gain bandwidth. Therefore, a constant A; defined in terms of the small-signal saturable absorption $\alpha_o L^B$ by

$$A = e^{-\alpha_o L^B/2} , \qquad \text{(F-4)}$$

is used for the loss frequency distribution $L(\omega)$. The frequency transfer function, $T(\omega) = G(\omega)L(\omega)$, is allowed to act on the initial noise distribution. This gives a filtered noise distribution, denoted by $S_n(\omega)$, such that

$$\begin{aligned} S_1(\omega) &= T_1(\omega)\, N(\omega) \\ S_2(\omega) &= T_2(\omega)\, T_1(\omega)\, N(\omega) = T_2(\omega)\, S_1(\omega) \qquad \text{(F-5)} \\ &\vdots \\ S_N(\omega) &= T_N(\omega)\, S_{N-1}(\omega) . \end{aligned}$$

N is defined as the number of round trips in a laser cavity of length L and in a time interval from t_o to t_d, i.e.,

$$N = (t_d - t_o)/(2L/c) \quad . \tag{F-6}$$

After substitution for $G(\omega)$, $L(\omega)$ and $N(\omega)$, we obtain

$$S_N(\omega) = \Delta t_{f\ell} E_o A^N G_o^N e^{-(\omega - \omega_o)^2[NgL_aT_2^2 + \Delta t_{f\ell}^2/4]} \quad . \tag{F-7}$$

The corresponding amplitude function in the time domain $f_N(t)$ can be obtained from $S_N(\omega)$ using Fourier transform theory.

$$f_N(t) = FT^{-1}[S_N(\omega)] \tag{F-8}$$

$$f_N(t) = \frac{1}{\sqrt{2\pi}} \int_{-\infty}^{\infty} S_N(\omega)\, e^{-i\omega t}\, d\omega \quad . \tag{F-9}$$

We are generally interested in the cases where $N > 50$, $gL_a \sim 1.0$, and $\Delta t_{f\ell}$ is a few times T_2. Thus $gL_aNT_2^2 >> (\Delta t_{f\ell}/2)^2$ and $\Delta t^2/4$ can be neglected compared to $gL_aNT_2^2$ in Eq. (F-7). In this case the final pulse duration will be independent of the initial pulse duration. Eq. (F-9) can therefore be written as

$$f_N(t) = \frac{\Delta t_{f\ell} E_o A^N G_o^N}{\sqrt{2\pi}} e^{-gL_aNT_2^2\omega_o^2} \int_{-\infty}^{\infty} \exp - (gL_aNT_2^2\omega^2 - 2gL_aNT_2^2\omega\omega_o) \exp - (i\omega t)d\omega. \tag{F-10}$$

This integral is a generalized Gaussian integral of the form

$$J_o = \int_{-\infty}^{\infty} e^{-\alpha x^2 - \beta x}\, dx \,, \tag{F-11}$$

where

$$\beta = -2gL_a NT_2^2 \omega_o + it$$

$$\alpha = gL_a NT_2^2 \tag{F-12}$$

$$x = \omega$$

The solution of Eq. (F-11) is

$$J_o = \sqrt{\frac{\pi}{\alpha}}\, e^{B^2/4\alpha} \tag{F-13}$$

Therefore

$$f_N(t) = \frac{\Delta t_{f\ell} E_o A^N G_o^N}{\sqrt{2\pi}}\, e^{-NgLaT_2^2\omega_o^2} \sqrt{\frac{\pi}{gL_a NT_2^2}}\, e^{\left(\frac{-t^2+(2gL_a NT_2^2)^2\omega_o^2}{4\Delta gL_a NT_2^2}\right)}\, e^{\frac{-i4gL_a NT_2^2\omega_o t}{4\Delta gL_a NT_2^2}} \,, \tag{F-14}$$

which reduces to

$$f_N(t) = \frac{\Delta t_{f\ell} E_o A^N G_o^N}{\sqrt{2gLNT_2^2}}\, e^{\frac{-t^2}{4gL_a NT_2^2}}\, e^{-i\omega_o t} \tag{F-15}$$

The noise pulse intensity distribution after N round trips is given by

$$I(t) = f_N(t) f_N^*(t) \quad , \tag{F-16}$$

or

$$I(t) = \frac{\Delta t_{f\ell}^2 |E_o|^2}{2gL_a N T_2^2} \, e^{N(gL_a - \alpha_o L^B)} \, e^{\frac{-t^2}{2gL_a N T_2^2}} \quad . \tag{F-17}$$

The FWHM of the Gaussian noise pulse, e^{-t^2/γ^2}, is

$$\sqrt{4\ell n 2\gamma^2} \quad , \tag{F-18}$$

which results, for our case, in a pulse duration

$$t_p(\text{FWHM}) = T_2 \sqrt{8\ell n 2 g L_a N} \quad , \tag{F-19}$$

provided that $\Delta t_{f\ell}^2/4 << gL_a N T_2^2$.

The above expression can be generalized to include the small contribution due to the initial noise duration $\Delta t_{f\ell}$ and the contribution due to a 2-level time-dependent gain defined by

$$g_n(t) = g_o(e^{-(t_o + n2L/c)/t_2} - e^{-(t_o + n2L/c)/t_1}), \tag{F-20}$$

where t_1 and t_2 are the times which characterise the rise and fall times, respectively of the gain. The resulting expression for the broadening due to the n^{th} double pass in the gain medium is given by

$$t_p(\text{FWHM}(n)) = \sqrt{8\ell n 2 g_n(t) L_a T_2^2 + 2\ell n 2 \Delta t_{f\ell}^{\ 2}} \quad ; \tag{F-21}$$

The total duration is found by iterating Eq. (F-21) over n until n = N. In most cases there is less than a 15% difference between calculations employing this expression and Eq. (F-19) since for most of the N round trips the gain is nearly flat.

REFERENCES

1. P.W. Smith, Proc. IEEE, 58, 1342 (1970).
2. D.H. Auston, IEEE J. Quantum Electron. (Corresp.), QE-4, 420 (1968).
3. M.H. Crowell, IEEE J. Quantum Electron., QE-1, 12 (1965).
4. J. Gilbert and J.L. Lachambre, Appl. Phys. Lett., 18, 187 (1971).
5. L.E. Hargrove, R.L. Fork, and M.A. Pollock, Appl. Phys. Lett., 5, 4 (1964).
6. L. Huff and L.G. DeShazer, J. Opt. Soc. Am., 60, 157 (1970).
7. A.J. DeMaria, D.A. Stetser and H. Heynau, Appl. Phys. Lett., 8, 174 (1966).
8. D.J. Bradley, Opto-electronics, 6, 25 (1974).
9. O.R. Wood and S.E. Schwarz, Appl. Phys. Lett., 12, 263 (1968).
10. K. Washio, K. Koizumi, and Y. Ikeda, IEEE J. Quantum Electron., QE-13, 47 (1977).
11. A.J. Beaulieu, Appl. Phys. Lett., 16, 504 (1970).
12. A.J. Alcock and A.C. Walker, Appl. Phys. Lett., 25, 299 (1974).
13. D.L. Lyon, E.V. George, and H.A. Haus, Appl. Phys. Lett., 17, 474 (1970).
14. J.L. Lachambre, F. Rheault and J. Gilbert, The Radio and Electronic Engineer, 42, 351 (1972).
15. H. Baumhacker and R.S. Lang, Phys. Lett., 47A, 429 (1974).
16. A.F. Gibson, M.F. Kimmitt and C.A. Rosito, Appl. Phys. Lett., 18, 546 (1971).

17. R. Fortin, F. Rheault, J. Gilbert, M. Blanchard, and J.L. Lachambre, Can. J. Phys., 51, 414 (1973).

18. P. Lavigne, J. Gilbert and J.L. Lachambre, Opt. Commun., 14, 194 (1975).

19. A.F. Gibson, C.A. Rosito, C.A. Raffo, and M.F. Kimmitt, Appl. Phys. Lett., 21, 356 (1972).

20. F. Keilmann, IEEE J. Quantum Electron., QE-12, 592 (1976).

21. A.F. Gibson, M.F. Kimmitt and B. Norris, Appl. Phys. Lett., 24, 306 (1974).

22. P.E. Dyer and D.J. James, Appl. Phys. Lett., 26, 331 (1975).

23. R.S. McDowell, H.W. Galbraith, B.J. Krohn and C.D. Cantrell, Opt. Commun., 17, 178 (1976).

24. B.J. Feldman and J.F. Figueira, Appl. Phys. Lett., 25, 301 (1974).

25. R. Fortin, M. Gravel, and R. Tremblay, Can. J. Phys., 49, 1783 (1971).

26. H.J. Seguin, K. Manes and J. Tulip, Rev. Sci. Instr., 43, 1134 (1972).

27. Yu-Li Pan, A.F. Bernhardt and J.R. Simpson, Rev. Sci. Instr., 43, 662 (1972).

28. C. Grigoriu and H. Brinkschulte, Phys. Lett., 42A, 347 (1973).

29. M.C. Richardson, A.J. Alcock, K. Leopold, and P. Burtyn, IEEE J. Quantum Electron., QE-9, 236 (1973).

30. P.R. Pearson and H.M. Lamberton, IEEE J. Quantum Electron., QE-8, 145 (1972).

31. A.K. Laflamme, Rev. Sci. Instr., 41, 1578 (1970).

32. P.W. Smith, M.A. Duguay and E.P. Ippen, "Mode-locking of Lasers", in Progress of Quantum Electronics, edited by J.H. Sanders and S. Stenholm (Pergamon, Oxford, 1974), Vol. 3.

33. J.A. Harrison, Brit. J. Appl. Phys., 18, 1617 (1967).

34. J.D. Cobine, Gaseous Conductors, (McGraw-Hill, New York, 1941) page 120.

35. J. Reid, E.A. Ballik and B.K. Garside, Opt. Commun., 12, 354 (1974).

36. H. Kogelnik, Bell Syst. Tech. J., 44, 455 (1965).

37. H. Kogelnik, E.P. Ippen, A. Dienes and C.V. Shank, IEEE J. Quantum Electron., QE-8, 373 (1972).

38. A.F. Gibson, M.F. Kimmitt and A.C. Walker, Appl. Phys. Lett., 17, 75 (1970).

39. P.J. Bishop, A.F. Gibson and M.F. Kimmitt, IEEE J. Quantum Electron., QE-9, 1007 (1973).

40. H. Brunet, IEEE J. Quantum Electron., QE-6, 678 (1970).

41. R.L. Abrams and A. Dienes, Appl. Phys. Lett., 14, 237 (1969).

42. Y.J. Kaufman, Appl. Opt., 15, 1530 (1976).

43. C.K. Rhodes and A. Szöke, Phys. Rev., 184, 25 (1969).

44. J.P. Gordon, C.H. Wang, C.K.N. Patel, R.E. Slusher, and W.J. Tomlinson, Phys. Rev., 179, 294 (1969).

45. N. Bloembergen, Opt. Commun., 15, 416 (1975).

46. W.E. Barch, H.R. Fetterman and H.R. Schlossberg, Opt. Commun., 15, 358 (1975).

47. J.I. Steinfeld, I. Burak, D.G. Sutton, and A.V. Nowak, J. Chem. Phys., 52, 5421 (1970).

48. A.V. Nowak and J.L. Lyman, J. Quant. Spectrosc. Radiat. Transfer, 15, 945 (1975).

49. I. Burak, J.I. Steinfeld and D.G. Sutton, J. Quant. Spectrosc. Radiat. Transfer, 9, 959 (1969).

50. O.R. Wood, II, P.L. Gordon and S.E. Schwarz, IEEE J. Quantum Electron., QE-5, 502 (1969).

51. J.P. Aldridge, H. Filip, H. Flicker, R.F. Holland, R.S. McDowell, N.G. Nereson and K. Fox, J. Mol. Spectrosc., 58, 165 (1975).

52. C.K. Patel and R.E. Slusher, Phys. Rev. Lett., 19, 1019 (1967).

53. F. Shimizu, Appl. Phys. Lett., 14, 378 (1969).

54. R.S. Taylor, E.A. Ballik, and B.K. Garside, J. Appl. Phys., 48, 662 (1977).

55. B.K. Garside, R.S. Taylor, and E.A. Ballik, Can. J. Phys., 55, 849 (1977).

56. J.L. Lyman and S.D. Rockwood, J. Appl. Phys., 47, 595 (1976).

57. J.J. Armstrong and O.L. Gaddy, IEEE J. Quantum Electron., 8, 797 (1972).

58. R.V. Ambartzumian, N.P. Furzikov, Yu. A. Gorokhov, V.S. Letokhov, G.N. Makarov, and A.A. Puretzky, Opt. Commun., 18, 517 (1976).

59. N.R. Isenor, V. Merchant, R.S. Hallsworth, and M.C. Richardson, Can. J. Phys. 51, 1281 (1973).

60. D.S. Frankel, Jr., J. Chem. Phys. 65, 1696 (1976).

61. K. Fox, Opt. Commun., 19, 397 (1976).

62. G. Herzberg, Infrared and Raman Spectra of Polyatomic Molecules, (Van Nostrand Reinhold Co., New York, N.Y., 1945).

63. W.H.J. Childs and H.A. Jahn, Proc. R. Soc. Lond., 169A, 451 (1939).

64. R.S. McDowell, J.P. Aldridge, and R.F. Holland, J. Phys. Chem., 80, 1203 (1976).

65. G.Z. Whitten and B.S. Rabinovitch, J. Chem. Phys., 38, 2466 (1963).

66. C.C. Jensen, W.B. Person, B.J. Krohn, and J. Overend, Opt. Commun., 20, 275 (1977).

67. C.B. Moore, J. Chem. Phys., 43, 2979 (1965).

68. R.V. Ambartzumian, Yu. A. Gorokhov, V.S. Letokhov, G.N. Makarov, and A.A. Puretskii, JETP Lett., 23, 22 (1976).

69. N.G. Basov, V.T. Galochkin, A.N. Oraevskii, and N.F. Starodubtsev, JETP Lett., 23, 521 (1976).

70. J.T. Knudtson and G.W. Flynn, J. Chem. Phys., 58, 1467 (1973). See also, R.D. Bates, Jr., J.T. Knudtson, G.W. Flynn, and A.M. Ronn, Chem. Phys. Lett., 8, 103 (1971).

71. W. Frie, Zeitschrift für Physik, 201, 269 (1967).

72. A.B. Petersen, J. Tiee, and C. Wittig, Opt. Commun., 17, 259 (1976).

73. R.S. Taylor, T.A. Znotins, E.A. Ballik, and B.K. Garside, J. Appl. Phys., in press.

74. Y.J. Kaufman, S. Ruschin, and U.P. Oppenheim, Appl. Opt., 16, 1187 (1977).

75. N. Bloembergen, C.D. Cantrell, and D.M. Larsen, "Collisionless Dissociation of Polyatomic Molecules by Multiphoton Infrared Absorption", in Tunable Lasers and Applications edited by A. Mooradian, T. Jaeger and P. Stokseth (Springer-Verlag, Berlin, 1976) page 162.

76. A.V. Nowak, 1977. Private communication.

77. E.A. Ballik, B.K. Garside, R.S. Taylor, and T.A. Znotins, Can. J. Phys., in press.

78. J. Reid, E.A. Ballik, and B.K. Garside, Opt. Commun., 13, 126 (1975).

79. A. Gondhalekar, N.R. Heckenberg, and E. Holzhauer, IEEE J. Quantum Electron., QE-11, 103 (1975).

80. A. Nurmikko, T.A. De Temple, and S.E. Schwarz, Appl. Phys. Lett., 18, 130 (1971).

81. T. DeTemple and A. Nurmikko, Opt. Commun., 4, 231 (1971).

82. W.R. Sooy, Appl. Phys. Lett., 7, 36 (1965).

83. R.G. Harrison, J. Phys. D.: Appl. Phys., 8, L203 (1975).

84. K. Boyer, Astronautics and Aeronautics, 11, No. 1, 28 (1973).

85. D.O. Ham and M. Rothschild, Opt. Lett., 1, 28 (1977).

86. B.J. Feldmann, IEEE J. Quantum Electron., QE-9, 1070 (1973).

87. V. Wang, C.R. Giuliano, S.D. Allen, R.C. Pastor, Proc. of a Symposium on Laser Induced Damage in Optical Materials, Boulder, Colo. U.S.A., 29-31 July 1975, (Washington, D.C., U.S.A: Nat. Bur. Stand. 1976) page 118-125.

88. T. Kamibayashi, S. Yonemochi, and T. Miyakawa, Appl. Phys. Lett. 24, 119 (1973).

89. B.K. Garside and T.K. Lim, J. Appl. Phys. 44, 2335 (1973).

90. J. Reid, B.K. Garside, and E.A. Ballik, IEEE J. Quantum Electron., QE-8, 449 (1972).

91. J. Reid, 1977. Private communication.

92. B.K. Garside, J. Reid, and E.A. Ballik, IEEE J. Quantum Electron., QE-11, 583 (1975).

93. G.T. Schappert, Appl. Phys. Lett., 23, 319 (1973).
94. E. Armandillo and I.J. Spalding, J. Phys. D.: Appl. Phys., 8, 2123 (1975).
95. H.G. Heard, Laser Parameter Measurements Handbook, (J. Wiley and Sons, New York, 1968) page 203. See also, A.M. Robinson, Tech. Note, DREV TN - 1989/71, (1971).
96. E.T. Gerry and D.A. Leonard, Appl. Phys. Lett., 8, 227 (1966).
97. P. Lorrain and D.R. Corson, Electromagnetic Fields and Waves, (W.H. Freeman and Co., San Francisco, 1970) page 471.
98. H. Risken and K. Nummedal, J. Appl. Phys., 39, 4662 (1968).
99. M. Sargent, III, Opt. Commun., 20, 298 (1977).
100. C.R. Phipps, S.J. Thomas, J. Ladish, S.J. Czuchlewski, and J.F. Figueira, Proc. of IEEE/OSA Conference on Laser Engineering and Applications, Washington, DC, U.S.A., June 1-3, 1977.
101. V.S. Letokhov, Sov. Phys. JETP, 28, 562 (1969).
102. P.G. Kryukov and V.S. Letokhov, IEEE J. Quantum Electron., QE-8, 766 (1972).
103. W.H. Glenn, IEEE J. Quantum Electron., QE-11, 8 (1975).
104. J. Gilbert, J.L. Lachambre, F. Rheault, and R. Fortin, Can. J. Phys., 50, 2523 (1972).
105. C.P. Ausschnitt, IEEE J. Quantum Electron., QE-13, 321 (1977).
106. A.J. Alcock, P.B. Corkum, and D.J. James, Appl. Phys. Lett., 30, 148 (1977).
107. E.D. Capron and O.L. Brill, Appl. Opt., 12, 569 (1973).
108. W. Kaiser, R.J. Collins, and H.Y. Fan, Phys. Rev., 91, 1380 (1953).

109. P.J. Bishop and A.F. Gibson, Appl. Opt., 12, 2549 (1973).

110. E.M. Garmire and A. Yariv, IEEE J. Quantum Electron., QE-3, 223 (1967).

111. A. Schmackpfeffer and H. Weber, Phys. Lett., 24A, 190 (1967).

112. E.A. Ballik, B.K. Garside, J. Reid, and T. Tricker, J. Appl. Phys., 46, 1322 (1975).

113. L. Mandel and E. Wolf, Reviews of Modern Physics, 37, 231 (1965).

114. F. Rheault, J.L. Lachambre, J. Gilbert, R. Fortin, and M. Blanchard, Opt. Commun., 8, 132 (1973).

115. J. Reid and K. Siemsen, Appl. Phys. Lett., 29, 250 (1976).